Exploring Immersed FEM, Material Design, and Biological Tissue Material Modeling

Srivatsa Bhat Kaudur

Dissertation submitted to the Faculty of the

Virginia Polytechnic Institute and State University

in partial fulfillment of the requirements for the degree of

Doctor of Philosophy

in

Aerospace Engineering

Mayuresh J. Patil, Co-chair

Rakesh K. Kapania, Co-chair

Daniel C. Hammerand

Gary D. Seidel

February 20, 2024

Blacksburg, Virginia

Keywords: Immersed FEM, Shape Optimization, Material Design, Lung Material Modeling, Hyperelasticity, Hyperviscoelasticity, Acoustics, Damage.

Exploring Immersed FEM, Material Design, and Biological Tissue Material Modeling

Srivatsa Bhat Kaudur

(ABSTRACT)

This thesis utilizes the Immersed Interface Finite Element Method (IIFEM) for shape optimization and material design, while also investigating the modeling and parameterization of lung tissue for Diver Underwater Explosion (UNDEX) simulations.

In the first part, a shape optimization scheme utilizing a four-noded rectangular immersed-interface element is presented. This method eliminates the need for interface-fitted mesh or mesh morphing, reducing computational costs while maintaining solution accuracy. Analytical design sensitivity analysis is performed to obtain gradients for the optimization formulation, and various parametrization techniques are explored. The effectiveness of the approach is demonstrated through verification and case studies. For material design, the study combines topological shape optimization with IIFEM, providing a computational approach for architecting materials with desired effective properties. Numerical homogenization evaluates effective properties, and level set-based topology optimization evolves boundaries within the unit cell to generate optimal periodic microstructures. The design space is parameterized using radial basis functions, facilitating a gradient-based optimization algorithm for optimal coefficients. The method produces geometries with smooth boundaries and distinct interfaces, demonstrated through numerical examples.

The thesis then delves into modeling the mechanical response of lung tissues, particularly focusing on hyperelastic and hyperviscoelastic models. The research adopts a phased

approach, emphasizing hyperelastic model parametrization while reserving hyperviscoelastic model parametrization for future studies. Alternative methods are used for parametrization, circumventing direct experimental tests on biological materials. Representative material properties are sourced from literature or refit from existing experimental data, incorporating both empirically derived data and practical values suitable for simulations. Damage parameter quantification relies on asserted quantitative relationships between injury levels and the regions or percentages of affected lung tissue.

Exploring Immersed FEM, Material Design, and Biological Tissue Material Modeling

Srivatsa Bhat Kaudur

(GENERAL AUDIENCE ABSTRACT)

This research explores the following themes: optimizing shapes, designing materials using repetitive identical building blocks, and understanding how divers' lungs respond to underwater explosions. When computationally analyzing structures with multiple materials, the conventional method involves creating meshes that align with material interfaces, which can be intricate and time-consuming. The Immersed Interface Finite Element Method (IIFEM) is introduced as a computational approach that simplifies this process, utilizing a uniform grid for analysis regardless of interface shape.

Consider a plate with a hole or other inclusions. Shape optimization seeks the optimal hole/inclusion shape for withstanding specific loading. Traditional optimization processes necessitate iterative mesh recreation, a step circumvented by employing IIFEM. This technique also extends to creating micro-building blocks of materials, enabling the architectural design of materials with desired qualities. Materials with specific properties, like strength or flexibility can be achieved.

This thesis also addresses the challenge of understanding how divers' lungs respond to underwater explosions, a crucial aspect of safety. Advanced computer models are used to mimic the behavior of lung tissue under shock loads. Directly testing materials and tissues can be difficult and restricted. Techniques like gathering data from scientific papers and refitting existing experimental data are utilized to obtain the information needed. Also, it is hard to directly measure how much damage an underwater explosion does to a diver's lungs.

Thus, the level of damage was quantified based on assertions about the relationship between different injury severities and how much lung tissue is affected.

Acknowledgments

First and foremost, I owe a debt of gratitude to all the teachers, both past and present, who have played a role in nurturing my passion for learning and fostering a scientific mindset. Their guidance, both direct and indirect, has been instrumental in shaping my academic journey.

I would also like to take this opportunity to express my gratitude to a few individuals whom I may not acknowledge as frequently as they deserve: my parents, my wife, my sister, and my brother. Their well wishes and support are the driving forces that have brought me to where I am today. It is because of you that this journey has been both possible and meaningful.

I would like to express my gratitude to Dr. Patil. The academic freedom that he provided encouraged me to take on challenges during my Ph.D. I have gained invaluable knowledge from our weekly discussions, which I always eagerly anticipated, and for that, I am truly thankful. A heartfelt thank you to Dr. Kapania for being an exceptionally supportive advisor, and for his guidance and encouragement. I am immensely grateful to Dr. Hammerand for extensive discussions, both during and outside working hours. Your time and assistance played a crucial role in my rapid acquisition of knowledge on various new topics during the latter part of my Ph.D. journey.

Lastly, I want to extend my appreciation to my roommates and friends. You made Blacksburg feel like home.

Contents

List of Figures

List of Tables

Chapter 1

Introduction

1.1 Overview of Finite Element Methods to handle discontinuities

There are two fundamentally different approaches to deal with non-smooth solutions. The first strategy is to use trial function spaces and meshes that conform to discontinuities and are refined near singularities and high gradients. Remeshing will be required to treat the evolution of such solutions. An efficient way to construct trial function spaces is given by classical finite element (FE) shape functions [1, 2]. There are also many meshfree shape functions which rely on the approximation properties of polynomials [3, 4] hence, there is great flexibility in the construction of polynomial approximation spaces.

The second technique is to enrich a trial function space such that the non-smooth solutions can be obtained independent of the mesh. Methods that extend the polynomial approximation spaces are called 'enriched methods' [5]. The enrichment can be of two flavors. One is called the 'extrinsic enrichment' where special shape functions are added (which are customized so as to capture jumps, singularities, etc.) to the polynomial approximation space. More shape functions and unknowns result in this kind of approximation. An alternative for this enrichment is to replace some or all of the shape functions in the polynomial approximation space by special shape functions that can capture discontinuous

solutions. This approach is called 'intrinsic enrichment' and the number of shape functions and unknowns is unchanged. These enriched methods can be further distinguished based on whether they are applied in the whole domain or in local subregions only. When the solution is considered globally non-smooth, a global enrichment is used; for example the high-frequency solutions of the Helmholtz equation. However, most non-smooth solution properties, such as jumps, kinks, and singularities, are local phenomena and it is then natural to employ the enrichment in local subdomains. Enriched methods can be thus classified based on the following: (i) the shape functions are meshfree or mesh-based, (ii) the enrichment is extrinsic or intrinsic, and (iii) the enrichment is realized globally or locally.

Special characteristics of the solution can be introduced to the trial function space by various methods: the partition of unity method (PUM) [6, 7] is considered as a basis for many of these methods. Partition of unity FEM (PUFEM) [8], the generalized FEM (GFEM) [9, 10], and the extended FEM (XFEM) [11, 12] are some of the examples where one uses this concept. The approximation in all of these methods is of the form

$$u^h(x) = \sum_i N_i(x)u_i + \text{enrichment terms} \tag{1.1}$$

where $N_i(x)$ are often classical FE shape functions. These type of approximation are called extrinsically enriched. With the methods based on the PUM-concept, arbitrary discontinuities may be treated on a fixed mesh. Because of the additional unknowns, this method is computationally expensive. In contrast to the standard PUM, in XFEM one can use a local extrinsic enrichment of the approximation space. Thereby, the number of additional unknowns is kept at a minimum.

Intrinsic enrichment for the treatment of arbitrary discontinuities uses an approximation of the form

$$u^h(x) = \sum_i N_i(x)u_i \tag{1.2}$$

so that no extrinsic enrichment terms are present. No additional unknowns are involved. The shape functions $N_i(x)$ are standard FE shape functions in those parts of the domain where a regular trial function space is locally adequate. Special shape functions are employed near discontinuities which are specifically designed so that they are able to capture them. Similarly, the method can be used to enrich the solution with known characteristics, such as the singular fields at a crack-tip. The resulting approximation may be called intrinsically enriched because the enrichment is implicitly incorporated in the basis [3]. The enrichment takes place on the level of this intrinsic basis. The same enrichment functions which are added extrinsically to the trial function space in standard XFEM may be used in this method in an intrinsic way.

Different enrichments can be realised in different parts of the domain based on the characteristics of the solution. This can be done by decomposing the domain into overlapping subdomains. In each subdomain, based on a corresponding nodal subset, a set of shape functions is either constructed by means of the Moving Least Square (MLS) technique or by using standard FE shape functions. The shape functions build a partition of unity over the subdomain. In order to obtain one final set of shape functions over the entire domain, for an approximation as in Equation (1.2), a coupling technique can be used. In this work, the focus is on one of the intrinsic extended FEM method known as the Immersed Interface Finite Element Method (IIFEM).

1.2   Immersed Interface Finite Element Method

Immersed interface methods use meshes that are not required to fit the interface. Hence, a uniform Cartesian grid or mesh can be used to solve partial differential equations with any boundary or with multiple domains with discontinuous coefficients. Immersed interface methods have been successfully used to solve problems in several areas including projectile penetration, propellant burn, metal forging, high energy deposition physics, fluid structure interaction, and shape optimization. Both finite difference and finite element based immersed methods have been developed. Immersed boundary method which uses finite difference scheme was developed by Peskin [13] to simulate cardiac mechanics. The main difference of the immersed boundary method relative to the conventional method is that the analysis is conducted on a Cartesian grid rather that a grid that conforms to the geometry of the immersed body. Similar methods that use finite difference methods include the following: the immersed interface method, where Leveque and Li [14] modified the standard central difference approximation on a uniform grid to guarantee second-order accuracy, the matched interface and boundary method [15], which generalizes interface and boundary method, and the cut cell method [16], where the cells cutting the interface or the body are treated specially. Additionally "Cartesian grid methods", variants of the immersed boundary method were developed for simulating inviscid flows over solid boundaries [17] and unsteady viscous flows [18]. Mittal and Iaccarino [19] has provided a comprehensive overview of the immersed boundary methods and its variants applied to fluid-structure interaction problems.

The finite element method (FEM) can also be used to solve problems over a uniform mesh with immersed interfaces. The penalty finite element method [20], extended FEM (XFEM) [21], generalised FEM (GFEM) [22], interface-enriched generalised FEM (IGFEM) [23], hierarchical interface-enriched generalised FEM (HIFEM) [24], cut FEM [25], and immersed

interface finite element method [26] are examples to name a few. Our study uses IIFEM [27, 28, 29] which modifies the trial functions in an element with immersed-interface. It has been predominantly used to solve elliptic interface problems [30, 31, 32]. The shape functions have been developed for both triangular [33] and rectangular elements [34, 35]. The IIFEM has also been applied to time dependent problems involving moving interfaces [36, 37].

IIFEM methods modify the Lagrange-type finite element spaces whose degree of freedom are the values at element nodes. The immersed finite element (IFE) spaces obtained from Lagrange-type finite element spaces are non-conforming as they are discontinuous across the edges. A partially penalised immersed finite element method [38, 39] was developed to handle the discontinuous IFE space. The approximation capabilities of such spaces for linear elasticity problems has been studied [40]. This method was extended to multi-domain and triple-junction points [41, 42]. Another class of IFE approximations [43] were based on nonconforming finite elements [44] whose continuity is imposed weakly through mean values over edges/faces. An unfitted discontinuous Galerkin formulation [45] has also been developed to solve interface problems. An alternative approach is to use a boundary capturing method [46] to formulate a second-order accurate FEM [47, 48], which was written in a weak form using Petrov-Galerkin formulation. A modified basis function is used as the approximating function and the conventional FEM basis functions are used as test functions. The method has been applied to $2D$ as well as $3D$ problems [49]. Patil [50] used a similar Petrov-Galerkin formulation with immersed FE space for triangular elements. A conceptual basis for bi-material patch test was also provided and an optimal convergence was shown. The patch test [51, 52, 53] is one of the techniques which is helpful in proving the consistency and convergence of the developed finite elements. Our work extends this to rectangular elements and uses the new method for shape optimization. The optimal error estimates of some IIFEMs for elasticity interface problems were also proved in [39, 54].

1.3 Shape Optimization using IIFEM

Structural shape optimization involves finding the optimal geometry of a structure to minimize or maximize certain structural properties/behaviours such as weight, compliance, stresses, or displacements subject to certain constraints. Usually shape optimization comprises of a design model, the analysis model, and the optimization algorithm [55]. A design model, typically employed in shape optimization, refers to the representation of the geometry or configuration of a structure or system that is subject to optimization. This model defines the shape, dimensions, and other geometric characteristics of the structure under consideration. It serves as the foundation for the optimization process, where adjustments and modifications are made to optimize certain performance criteria. In the context of shape optimization, the design model is often coupled with an analysis model, which simulates the behavior and performance of the structure under various conditions. The optimization algorithm then iteratively adjusts the design parameters of the design model based on feedback from the analysis model to achieve the desired objectives. The need for the link between the analysis and the design model is the source of inefficiency and inaccuracy [56].

Lagrangian shape optimization approaches consider the position of the boundary points or the material interfaces as a function of the shape design variables. The initial finite-element-based shape optimization studies used the nodal coordinates as the design variables [57, 58]. However, this approach leads to unrealistic design, mesh irregularities, and excessive number of design parameters [59]. For smooth boundaries, different geometric representations of the boundaries were considered. One such method considered coefficients of polynomials as design variables [60]. The main issue was highly oscillatory boundaries and the lack of local control as a change in one coefficient lead to a change in the entire shape. Both issues can be overcome by the use of splines such as B-splines and Non-Uniform Rational

B-Splines (NURBS). In all these methods, to define the relation between design and analysis models, a parameterization between design variables and finite element model is required during the optimization process. The design element concept [61], adaptive meshing [62], or remeshing [63] facilitates the link between the analysis and the design model. Some more techniques used are natural design variable concept [64], which uses loads as design variables and a parameter-free approach [65, 66], which eliminates communication between design and analysis model and uses filtering techniques [67] to ensure boundary smoothness. Even these methods require remeshing to accommodate large shape changes. The boundary element approach [68, 69] has been used to solve shape optimization problems. The main advantage of such methods is that they reduce the dimension by one and thus only boundary discretization is required. Isogeometric Analysis (IGA) based shape optimization [55] also avoids the communication between the design model and the analysis model as they are unified [70]. Mesh deformation and remeshing are the major drawback of the Lagrangian shape optimization methods. To update the mesh during each optimization iteration, both mesh deformation and remeshing can be used.

Mesh morphing is preferred for many problems because between successive iterations similar meshes, which have the same connectivity, are desired. Some examples of the mesh movement method are the spring analogy method [71], where the dynamic grid can be thought of as a network of fictitious linear and torsional springs, optimization based methods [72] which changes the mesh vertex positions and tackles problems like shape improvement, sliver removal and edge length equalization, the inverse distance weighted method [73] which interpolates the boundary node displacements to the interior of the domain, Delaunay graph method [74] and the radial basis function method [75, 76]. Different partial differential equations (PDE) can be used for mesh deformations like Laplace's equation [77], biharmonic PDEs [78], elasticity PDEs which when used is termed as pseudo-solid mesh movement or

the elastic solid method [79, 80, 81]. In the elastic solid method, the domain is assumed to be pseudo-elastic solid where the displacement of the boundary or an interface is specified and the other nodal displacements are obtained by solving the elasticity problem. We will use this technique for shape optimization to show the contrast between the developed method. These methods can result in tangled meshes with inverted elements which produce physically invalid solutions. To tackle this problem, a finite element method on the tangled mesh [82] has been developed, but this results in poor conditioned stiffness matrix. The creation of inverted elements can be decreased by choosing problem dependent stiffness coefficients [83]. The log-barrier approach [84] for the worst element mesh quality improvement and untangling is also proposed, and shows better untangling performance.

Eulerian shape optimization methods avoid mesh distortion issues arising from mesh morphing or remeshing as the computational finite element mesh is fixed during the optimization process. The common methods are level-set method [85, 86], fictitious domain method [87, 88], meshless method [89], density based topology [90], evolutionary structural optimization [91], material perturbation methods [92], trimmed IGA methods [93, 94], X/GFEM optimization method [95, 96], interface enriched generalized finite element [97] and the NURBS-based interface enriched GFEM [98]. A partially penalized immersed finite element method [99] has also been used to study shape optimization problems. Our study uses the immersed interface finite element method with Petrov-Galerkin formulation to perform shape optimization on a fixed mesh. Multi-material systems are considered. We use a Fourier-like representation to describe the shape of the material interface. The design variables are the coefficients of the Fourier-like curve. Analytical sensitivities are derived which avoids the inaccuracies encountered in finite differencing.

1.4   Material Design using Immersed FEM

Material design blurs the traditional distinction between structure and materials by shifting the focus from designing a structure with pre-existing materials to designing the material itself as an integral part of the structure. This approach challenges the conventional boundaries of engineering and opens up new possibilities for creating innovative and optimized designs. By modifying the microstructural architecture in unit cells, porous and composite materials can be designed that exhibit previously unattainable combinations of material properties at the bulk scale or with specific mechanical, thermal, or functional properties, leading to enhanced overall performance [100]. The term metamaterial is used if the material exhibits unusual material properties from the microstructural topology or geometry rather than the material composition. Material design deals with creating these artificial structures with unconventional or extreme responses suitable for specific applications.

Topology optimization has become a pivotal tool in the design and innovation of structures and materials [101]. It is a powerful computational technique used to discover the optimal configuration of structures and materials within a given design space for performance, efficiency, and sustainability aspects. Over the past few decades, this methodology has evolved significantly, leading to a wide range of applications across various industries [102, 103, 104, 105]. It has been used to create lightweight, high-performance components, improve energy efficiency, and streamline manufacturing processes. Topology optimization has its roots in the field of structural mechanics, with early work focusing on linear elasticity and compliance-based objectives. The seminal work by Bendsoe and Kikuchi [106] laid the foundation for the density-based approach, which involved distributing material continuously in a design space. This approach has since been extended and refined, incorporating various mathematical techniques and optimization algorithms. The density-

based approaches involve homogenization [107, 108, 109] and solid isotropic material with penalization (SIMP) [90, 110, 111, 112] methods. The other approaches include level set [113, 114, 115, 116, 117, 118, 119, 120], topological derivative [121], phase field [122], and evolutionary methods [91, 123]. A review paper by Sigmund and Maute [124] provides an overview of each of these approaches.

In this study, a level-set method will be used where an implicit description of the boundary is used to represent the geometry. Interested readers can refer to the review paper by van Dijk [125] for the details on the developmental history of the level-set method. Level set-based topology optimization involves three important components, the structural model, the level set function parametrization, and the optimization algorithm. The model selection includes choices of discretization, FEM type, and material/structural behavior choices like linear elastic, geometric nonlinearity, plasticity, etc. A widely used choice for parametrization is the use of basis functions and the design variables being the coefficients of these functions. The basis functions commonly used are standard FEM basis function [126, 127, 128], radial basis functions [129, 130], and spectral representations [131]. Optimization procedures that are widely used are Hamilton-Jacobi equations [132], generalized Hamilton-Jacobi with diffusion reaction terms [133], and mathematical programming methods such as sequential quadratic programming [134], convex linear approximations [135], method of moving asymptotes [136] and optimality criteria methods [137, 138]. Various regularization techniques are available in the literature [125] to suppress numerical artifacts, material islands, and sub-optimal local minima and to accelerate the convergence rate of the optimization algorithm. Level set methods have several merits such as smooth and distinct boundary description, higher topological flexibility, shape fidelity, and the ability to perform shape and topology optimization simultaneously.

Designing microstructure or a periodic unit cell with desired properties using numerical

homogenization was introduced by Sigmund [139]. The term inverse homogenization was used for this approach. The initial applications are in the field of elasticity such as designing microstructures with zero or negative Poisson's ratio [140, 141, 142, 143, 144], vanishing shear modulus [145, 146, 147], negative stiffness [148], negative compressibility [149], customised topological microstructures [150, 151, 152], maximum shear and bulk modulus [153, 154], increased bulk strength [155, 156], prescribed properties [157] and concurrent multiscale design [158]. Other applications include combined stiffness and fluid permeability problems [159], thermal expansion problems [160], thermal and electric conductivity problems [161] and phononic and photonic materials [162, 163]. The level set-based topology optimization has been extensively used for designing microstructures with desired effective properties. The parametric level set method (PLSM) [95, 164], stands out as a convenient and robust form of the level set method. It not only retains the advantageous aspects of the standard level-set method but also effectively eliminates its drawbacks [165]. Within the framework of PLSM, the level set function is interpolated through compactly supported radial basis functions. Consequently, the progression of structural boundaries corresponds to the evolution of expansion coefficient values. PLSM readily accommodates various established and efficient optimization algorithms [166, 167], such as the optimality criteria, method of moving asymptotes, sequential quadratic programming, etc. PLSM demonstrates remarkable proficiency in solving diverse optimization problems, including challenges like functionally graded materials [168], multi-material systems [169, 170], and robust optimization [171].

In this work, we utilize the rectangular IIFEM elements [172] with Petrov-Galerkin formulation in conjunction with level set-based topological shape optimization for the design of optimal material microstructures.

1.5   Overview of Lung Material Modeling

Lungs are natural porous structures [173]. They are tree-shaped structures with clusters of air sacs called alveoli [174]. Each air sac is surrounded by tiny capillaries. The alveoli, alveolar ducts, and bronchioles together are termed lung parenchyma. A typical adult human has around 480 million alveoli in their lungs [175], where gas exchange occurs between the lungs and the bloodstream. Each lung is divided into lobes: the right lung typically has three lobes (upper, middle, and lower), while the left lung has two lobes (upper and lower), allowing for efficient oxygenation and ventilation. The bronchial tube tree refers to the branching network of airways that conduct air into and out of the lungs. It starts with the trachea, which bifurcates into the left and right main bronchi, further branching into smaller bronchi, bronchioles, and ultimately terminating in the alveoli. This intricate network provides pathways for air to travel and ensures proper distribution of air throughout the lungs, facilitating gas exchange and maintaining respiratory function.

Depending on the analysis type and the response being sought, either lung geometry and airflow characteristics or its material/structural response characteristics are studied. If the flow characteristics are of interest, lung airways, and other branching transport networks can be thought of as fractal-like structures [176]. For the material/structural response the lung material is usually assumed to be viscoelastic and highly nonlinear. To get the overall constitutive relations between stress and strain in lung tissue, one approach widely used is homogenization [177, 178, 179]. In this approach a representative substructural lung element is considered, its geometry is idealized, and its elastic properties are specified. From the applied homogeneous strain, the average stresses are calculated to get the effective material properties of the lung.

Mechanical properties of the airways, lung parenchyma, interstitial matrix, alveolar surface,

and pulmonary circulation contribute to the combined mechanics of the lung. The behavior of lung tissue emerges as a macroscopic phenomenon from the interactions of its microscopic constituents [180]. The emergence behavior implies that the lung response is not a sum of the response of its individual constituent parts. The way in which the components are arranged with respect to each other and the way they interact matters. Lung mechanics can be classified into static and dynamic lung mechanics based on whether we consider properties accounting for the changing volume of lung and chest wall motion. The dynamic and static structural behavior of the lung depends on its viscoelastic properties. The dynamics of gas flow into a viscoelastic porous medium that models the lung structure can be taken into account to increase the complexity and fidelity of a model.

Experimentally, lung behavior is studied as a time-dependent measure of pressure and flow [181]. Mathematical models of the pressure-volume curve of a microscopic element of the lung based upon the structural and elastic properties of the constituent materials have been developed so as to match the pressure-volume curves of the whole lung [182]. Mathematical frameworks were also developed to model lung tissue stress relaxation and tissue impedance accurately. An empirical equation involving a power law was used to capture stress relaxation and a constant phase impedance was used for the impedance function. It was also identified that five classes of input-output systems can provide this behavior [183]: (i) nonlinear constitutive equations, (ii) differential equations with time dependent coefficients, (iii) continuous distribution of time constants, (iv) complex dynamic systems exhibiting self-similar properties, and (v) input-output relationships that include fractional derivatives.

Models closely resembling the quasilinear viscoelasticity, in which the static stress-strain behavior is separable from the dynamic stress relaxation have also been developed [184]. The bulk rheological behavior of lung tissue is linked to the properties of its constituents and their

interactions. These properties contribute significantly to both complex and nonlinear elastic and dissipative mechanical properties of the lung. These are purely phenomenological and governed by ordinary differential equations, such as those consisting of a collection of springs and dashpots. Elastoplastic elements [185] and nonparametric Volterra series expansions [186] have also been used for modeling these behaviors. However, these models have no clear physiological or anatomic analogs. Mechanistically-based models of the complex rheology of biological soft tissue [187] and soft tissue viscoelasticity based on gradual recruitment of linearly viscoelastic fibers have also been developed [188]. The constant phase model for the lung was based on an empirical pressure response to step changes in gas volume as performed with rubber balloons and excised lung tissue [189]. However, the model did not directly address the link between tissue properties and lung properties [173]. If the lung was identical to a rubber balloon, then the lung input impedance would have matched the parenchymal tissue impedance. However, anatomically, the lung structure is more complex with cavities present. Thus, the constant phase model is only good for isolated tissue strips and intact lungs. It does not establish or help describe the theoretical linkage between them. To capture all of the effects, the lung can be considered as a fluid-solid system described by Navier-Stokes equations with stress-strain relations for alveolar tissues [190]. Thus, for dynamic lung biomechanics, the Navier-Stokes equations for gas transport, together with the viscoelastic equations for porous material at the micro- and macro-levels can be used.

Complicated and very high-fidelity models exist that couple detailed gas-flow modeling with the biomechanical properties of the lung at the alveolar level to fully describe pressures and flow in the lung. The fluid dynamics of the air, the mechanics of the bronchial network walls, and the coupling between these motions can be completely described using equations of continuum mechanics [190]. However, the geometric complexity of the lung makes computing a numerical solution of these equations computationally unrealizable. It is realistic to only

get solutions for a tiny fraction of the whole lung, such as a few airways or the alveoli.

In this study, the focus will be on using hyperelastic and hyperviscoelastic models for lung undamaged and damaged mechanical response. Lung parenchyma features an open-foam-like architecture which contributes to its nonlinear response which typically can be modeled using hyperelastic or hyperviscoelastic material models. Here "hyperviscoelastic" refers to a viscoelastic generalization of the hyperelastic models. Under blast loading, a number of damage mechanisms are expected. This includes physiological alterations such as contusions/hematoma, perforations, and lacerations which result from peak stresses and strains or continued large amplitude oscillation. Contusions/hematoma and large-scale tearing can be represented using continuum damage modeling and element failure.

1.6 Lung and Biological Tissue Material Parameterization

Parameterizing the hyperelastic and hyperviscoelastic material models, along with damage initiation and evolution, is essential. In this thesis, a deliberate choice has been made to place the primary emphasis on the parametrization of hyperelastic models, reserving the parametrization of the hyperviscoelastic models for future studies. The reason behind this decision stems from the complex and multifaceted nature of the research, which demands a phased approach.

Ideally, material parametrization would involve calibrating the models using experimental data to guide the selection of material and damage properties. However, the necessary material constitutive data is not collected, and blast measurements on biological materials are not conducted. Blast testing, particularly involving live tissue, is inherently constrained

due to ethical considerations and safety concerns. The primary focus of this study is on developing the modeling framework. Also, this research involves a collaborative effort among multiple team members [1]. The task of conducting a partial validation using representative engineering materials is undertaken by other members of the team. To address the limitation of not directly performing the experimental testing on biological materials, various techniques will be utilized to obtain representative properties. Numerous literature sources are gathered and cataloged. Many of these sources provide experimentally based values for lung and other biological tissue responses, while others offer practical values for meaningful simulations. In addition to using values directly from these sources or refitting any experimental data contained therein, we conduct a series of small-scale trade studies. These studies will involve simulating material responses both with and without damage, providing stress-strain responses. These responses will be analyzed against engineering judgment in trying to correlate incurred lung damage with probable lung injuries for a range of blast loads.

1.7　Dissertation Organization

The thesis sets off by providing an overview of the methodologies employed and the existing body of literature on the subject. Thereafter, each proceeding chapter deals with the details of the models employed and their implementations. This includes a description of the theoretical and computational frameworks, and mathematical formulations that underpin these models. The highlights of each chapter are given below:

1. Chapter 2 - Shape Optimization with Immersed Finite Element Method.

    (a) A new trial function space for rectangular elements with an immersed interface

---

to solve linear, 2D elasticity problems.

    i. A non-conformal, Petrov-Galerkin (ncPG) formulation.

    ii. Numerical conditioning, convergence, and bi-material patch test.

(b) Sensitivity analysis for gradient calculations during shape optimization.

    i. Analytical sensitivity of the solutions to the interface shape.

    ii. The sensitivity of the element stiffness matrix to compute the sensitivity of the global stiffness matrix, and then of the solution of the problem to change in the interface and the shape design variables.

    iii. Straightforward implementation unlike Lagrangian methods for shape optimization

(c) Various verification and example test cases showing ncPG-IIFEM based on rectangular elements' accuracy compared to conventional interface-fitted finite elements.

(d) Gradient-based design optimization based on the analysis and sensitivity calculation leading to optimal solutions to verification test cases and interesting results for other test cases.

2. Chapter 3 - Material Design using Topology Optimization with Immersed Interface FEM.

(a) Periodic boundary conditions are applied and numerical homogenization is used to evaluate the effective stiffness tensor.

    i. Application of periodic boundary conditions is straightforward in IIFEM.

    ii. Edge nodal forces are considered as unknowns of the IIFEM formulation for the applied periodic boundary conditions.

iii. Effective stiffness tensor calculated using the summation of edge nodal forces.

(b) The design space is parameterized using Wendland radial basis functions.

i. Compactly supported Wendlands functions used for the level set representation reduce the computational cost for gradient calculations.

(c) Standard gradient-based optimization algorithms are used to find the optimal coefficients of the radial basis functions.

i. Adjoint formulation for sensitivities.

(d) Topology optimization of a cantilever beam and a Michell structure subjected to specific point loads.

(e) Metamaterials with extreme bulk modulus, shear modulus, and negative Poisson's ratio are obtained.

i. A range of new and interesting microstructured materials exhibiting specific mechanical properties.

3. Chapter 4 - Material Modeling with Damage for Diver UNDEX Simulations.

(a) Hyperelastic material models as Abaqus/Explicit VUMAT user subroutines.

(b) Hyperviscoleastic models as Abaqus/Standard UMAT and Abaqus/Explicit VUMAT user subroutines.

(c) Hyperelastic and hyperviscoleastic models with damage as Abaqus/Explicit VUMAT user subroutines.

4. Chapter 5 - Biological Material Response Parametrization

(a) Parameterize the hyperelastic material models, as well as the associated damage initiation and final failure.

        i. Optimization in Isight to fit model parameters to available experimental data.

       ii. Utilize available injury assessment data.

   (b) Diver Torso UNDEX Simulations.

5. Chapter 6 - Summary and Outlook

Chapter 2

Shape Optimization using IIFEM

Shape Optimization using conventional interface-fitted finite element method requires either mesh morphing or remeshing, which is computationally expensive and prone to errors due to sub-optimal mesh or solution interpolation. In this chapter, we present a shape optimization scheme which uses a four-noded rectangular immersed-interface element circumventing the need for interface-fitted mesh for finite element analysis, and mesh morphing or re-meshing for shape optimization. The analysis problem is solved using a non-conformal, Petrov-Galerkin (ncPG) formulation. We use non-conformal trial functions with conformal test functions. A fixed structured grid with a linear approximation for the interface within each element is used. We perform a bi-material patch test to confirm the consistency and convergence of the immersed-interface finite element method (IIFEM). The convergence of the displacement and stress error norms are of the same or slightly better order compared to the interface-fitted FEM. Thus, IIFEM reduces the cost of meshing without compromising the accuracy of the solutions obtained. We then perform analytical design sensitivity analysis to obtain the gradient of the global stiffness matrix with respect to shape design variables. The sensitivities are used in the gradient-based optimization formulation of the shape design problem. We present several ways to parametrize the design space. Finally, verification and case studies are presented to demonstrate the accuracy and potential of the approach.

2.1 Trial Functions for the IIFEM and the Petrov-Galerkin Formulation

2.1.1 Calculation of trial functions

Consider a rectangular immersed-interface element as shown in Figure 2.1. We consider a linear approximation of the interface in each element. Bilinear polynomials are used to form the trial functions on each rectangular element. For elements with immersed-interface, we start with independent bilinear polynomial in each domain [33]. Conventional finite element trial functions are uncoupled and are written independently for each displacement component; however, the trial functions for IIFEM are written for the displacement vector as the displacement components are coupled. The linear interface $\mathbf{\Gamma}_e$ divides the rectangular domain Ω_e into two subdomains $\mathbf{\Omega}_e^b$ and $\mathbf{\Omega}_e^y$ as shown in Figure 2.1. The trial function vector $\mathbf{\Phi}(x, y)$ can be represented as follows:

$$
\mathbf{\Phi}(x, y) =
\begin{cases}
\mathbf{\Phi}^b(x, y) = \begin{pmatrix} u^b(x, y) \\ v^b(x, y) \end{pmatrix} = \begin{cases} c_1 + c_2 x + c_3 y + c_4 xy \\ c_5 + c_6 x + c_7 y + c_8 xy \end{cases} & \forall (x, y) \in \mathbf{\Omega}_e^b \\
\mathbf{\Phi}^y(x, y) = \begin{pmatrix} u^y(x, y) \\ v^y(x, y) \end{pmatrix} = \begin{cases} c_9 + c_{10} x + c_{11} y + c_{12} xy \\ c_{13} + c_{14} x + c_{15} y + c_{16} xy \end{cases} & \forall (x, y) \in \mathbf{\Omega}_e^y
\end{cases}
\tag{2.1}
$$

Two assumptions are made to simplify the approximation of the interface: (i) The mesh size is assumed to be sufficiently small, thus the interface will not intersect the boundary at more than two points unless it is a part of that edge, and (ii) if the interface intersects the boundary of a rectangular element at two points, then these two points will be on different edges of
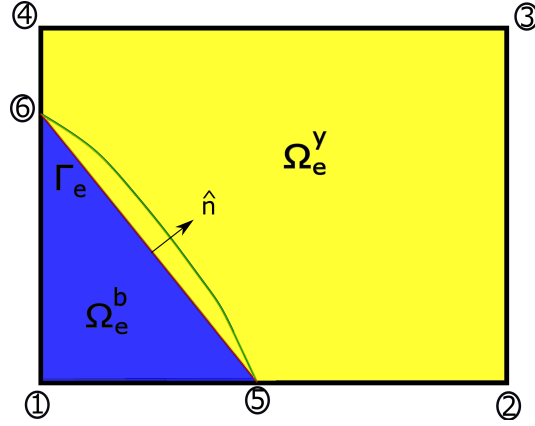
Figure 2.1: Local linear approximation of an interface separating two materials in an immersed rectangular element.
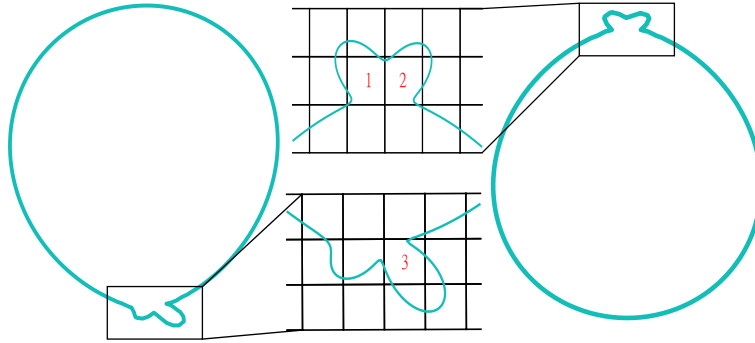
Figure 2.2: Examples of multiple intersections in a single element for an interface.

this element [35]. Any parametric representation that allows for a wide range of curves has the possibility of producing more than two intersection points. Some configurations of multiple intersection points as shown in elements 1, 2, and 3 in Figure 2.2 can be avoided by either finer mesh or smoother design space. The 16 unknown constants in the trial functions are calculated by solving 16 linear equations. The value of the FE function at the four nodes provides 8 conditions, the continuity of the FE function over the interface requires 6 equations because of the bilinear nature of the approximating functions, and the traction continuity in an integral sense at the interface provides 2 more equations. The prescribed

displacement vector on each node is given as follows:

$$\boldsymbol{\Phi}(x_j, y_j) = \begin{pmatrix} u_{2j-1} \\ u_{2j} \end{pmatrix} \qquad j = 1, 2, 3, 4 \tag{2.2}$$

where (x_j, y_j) is the jth nodal coordinate and $\begin{pmatrix} u_{2j-1} & u_{2j} \end{pmatrix}^T$ is the prescribed value of the trial function vector at that node.

The basic idea of IFE methods is to employ local basis functions formed according to the interface jump/continuity conditions. The IFE methods do not locally solve the interface problem and the trial functions are always piecewise polynomials. To satisfy continuity, the standard method is to impose continuity over two interface points and continuity of the mixed partial derivative. The displacement interface continuity restrictions are as follows:

$$\begin{aligned} \boldsymbol{\Phi}^b(x_5, y_5) &= \boldsymbol{\Phi}^y(x_5, y_5) \\ \boldsymbol{\Phi}^b(x_6, y_6) &= \boldsymbol{\Phi}^y(x_6, y_6) \\ \frac{\partial^2 \boldsymbol{\Phi}^b}{\partial x \partial y} &= \frac{\partial^2 \boldsymbol{\Phi}^y}{\partial x \partial y} \end{aligned} \tag{2.3}$$

It is shown later that these set of equations lead to ill-conditioning when the interface length approaches zero. Therefore, we replace them with displacement, slope and the mixed partial derivative continuity at the midpoint of the interface. Because the trial function is piecewise bilinear, the stress is not constant along the interface and thus the traction continuity will be weakly imposed in the integral form as follows:

$$\int_c \boldsymbol{n}^T \cdot \boldsymbol{C}^b \cdot \boldsymbol{\mathcal{D}} \cdot \boldsymbol{\Phi}^b ds = \int_c \boldsymbol{n}^T \cdot \boldsymbol{C}^y \cdot \boldsymbol{\mathcal{D}} \cdot \boldsymbol{\Phi}^y ds \tag{2.4}$$

where $\boldsymbol{\mathcal{D}}$ is the 3×2 differential operator in Voigt notation, $\boldsymbol{C}^b$ and $\boldsymbol{C}^y$ is the stiffness matrices

for the material domains $\boldsymbol{\Omega}_e^b$ and $\boldsymbol{\Omega}_e^y$ respectively, and $\boldsymbol{n}$ is a 3×2 matrix of outward normals at the interface:

$$\boldsymbol{n}^T = \begin{bmatrix} n_1 & 0 & n_2 \\ 0 & n_2 & n_1 \end{bmatrix} \tag{2.5}$$

where n_1 and n_2 are the components of $\boldsymbol{n}$.

Combining Equations 2.2, 2.3, and 2.4, we get the following set of equations:

$$\begin{bmatrix} \boldsymbol{I}_{8 \times 8} \\ \boldsymbol{0}_{8 \times 8} \end{bmatrix} \begin{bmatrix} u_1 & u_2 & \dots & u_7 & u_8 \end{bmatrix}^T = \begin{bmatrix} \boldsymbol{C_f} \end{bmatrix}_{16 \times 16} \begin{bmatrix} c_1 & c_2 & \dots & c_{15} & c_{16} \end{bmatrix}^T \tag{2.6}$$

The coefficient matrix $\boldsymbol{C_f}$ [33] is modified to avoid ill-conditioning. We replace the first two equations from equation 2.3 by the displacement and slope continuity at the midpoint of the interface. Also, the traction continuity equation is length scaled and modulus scaled, the reason for which will be discussed in the upcoming sections. Because the traction continuity equation has the constitutive matrix, $\boldsymbol{C_f}$ depends on whether the element is plane stress or plane strain.

From Equation 2.6 and 2.1 we have,

$$\begin{aligned} \begin{bmatrix} u^b & v^b & u^y & v^y \end{bmatrix}^T &= [\boldsymbol{T}] \begin{bmatrix} c_1 & c_2 & \dots & c_{15} & c_{16} \end{bmatrix}^T \\ &= [\boldsymbol{T}] \begin{bmatrix} \boldsymbol{C_f} \end{bmatrix}_{16 \times 16}^{-1} \begin{bmatrix} \boldsymbol{I}_{8 \times 8} \\ \boldsymbol{0}_{8 \times 8} \end{bmatrix} \begin{bmatrix} u_1 & u_2 & \dots & u_7 & u_8 \end{bmatrix}^T \end{aligned} \tag{2.7}$$

where T is given by

$$\boldsymbol{T} = \boldsymbol{I}_{4\times4} \bigotimes \begin{bmatrix} 1 & x & y & xy \end{bmatrix} = \begin{bmatrix} 1 & x & y & xy & \boldsymbol{0}_{1\times12} \\ \boldsymbol{0}_{1\times4} & 1 & x & y & xy & \boldsymbol{0}_{1\times8} \\ \boldsymbol{0}_{1\times8} & 1 & x & y & xy & \boldsymbol{0}_{1\times4} \\ \boldsymbol{0}_{1\times12} & 1 & x & y & xy \end{bmatrix} \tag{2.8}$$

where the the tensor product of two matrices $\boldsymbol{A}_{m\times n} = [a_{ij}]$ and $\boldsymbol{B}_{p\times q}$ is as follows:

$$\boldsymbol{A} \bigotimes \boldsymbol{B} = \begin{bmatrix} a_{11}\boldsymbol{B} & a_{12}\boldsymbol{B} & \dots & a_{1n}\boldsymbol{B} \\ \vdots & \vdots & \ddots & \vdots \\ a_{m1}\boldsymbol{B} & a_{m2}\boldsymbol{B} & \dots & a_{mn}\boldsymbol{B} \end{bmatrix} \tag{2.9}$$

Equation 2.7 can thus be rewritten in terms of shape functions as:

$$\begin{bmatrix} u^b & v^b & u^y & v^y \end{bmatrix}^T = [\boldsymbol{N}]_{4\times8} \begin{bmatrix} u_1 & u_2 & \dots & u_7 & u_8 \end{bmatrix}^T \tag{2.10}$$

where the shape functions for the displacement components are given by

$$[\boldsymbol{N}]_{4\times8} = [\boldsymbol{T}] \left[\boldsymbol{C_f}\right]_{16\times16}^{-1} \begin{bmatrix} \boldsymbol{I}_{8\times8} \\ \boldsymbol{0}_{8\times8} \end{bmatrix} \tag{2.11}$$

Henceforth, we denote $\boldsymbol{\phi}_i$ as the ith column of the 1st two rows in Equation 2.11, if $(x,y) \in \boldsymbol{\Omega}_e^b$ or the next two rows if $(x,y) \in \boldsymbol{\Omega}_e^y$.

The trial functions of the IIFEM are coupled. A nodal deformation in the x-direction will lead to a deformation in x as well as y-direction and vice versa. Figure 2.3 illustrates this effect by providing the eight nodal elemental trial function for an example interface element.
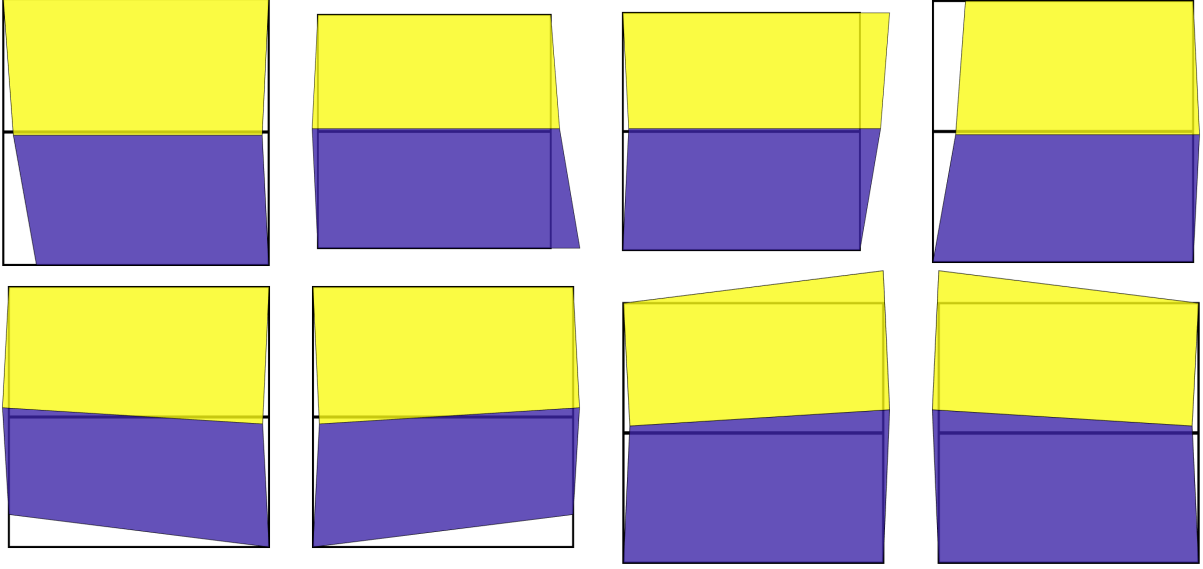
Figure 2.3: Nodal IIFEM trial functions corresponding to the eight nodal degrees of freedom for an example immersed-interface finite element.

(a)   (b)   (c)
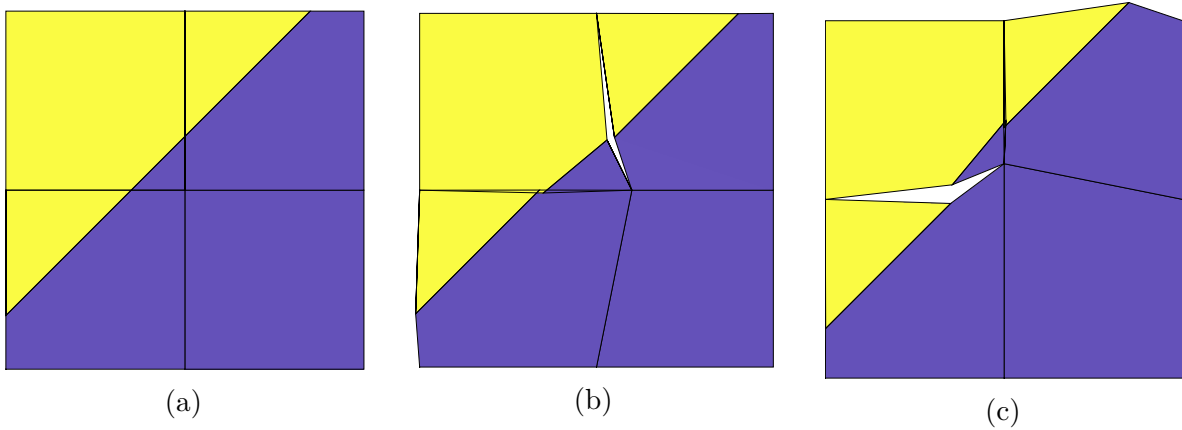
Figure 2.4: Global IIFEM trial functions: (a) an example patch of elements with the interface passing through three elements; (b) trial function corresponding to x-direction displacement degree of freedom of the central node; (c) trial function corresponding to y-direction displacement degree of freedom of the central node.

Just the x-deformation of the nodes causes a deformation in the y-direction which can be seen from the displacement of the interface of the top four elements in Figure 2.3. Similarly, the bottom four deformations in Figure 2.3 illustrate the existence of the displacement in the horizontal direction dependent on the vertical degrees of freedom.

IIFEM trial functions lead to a nonconformal displacement field at the element edges. Only the edges that intersect with an immersed material interface exhibit nonconformality. To illustrate this, we consider a patch ($E_b = 1, E_y = 10, \nu_b = \nu_y = 0.3$) which includes all the elements connected to a given node and a straight line interface that passes through three elements. Figure 2.4 shows the nodal trial functions over the compact support of four rectangular elements. Non-material region or an overlap region is visible across the edges through which the interface passes. The displacements, even though they look nonphysical, are highly unlikely to occur unless a very coarse grid is used. As the mesh size reduces, the solution approaches piecewise-constant strain and stress state, and the above trial function space can exactly represent this general solution.

2.1.2 Assessment of ill-conditioning during trial function calculation

During the calculation of trial functions, the obtained coefficient matrix $\left[C_f\right]_{16\times16}$ in Equation 2.6 has to be inverted. There are a few possible interface configurations and conditions which generate an ill-conditioned coefficient matrix. Physically, there should not be any issues in calculating the trial functions as the transition from a single material element to an immersed interface element and back is smooth. Computationally calculating these trial functions involves solving a set of linear equations and thus, might become ill-conditioned if proper care is not taken to normalize, scale or non-dimensionalize these equations. The ill-conditioning in the immersed interface case occurs due to the interface length, element size or the ratio of material properties being at their extremes. One such case is shown in [33]. To avoid ill-conditioning, the equations are modified in a similar fashion as done in the case of triangular elements [50]:

- Use normalized coordinates instead of global coordinates. This guarantees that the coordinates and the element size are of the same order.

- Convert the two point displacement continuity to a displacement and slope continuity at the midpoint of the interface. This eliminates ill-conditioning due to the intersection nodes of the interface coming close to each other.

- Normalize the traction continuity equations using the largest material stiffness. This guarantees well-conditioning even when the material property ratios are large.

- Normalize the traction continuity equations using the length of the interface. This eliminates the ill-conditioning due to the interface length approaching zero.

Figure 2.5a shows the increase in the condition number with an increase in the ratio of the absolute value of the global nodal coordinates to the size of the element h, without normalization of the nodal coordinates. This ratio is proportional to the number of elements. The plot also shows that the use of normalized coordinates eliminates this ill-conditioning. Figure 2.5b shows the increase in ill-conditioning as the interface length approaches zero. Using slope and displacement continuity instead of two-point displacement continuity eliminates ill-conditioning. Figure 2.5c shows the variation of condition number as the interface length approaches zero with and without interface length scaled traction continuity equations. The plot shows that the use of scaled equations eliminates this ill-conditioning. Figure 2.5d shows the variation in the condition number with the material stiffness ratio E_2/E_1, with and without modulus scaled traction equation. The use of normalized traction continuity equation assures a well-conditioned system of equations for the trial function calculations. With the following recommendation, the system of equations is well-conditioned for any combination of large stiffness ratios, small element size to coordinate ratio, and arbitrary interface length/orientation.
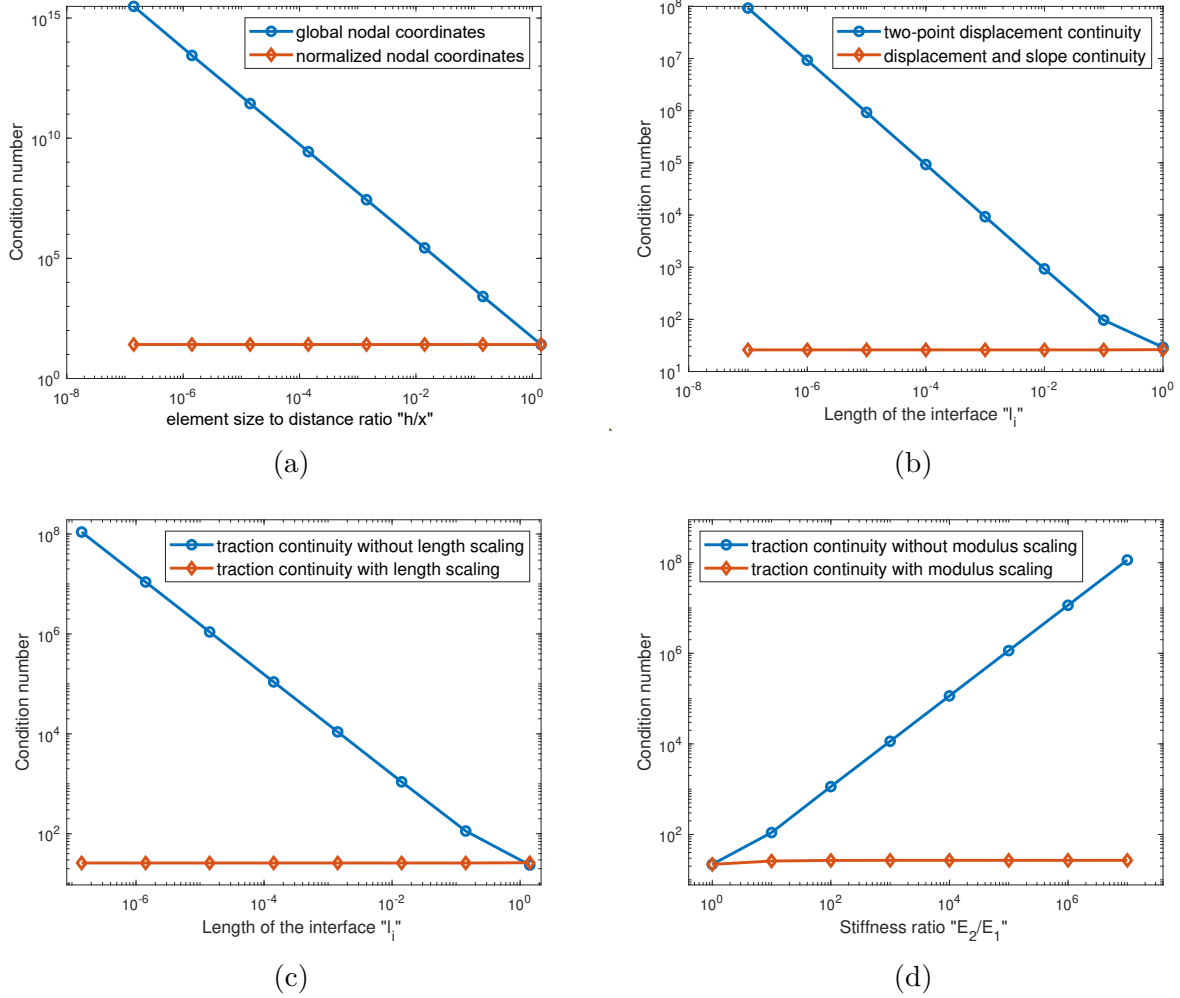
Figure 2.5: Comparison of condition number with and without the recommended normalizations: (a) the effect of global vs local normalized coordinates; (b) the effect of using two point displacement continuity vs displacement and slope continuity at the center of the interface; (c) the effect of length of the interface on the traction continuity equations; (d) the effect of stiffness ratio of the two materials.

2.1.3 Petrov-Galerkin formulation

A Petrov–Galerkin approximation is used to convert the vector equillibrium equation in the differential form to a weak form. The 2D linear elasticity equilibrium equation in Voigt

notation is as follows:

$$\mathcal{D}^T \cdot (C(\boldsymbol{x}) \cdot \mathcal{D} \cdot \boldsymbol{u}(\boldsymbol{x})) + \boldsymbol{f} = 0 \quad x \in \boldsymbol{\Omega} \tag{2.12}$$

where $\mathcal{D}$ is the 3×2 differential operator in Voigt notation, C is the stiffness matrix or strain/stress matrix, $\boldsymbol{u}$ is the 2×1 displacement field over the domain $\boldsymbol{\Omega}$, and $\boldsymbol{f}$ is the 2×1 applied body force field per unit area. A Petrov–Galerkin approximation of the vector equillibrium equations in the strong form is given as:

$$\int_{\Omega} [\mathcal{D}^T \cdot (C(\boldsymbol{x}) \cdot \mathcal{D} \cdot \boldsymbol{u}(\boldsymbol{x}))] \cdot \boldsymbol{v}(\boldsymbol{x}) dA + \int_{\Omega} \boldsymbol{f} \cdot \boldsymbol{v}(\boldsymbol{x}) dA = 0 \tag{2.13}$$

where $\boldsymbol{v}(\boldsymbol{x})$ is the vector test function or the weight function of the equivalent weighted residual formulation. The weak form can be obtained by integration by parts and applying Green's theorem:

$$- \int_{\Omega} [(C(\boldsymbol{x}) \cdot \mathcal{D} \cdot \boldsymbol{u}(\boldsymbol{x}))] \cdot [\mathcal{D} \cdot \boldsymbol{v}(\boldsymbol{x})] dA + \int_{\partial\Omega} \boldsymbol{T} \cdot \boldsymbol{v}(\boldsymbol{x}) ds + \int_{\Omega} \boldsymbol{f} \cdot \boldsymbol{v}(\boldsymbol{x}) dA = 0 \tag{2.14}$$

where $\partial\Omega$ is the boundary of the domain, and $\boldsymbol{T}$ is the traction on the boundary given by $\boldsymbol{T} = \boldsymbol{n}^T \cdot C \cdot \mathcal{D} \cdot \boldsymbol{u}(x)$, and $\boldsymbol{n}$ represents 3×2 matrix of the outward normals.

Assume that the domain $\boldsymbol{\Omega}$ is rectangular and let it be discretized into a set of nonoverlapping rectangular elements Ω_e such that $\bigcup \boldsymbol{\Omega}_e = \boldsymbol{\Omega}$. Now, the weak formulation is discretized using a finite element discretization. Let g be the set of all interior edges between elements and let b be the set of all boundary edges. The trial function is non-conformal, but the test functions are the standard FE shape functions and are conformal. The interelement traction term, which can be split into traction continuity and test function continuity terms, cancels out on each interior edge g due to the opposing contribution of the elements that share

the edge and the conformality of the test functions [50]. Thus, the above integral can be distributed over the elements as:

$$-\sum_e \int_{\Omega_e} [(\boldsymbol{C}(\boldsymbol{x}) \cdot \boldsymbol{D} \cdot \boldsymbol{u}(\boldsymbol{x}))] \cdot [\boldsymbol{D} \cdot \boldsymbol{v}(\boldsymbol{x})] dA + \sum_b \int_{\gamma_b} \boldsymbol{T}^b \cdot \boldsymbol{v}(\boldsymbol{x}) ds + \sum_e \int_{\Omega_e} \boldsymbol{f} \cdot \boldsymbol{v}(\boldsymbol{x}) dA = 0 \quad (2.15)$$

where e is a set of all elements, $\boldsymbol{\Omega}_e$ is the domain of each element, γ_b is the intersection of an element boundary with the domain boundary, and $\boldsymbol{T}^b$ is the prescribed or unknown traction on the boundary.

The nodal trial functions for each element is given by:

$$\boldsymbol{u}^e(\boldsymbol{x}) = \sum_{i=1}^{8} \boldsymbol{\phi}_i^e(\boldsymbol{x}) u_i^e \quad (2.16)$$

where u_i^e are the eight element nodal degrees of freedom. As described earlier, $\boldsymbol{\phi}_i$ is the ith column of the first two rows in Equation 2.11 if $(x, y) \in \boldsymbol{\Omega}_e^b$, or the next two rows if $(x, y) \in \boldsymbol{\Omega}_e^y$

The test function is represented by conventional nodal FE shape functions:

$$\boldsymbol{v}^e(\boldsymbol{x}) = \sum_{i=1}^{8} \boldsymbol{\psi}_i^e(\boldsymbol{x}) v_i^e \quad (2.17)$$

where $\boldsymbol{v}^e(\boldsymbol{x})$ is test function over the element, represented as a linear combination of linearly independent nodal test functions $\boldsymbol{\psi}_i^e(\boldsymbol{x})$

For a node, we have a set of elements e_d connected to it and if it is on the boundary, we also have a set of boundary faces b_d connected to it. The equation of equilibrium corresponding

to the global degree of freedom d is given as:

$$\sum_{e_d} \int_{\Omega_e} [(\boldsymbol{C}(\boldsymbol{x}) \cdot \boldsymbol{\mathcal{D}} \cdot \sum_{i=1}^{8} \boldsymbol{\phi}_i^e(\boldsymbol{x})u_i^e] \cdot [\boldsymbol{\mathcal{D}} \cdot \boldsymbol{\psi}_{i_{d-e}}^e(\boldsymbol{x})]dA = \underbrace{\sum_{b_d} \int_{\gamma_b} \boldsymbol{T}^b \cdot \boldsymbol{\psi}_{i_{d-e}}^e(\boldsymbol{x})ds}_{\text{zero for an interior node}} \qquad (2.18)$$
$$+ \sum_{e_d} \int_{\Omega_e} \boldsymbol{f} \cdot \boldsymbol{\psi}_{i_{d-e}}^e(\boldsymbol{x})dA$$

where i_{d-e} is the element degree of freedom corresponding to the global degree of freedom d in element e, and $\boldsymbol{T}^b$ is the traction on the boundary.

2.1.4   Numerical integration

There are two types of rectangular interface elements, one in which the interface intersects the adjacent edges and the other in which it intersects the opposite edges. When the interface cuts the adjacent edges, we choose the following numbering scheme: the node of the rectangular element that forms the triangular sub-region will be numbered 1 (the triangular region can either be blue or yellow). For the other nodes, we follow the numbering scheme as shown in Figure 2.6. For the case where the interface intersects the opposite edges, the rectangle is transformed in such a way that nodes 1 and 2 are on the same side of the interface. Two extreme cases arise: the interface passes exactly through one of the nodes which results in the rectangle being split into triangular and quadrilateral sub-regions, and the other in which the interface passes through two opposite nodes which results in two triangular sub-regions. The four interface configurations are shown in Figure 2.6.

For integration in elements with interfaces as described in case 1, we divide the pentagonal region into triangular and quadrilateral regions as shown in Figure 2.7. The area of the triangle within the pentagonal region (region 3 in Figure 2.7) goes to zero when the interface
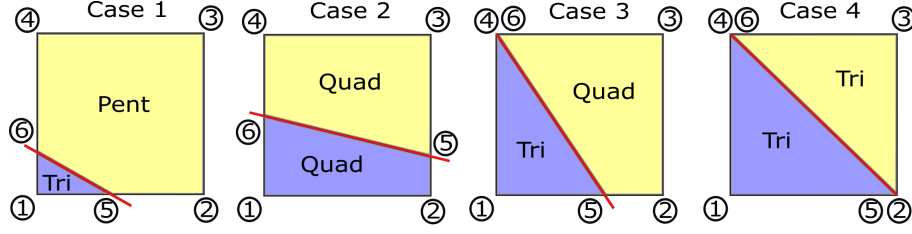
Figure 2.6: Four possible configurations of an interface element.
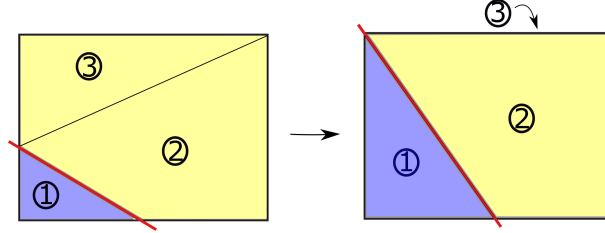
Figure 2.7: Area of region 3 going to zero in the limiting case of an interface passing exactly through one of the nodes.

passes exactly through one of the nodes. Similar zero-area regions are obtained for the other special cases as well. This will not cause any problems during analysis, but singularity issues arise during sensitivity calculations. Extreme cases will thus be handled separately.

From the Petrov-Galerkin formulation, the element stiffness matrix is given as:

$$K_{ij}^{ele} = \int_{\Omega_e} [(\boldsymbol{C}(x) \cdot \boldsymbol{D} \cdot \boldsymbol{\phi}_j(x)] \cdot [\boldsymbol{D} \cdot \boldsymbol{\psi}_i(x)] dA \qquad (2.19)$$

For case 1 interface elements shown in Figure 2.7, the integral can be split into three domains, one blue material domain, and two yellow triangular and quadrilateral domains. The integral

for this immersed element is given as:

$$
\begin{aligned}
K_{ij}^{ele} = &\int_{\Omega_e^b(1-5-6)} [(\boldsymbol{C}(x) \cdot \boldsymbol{D} \cdot \boldsymbol{\phi}_j(x)] \cdot [\boldsymbol{D} \cdot \boldsymbol{\psi}_i(x)] dA \\
&+ \int_{\Omega_e^y(6-5-2-3)} [(\boldsymbol{C}(x) \cdot \boldsymbol{D} \cdot \boldsymbol{\phi}_j(x)] \cdot [\boldsymbol{D} \cdot \boldsymbol{\psi}_i(x)] dA \\
&+ \int_{\Omega_e^y(6-3-4)} [(\boldsymbol{C}(x) \cdot \boldsymbol{D} \cdot \boldsymbol{\phi}_j(x)] \cdot [\boldsymbol{D} \cdot \boldsymbol{\psi}_i(x)] dA
\end{aligned}
\tag{2.20}
$$

For case 2 interface elements in Figure 2.6, the integral can be split into two domains, a blue and a yellow quadrilateral material domain. The integral for this immersed element is given as:

$$
\begin{aligned}
K_{ij}^{ele} = &\int_{\Omega_e^b(1-2-5-6)} [(\boldsymbol{C}(x) \cdot \boldsymbol{D} \cdot \boldsymbol{\phi}_j(x)] \cdot [\boldsymbol{D} \cdot \boldsymbol{\psi}_i(x)] dA \\
&+ \int_{\Omega_e^y(6-5-3-4)} [(\boldsymbol{C}(x) \cdot \boldsymbol{D} \cdot \boldsymbol{\phi}_j(x)] \cdot [\boldsymbol{D} \cdot \boldsymbol{\psi}_i(x)] dA
\end{aligned}
\tag{2.21}
$$

Similar integrals can be written for the other two cases of interface elements. These integrals are evaluated numerically. A four point Gauss integration is used to compute the integrals over each sub-domain. As an example, for case 2 interface elements, the Gauss quadrature numerical integration can be written as follows:

$$
\begin{aligned}
K_{ij}^{ele} = &\sum_{(\Omega_e^b)k=1}^{4} [(\boldsymbol{C}^b) \cdot \boldsymbol{D} \cdot \boldsymbol{\phi}_j(x_{gp}^{b_k})] \cdot [\boldsymbol{D} \cdot \boldsymbol{\psi}_i(x_{gp}^{b_k})] \cdot W_{gp}^{b_k} \\
&+ \sum_{(\Omega_e^y)k=1}^{4} [(\boldsymbol{C}^y) \cdot \boldsymbol{D} \cdot \boldsymbol{\phi}_j(x_{gp}^{y_k})] \cdot [\boldsymbol{D} \cdot \boldsymbol{\psi}_i(x_{gp}^{y_k})] \cdot W_{gp}^{y_k}
\end{aligned}
\tag{2.22}
$$

where $x_{gp}^{b_k}$ and $x_{gp}^{y_k}$ are the coordinate vectors of the Gauss points in the blue and yellow domain, respectively, and $W_{gp}^{b_k}$ and $W_{gp}^{y_k}$ are the Gauss weights for the corresponding points. The immersed element stiffness matrix has the same size and uses the same nodal degrees

of freedom as the conventional FEM one. The elemental stiffness matrix for the immersed element depends on the interface location and material properties of the two domains. The element stiffness matrix generated using ncPG-IIFEM will be asymmetric due to different trial and test functions. An asymmetric element stiffness matrix leads to an asymmetrical global stiffness matrix.

2.2 Verification: Bi-material patch test

A detailed description of the conceptual basis for the bi-material patch test is provided in [50]. For an elastic solid made up of a single homogeneous material, the basic solutions are the rigid body motions and the state of constant strain or stress. Any consistent FE formulation should represent these solutions exactly. The reason being that any local solution at a point resembles a state of constant strain or stress, and when the mesh is refined, or the size of the elements tends to zero, the finite element approximation approaches this solution. This can be extended to multi-material/bi-material systems. Any consistent solution of a bi-material system should satisfy the Hadamard jump conditions and traction continuity given by

$$
\begin{aligned}
\epsilon_{tt}^b = \epsilon_{tt}^y \quad & \sigma_{tt}^b \neq \sigma_{tt}^y \\
\sigma_{tn}^b = \sigma_{tn}^y \quad & \epsilon_{tn}^b \neq \epsilon_{tn}^y \\
\sigma_{nn}^b = \sigma_{nn}^y \quad & \epsilon_{nn}^b \neq \epsilon_{nn}^y
\end{aligned}
\tag{2.23}
$$

where ϵ is the strain, σ is the stress, the superscript represents the material domain, and the subscript represents tensor components. Here t is along the interface and n is perpendicular to the interface (Figure 2.8a).

The basic solutions for the bi-material system that satisfies the above condition are the rigid body motions and the constant strain or stress solutions which can be built up as linear

combinations of constant ϵ_{tt}, σ_{tn} and σ_{nn} solutions. There will be jumps in the other stress
and strain components, but they are constants over each material subdomain. These states
lead to continuous, piecewise linear displacements which are in the span of the immersed
finite element trial function space, and thus are represented exactly by ncPG-IIFEM.

(a)   (b)   (c)   (d)
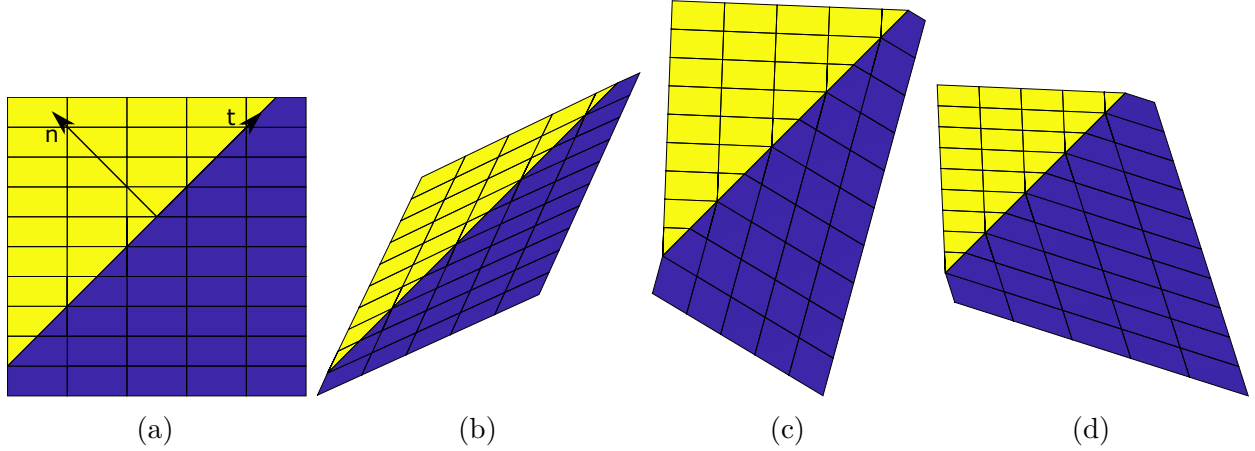
Figure 2.8: The three linear displacement solutions which can be represented exactly by the
continuous, piecewise-bilinear trial function space of the immersed elements: (a) an example
mesh; (b) an extensional strain in the tangential direction; (c) a shear stress in the normal-
tangential direction; (d) an extensional stress in the normal direction.

Consider a patch as shown in Figure 2.8 (a). The interface slope is taken as 1. The material
properties are as follows: $E^b = 1$, $\nu^b = 0.25$ are the Young's modulus and Poisson's ratio
of the blue region, and $E^y = 10$, $\nu^y = 0.3$ are the Young's modulus and Poisson's ratio of
the yellow region. We label the axes as t and n and they are oriented along the interface,
and along the direction normal to the interface respectively as shown in Figure 2.8 (a). The
three linear displacement solutions that are presented are: 1) $\epsilon_{tt} = 1$, $\sigma_{tn} = 0$ and $\sigma_{nn} = 0$,
extensional strain in the tangential direction, 2) $\epsilon_{tt} = 0$, $\sigma_{tn} = 0.3$ and $\sigma_{nn} = 0$, shear stress
in the normal-tangential direction, and 3) $\epsilon_{tt} = 0$, $\sigma_{tn} = 0$ and $\sigma_{nn} = 1$, extensional stress in
the normal direction. We prescribe the boundary displacements corresponding to the above
states and obtain the solution. Figures 2.8 (b),(c) and (d) show the solution for cases 1, 2,
and 3, respectively.

The results obtained for stresses and displacements are accurate to machine precision. The displacements in the interior nodes also exactly match the analytical solutions. The developed finite element passes the patch test. Thus, it is consistent and leads to optimal convergence of stresses throughout the domain, including near the interface, and optimal convergence of displacement.

2.3 Test Case and Analysis Results

Consider an axisymmetric bi-material problem as shown in Figure 2.9a. The material properties are constant in blue and yellow regions, but there is a discontinuity across the interface at $r = 0.4$. The Young's modulus and Poisson's ratio of the blue region are $E_b = 1$, $\nu_b = 0.25$ and the yellow region is $E_y = 10$, $\nu_y = 0.3$. The outer radius is $r = 2$. The loading of the structure is such that the displacement at the outer boundary is as follows: $u_r = r$ and $u_\theta = 0$ This problem has an analytical solution [5, 191]. We assume plane stress condition contrary to the plane strain condition assumed in these papers. For our numerical model, we consider a square domain of length 1×1, and prescribe boundary displacements.

(a) (b) (c)
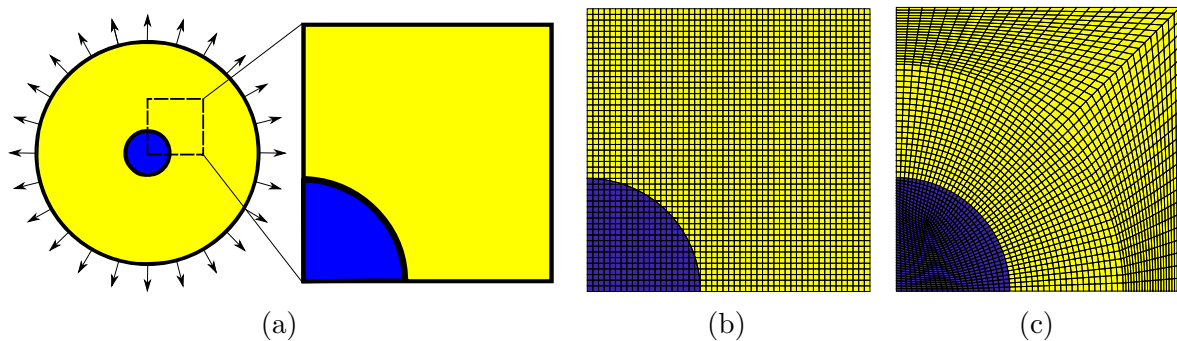
Figure 2.9: Domain definition of the problem: (a) an axisymmetric bi-material problem with prescribed radial displacement or traction at the outer edge with a square domain as shown considered for the analysis; (b) a structured rectangular mesh with immersed interfaces; (c) an interface-fitted mesh.
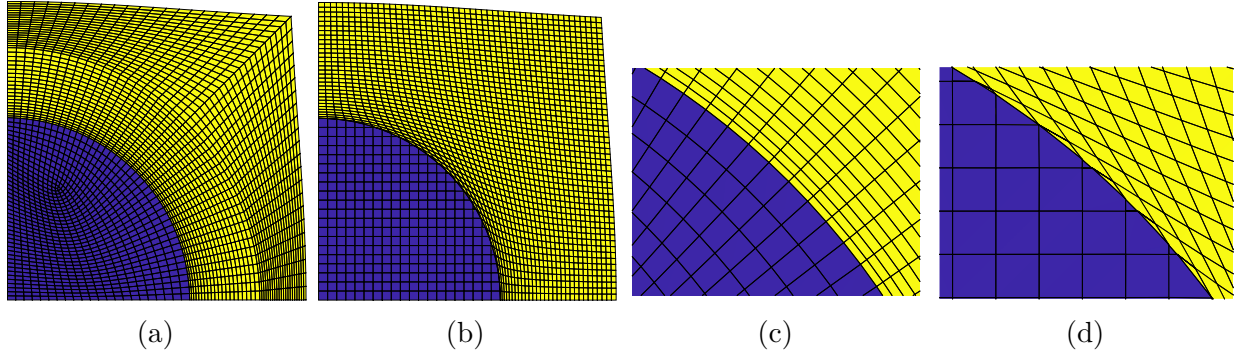
Figure 2.10: Sample displacement results: (a) total displacement using FEM with an interface-fitted mesh; (b) total displacement using ncPG-IIFEM with a Cartesian mesh; (c) Magnified view of the FEM solution near the interface; (d) Magnified view of the ncPG-IIFEM solution near the interface. The ncPG-IIFEM solution has negligible non-conformal displacements on an edge through which an interface passes.

Figures 2.10(a) and (b) show the total displacement of the square domain obtained from the interface-fitted FEM and the ncPG-IIFEM, respectively. The zoomed-in view in Figures 2.10(c) and (d) show the coupled nature of the solution near the interface. Comparing Figures 2.9b and 2.10d, we see that blue rectangles remain as rectangles, thus this region is in a state of uniform hydrostatic stress and strain; whereas the yellow region undergoes a tensile hoop strain and a corresponding compressive radial strain near the interface due to Poisson's effect. There is a jump in the radial strain and hoop stress at the interface. From the figures, it is also evident that both the conventional, interface-fitted, FEM and the ncPG-IIFEM captures this solution near the interface. It can also be noted that the jump in the hoop strain within the element is captured by ncPG-IIFEM. As discussed earlier, ncPG-IIFEM solution is nonconformal, but the discontinuity in displacement along the edges is very small and is due to insufficiently fine FE discretization. The non-conformity, like any error, decreases with mesh refinement.

Figure 2.11(a) shows the radial stress distribution obtained from the interface-fitted FEM and ncPG-IIFEM. Figure 2.11(b) shows the error in radial stress distribution when compared with the analytical exact solution. The errors in the ncPG-IIFEM are an order of magnitude
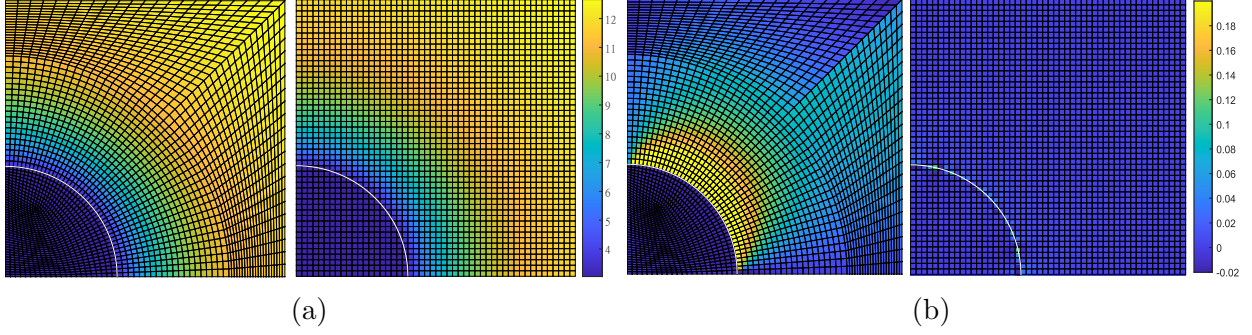
Figure 2.11: Sample stress results: (a) stress contours from the FEM solution with interface-fitted mesh, and from the ncPG-IIFEM; (b) error in the element radial normal stress calculated from the FEM solution with interface-fitted mesh, and from the ncPG-IIFEM solution with cartesian mesh.

lower than the errors in conventional interface-fitted FEM. Also, the errors in ncPG-IIFEM are concentrated near the interface.

Convergence studies are performed to compare the accuracy and conditioning of the ncPG-IIFEM to the interface-fitted FEM. We define mesh fineness as the square root of the number of nodes in the mesh. The normalized L_2-error norm and L_∞-error norm are defined as follows:

$$||u_{error}||_2 = \frac{||u_{exact} - u_{FEM}||_2}{||u_{exact}||_2} \tag{2.24}$$

$$||u_{error}||_\infty = \frac{||u_{exact} - u_{FEM}||_\infty}{||u_{exact}||_\infty} \tag{2.25}$$

Figures 2.12(a) and (b) show the convergence of displacement error norm with the refinement of the mesh. Both interface-fitted FEM and ncPG-IIFEM converge at the optimal second-order convergence rate for the L_2-error norm, and the L_∞-error norm. Even the interface elements in ncPG-IIFEM have lower or similar error values compared to the non-interface counterparts in the interface-fitted FEM. As for the other elements, ncPG-IIFEM is significantly better because of the regularity of the mesh. Thus, in general ncPG-IIFEM with rectangular elements has lower magnitude of error values when compared with the
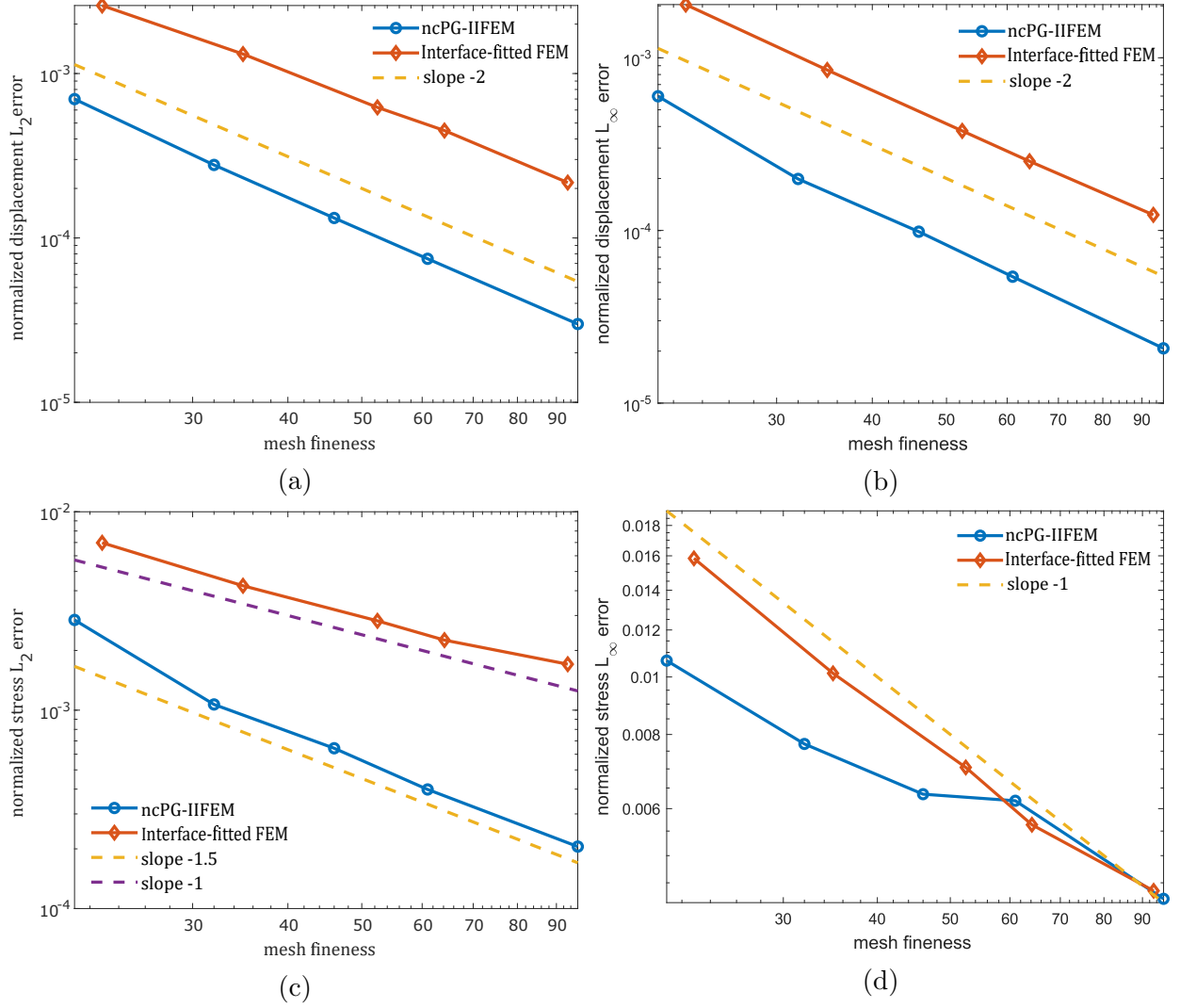
Figure 2.12: Error convergence with mesh refinement: (a) displacement L_2-error; (b) displacement L_∞-error; (c) radial normal stress L_2-error; (d) radial normal stress L_∞-error.

interface-fitted FEM with quadrilateral elements.

Figures 2.12(c) and (d) show the convergence of radial stress error norm with mesh refinement. The ncPG-IIFEM converge at an order of 1.5 for the L_2-error norm and 1 for the L_∞-error norm, whereas interface-fitted FEM has a first-order convergence rate for both norms. The lower magnitude of the absolute error values for the ncPG-IIFEM can be attributed to the regularity of the mesh. For the stress error norms, the measurement of stress values is taken
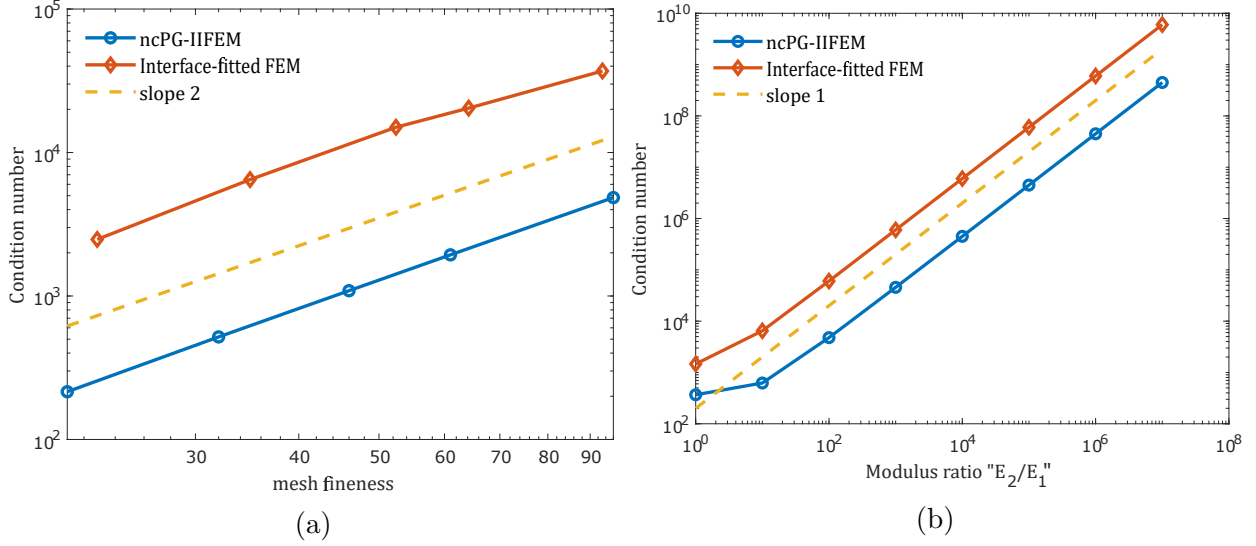
Figure 2.13: The comparison of the condition number of the global stiffness matrix between the interface-fitted FEM and the ncPG-IIFEM: (a) condition number with mesh refinement; (b) condition number with increase in stiffness ratio of the two materials.

at the element midpoint. In the case of immersed-interface elements, as the midpoint gets closer to the interface, the error in the stress increases. Depending on the mesh, because of the variability of the point at which the stress is calculated, even with mesh refinement, the maximum value of stress might decrease only a small amount, or might even remain the same. This is the reason for the similar magnitude of L_∞-error norm for both methods and the irregularity that can be observed in the plot of stress L_∞-error norm for the ncPG-IIFEM.

Ill-conditioning during trial function calculation due to various factors was already discussed. We do a similar analysis of the condition number of the global stiffness matrix. Figure 2.13 shows the increase in condition number of the global stiffness matrix with mesh refinement and modulus ratio (E_2/E_1). Conditioning determines the purely computational errors added to the solutions. It is important to study this as we are solving a discretized system of equations in a finite precision machine. Figure 2.13(a) shows the comparison between conventional, interface-fitted, FEM and ncPG-IIFEM. The ncPG-IIFEM has a lower condition number, but both methods show the same second-order growth with mesh

refinement. Both methods lead to a first-order increase in condition number with an increase in the modulus ratio of the materials as shown in Figure 2.13(b).

2.4 Sensitivity analysis

Design sensitivity analysis calculates the effect of changes in the design variables on the response of a structure. Hence, design sensitivities are essentially gradients of response parameters with respect to the shape design variables, that define the shape of a boundary or a material interface. These gradients can be used to apply gradient-based methods in shape optimization. There are several methods to obtain the sensitivities including discrete and continuum sensitivities. Here, we differentiate the discretized finite element system. For a gradient-based structural shape optimization problem, it is essential to calculate the derivative of the global stiffness matrix with respect to a shape design variable. For the bi-material problems considered, the shape design variables, d_i, are the variables that control the shape of the inclusions. For example, the radius of a circle is a shape design variable if the inclusion is circular. Our aim is to obtain the sensitivity of the global stiffness matrix with respect to these design variables. The elemental stiffness matrix of the interface elements is sensitive to a change in the shape of the inclusion, whereas the stiffness matrix of the non-interface elements does not change with d_i. Let $p_5 = (x_5, y_5)$ and $p_6 = (x_6, y_6)$ be the intersection points, and $p_{gp}^i = (x_{gp}^i, y_{gp}^i)$ be the Gauss points. Let $lsf(x, y, d_i)$ be the level set function whose value is zero on the material interface. Intersection points for case 1 interface element (Figure 2.6) are obtained from the level set values at the nodes as follows:

$$
\begin{aligned}
(x_5(d_i), y_5(d_i)) &= (x_1, y_1) - \frac{lsf(x_1, y_1, d_i) * ((x_2, y_2) - (x_1, y_1))}{lsf(x_2, y_2, d_i) - lsf(x_1, y_1, d_i)} \\
(x_6(d_i), y_6(d_i)) &= (x_4, y_4) - \frac{lsf(x_4, y_4, d_i) * ((x_1, y_1) - (x_4, y_4))}{lsf(x_1, y_1, d_i) - lsf(x_4, y_4, d_i)}
\end{aligned}
\tag{2.26}
$$

Intersection point p_6 for case 2 interface elements is the same as in case 1 interface elements, as it lies between nodes 1 and 4. Whereas, p_5 lies between nodes 2 and 3, and is given by

$$(x_5(d_i), y_5(d_i)) = (x_3, y_3) - \frac{lsf(x_3, y_3, d_i) * ((x_2, y_2) - (x_3, y_3))}{lsf(x_2, y_2, d_i) - lsf(x_3, y_3, d_i)} \tag{2.27}$$

The extreme cases are limiting cases from either case 1 or case 2. Thus, we can use either Equation 2.26, or 2.27 for cases 3 and 4. Any one of these expressions can be used when calculating the sensitivities for these extreme cases.

We assume the following for notational convenience. For any function, $f \equiv f(x_5(d_i), y_5(d_i), x_6(d_i), y_6(d_i))$, we write f as $f(p_5(d_i), p_6(d_i))$, and what we mean by $\frac{\partial f}{\partial p_5} \frac{\partial p_5}{\partial d_i}$, and $\frac{\partial f}{\partial p_6} \frac{\partial p_6}{\partial d_i}$ is the following:

$$\begin{aligned} \frac{\partial f}{\partial p_5} \frac{\partial p_5}{\partial d_i} &\equiv \frac{\partial f}{\partial x_5} \frac{\partial x_5}{\partial d_i} + \frac{\partial f}{\partial y_5} \frac{\partial y_5}{\partial d_i} \\ \frac{\partial f}{\partial p_6} \frac{\partial p_6}{\partial d_i} &\equiv \frac{\partial f}{\partial x_6} \frac{\partial x_6}{\partial d_i} + \frac{\partial f}{\partial y_6} \frac{\partial y_6}{\partial d_i} \end{aligned} \tag{2.28}$$
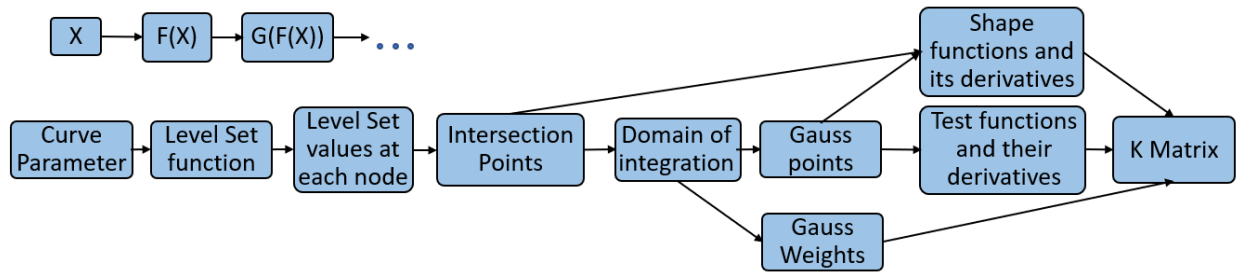
Figure 2.14: Functional relationship between stiffness matrix and various quantities of interest.

Figure 2.14 illustrates the functional relationship between various quantities of interest. Gauss points, Gauss weights, and shape functions of the interface elements have the following

functional relationship:

$$p_{gp} \equiv p_{gp}(p_5(lsf(;,d_i)), p_6(lsf(;,d_i)))$$

$$W_{gp} \equiv W_{gp}(p_5(lsf(;,d_i)), p_6(lsf(;,d_i))) \tag{2.29}$$

$$\boldsymbol{\phi}_j \equiv \boldsymbol{\phi}_j(p_{gp}(d_i), p_5(lsf(;,d_i)), p_6(lsf(;,d_i))) \equiv \boldsymbol{\phi}_j(p_{gp}(d_i), d_i)$$

We compress this and write the above functional relationship: $p_{gp} \equiv p_{gp}(d_i)$ and $W_{gp} \equiv W_{gp}(d_i)$. Using chain rule, the derivatives of Gauss points and Gauss weights can be written as follows:

$$\frac{dp_{gp}}{dd_i} = \frac{\partial p_{gp}}{\partial p_5}\frac{\partial p_5}{\partial d_i} + \frac{\partial p_{gp}}{\partial p_6}\frac{\partial p_6}{\partial d_i}$$
$$\frac{dW_{gp}}{dd_i} = \frac{\partial W_{gp}}{\partial p_5}\frac{\partial p_5}{\partial d_i} + \frac{\partial W_{gp}}{\partial p_6}\frac{\partial p_6}{\partial d_i} \tag{2.30}$$

Henceforth, we denote

$$\frac{d}{dd_i} \equiv \frac{\partial p_5}{\partial d_i}\frac{\partial}{\partial p_5} + \frac{\partial p_6}{\partial d_i}\frac{\partial}{\partial p_6} \tag{2.31}$$

$\frac{\partial p_5}{\partial d_i}$, and $\frac{\partial p_6}{\partial d_i}$ can be calculated from Equation 2.26. Here, $\frac{\partial p_{gp}}{\partial p_5}, \frac{\partial p_{gp}}{\partial p_6}$ and $\frac{\partial W_{gp}}{\partial p_5}, \frac{\partial W_{gp}}{\partial p_6}$ are the Gauss point and weight sensitivity with respect to the nodal coordinate of the subdomain, which can be calculated from the definition of Gauss points and weights on a general rectangular domain. Similarly, the shape functions can be written as: $\boldsymbol{\phi}_j \equiv \boldsymbol{\phi}_j(p_{gp}(d_i), d_i)$. From Equation 2.29, using the chain rule, we obtain the total derivative as follows:

$$\frac{D\boldsymbol{\phi}_j}{Dd_i} = \sum_k \left.\frac{\partial \boldsymbol{\phi}_j}{\partial x}\right|_{x_{gp}^k} \frac{\partial x_{gp}^k}{\partial d_i} + \sum_k \left.\frac{\partial \boldsymbol{\phi}_j}{\partial y}\right|_{y_{gp}^k} \frac{\partial y_{gp}^k}{\partial d_i} + \frac{d\boldsymbol{\phi}_j}{dd_i} \tag{2.32}$$

The shape function partial derivatives $\frac{d\boldsymbol{\phi}_j}{dd_i}, \frac{\partial \boldsymbol{\phi}_j}{\partial x}, \frac{\partial \boldsymbol{\phi}_j}{\partial y}$ are $\frac{d}{dd_i}[\boldsymbol{N}]_{4\times8}, \frac{\partial}{\partial x}[\boldsymbol{N}]_{4\times8}, \frac{\partial}{\partial y}[\boldsymbol{N}]_{4\times8}$, which

are given as follows:

$$
\frac{d}{dd_i}[\boldsymbol{N}]_{4\times8} = [\boldsymbol{T}]\left(-\left[\boldsymbol{C_f}\right]^{-1}\left(\frac{d}{dd_i}\left[\boldsymbol{C_f}\right]\right)\left[\boldsymbol{C_f}\right]^{-1}\right)\begin{bmatrix}\boldsymbol{I}_{8\times8}\\\boldsymbol{0}_{8\times8}\end{bmatrix}
$$

$$
\frac{\partial}{\partial x}[\boldsymbol{N}]_{4\times8} = \left[\frac{\partial \boldsymbol{T}}{\partial x}\right]\left(\left[\boldsymbol{C_f}\right]^{-1}\right)\begin{bmatrix}\boldsymbol{I}_{8\times8}\\\boldsymbol{0}_{8\times8}\end{bmatrix} \tag{2.33}
$$

$$
\frac{\partial}{\partial y}[\boldsymbol{N}]_{4\times8} = \left[\frac{\partial \boldsymbol{T}}{\partial y}\right]\left(\left[\boldsymbol{C_f}\right]^{-1}\right)\begin{bmatrix}\boldsymbol{I}_{8\times8}\\\boldsymbol{0}_{8\times8}\end{bmatrix}
$$

where $\frac{\partial \boldsymbol{T}}{\partial x}$, and $\frac{\partial \boldsymbol{T}}{\partial y}$ can be calculated from Equation 2.8. $\frac{d}{dd_i}\left[\boldsymbol{C_f}\right]$ is given as follows

$$
\frac{d}{dd_i}\left[\boldsymbol{C_f}\right] = \frac{\partial}{\partial x_5}\left[\boldsymbol{C_f}\right]\frac{\partial x_5}{\partial \boldsymbol{d_i}} + \frac{\partial}{\partial y_5}\left[\boldsymbol{C_f}\right]\frac{\partial y_5}{\partial \boldsymbol{d_i}} + \frac{\partial}{\partial x_6}\left[\boldsymbol{C_f}\right]\frac{\partial x_6}{\partial \boldsymbol{d_i}} + \frac{\partial}{\partial y_6}\left[\boldsymbol{C_f}\right]\frac{\partial y_6}{\partial \boldsymbol{d_i}} \tag{2.34}
$$

Now, we have all the sensitivities required to calculate the stiffness matrix sensitivity. From Figure 2.14, it is clear that the stiffness matrix of the interface element has the following functional relationship in compact notation:

$$
K_{ij} \equiv K_{ij}(\frac{\partial \phi_j}{\partial x}(p_{gp}(d_i), d_i), \frac{\partial \phi_j}{\partial y}(p_{gp}(d_i), d_i), \frac{\partial \psi_i}{\partial x}(p_{gp}(d_i)), \frac{\partial \psi_i}{\partial y}(p_{gp}(d_i)), W_{gp}(d_i), d_i) \tag{2.35}
$$

The sensitivity of the stiffness matrix with respect to shape design variables using the chain rule can be written as follows:

$$
\frac{DK_{ij}}{Dd_k} \equiv \frac{\partial K_{ij}}{\partial \phi_{j,x}}\frac{D\phi_{j,x}}{Dd_k} + \frac{\partial K_{ij}}{\partial \phi_{j,y}}\frac{D\phi_{j,y}}{Dd_k} + \frac{\partial K_{ij}}{\partial \psi_{i,x}}\frac{D\psi_{i,x}}{Dd_k} + \frac{\partial K_{ij}}{\partial \psi_{i,y}}\frac{D\psi_{i,y}}{Dd_k} + \frac{\partial K_{ij}}{\partial W_{gp}}\frac{dW_{gp}}{dd_k} + \frac{dK_{ij}}{dd_k}
$$

$$
\tag{2.36}
$$

where $\frac{\partial K_{ij}}{\partial \phi_{j,x}}, \frac{\partial K_{ij}}{\partial \phi_{j,y}}, \frac{\partial K_{ij}}{\partial \psi_{i,x}}, \frac{\partial K_{ij}}{\partial \psi_{i,y}}$, and $\frac{\partial K_{ij}}{\partial W_{gp}}$ can be obtained from Equation 2.22, $\frac{dK_{ij}}{dd_k}$ can be

obtained using the definition of $\frac{d}{dd_k}$ and from Equation 2.22, $\frac{D\phi_{j,x}}{Dd_k}$, $\frac{D\phi_{j,y}}{Dd_k}$, $\frac{D\psi_{i,x}}{Dd_k}$, and $\frac{D\psi_{i,y}}{Dd_k}$ are obtained by replacing ϕ_j in Equation 2.32 by the corresponding quantity of interest, $\frac{d\psi_{i,x}}{dd_k}$ and $\frac{d\psi_{i,y}}{dd_k}$ are zero as the test functions are standard FE test functions and are the same for any type of element.

2.5 Optimization Problem Formulation

A general immersed interface finite-element-based shape optimization problem can be formulated as follows:

$$
\begin{aligned}
\min_{d} \quad & f(U(d_k), d_k) \\
\text{s.t.} \quad & K(d_k)U(d_k) = F \\
& h_i(U(d_k), d_k) = 0 \\
& g_j(U(d_k), d_k) \leq 0 \\
& d_k^{lb} \leq d_k \leq d_k^{ub} \\
\text{with} \quad & i = 1, 2, .., n \quad \& \quad j = 1, 2, .., m
\end{aligned}
\tag{2.37}
$$

where f is the objective function, h_i denotes equality constraint functions, g_j denotes the inequality constraint functions, d_k are the design variables, $U(d_k)$ is the solution of the analysis equations, $K(d_k)U(d_k) = F$, where, $K(d_k)$ is the global stiffness matrix, and F is the force vector.

We have to compute gradients of the objective and the constraint functions with respect to the design variables to perform gradient-based shape optimization. The design variables are the geometric parameters that define the shape of the material interface. For example, consider a plate with a soft elliptic inclusion embedded in a stiffer matrix. The shape design

variables are the semi-minor, semi-major axis length, and the orientation of the ellipse. One of the main challenges in the conventional shape optimization schemes arises due to the dependence of nodal coordinates of a FEM discretization on the design variables, which in turn necessitates the computation of the sensitivity of nodal coordinates w.r.t the design variables. Immersed interface-based optimization scheme avoids this computation. The objective function gradient obtained by applying chain rule to Equation 2.37 is as follows:

$$\frac{Df}{Dd_k} = \frac{\partial f}{\partial U}\frac{DU}{Dd_k} + \frac{\partial f}{\partial d_k} \tag{2.38}$$

Since, $KU = F$, and in the cases considered in this paper, F is independent of the design variables, we can write

$$K\frac{DU}{Dd_k} + \frac{DK}{Dd_k}U = 0 \tag{2.39}$$

$$\frac{DU}{Dd_k} = -K^{-1}\frac{DK}{Dd_k}U \tag{2.40}$$

where $\frac{DK}{Dd_k}$ can be calculated from Equation 2.36. Similar expressions can be written for equality and inequality constraint functions.

2.5.1 Design space parametrization

We use a parametric representation to describe the shape of an inclusion. Specifically, a polar representation, where the radius of the inclusion is a function of the angle, will be used. We investigate few candidate representations of the form $r(\theta)$. We start with a Fourier series representation for a closed curve and show some shortcomings of the design space generated by this representation. Later, we add terms, which are problem dependent, to expand this space and eliminate any shortcomings. Consider the following Fourier series for the radius

of inclusion:

$$r(\theta) = d_1 + \sum_{n=1}^{k} d_{2n} \sin(n\theta) + \sum_{n=1}^{k} d_{2n+1} \cos(n\theta) \qquad (2.41)$$

where, d_i's, are the design variables. It is linear in terms of the design variables. The first term in Equation 2.41 is a circle of radius d_1. The other terms represent limacons, lemniscates, cardioids, and roses. Thus, Equation 2.41 can represent any inclusion that is a linear combination of these curves exactly. For any inclusion outside this set, Equation 2.41 provides an approximate curve.

Two main problems arise with the Fourier representation. Firstly, the description requires significantly higher number of terms to accurately represent (i) an ellipse and (ii) any shape with sharp corners. To overcome this, we add terms which can describe ellipse and sharp corners exactly. Figure 2.15a shows a comparison between the ellipse and the Fourier representation of the ellipse with three and seven terms. The best approximation with a three-term Fourier expansion for an ellipse is a dumble-like shape, as shown in Figure 2.15b. From the plots, it is also obvious that even seven-term Fourier expansion is not an accurate representation of the ellipse. Similarly, Figure 2.15c provides a comparison between Fourier expansion of a diamond shape (a shape with a sharp corner) with the actual shape. With a three term Fourier expansion, a circle is the closet approximation, as shown in Figure 2.15d.

Secondly, increasing the number of terms in the Fourier expansion increases the number of design variables with slow improvement in the approximation capability. Therefore, we add a term that represents ellipses exactly to Equation 2.41. An ellipse in polar form can be written as follows: $r(\theta) = \frac{ab}{\sqrt{a^2 \sin^2(\theta) + b^2 \cos^2(\theta)}}$, where a and b are semi-major and semi-minor
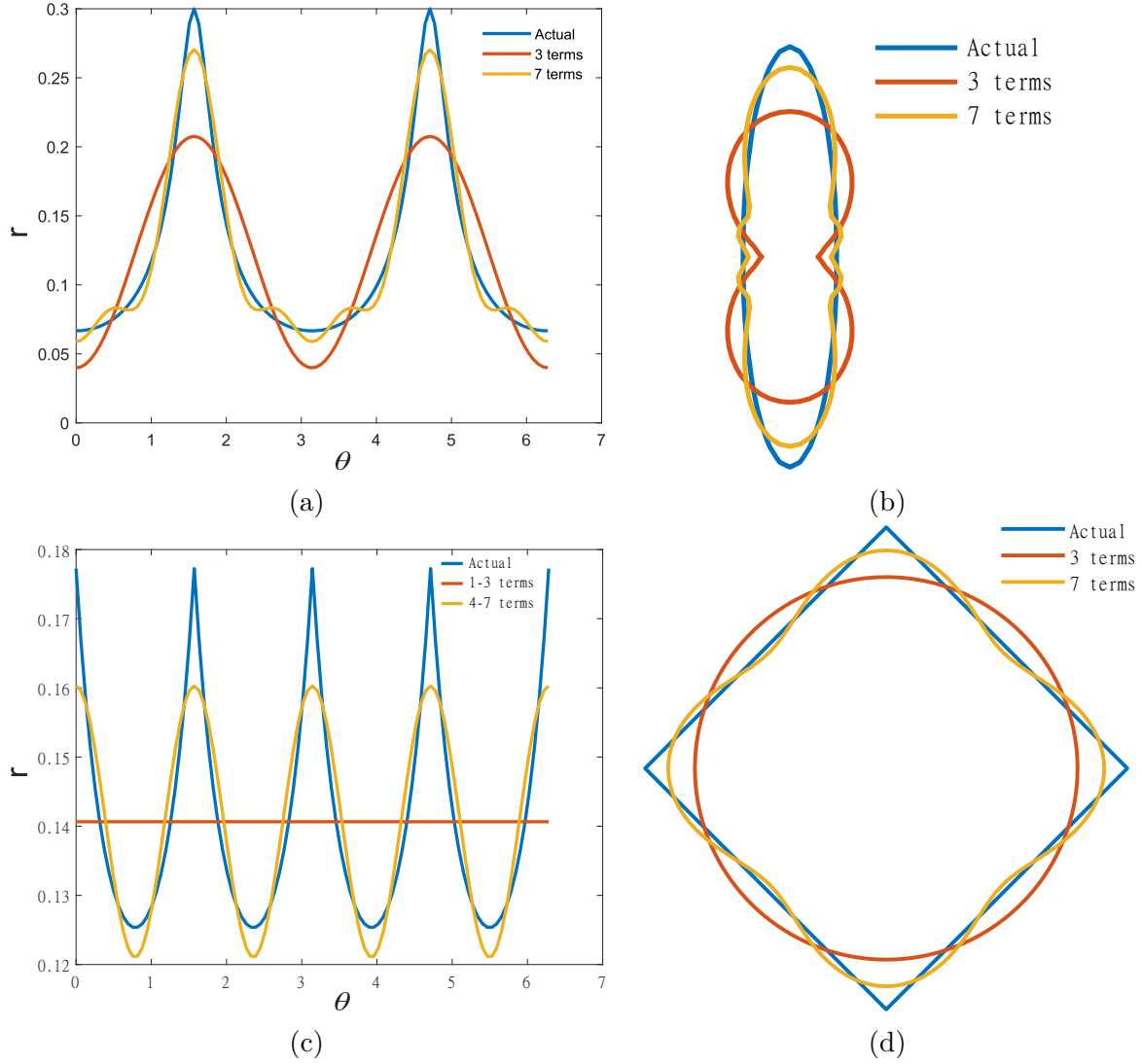
Figure 2.15: Comparison of the actual curves with their Fourier representations: (a) change in the radial distance of an ellipse and its Fourier representations as a function of the angle relative to the horizontal axis; (b) an actual ellipse and the Fourier representation of the ellipse; (c) change in the radial distance of a diamond shape and its Fourier representations as a function of the angle relative to the horizontal axis; (d) an actual diamond shape and the Fourier representation of the ellipse.

axis respectively. The modified polar representation of the inclusion is as follows:

$$r(\theta) = d_1 + \sum_{n=1}^{3} d_{2n} \sin(n\theta) + \sum_{n=1}^{3} d_{2n+1} \cos(n\theta) + \frac{d_8 d_9}{\sqrt{d_8^2 \sin^2(\theta) + d_9^2 \cos^2(\theta)}} \quad (2.42)$$
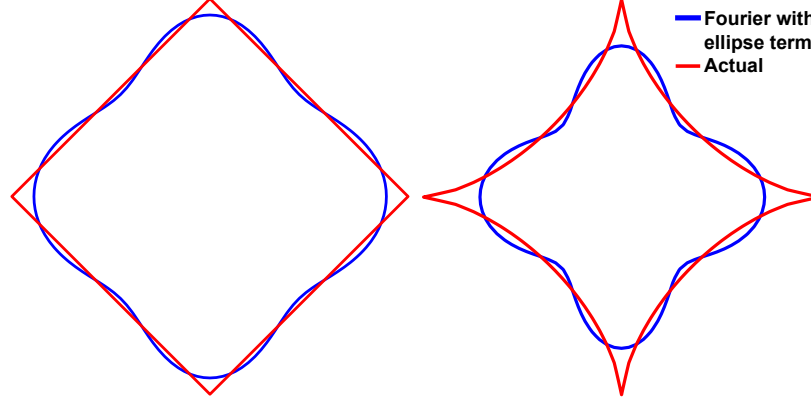
Figure 2.16: Best approximation of sharp curves with mathematical description given by Equation 2.42 using least square error minimization.

Equation 2.42 is an accurate mathematical description for a wide class of smooth closed curves. We also investigate the capability of the new representation in describing curves with sharp edges or cusps. Figure 2.16 shows two curves with sharp corners and their comparison with the best approximation (in terms of minimization of least square error) using Equation 2.42. Figure 2.16 also illustrates that as the sharpness increases, the approximation capability decreases.

To improve the approximation capability of Equation 2.42 when the curve has a sharp cusp, we include the following term: $(|\sin(\theta)|^k + |\cos(\theta)|^k)^{\frac{-1}{k}}$, where k can be any number between 0 and 1 depending on the required sharpness of the cusp. Thus, the modified description of the inclusion for sharp edges or cusps is as follows:

$$
\begin{aligned}
r(\theta) =& d_1 + \sum_{n=1}^{3} d_{2n} \sin(n\theta) + \sum_{n=1}^{3} d_{2n+1} \cos(n\theta) + \frac{d_8 d_9}{\sqrt{d_8^2 \sin^2(\theta) + d_9^2 \cos^2(\theta)}} \\
&+ \frac{d_{10}}{(|\sin(\theta)|^k + |\cos(\theta)|^k)^{\frac{1}{k}}}
\end{aligned}
\tag{2.43}
$$

We can exactly represent the diamond-shape and the star shape shown in Figure 2.16a if

$k = 1$ and $k = \frac{2}{3}$ respectively.

Finally, for some of the problems, we consider the coordinates of the center of the inclusion (d_{11} and d_{12}) as design variables.

2.5.2   Verification problems

We consider two cases for verification. In both cases, the objective is to minimize the compliance of a plate with softer inclusion embedded in a stiff matrix, the loading conditions are different and given as follows: (i) a constant uniform traction along the top edge, and (ii) a uniform shear traction along all the edges as shown in Figure 2.17(a) and (b). Plane strain conditions are assumed for both problems. A square domain (size $L = 1$) with a roller boundary along the bottom edge for constant uniform traction and pinned at the opposite corners for the pure shear is considered to prevent rigid body motion. The matrix is stiffer than the inclusion with material properties $\frac{E_1}{E_2} = 10$ and $\nu_1 = \nu_2 = 0.3$. The center of the inclusion is fixed at the center of the plate for both cases. The total inclusion area is also held fixed with specific minimum and maximum bounds for the inclusion radius in all directions.

For the first case, if only elliptic and circular inclusions are allowed, then the analytical optimum is an ellipse whose longer axis aligns with the applied load direction [192]. For the second case, the analytical solution for the optimum cavity in an infinite 2D elastic domain with pure shear is a diamond shape given in [193]. A similar optimum is obtained for a finite domain for the problem in Figure 2.17b [65].

The steps involved in the ncPG-IIFEM based shape optimization can be summarized as follows:

1. Define a multi-material boundary value problem. Generate a uniform mesh.
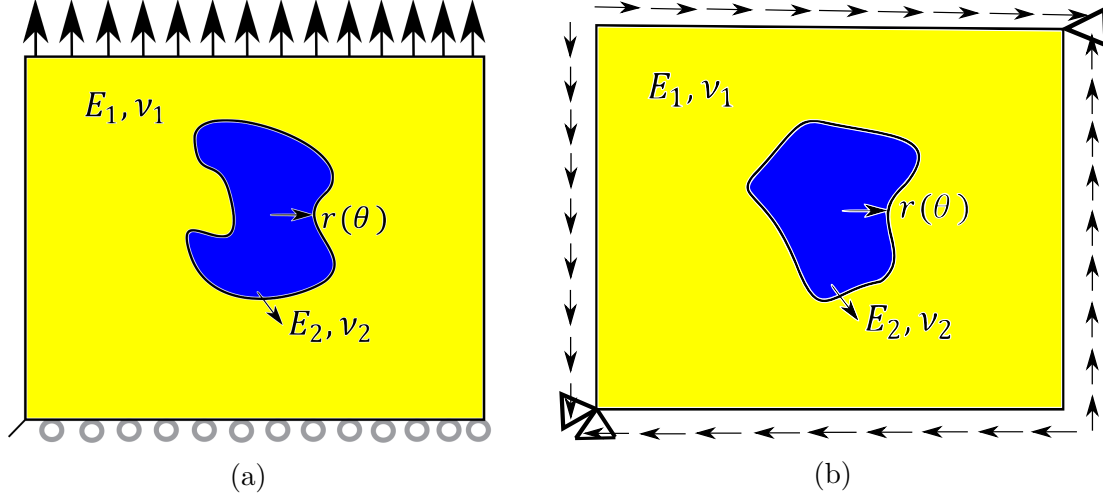
Figure 2.17: A plate with softer inclusion embedded in a stiff matrix under two different loading conditions: (a) a constant load; (b) a pure shear load.

2. Initialize the design variables $d_i = d_{i_0}$.

3. Implement ncPG-IIFEM:

   (a) Generate the trial functions for the immersed interface elements.

   (b) Consider standard FE shape functions for non-interface elements.

   (c) Generate the elemental stiffness matrix and the force vector by applying the Petrov-Galerkin formulation.

4. Solve for the nodal displacements using the finite element equation. Global stiffness matrix and force vector are obtained from assembling the elemental stiffness matrix and the elemental force vector.

5. Compute objective and constraint functions.

6. Compute the sensitivities of the objective and the constraint functions.

7. Use a suitable gradient based optimization algorithm.

8. Select suitable stopping criteria based on the optimization algorithm.

9. Obtain the optimized value of the design variables.

(a)

(b)
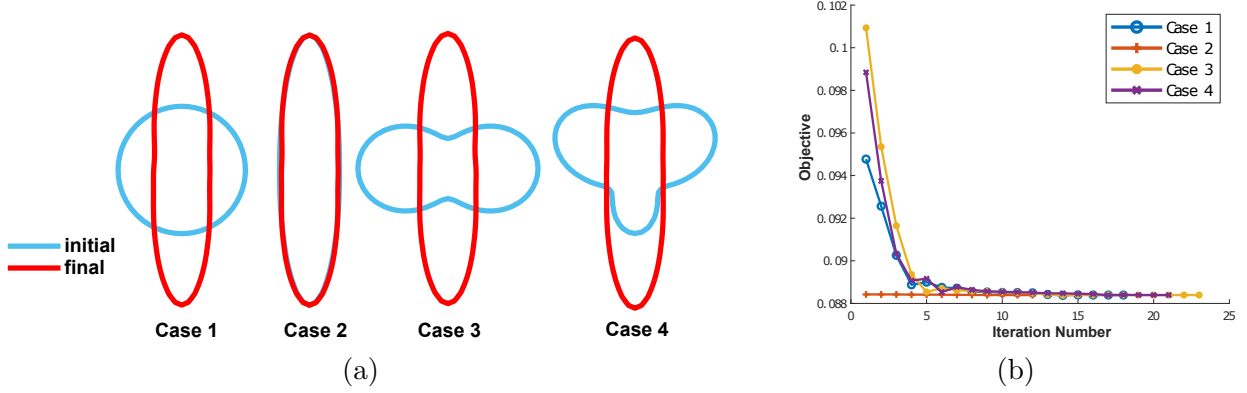
Figure 2.18: Results for a plate under an applied constant load as shown in Figure 2.17a: (a) optimal designs obtained for four different initial designs; (b) convergence history of the objective function for the four initial designs.

Table 2.1: Compliance and design variable values for the pure shear case for various initial and optimum designs

Case No.		d_1	d_2	d_3	d_4	d_5	d_6	d_7	d_{10}	Objective
1	Initial	0.2	0	0	0	0	0	0	0	0.3618
	Final	0.0217	0	0	0	0	0	0	0.1501	0.2992
2	Initial	0.2	0	0	0.1	0	0	0	0	0.4108
	Final	0.0217	0	0	0	0	0	0	0.1501	0.2992
3	Initial	0.2	0	0.1	0	0	0	0	0	0.3850
	Final	0.0217	0	0	0	0	0	0	0.1501	0.2992
4	Initial	0.2	0	0	0	0	0.1	0	0	0.4039
	Final	0.0217	0	0	0	0	0	0	0.1501	0.2992

We use a Sequential Quadratic Programming (SQP) [194, 195] as the optimization algorithm. The algorithm involves solving a quadratic programming subproblem, where a merit function with certain penalty parameters are used for the line search procedure. The BFGS quasi-Newton method is used to approximate the Hessian. The stopping criteria used are as follows: maximum constraint violation, maximum magnitude of the search direction and the modified Lagrangian gradient has to be less than the specified values.
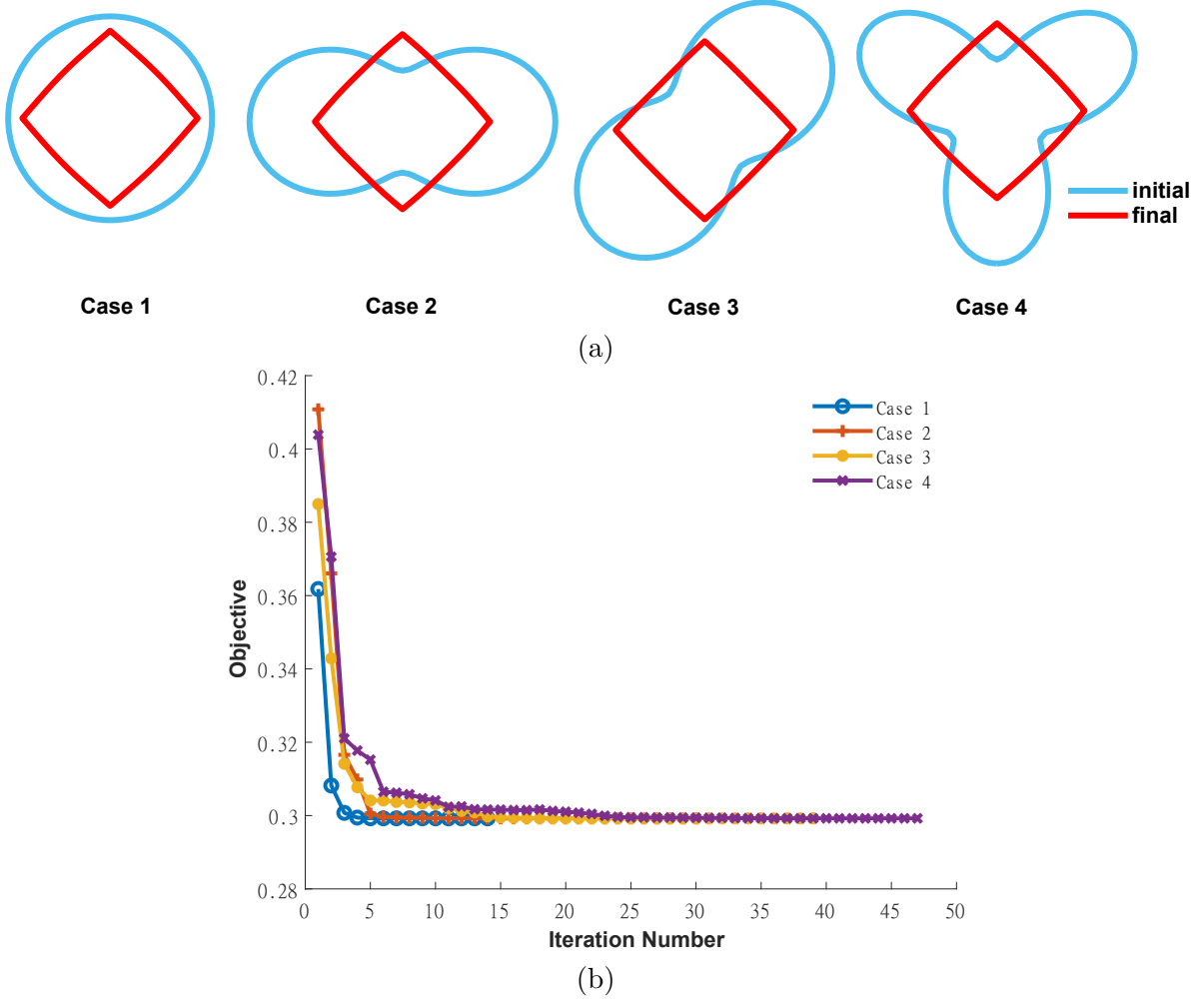
Figure 2.19: Results for a plate under an applied shear loading as shown in Figure 2.17b: (a) optimum designs obtained from five different initial designs; (b) convergence history of the plate compliance for the five initial designs.

The compliance or stored elastic energy is given as $f = F^T U$. For the first case, we consider Equation 2.42 to describe the shape of the inclusion. d_i's in Equation 2.42 are the design variables. The inclusion area constraint is the equality constraint and is set to 0.02π. Area of the finite element approximation of the inclusion (discrete area) is considered for area calculations. The inequality constraints are the minimum and maximum radius constraints. For the problem in Figure 2.17a, we set the minimum radius in any direction to be 0.025 and the maximum radius to be 0.3. This will be satisfied discretely at 360 points with one degree

increment in angle. The stopping criteria used for SQP is as follows: maximum constraint violation (max(g)) is less than equal to 10^{-5}, modified Lagrangian gradient (KTO) is less than equal to 10^{-6}, maximum magnitude of the search direction (max(S)) is less than equal to 10^{-3} [194]. We use a 64×64 mesh. The optimum shape obtained for any initial condition, if only ellipses are allowed, is d_8, d_9 equals 0.06667, 0.3 respectively. The objective value is 0.08842. The developed method provides the expected optimum.

If we consider all the design variables in Equation 2.42, the optimum shape obtained when we start with the optimum ellipse as the initial shape closely resembles the same ellipse as shown in Figure 2.18a, and its objective value is 0.08839. Even with other starting designs we get a similar optimum whose objective is 0.08839. Thus, no significant improvement is achieved in this particular case by including the other design variables. Figure 2.18a shows the optimum for various initial configurations. All initial shapes go to an optimum with the same compliance value. Figure 2.18b provides the iteration history of the compliance value for four trial cases. Convergence to the optimum is within 25 iterations.

Consider the pure shear case as shown in Figure 2.17b. The domain, material properties, mesh size, constraints and the objective are the same as the previous verification problem. The stopping criteria used is: max(g) $= 10^{-6}$, KTO $= 10^{-6}$, max(S) $= 10^{-4}$. We consider Equation 2.43 with $k = 1$ and without the ellipse term i.e., the design variables d_9 and d_{10} to describe the shape of the inclusion. The ellipse term is unnecessary for this particular case as it does not participate in providing the final optimum. Figure 2.19a shows the optimum for various initial configurations. All initial shapes go to an optimum with the same compliance value. Figure 2.19b provides the objective vs iteration history. Convergence to the optimum is within 50 iterations. Table 2.1 provides the initial and final values of design variables and their corresponding compliance values. The results qualitatively match with the analytical results for the infinite domain.

2.6   Case studies

In this section, we provide three cases to show the capability of the shape optimization framework in conjunction with the ncPG-IIFEM. All cases assume plane strain conditions. We allow sharp corners in one of the cases, movement of the center of the inclusion in the other, and finally a case with multiple inclusions.
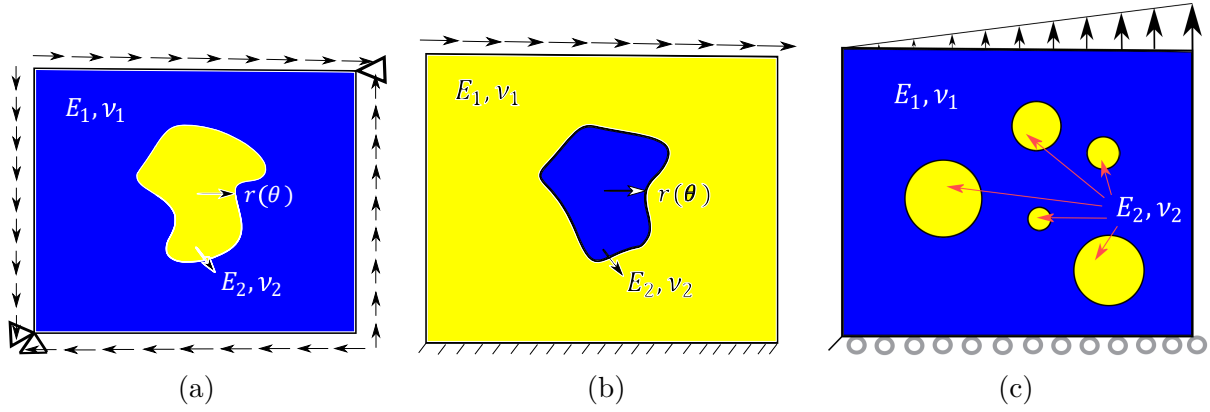
Figure 2.20: Problem description: (a) a case featuring first enrichment, depicting a square plate with a stiff inclusion subjected to pure shear loading; (b) a scenario involving center movement, depicting a square plate with a soft inclusion under shear loading applied to the top edge; (c) a case involving multiple inclusions, depicting a square plate with five stiff circular inclusions under a linearly varying distributed load on the top edge.

2.6.1   A case with sharp corners

A pure shear ($\tau_0 = 0.1$) load is applied on a square plate (size $L = 1$) with pinned support at the opposite corners as shown in Figure 2.20a. This case is similar to the case in Figure 2.17b, except here the inclusion is stiffer than the matrix with material properties $\frac{E_2}{E_1} = 100$, and $\nu_1 = \nu_2 = 0.3$. The center of the inclusion is fixed at the center of the plate. The objective is to minimize the compliance. For this problem, we use first enrichment (Equation 2.43 with $k = \frac{2}{3}$). The area constraint is the same as the verification case. We set a convenient

minimum radius to avoid double intersections. Discrete area is used for area calculations. We use a 64×64 mesh. A few local optimums obtained from different starting points are as shown in Figure 2.21a. Figure 2.21b provides the iteration history of compliance for the trials. Table 2.2 provides the initial and final values of design variables and their corresponding compliance values.

The best optimum from the literature is a star-shape [196]. So, we investigate perfect star shapes (shown in Figure 2.21b) by considering just the k term in the parametric representation. The compliance values for the shapes with $k = 2/3, 2/4, 2/5$, and $2/6$ are $0.0225, 0.02216, 0.02207$, and 0.02228 respectively. If we perform an optimization just with the final term of the representation, then $k = 0.41$ is the obtained optimum value with compliance value of 0.02202. But, there are shapes with lower compliance than the star-shapes. The rotated butterfly-like shapes, as in cases 2,3 and 6, are better than the best star-shape. Better shapes obtained from this method can be attributed to expanded design space.

Table 2.2: Objective and design variable values for the initial and optimum designs for a square plate with stiff inclusion under pure shear loading.

Case		d_1	d_2	d_3	d_4	d_5	d_6	d_7	d_8	d_9	d_{10}	Objective
1	Initial	0	0	0	0	0	0	0	0.1416	0.1416	0	0.02375
	Final	-0.18850	-0.02176	0.012839	-0.01461	-0.00924	0.00191	-0.00703	0.05489	0.03994	0.44742	0.02203
2	Initial	0	0	0	0	0	0	0	0.1	0.2	0	0.02386
	Final	-0.22893	-0.00061	-0.00415	0.03911	0.01291	-0.00059	-0.00190	0.07820	0.11003	0.43727	0.02182
3	Initial	0	0	0	0	0	0.0202	0.0202	0.0907	0.0907	0.0806	0.02329
	Final	-0.13813	-0.00737	0.00172	-0.03277	0.00428	0.00285	-0.00794	0.01252	0.00154	0.43476	0.02190
4	Initial	0	0	0	0.07833	0.07833	0	0	0.11749	0.11749	0	0.02332
	Final	0.07764	0.00084	0.00084	0.10634	0.00034	0.00084	-0.00084	0.16971	0.17039	-0.21269	0.02262
5	Initial	0	-0.04	-0.07	-0.02	0.04	0	0	0.16	0.08	0	0.02389
	Final	0.05211	-0.03048	-0.02088	0.04810	-0.00027	-0.05369	0.05808	0.16557	0.15104	-0.14521	0.02289
6	Initial	0.0575	-0.00855	-0.02534	0	0.0575	0	0	0.02634	0.2	0	0.02376
	Final	-0.11270	-0.00664	-0.01328	-0.00569	-0.01287	-0.00723	-0.00474	-0.00822	0.01597	0.42168	0.02197
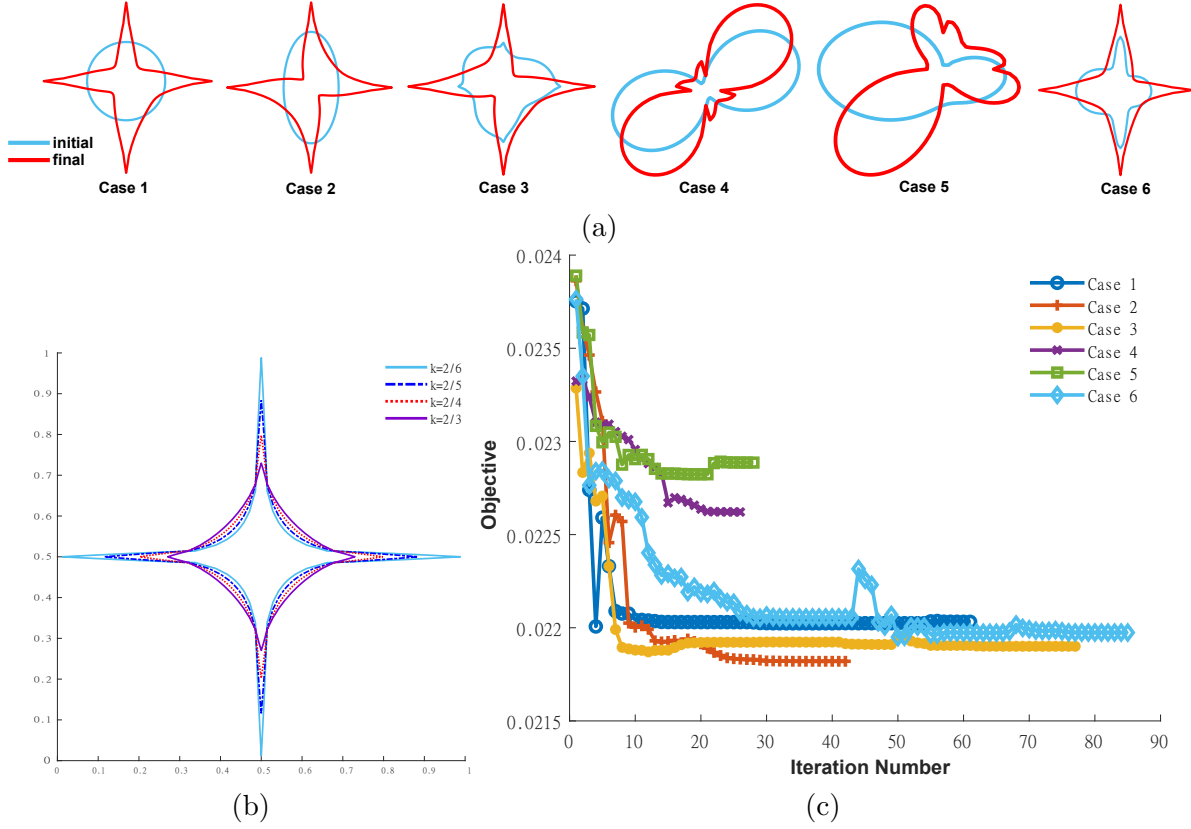
Figure 2.21: Optimization results for the case depicted in Figure 2.20a: (a) optimal designs obtained for six different initial designs; (b) comparison of perfect star shapes; c) convergence history of the plate compliance for the six initial designs.

2.6.2   A case with center movement

We consider a case where the second enrichment of the parametrization is used. Equation 2.42 with center of the inclusion as design variables is utilized. A shear load ($\tau_0 = 0.5$) is applied to a square plate (size $L = 1$) with fixed support at the bottom edge as shown in Figure 2.20a. The inclusion is softer than the matrix with material properties $\frac{E_1}{E_2} = 10$, and $\nu_1 = \nu_2 = 0.3$. The equality constraint is the same area constraint as the previous case. We use a 64×64 mesh. Local minima at three different locations are obtained. The shapes move to the top-right corner, the top-left corner, or the bottom middle depending on the starting designs. The ones at the top-right and left locations have similar objective values.

(a)

(b)
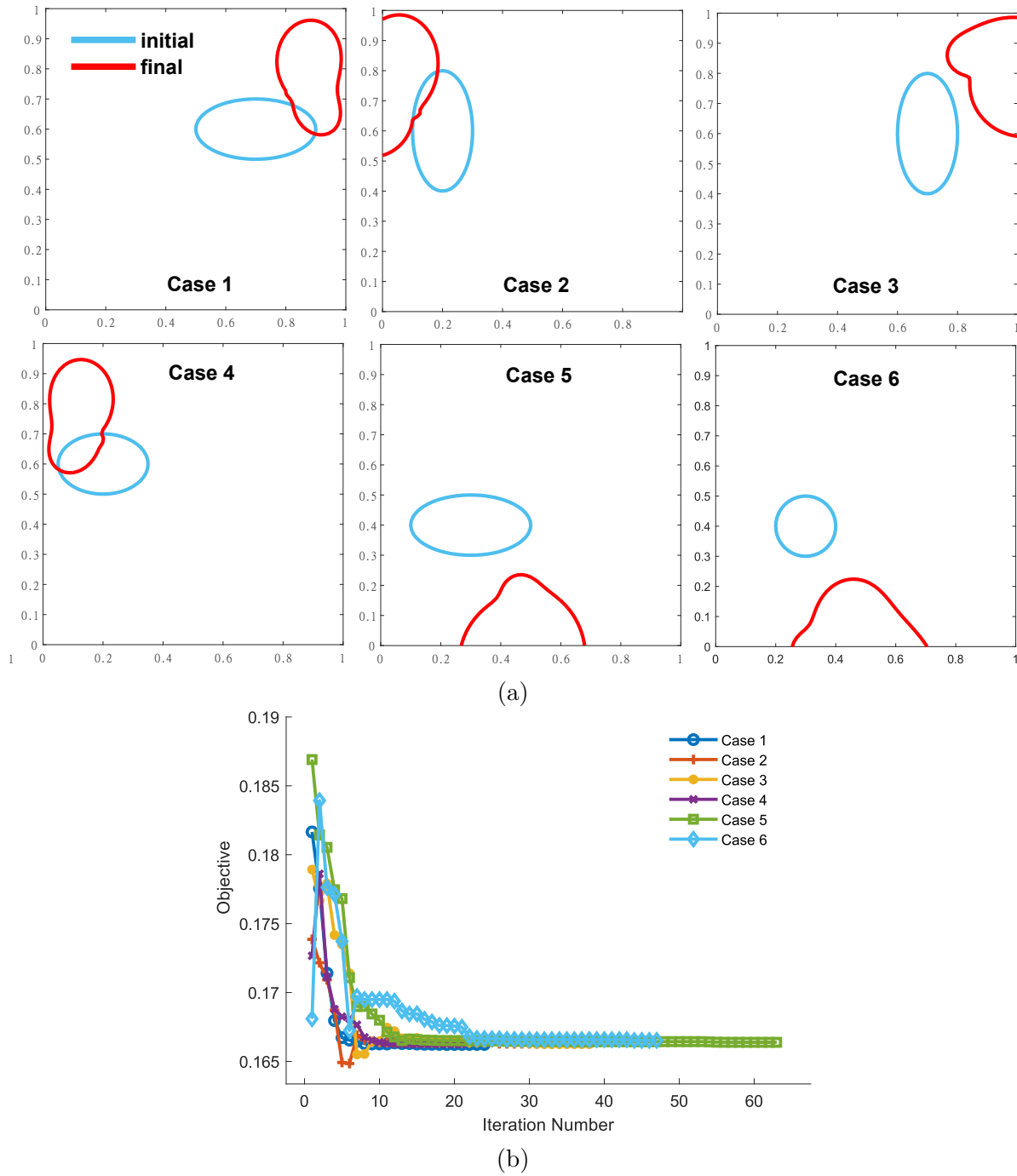
Figure 2.22: Optimization results for the case depicted in Figure 2.20b: (a) optimal designs obtained from six different initial designs; (b) convergence history of the plate compliance for the six initial designs.

Table 2.3: Objective and design variable values for the initial and optimum designs for a square plate under shear loading over the top edge.

Case		d_1	d_2	d_3	d_4	d_5	d_6	d_7	d_8	d_9	d_{11}	d_{12}	Objective
1	Initial	0	0	0	0	0	0	0	0.2	0.1	0.7	0.6	0.18165
	Final	-0.02125	0.05938	0.07295	-0.00311	-0.05838	-0.02457	-0.02245	0.1569	0.12576	0.8442	0.70789	0.16617
2	Initial	0	0	0	0	0	0	0	0.1	0.2	0.2	0.6	0.17386
	Final	0.00639	0.07998	-0.09305	0.01581	-0.01051	-0.03744	0.01031	0.12588	0.17873	0.08597	0.66785	0.16628
3	Initial	0	0	0	0	0	0	0	0.1	0.2	0.7	0.6	0.17892
	Final	0.01905	0.00264	0.12635	-0.03745	0.01994	0.00373	-0.00318	0.16984	0.1474	0.87131	0.81435	0.16625
4	Initial	0	0	0	0	0	0	0	0.15	0.1	0.2	0.6	0.17266
	Final	-0.0313	0.06722	-0.04964	0.01033	-0.056	-0.02476	0.01378	0.1591	0.14735	0.13886	0.69007	0.16616
5	Initial	0	0	0	0	0	0	0	0.2	0.1	0.3	0.4	0.18691
	Final	0.02410	-0.08631	-0.02347	0.01891	-0.03340	-0.00731	0.01913	0.16033	0.1541	0.4968	0.10972	0.16651
6	Initial	0	0	0	0	0	0	0	0.1	0.1	0.3	0.4	0.16809
	Final	0.04123	-0.1354	0.02966	0.00783	-0.05459	0.00526	0.00653	0.18934	0.18907	0.46226	0.07206	0.16640

The optimums obtained from various initial configurations are shown in 2.22a. Table 2.3 provides final designs obtained from a few initial designs. Figure 2.22b provides the objective vs iteration history.

This case showcases an important advantage of ncPG-IIFEM based shape optimization method over any mesh movement based methods. Mesh movement based methods would have caused extreme distortions in the mesh due to the movement of the inclusions, which would have added significant errors in the analysis and the optimum obtained, thus necessitating remeshing after each iteration which increases the computational costs.

2.6.3   A case with multiple inclusions- particulate composites

We consider an example problem presented in [97]. A square domain of length $L = 1$ with five stiff circular inclusions is considered. A linearly varying distributed traction is applied along its upper edge as shown in Figure 2.20c. The design variables are the radii and locations of five circular inclusions. The ratio of Young's modulus is $\frac{E_2}{E_1} = 10$ and Poisson's ratio $\nu_1 = \nu_2$
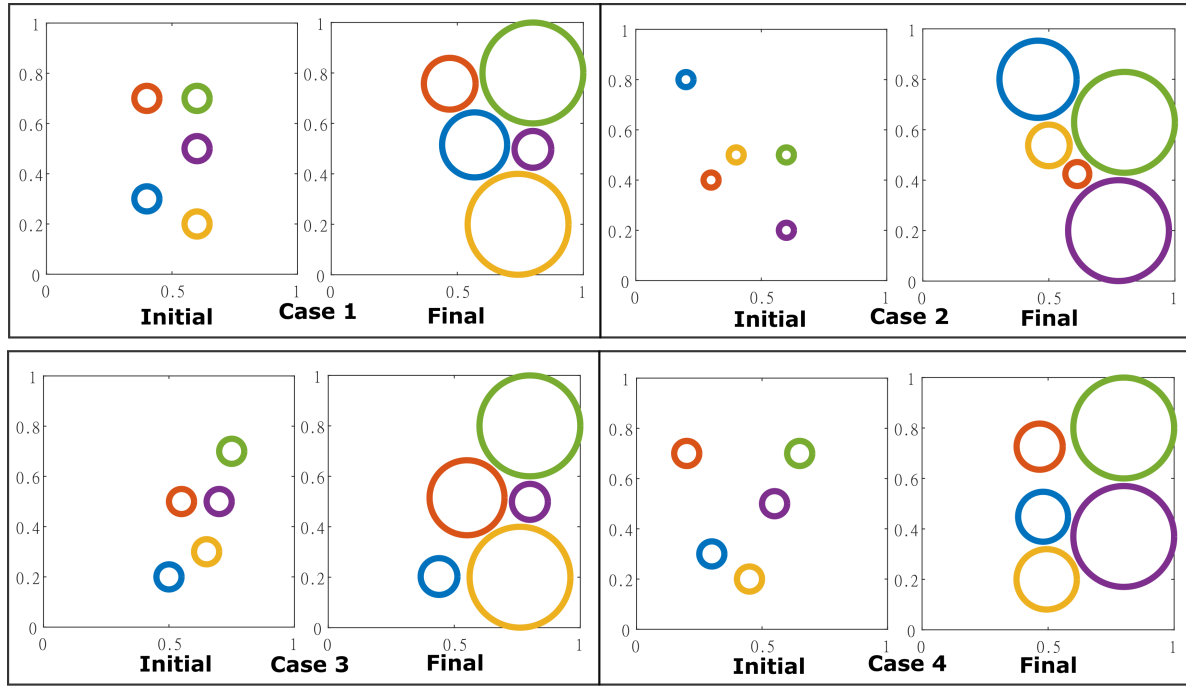
(a)
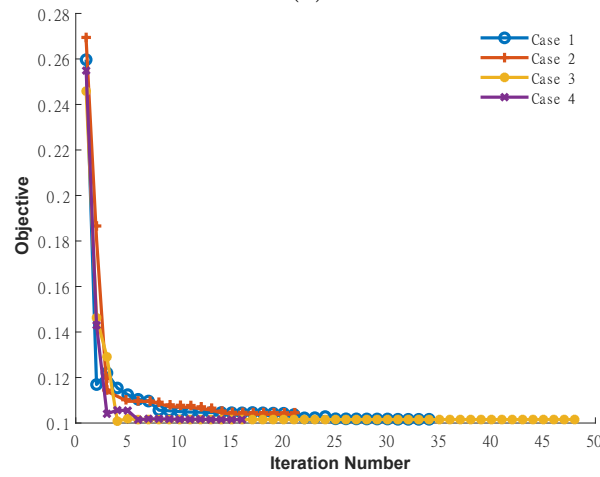
(b)

Figure 2.23: Optimization results for the case depicted in Figure 2.20c: (a) optimal designs obtained for four different initial designs; (b) convergence history of the plate compliance for the four initial designs.

$= 0.3$). The objective is to minimize the compliance of the composite subject to a maximum inclusions area fraction constraint ($A_{total} \leq 0.1125\pi$). The distance C_{ij} between the centers of the inclusions i and j satisfy $C_{ij} \geq R_i + R_j + 0.03L$ to prevent overlapping. The radii and

the centers of the inclusions are bounded as $0.03L \leq R_i \leq 0.2L$ and $0.2L \leq x_{ci}, y_{ci} \leq 0.8L$.

The initial and final configurations for four trials with different initial configurations are illustrated in Figure 2.23a. The iteration histories of the compliance for these four trials are presented in Figure 2.23b. Because of the linearly increasing loading the stiff circles move to the right to reduce the compliance, which is apparent from the local optimum designs.

Chapter 3

Material Design using Topology Optimization with IIFEM

Materials can be architectured to have desired effective properties, including properties not usually found in nature. Topology optimization has been extensively used in the past to design the topology of a unit cell with the effective material properties calculated using homogenization. In this study, we utilize topological shape optimization in conjunction with the Immersed Interface Finite Element Method (IIFEM) for the computational design of materials with desired effective mechanical properties. Remeshing or mesh movement is not required for the IIFEM-based shape optimization thus reducing the computational cost and complexity. Numerical homogenization is used to evaluate the effective properties of the microstructure. Level set-based topology optimization is used to evolve the boundaries within the unit cell to generate effective materials consisting of optimal periodic microstructure. The design space is parameterized using radial basis functions which are used to interpolate the level set function. A standard gradient-based optimization algorithm is used to find the optimal coefficients of the radial basis functions. This method produces geometries with smooth boundaries and distinct interfaces. The compactness of the level set function, the IIFEM, and performance/constraint dependence on just the interface elements make the calculation of gradients straightforward and computationally efficient. Several numerical examples are shown to demonstrate the potential of the approach.

3.1   Numerical Homogenization

In this section, a brief overview of the continuum micromechanics theory for calculating the effective properties of a metamaterial is presented. The approach followed is based on energy equivalence and averaging methods. This involves establishing a correspondence between the microscale representative volume element (RVE) and a representation of that RVE as an effective homogeneous medium [197, 198, 199]. A more rigorous multi-scale approach is based on oscillating coefficients in the governing differential equations with periodicity assumptions and the use of theoretical framework of asymptotic expansion theory [109, 199]. Three kinds of boundary conditions can be applied, a linear displacement boundary condition where the prescribed displacement vector on the boundary is a linear function of the position vector, uniform boundary traction where a constant traction is applied on any boundary which is straight, and the periodic boundary condition (PBC). All three conditions admit a single solution, up to a rigid body motion for the traction boundary condition and a translation for PBC if the constitutive behavior of the components is described by linear elasticity [200].

The linear displacement and uniform traction boundary conditions, when used for homogenization, give the same effective properties as PBC. If PBC is applied, effective properties calculation using boundary stresses can be further simplified leading to computationally efficient sensitivity analysis. Moreover, PBC is the most appropriate boundary condition when the metamaterial is considered to be a periodical array of the RVEs. In such periodic unit cells, PBC-based analysis results can also be used to accurately calculate local stresses. Therefore, in this work, we apply PBC to the unit cell.

Let $\hat{\sigma}_{ij}$, $\hat{\epsilon}_{ij}$, $\hat{u}_i$ and $\hat{x}_i$, be the macroscale stress, strain, displacements, and coordinate systems, respectively. Let σ_{ij}, ϵ_{ij}, u_i and x_i, be the microscale RVE stress, strain, displacements, and coordinate systems, respectively. For linear elastic materials and from asymptotic

expansion theory, it can be shown that the macroscale and microscale can be related to one another through the definition of the effective stiffness tensor (L^{eff}_{ijkl}). Thus, the macroscale constitutive relation is given as

$$\hat{\sigma}_{ij} = L^{\text{eff}}_{ijkl}\hat{\epsilon}_{kl} \tag{3.1}$$

where the microscale RVE is used to obtain the effective stiffness.

Considering all the materials in the RVE to be linear elastic, the Cauchy stress and infinitesimal strain tensor in the RVE are related as follows

$$\sigma_{ij} = L_{ijkl}\epsilon_{kl} \tag{3.2}$$

where L_{ijkl} is a function of the microscale coordinate system and depends on the microstructure of the metamaterial. A computational approach is taken to calculate the effective stiffness (L^{eff}_{ijkl}) from the contribution and the influence of the collective behavior of the materials at a microstructural level including the geometry, orientation and composition (L_{ijkl}) of the individual constituents of the RVE.

For a periodic unit cell, the periodic displacement field on the boundary can be expressed as follows [201]:

$$u_i(x_1, x_2, x_3) = \epsilon^0_{ik}x_k + u^*_i(x_1, x_2, x_3) \tag{3.3}$$

where ϵ^0_{ik} is a constant symmetrical tensor and $u^*_i(x_1, x_2, x_3)$ is a periodic function from one unit cell to the another and represents a modification to the linear boundary displacement field due to the heterogeneous structure of the composite/porous material.

Every periodic unit cell must exhibit boundary edges that appear in pairs. For the case of

parallel periodic edges, the displacements can be expressed as follows:

$$
\begin{aligned}
u_i^{p+} &= \epsilon_{ik}^0 x_k^{p+} + u_i^* \\
u_i^{p-} &= \epsilon_{ik}^0 x_k^{p-} + u_i^*
\end{aligned}
\tag{3.4}
$$

where $'p+'$ and $'p-'$ correspond to the pth pair of opposite parallel boundary edges of the unit cell. The difference of the above equations is applied as displacement constraint boundary conditions in the finite element analysis, i.e.,

$$
u_i^{p+} - u_i^{p-} = \epsilon_{ik}^0 (x_k^{p+} - x_k^{p-})
\tag{3.5}
$$

Two conditions are met at the boundaries of adjacent periodic unit cells because of the periodic displacements prescribed above. Firstly, the above condition ensures displacements remain continuous, and the unit cells don't separate or overlap at their boundaries post-deformation. Secondly, if the displacement-based finite element method is used, the continuity of traction distributions along the boundaries of adjacent periodic unit cells is automatically satisfied, i.e.,

$$
\sigma_{ik}^{p+} n_k^{p+} = -\sigma_{ik}^{p-} n_k^{p-}
\tag{3.6}
$$

It can be shown that the average strain in the unit cell is completely determined by the applied displacements at the boundary. Let the notation for volume averages be $\langle \bullet \rangle = \frac{1}{V} \int_V \bullet \, dV$. In the case of the applied periodic displacements as shown in Equation 3.5, the average strain is

$$
\langle \epsilon_{ij} \rangle = \epsilon_{ij}^0
\tag{3.7}
$$

Similarly, the average stress in the unit cell is completely determined by the boundary tractions. Further simplifications on the calculation of average stresses can be carried out because of the applied periodic boundary conditions. For the 2D cases, utilizing the divergence theorem and equilibrium conditions, the area-averaged stresses are as follows:

$$\langle \sigma_{ij} \rangle = \frac{1}{A} \int_{\partial A} \sigma_{ik} x_j n_k ds \tag{3.8}$$

where n_k is the unit outward normal on the boundary ∂A. Consider a rectangular unit cell, then

$$\frac{1}{A} \int_{\partial A} \sigma_{ik} x_j n_k ds = \sum_{p=1}^{2} \left(\frac{1}{A} \int_{\partial A^{p+}} \sigma_{ik}^{p+} x_j^{p+} n_k^{p+} ds + \frac{1}{A} \int_{\partial A^{p-}} \sigma_{ik}^{p-} x_j^{p-} n_k^{p-} ds \right) \tag{3.9}$$

where $'p+'$ and $'p-'$ are the pth parallel pair of boundary edges. From the periodicity assumption, we have $\sigma_{ik}^{p-} n_k^{p-} = -\sigma_{ik}^{p+} n_k^{p+}$. Applying these conditions to equation 3.9, we have

$$\langle \sigma_{ij} \rangle = \sum_{p=1}^{2} \frac{1}{A} \int_{\partial A^{p+}} \sigma_{ik}^{p+} (x_j^{p+} - x_j^{p-}) n_k^{p+} ds = \sum_{p=1}^{2} \frac{1}{A} \int_{\partial A^{p+}} T_i^{p+} \Delta^p x_j ds \tag{3.10}$$

where T_i^{p+} is the traction on the edges corresponding to ∂A^{p+} and $\Delta^p x_j$ is the difference in x_j coordinate between the $p+$ and $p-$ edges. The final integral involves the sum of ith component of traction on the corresponding edges and the difference of the coordinate along the jth dimension between the corresponding parallel edges. For one of the parallel pairs of edges, $p \neq j$, when we compare the coordinates along the jth dimension, the values are the same, and thus $\Delta^p x_j = 0$. In other words, we will only have one edge pair for which the difference between the jth coordinates is non-zero. Thus, we have

$$\langle \sigma_{ij} \rangle = \frac{1}{A} \int_{\partial A^{j+}} T_i^{j+} \Delta^j x_j ds \tag{3.11}$$

which is the average of the corresponding traction component over one edge.

From the assumption of effective homogeneous material being energetically equivalent to that of the RVE, i.e., $W^{\mathrm{RVE}} = W^{\mathrm{eff}}$, and the Hill-Mandel theorem, the expression for effective stiffness can be derived. The Hill-Mandel theorem states that the average of the product of stress and strain tensors equals the product of the averaged stress and strain tensors if certain boundary conditions are satisfied. Under the prescribed PBC, it can be shown that the Hill-Mandel theorem is applicable if the mean spacing between heterogeneities are small compared to the sample length [202]. Under these assumptions, the following expression is obtained

$$\langle \sigma_{ij} \rangle = L^{\mathrm{eff}}_{ijkl} \langle \epsilon_{kl} \rangle \tag{3.12}$$

Thus, the effective stiffness tensor L^{eff}_{ijkl} can be evaluated from the volume averaged stress of an RVE when PBC is applied. The effective properties of the metamaterial will be influenced by both the material symmetries of its components and how they are arranged within the microscale RVE. Computationally, periodic displacement boundary conditions corresponding to appropriate unit average strains are applied, and then the average stresses are calculated using FEM of choice to obtain the effective stiffness matrix.

For PBC, the average stress is calculated from the average of a particular traction over a particular edge as derived above. When using FEM, the average tractions are calculated from the corresponding edge nodal forces. The expression in Equation 3.11 is utilized in the immersed interface FEM to calculate the effective stiffness matrix. Nodal forces, as shown in the upcoming section, are considered direct outputs of the FEM, thus simplifying the sensitivity analysis.

3.2   Immersed Interface FEM

The Petrov-Galerkin formulation for a rectangular immersed-interface element has been presented in Chapter 2 (Kaudur and Patil [172]). A brief overview of the formulation will be provided in this section. The IIFEM code was specialized for periodic displacement constraints. Also, nodal forces along the edge are considered as unknowns along with the nodal displacements. This facilitates the efficient calculation of the effective stiffness matrix and performing sensitivity analysis.

A linear approximation of the interface is considered in each immersed element as shown in Figure 3.1. The linear interface $\mathbf{\Gamma}_e$ divides the rectangular domain of the finite element Ω_e into two subdomains $\mathbf{\Omega}_e^-$ and $\mathbf{\Omega}_e^+$ as shown in Figure 3.1. Independent bilinear polynomials are used in each domain[33]. The trial functions in the immersed element are such that the displacement components are coupled. The trial function vector $\mathbf{\Phi}(x,y)$ can be represented as follows:

$$
\mathbf{\Phi}(x,y) = \begin{cases} \mathbf{\Phi}^-(x,y) = \begin{pmatrix} u^-(x,y) \\ v^-(x,y) \end{pmatrix} = \begin{Bmatrix} c_1 + c_2 x + c_3 y + c_4 xy \\ c_5 + c_6 x + c_7 y + c_8 xy \end{Bmatrix} \quad \forall (x,y) \in \mathbf{\Omega}_e^- \\[2em] \mathbf{\Phi}^+(x,y) = \begin{pmatrix} u^+(x,y) \\ v^+(x,y) \end{pmatrix} = \begin{Bmatrix} c_9 + c_{10} x + c_{11} y + c_{12} xy \\ c_{13} + c_{14} x + c_{15} y + c_{16} xy \end{Bmatrix} \quad \forall (x,y) \in \mathbf{\Omega}_e^+ \end{cases}
$$

$$(3.13)$$

To determine the 16 unknown constants within the trial functions, a system of 16 linear equations has to be solved. The FE function's value at the four nodes for the two displacements yields eight conditions. Due to the bilinear nature of the approximating functions, ensuring FE function continuity across the interface necessitates six equations. Additionally, maintaining traction continuity in an integral sense at the interface contributes
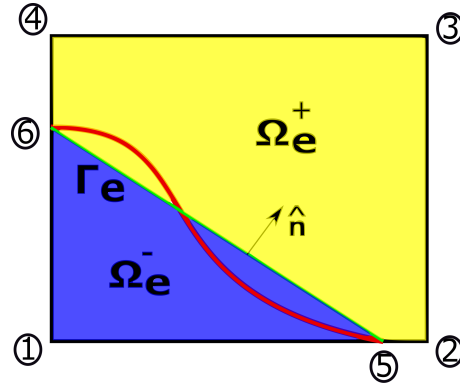
Figure 3.1: Immersed rectangular element: local linear approximation of an interface separating two materials.

two more equations.

To achieve continuity, the conventional approach involves enforcing continuity across two interface points and continuity of the mixed partial derivative. This leads to numerical ill-conditioning when the interface length approaches zero. To avoid this, it can be replaced with displacement, slope, and the mixed partial derivative continuity at the midpoint of the interface. Traction continuity implies the involvement of kinetics in the calculation of trial functions, unlike purely kinematical considerations for conventional FEM. Thus the trial functions are dependent on the interface geometry and relative material properties of the two materials.

The trial functions generated using the aforementioned procedure are coupled. A deformation at a node along the x-direction will result in deformations in both the x and y directions at locations other than the prescribed nodes. IIFEM trial functions result in a nonconforming displacement field along the edges that intersect with an immersed material interface. Along these edges, a non-material or overlap region can be observed. While the displacement discontinuity may appear nonphysical, it is small and converges to zero with mesh refinement (like any other discretization error). As the mesh size decreases, the local solution in the immersed element approaches a piecewise constant strain and stress state, and the

IIFEM trial function space can exactly represent this general solution. For more details on eliminating the ill-conditioning during trial function calculation, numerical integration, and verification such as patch test see Chapter 2 (Kaudur and Patil [172]).

Care needs to be taken when modeling voids in an immersed element. In general, voids can be modeled as an ersatz material [118] with modulus less than or equal to 10^{-3} times the solid material and the Poisson's ratio the same as that of the solid material that surrounds it. Trial functions of an immersed element for a high material property ratio with some interface configurations cannot be generated as the coefficient matrix used during its calculation becomes singular. The existence of such singular configurations for various modulus ratios and for some sets of Poisson's ratio has been shown in [33]. A specific case is provided for the triangular elements with linear trial functions, while only bounds ensuring solvability are provided for the rectangular elements with bilinear trial functions. The interface traction magnitudes are high for singular configurations. The traction discontinuity becomes very large for all the configurations very close to the singularity. This is the result of traction continuity being not exactly satisfied for bilinear rectangular elements. Remedies to overcome such issues for extreme moduli ratios and Poisson's ratio values is an ongoing research. When the modulus of the softer material is 10^{-2} times that of the solid material and for Poisson's ratio of 0.3, no singular configurations were found with bilinear IFE.

The displacement approximation over each element is given by:

$$\boldsymbol{u}^e(\boldsymbol{x}) = \sum_{i=1}^{8} \boldsymbol{\phi}_i^e(\boldsymbol{x}) u_i^e \tag{3.14}$$

where u_i^e are the eight element nodal degrees of freedom. $\boldsymbol{\phi}_i$'s are the trial functions. $\boldsymbol{\phi}_i$'s over non-immersed element are the same as conventional FE shape functions, while $\boldsymbol{\phi}_i$'s on immersed element are calculated as described above and are dependent on the properties of

the two materials and the geometry of the immersed interface.

The test function is represented by:

$$\boldsymbol{v}^e(\boldsymbol{x}) = \sum_{i=1}^{8} \boldsymbol{\psi}_i^e(\boldsymbol{x}) v_i^e \tag{3.15}$$

where $\boldsymbol{v}^e(\boldsymbol{x})$ is test function over the element, represented as a linear combination of linearly independent nodal test functions $\boldsymbol{\psi}_i^e(\boldsymbol{x})$ which are the conventional nodal FE shape functions for all elements.

A Petrov-Galerkin formulation is employed to transform the vector equilibrium equation from its differential (strong) form into a weak form. In Voigt notation, the $2D$ linear elasticity equilibrium equation is expressed as follows:

$$\boldsymbol{\mathcal{D}}^T \cdot (\boldsymbol{C}(\boldsymbol{x}) \cdot \boldsymbol{\mathcal{D}} \cdot \boldsymbol{u}(\boldsymbol{x})) + \boldsymbol{f} = 0 \quad \boldsymbol{x} \in \boldsymbol{\Omega} \tag{3.16}$$

where $\mathcal{D}$ is the 3×2 differential operator in Voigt notation, $\boldsymbol{C}$ is the constitutive matrix, $\boldsymbol{u}$ is the 2×1 displacement field over the domain $\boldsymbol{\Omega}$, and $\boldsymbol{f}$ is the 2×1 applied body force field per unit area (which for metamaterial design is zero). The weak form can be obtained by performing a dot product with test functions, followed by integration by parts and then applying Green's theorem:

$$- \int_{\Omega} [(\boldsymbol{C}(\boldsymbol{x}) \cdot \boldsymbol{\mathcal{D}} \cdot \boldsymbol{u}(\boldsymbol{x}))] \cdot [\boldsymbol{\mathcal{D}} \cdot \boldsymbol{v}(\boldsymbol{x})] dA + \int_{\partial\Omega} \boldsymbol{T} \cdot \boldsymbol{v}(\boldsymbol{x}) ds + \int_{\Omega} \boldsymbol{f} \cdot \boldsymbol{v}(\boldsymbol{x}) dA = 0 \tag{3.17}$$

where $\partial\Omega$ is the boundary of the domain, and $\boldsymbol{T}$ is the traction on the boundary given by $\boldsymbol{T} = \boldsymbol{n}^T \cdot \boldsymbol{C} \cdot \boldsymbol{\mathcal{D}} \cdot \boldsymbol{u}(x)$, $\boldsymbol{n}$ represents 3×2 matrix of the outward normals, and $\boldsymbol{v}(\boldsymbol{x})$ is the vector test function or the weight function of the equivalent weighted residual formulation. The above equation should hold for all admissible test functions.

Let e be the set of all elements, $\mathbf{\Omega}_e$ be the domain of each element, γ_b be the intersection of an element boundary with the domain boundary, and $\boldsymbol{T}^b$ be the prescribed or unknown traction on the boundary. Nodal trial functions and test functions are substituted into Equation 3.17 and after simplification, equilibrium equations can be written for each global degree of freedom. Consider an arbitrary node with corresponding global degree of freedom d. A set of elements e_d are connected to it. If it is on the boundary, we also have a set of boundary faces b_d connected to it. The equation of equilibrium corresponding to the global degree of freedom d is as follows:

$$\sum_{e_d} \int_{\Omega_e} [(\boldsymbol{C}(\boldsymbol{x}) \cdot \boldsymbol{\mathcal{D}} \cdot \sum_{i=1}^{8} \boldsymbol{\phi}_i^e(\boldsymbol{x}) u_i^e] \cdot [\boldsymbol{\mathcal{D}} \cdot \boldsymbol{\psi}_{i_{d-e}}^e(\boldsymbol{x})] dA = \underbrace{\sum_{b_d} \int_{\gamma_b} \boldsymbol{T}^b \cdot \boldsymbol{\psi}_{i_{d-e}}^e(\boldsymbol{x}) ds}_{\text{zero for an interior node}} \qquad (3.18)$$
$$+ \sum_{e_d} \int_{\Omega_e} \boldsymbol{f} \cdot \boldsymbol{\psi}_{i_{d-e}}^e(\boldsymbol{x}) dA$$

where i_{d-e} is the element degree of freedom corresponding to the global degree of freedom d in element e, and $\boldsymbol{T}^b$ is the traction on the boundary edges. The details of this derivation and the consequences of the trial functions being non-conformal and test functions being conformal are provided in [50]. This leads to discretized equation of the form $\boldsymbol{KU} = \boldsymbol{F}$.

3.2.1 Nodal forces as DOFs in the Petrov-Galerkin formulation

For a Galerkin-based approach, multipoint constraint problems can be framed as constrained optimization problems. The weak form of the governing equations can be obtained by finding a functional that should be minimized while satisfying specific constraints. Integrating the multipoint constraints directly into the functional involves using Lagrange multipliers or penalty methods.

Calculating Lagrange multipliers, which physically correspond to the nodal forces, provides a simple way of obtaining the average of the nodal forces along the edges. This can be used to calculate the effective stiffness matrix. It also facilitates sensitivity analysis. However, a functional minimization problem does not exist in the case of Petrov-Galerkin methods. A different approach will be taken for the Petrov-Galerkin based IIFEM which results in a set of discretized equations similar to those obtained from using Lagrange multipliers and Galerkin approach. In the Petrov-Galerkin case, once the weak form is generated, the terms involving tractions on the boundary edges can be assumed as unknowns calculated during the solution process.

Consider a rectangular domain of dimensions $a \times b$. The periodic boundary conditions can be expressed in terms of the displacement components on edge pairs. For instance, if we set the origin of the mesh coordinate system at the lower-left corner of the RVE, the periodic conditions for x-extension can be written as follows:

$$u(a, y) = u(0, y) + \epsilon_{xx}^0 a$$
$$v(a, y) = v(0, y)$$
$$u(x, b) = u(x, 0) \tag{3.19}$$
$$v(x, b) = v(x, 0)$$

For extension in y-direction, the relative displacement applied to obtain non-zero uniform strain is as follows:

$$v(x, b) = v(x, 0) + \epsilon_{yy}^0 b \tag{3.20}$$

For simple shear in the xy-plane, the relative displacement applied to obtain non-zero uniform

simple shear strain has multiple possibilities. The following condition will be used:

$$u(x, b) = u(x, 0) + \gamma_{xy}^0 b \qquad (3.21)$$

Because IIFEM always deals with Cartesian mesh, applying periodic displacement boundary conditions is straightforward even if the domain has complex inclusion shapes. For a rectangular domain, edge nodes corresponding to the same x coordinates at $y = 0$ and $y = b$ are always present. Similarly, there are edge nodes with identical y coordinates at $x = 0$ and $x = a$. The matrix form of the constraint equations in terms of nodal displacements of the FEM is as follows:

$$\boldsymbol{LU} - \boldsymbol{Q} = 0 \qquad (3.22)$$

where $\boldsymbol{U}$ are the unknown nodal displacements.

Similar to Lagrange multipliers-based equations in Galerkin-based approaches, the nodal forces show up in the equations of equilibrium with the same coefficients as the coefficients of the corresponding nodal displacements in the constraint equation 3.22.

Consider the equilibrium equation for a nodal degree of freedom on the boundary edges given by equation 3.18. The components of the term $\sum_{b_d} \int_{\gamma_b} \boldsymbol{T}^b \cdot \boldsymbol{\psi}_{i_{d-e}}^e(\boldsymbol{x}) ds$ represents the nodal force on the edge node associated with the direction of the corresponding nodal degree of freedom. When periodic displacement conditions are applied, the traction/nodal forces on these edges required to achieve such displacements will be unknown. Let λ_i^x and λ_i^y be the unknown x-direction and y-direction nodal force, respectively on a node in the positive boundary edges whose global node number is i. Here, the positive boundary edge corresponds to the edge whose outward normal aligns with the positive coordinate direction. It can be shown that the normal and tangential stresses on the boundary edges are also periodic if the displacements are periodic. Thus, the tractions on the positive/negative edge pairs are
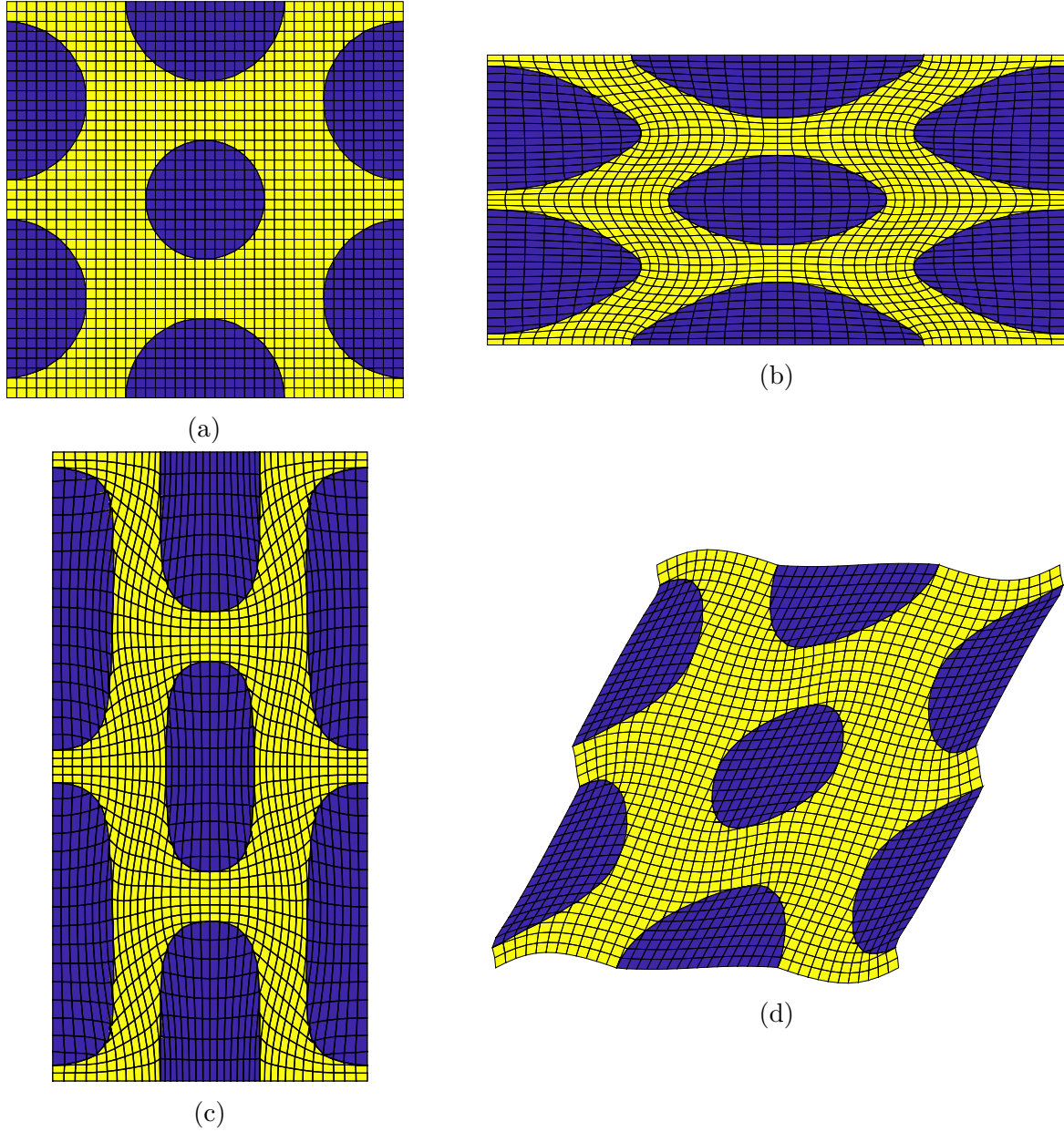
Figure 3.2: Applying periodic boundary conditions: (a) Domain definition and mesh for IIFEM; (b) x-direction extension; (c) y-direction extension; (d) simple shear deformation.

equal and opposite. This means the x and y-direction nodal force on the corresponding node in the negative boundary edge is equal to $-\lambda_i^x$ and $-\lambda_i^y$, respectively. Equation 3.18 after numerical integration, with both boundary nodal forces and all nodal displacements as

unknowns, can be written as follows:

$$
\begin{bmatrix} \boldsymbol{K} & \boldsymbol{L}^T \\ \boldsymbol{L} & \boldsymbol{0} \end{bmatrix} \begin{bmatrix} \boldsymbol{U} \\ \boldsymbol{\Lambda} \end{bmatrix} = \begin{bmatrix} \boldsymbol{F} \\ \boldsymbol{Q} \end{bmatrix}
\tag{3.23}
$$

where $\boldsymbol{K}$ is the global stiffness matrix, $\boldsymbol{\Lambda}$ is the set of unknown nodal forces. Note that $\boldsymbol{K}$ is not symmetric but the constraints and the effect of constraint forces is symmetric.

For illustration of the application of PBC, consider a square domain with Cartesian mesh as shown in Figure 3.2a. Figures 3.2b, 3.2c, and 3.2d correspond to x-extension, y-extension and shear cases with PBC, respectively. The four corner nodes belong to both right-left and top-bottom pairs of periodic boundary conditions. In total, there are eight equations for eight corner nodal degrees of freedom but two of the equations are redundant. These redundant equations (a few choices available), for example, displacement relation between the top-right and the bottom-right corner node can be replaced with pinned boundary condition of the origin node. Also, this necessitates the addition of two unknown nodal forces corresponding to these constraints. Restricting the degrees of freedom of the origin eliminates translation. In order to partially verify the effective property calculation using the edge nodal forces, a domain without inclusion was considered. The effective properties obtained from such a unit cell are the same as the prescribed material properties.

3.3 Design space parametrization and sensitivity analysis

3.3.1 Level set-based design parametrization

The Wendland function is a radial basis function that can be used to interpolate the level set function [203] for shape and topology optimization [165]. Globally supported and compactly supported radial basis functions (GSRBF and CSRBF) are the two variants that have been widely used. GSRBF generates a full dense matrix which affects the computational efficiency when approximating systems with a large amount of interpolating points. CSRBF with matrix sparseness, strictly positive definiteness, and Lipschitz continuity of the interpolation [204, 205, 206] is ideal for topological shape optimization problems. In this study, CSRBF with C^2 continuity will be used to represent the inclusion boundary for the topological shape optimization problems. The Wendland function with C^2 continuity is defined as follows [204]:

$$\phi(r) = \left[\max(0, (1-r))^4\right](4r + 1) \tag{3.24}$$

where r is the radial coordinate and is defined in two-dimensional space as follows:

$$r = \frac{\sqrt{(x - x_i)^2 + (y - y_i)^2}}{d_{mI}} \tag{3.25}$$

where (x, y) is the coordinate of a point, d_{mI} is the radius of support of a given function as it controls when r exceeds one, and (x_i, y_i), called a knot, is the center of the domain of the ith function.

Proper choice of the radius of support ensures the uniqueness of the function interpolation and guarantees computational efficiency. A large radius will increase the computational

cost whereas a small one will restrict the representation capability. Therefore, experience in selecting a radius of support is often needed [95]. With proper arrangement of the CSRBFs within the domain, they can approximate complicated functions with desirable completeness and high accuracy. A good choice of radius of support also ensures robustness with respect to small changes in the value of the support and the C^2 functions are smooth enough to ensure a good approximation. Using the CSRBF, the level set function can be obtained by placing the CSRBFs at their pre-specified knots over the whole design domain, as follows:

$$F(\boldsymbol{x}) = \sum_{i=1}^{N} \phi_i(\boldsymbol{x}) a_i \tag{3.26}$$

where $\phi_i(x) = \phi(r(\boldsymbol{x}, \boldsymbol{x_i}))$ are the Wendland functions and a_i's are the expansion coefficients and N denotes the number of knots.

The initial values for the generalized expansion coefficients are calculated by solving $B_{ij} a_i^{init} = b_j$, where the interpolation values $b_j \in \mathbb{R}$ at knot locations are assumed. The $\boldsymbol{B}$ matrix is well conditioned and invertible because of the positive definiteness of the CSRBF's [203]. Given the interpolating data of the level set function values at the knots, we can uniquely determine the level set function.

Nodal locations of the analysis mesh can be chosen as knot locations. If less number of knots are desired, a separate mesh can be created whose nodal locations are the knots. A few example inclusions (zero contour of the level set function) generated from the level set interpolation through Wendland functions are shown in Figure 3.3. Knots in these examples are nodal locations of a 40×40 square mesh. There are multiple ways to generate simple inclusions. For example, known level set functions can be used for circular or elliptical inclusions to find b_j at knot locations from which the expansion coefficients can be calculated. Scaling of coefficients should be properly done for optimization if a large

number of circular/elliptical inclusions are considered. For other simple shapes, appropriate positive and negative values can be assigned at desired nodal/knot locations and Wendland expansion coefficients can be calculated.
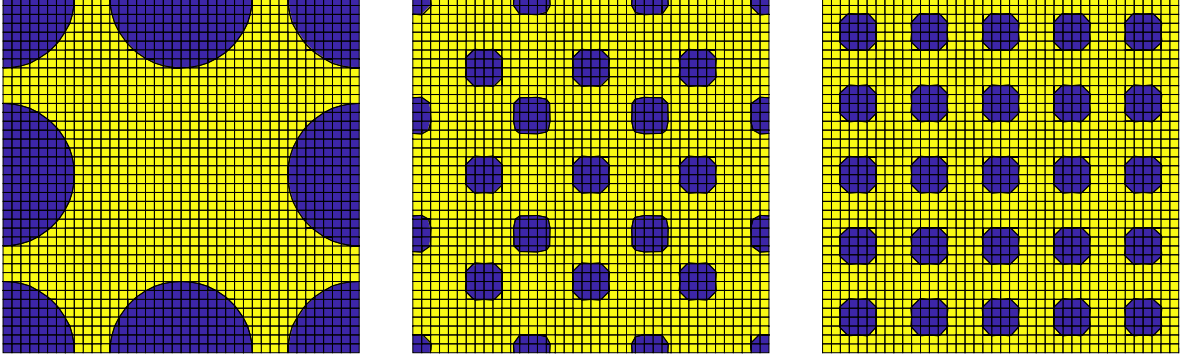
Figure 3.3: Example inclusions in a square domain: zero contours of the Wendland level set function.

3.3.2   Sensitivity analysis

For gradient-based optimization, the sensitivities of the response parameters with respect to the design variables are needed. In this study, the expansion coefficients of the Wendland level set function are the design variables. In structural optimization problems, to get the gradient of responses like displacements or stresses, it is essential to calculate derivatives of the global stiffness matrix with respect to the design variables. The elemental stiffness matrix of an immersed element has a functional dependence on the design variables that control the interface location, whereas the derivative of the elemental stiffness matrix of a non-immersed element is zero.

Consider the immersed interface finite element shown in Figure 3.1. Here $p_5 = (x_5, y_5)$ and $p_6 = (x_6, y_6)$ are the intersection points, and let $p_{gp}^i = (x_{gp}^i, y_{gp}^i)$ be the Gauss points. Let d_i be the design variables and $F(x, y, d_i)$ be the Wendland level set function whose value is zero on the material interface.

To efficiently calculate sensitivities for a large number of design variables, two things are considered. Firstly, an adjoint sensitivity formulation is used. Secondly, the stiffness matrix derivative is calculated with respect to intersection points first. This part of the calculation does not change with changes in design variables and can be calculated beforehand for a general immersed element. Then, the derivative of intersection points with respect to the design variables is calculated. That is, the derivative of the element stiffness matrix $K_{ij} \equiv K_{ij}(x_5(d_i), y_5(d_i), x_6(d_i), y_6(d_i))$, is as follows:

$$\frac{\partial K_{ij}}{\partial d_i} = \frac{\partial K_{ij}}{\partial x_5}\frac{\partial x_5}{\partial d_i} + \frac{\partial K_{ij}}{\partial y_5}\frac{\partial y_5}{\partial d_i} + \frac{\partial K_{ij}}{\partial x_6}\frac{\partial x_6}{\partial d_i} + \frac{\partial K_{ij}}{\partial y_6}\frac{\partial y_6}{\partial d_i} \tag{3.27}$$

Level set functions are used to calculate the intersection points. More specifically, level set values at the finite element node locations are utilized. The intersection points are thus related to the design variables via the level set functions. Hence, $\frac{\partial x_5}{\partial d_i}$, $\frac{\partial y_5}{\partial d_i}$, $\frac{\partial x_6}{\partial d_i}$ and $\frac{\partial y_6}{\partial d_i}$ can be easily calculated [172]. To calculate $\frac{\partial K_{ij}}{\partial x_5}$, $\frac{\partial K_{ij}}{\partial y_5}$, $\frac{\partial K_{ij}}{\partial x_6}$ and $\frac{\partial K_{ij}}{\partial y_6}$, functional dependence of the element stiffness matrix with respect to the intersection points has to be derived. The functional relationship is as follows:

$$
\begin{aligned}
K_{ij} \equiv K_{ij}(&\frac{\partial \phi_j}{\partial x}(p_{gp}(p_5, p_6), p_5, p_6), \frac{\partial \phi_j}{\partial y}(p_{gp}(p_5, p_6), p_5, p_6), \frac{\partial \psi_i}{\partial x}(p_{gp}(p_5, p_6)), \\
&\frac{\partial \psi_i}{\partial y}(p_{gp}(p_5, p_6)), W_{gp}(p_5, p_6))
\end{aligned}
\tag{3.28}
$$

The sensitivity of the stiffness matrix with respect to intersection point coordinates x_5 and y_5 using chain rule can be written as follows:

$$
\begin{aligned}
\frac{dK_{ij}}{dx_5} &\equiv \frac{\partial K_{ij}}{\partial \phi_{j,x}}\frac{D\phi_{j,x}}{Dx_5} + \frac{\partial K_{ij}}{\partial \phi_{j,y}}\frac{D\phi_{j,y}}{Dx_5} + \frac{\partial K_{ij}}{\partial \psi_{i,x}}\frac{D\psi_{i,x}}{Dx_5} + \frac{\partial K_{ij}}{\partial \psi_{i,y}}\frac{D\psi_{i,y}}{Dx_5} + \frac{\partial K_{ij}}{\partial W_{gp}}\frac{\partial W_{gp}}{\partial x_5} \\
\frac{dK_{ij}}{dy_5} &\equiv \frac{\partial K_{ij}}{\partial \phi_{j,x}}\frac{D\phi_{j,x}}{Dy_5} + \frac{\partial K_{ij}}{\partial \phi_{j,y}}\frac{D\phi_{j,y}}{Dy_5} + \frac{\partial K_{ij}}{\partial \psi_{i,x}}\frac{D\psi_{i,x}}{Dy_5} + \frac{\partial K_{ij}}{\partial \psi_{i,y}}\frac{D\psi_{i,y}}{Dy_5} + \frac{\partial K_{ij}}{\partial W_{gp}}\frac{\partial W_{gp}}{\partial y_5}
\end{aligned}
\tag{3.29}
$$

where $\frac{D}{Dx_5}$ is defined as follows:

$$\frac{D}{Dx_5} = \sum_k \frac{\partial x_{gp}^k}{\partial x_5} \frac{\partial}{\partial x}\bigg|_{x_{gp}^k} + \sum_k \frac{\partial y_{gp}^k}{\partial x_5} \frac{\partial}{\partial y}\bigg|_{y_{gp}^k} + \frac{\partial}{\partial x_5} \tag{3.30}$$

The final term in the above expression $\frac{\partial}{\partial x_5}$ can be ignored for the cases where such dependence is not present, such as in the case of test functions. Similar stiffness sensitivity equations can be written for derivatives with respect to x_6 and y_6. The derivatives $\frac{\partial K_{ij}}{\partial \phi_{j,x}}, \frac{\partial K_{ij}}{\partial \phi_{j,y}}, \frac{\partial K_{ij}}{\partial \psi_{i,x}}, \frac{\partial K_{ij}}{\partial \psi_{i,y}}, \frac{\partial K_{ij}}{\partial W_{gp}}$ are obtained from the definition of stiffness matrix [172]. Whereas, $\frac{D\phi_{j,x}}{Dx_k}, \frac{D\phi_{j,y}}{Dx_k}, \frac{D\psi_{i,x}}{Dx_k}, \frac{D\psi_{i,y}}{Dx_k}$ is obtained from the definition of trial functions of the immersed element [172]. As indicated earlier $\frac{\partial \psi_{i,x}}{\partial x_k}$ and $\frac{\partial \psi_{i,y}}{\partial x_k}$ are zero as the test functions are standard FE test functions and do not depend on the interface location. For more details on the evaluation of various intermediate derivatives and a slightly different treatment of sensitivities in the case of immersed elements, see Chapter 2 (Kaudur and Patil [172]).

3.4 Level set-based topology optimization

3.4.1 Optimization formulation

A general optimization problem with specified volume/area constraint can be formulated as follows:

$$
\begin{aligned}
\min_{d} \quad & f(U(d_k), d_k) \\
\text{s.t.} \quad & K(d_k)U(d_k) = F \\
& \frac{A(d_k)}{A_0} = A_f \\
& g_l(U(d_k), d_k) \leq 0 \quad \text{where} \quad l = 1, 2, .., n \\
& d_k^{lb} \leq d_k \leq d_k^{ub}
\end{aligned}
\tag{3.31}
$$

where, f is the objective function, $\frac{A(d_k)}{A_0}$ denotes volume fraction of the solid material, A_f is the specified volume fraction, g_j denotes the inequality constraint functions, d_k are the design variables, $U(d_k)$ is the solution of the analysis equations, $K(d_k)U(d_k) = F$, where, $K(d_k)$ is the global stiffness matrix, and F is the force vector.

One significant challenge in traditional level set-based optimization methods arises from the fact that the nodal coordinates in a FEM discretization depend on the design variables. Consequently, we must compute the sensitivity of nodal coordinates with respect to the design variables. However, an immersed interface-based optimization scheme eliminates the need for this computation.

To perform gradient-based optimization, gradients for both the objective and constraint functions with respect to the design variables have to be calculated. The objective function

gradient obtained by applying chain rule to Equation 3.35 is as follows:

$$\frac{Df}{Dd_k} = \frac{\partial f}{\partial U}\frac{DU}{Dd_k} + \frac{\partial f}{\partial d_k} \tag{3.32}$$

Since, $KU = F$, and F is independent of the design variables, we can write

$$\begin{aligned} K\frac{DU}{Dd_k} + \frac{DK}{Dd_k}U &= 0 \\ K\frac{DU}{Dd_k} &= -\frac{DK}{Dd_k}U \end{aligned} \tag{3.33}$$

where $\frac{DK}{Dd_k}$ can be calculated using Equation 3.29. Thus, $\frac{DU}{Dd_k}$ is obtained by solving the system of linear equations given by Equation 3.33. $\frac{DU}{Dd_k}$ is then substituted into Equation 3.32 to obtain $\frac{Df}{Dd_k}$. This is called the direct approach and involves solving the linear system of equations 3.33 N times, where N corresponds to the number of design variables. For problems with a large number of design variables, the direct approach is not computationally efficient. Substituting Equation 3.33 into Equation 3.32, we have

$$\frac{Df}{Dd_k} = -P^T\frac{DK}{Dd_k}U + \frac{\partial f}{\partial d_k} \tag{3.34}$$

where

$$P^T = \frac{\partial f}{\partial U}K^{-1} \implies K^TP = \frac{\partial f}{\partial U}^T \tag{3.35}$$

In order to calculate the sensitivities of the objective function, Equation 3.34 is utilized. The sensitivities of equality and inequality constraint functions can be calculated in a similar manner. The number of times the linear system of equations in Equation 3.35 needs to be solved is equal to the number of objective and constraint functions (for displacement-dependent constraint functions). This is called the adjoint approach. This approach is computationally efficient for a large number of design variables, and less number of objectives

and constraint functions.

For the optimization algorithm, Sequential Quadratic Programming (SQP) [194, 195] is used. The algorithm uses a quadratic programming subproblem in which a merit function with specific penalty parameters is used. A line search procedure is also employed once the SQP gives a direction. The Hessian is approximated using the BFGS quasi-Newton method. The stopping criteria used are the maximum constraint violation, the maximum magnitude of the search direction, and the modified Lagrangian gradient all being less than the corresponding specified values.

3.4.2   Topology optimization

To demonstrate the capability of the present approach in performing level-set based topology optimization, cantilever beam and Michell structure problems are considered in the context of minimizing structural compliance. The compliance or stored elastic energy is given as $f = F^T U$.

Cantilever beam

Consider a cantilever beam with a length-to-height ratio of 2 as shown in Figures 3.4a and 3.4b. The left edge is fixed, and a concentrated vertical force $F = 0.1$ is applied. Two cases are considered for the location of the load. For case 1, consider the load at the center point of the right edge as shown in Figure 3.4a. For case 2, the load is applied at the bottom corner of the right edge as shown in Figure 3.4b. The objective function is to minimize the structural strain energy or compliance. The design domain is discretized with a 64×64 Cartesian mesh with plane stress elements. The material properties are as follows: Young's modulus for solid material is 1, for the void it is 10^{-4} and Poisson's ratio for both materials

is 0.3. For the immersed elements, void modulus can be 10^{-2} to preclude any possibility of a singularity in the trial function calculation for any interface location.
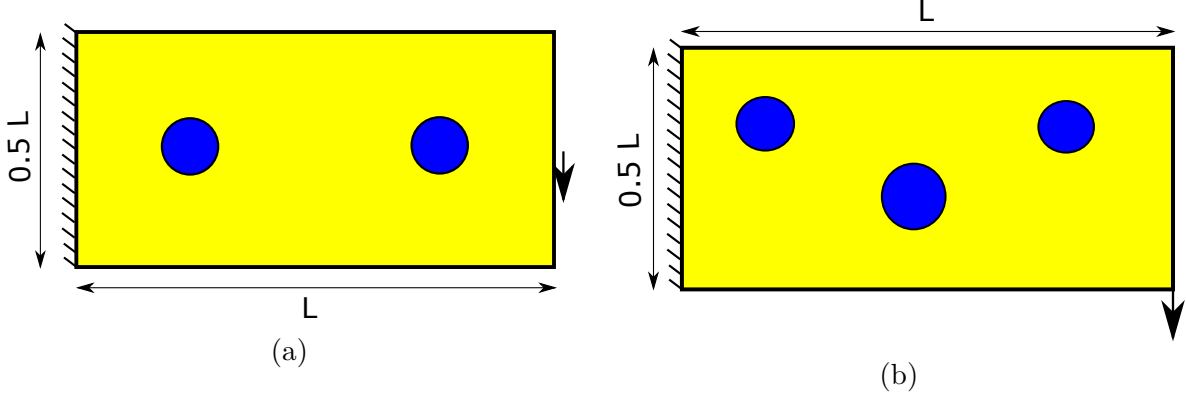
Figure 3.4: Cantilevered beams with voids are clamped on the left edge under two different loading conditions: (a) a load applied at the center of the right edge (referred to as case 1); (b) a load applied at the bottom of the right edge (referred to as case 2).

Two initial conditions are considered for each case as shown in Figures 3.5a and 3.5b. Symmetry is exploited while solving case 1. Just the bottom half of the domain is the design space and appropriate symmetry boundary conditions are applied. The material usage is limited to 50% in this case. The knots for the level-set parametrization coincide with the finite element nodes. Thus, the number of design variables is $65 \times 33 = 2145$. The support radius is 3.5 times the largest side length of an element. As indicated in the previous section, an experience or some trial runs were required to choose the support radius that ensures desired smoothness with high accuracy. A very high value increases the computational cost and a very low value does not provide desired flexibility.

The stopping criteria used for SQP are as follows: maximum constraint violation (max(g)) is less than equal to 10^{-5}, modified Lagrangian gradient (KTO) is less than equal to 10^{-6}, and maximum magnitude of the search direction (max(S)) is less than equal to 10^{-3} [194]. The optimized topology for case 1 obtained for the two starting conditions are as shown in Figures 3.6a and 3.6b. The compliance values for the final designs are 0.5908 and 0.5968,

<center>(a)   (b)</center>
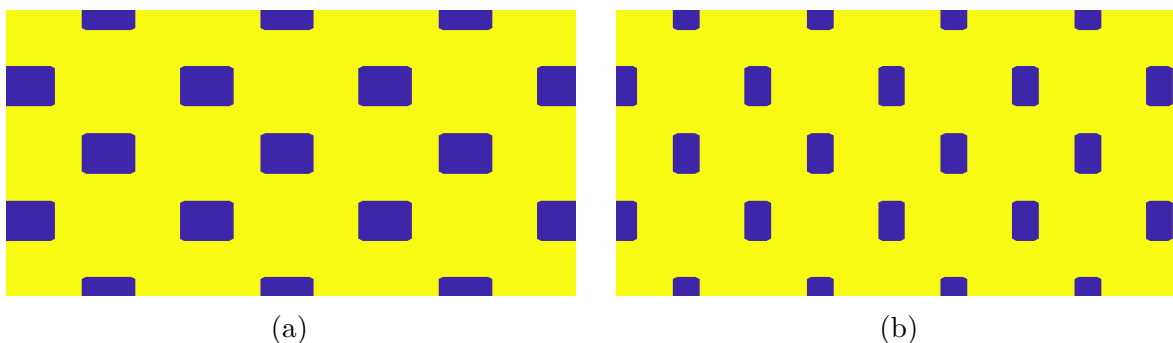
Figure 3.5: Initial designs considered for the compliance minimization problems for case 1 and case 2: (a) cases 1a & 2a; (b) cases 1b & 2b.

respectively. The iteration plots for these two designs are shown in Figure 3.7a. Beyond roughly 50 iterations, the optimizer primarily focuses on refining the boundaries. Proper scaling has to be employed for the design variables and the objective function to ensure fast convergence. The number of iterations also depends on the stopping criteria.

<center>(a)   (b)</center>

<center>(c)   (d)</center>
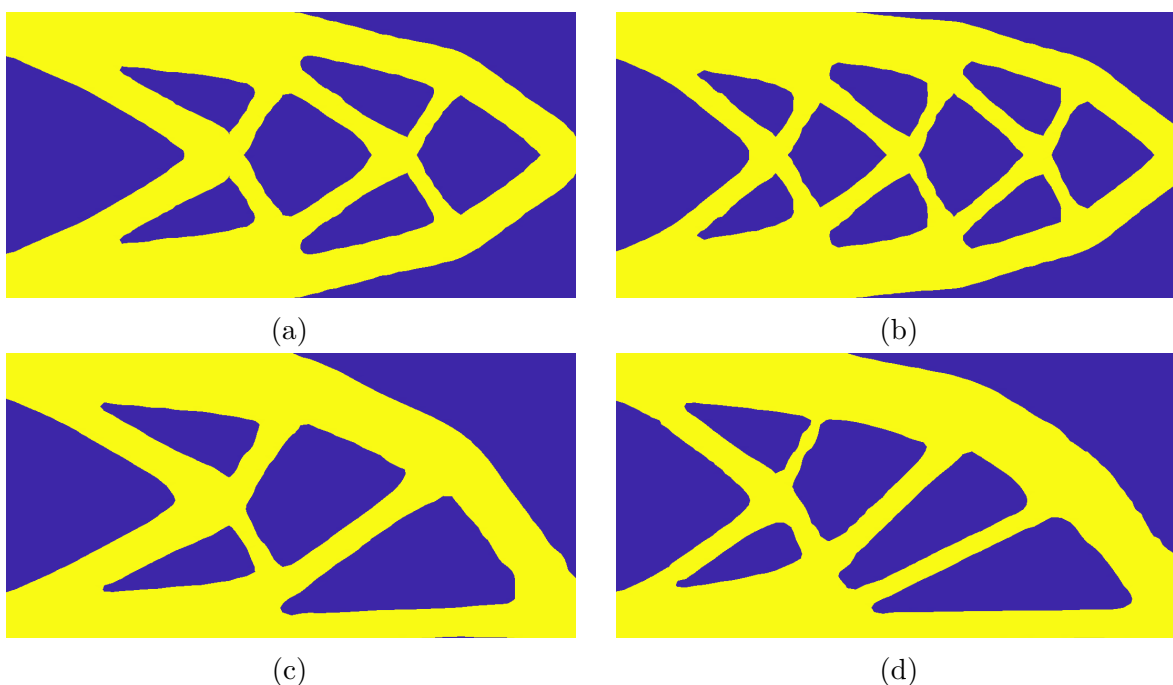
Figure 3.6: Optimal designs obtained from different initial designs for the cantilevered beam problem as given in case 1 and case 2: (a) case 1a; (b) case 1b; (c) case 2a; (d) case 2b.

For the optimization problem in case 2, the entire domain is considered. The knots
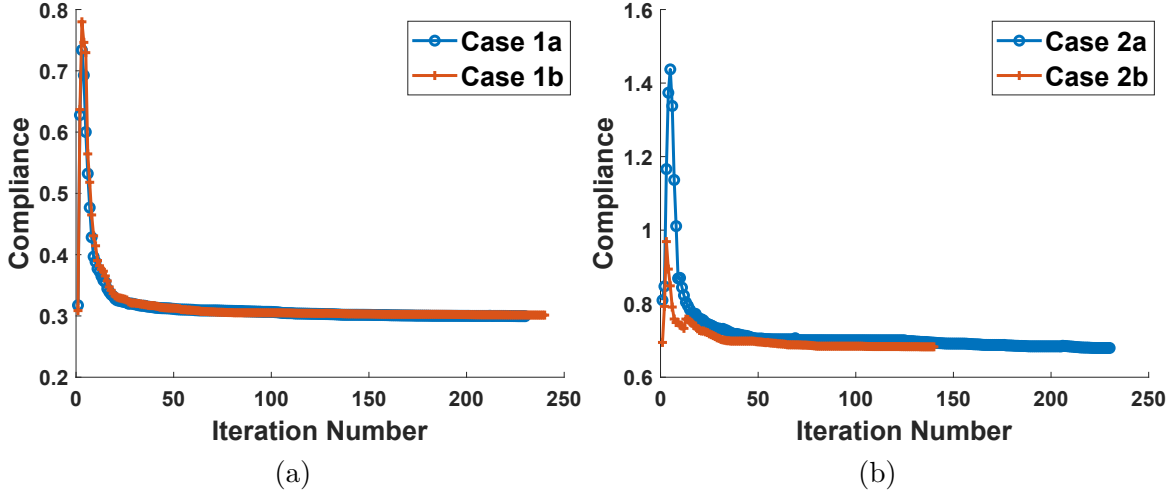
Figure 3.7: Convergence history of the cantilevered beam compliance for the considered initial designs: (a) case 1; (b) case 2.

coincide with the nodes of the finite element mesh. Thus, the number of design variables is $65 \times 65 = 4225$. The support radius is 3.5 times the largest side length of an element. The optimized topology obtained for the the two initial designs for case 2 is depicted in Figures 3.6c and 3.6d. The compliance values for the final designs are 0.6704 and 0.6708, respectively. The iteration plots are as shown in Figure 3.7b. Convergence is within 150 iteration for the first sub-case and 250 for the other design. Although not illustrated here, analogous final topologies with similar compliance values are obtained from alternate initial designs for both cases. The optimal design showcases variability in the number of holes, a trend consistent with findings reported in the literature.

Michell-type structure

A vertical point load is applied at the center point of the bottom edge of the Michell-type structure (Figures 3.8a,b). Two cases are considered for the boundary conditions. In one of the cases, the bottom-left corner is a pinned support while the bottom-right corner is supported as a roller shown in Figure 3.8a. We will call this case 3. In case 4, the bottom-

left and the bottom-right corner are pinned as shown in Figure 3.8b. Young's modulus for solid material is 1, for the void it is 10^{-4} and Poisson's ratio for both materials is 0.3. The allowed material usage is limited to 45% for both cases, and the applied concentrated force F is 0.1. The plate length to height ratio is 2. In both cases, symmetry is exploited. Only the right half of the domain is considered for optimization. Case 3 involves the implementation of a pinned support at the bottom left corner to eliminate rigid body rotation. To maintain symmetry, it can be presumed that rollers are positioned on both corners. The objective is to minimize compliance. The symmetry design domain is discretized with a 32×64 Cartesian mesh. The number of design variables is $33 \times 65 = 2145$. The support radius and the stopping criteria for the optimization algorithm are the same as in the previous example cases.

(a)   (b)
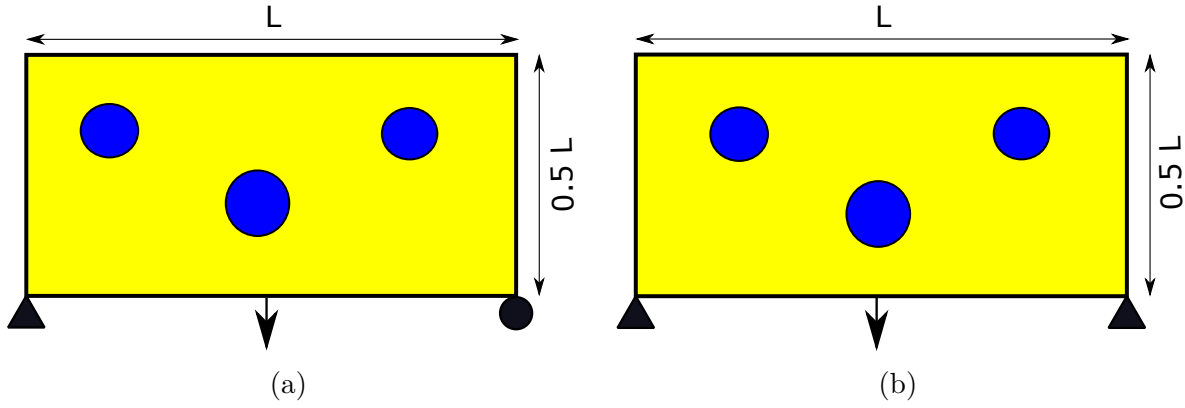
Figure 3.8: Illustration of two distinct boundary conditions considered for a rectangular plate with voids subjected to a concentrated load at the center of the bottom edge: (a) a configuration where the bottom-left corner is pinned while the bottom-right corner is supported as a roller (referred to as case 3); (b) a configuration where both the bottom-left and bottom-right corners are pinned (referred to as case 4).

Two initial conditions are considered. When projected to the whole domain it is as shown in Figures 3.9a and 3.9b. The design domain is just the right half of the plate, thus, a symmetry about $x = 1$ line can be observed in the considered initial designs. The optimized topology obtained for the the two initial designs for case 3 are given in Figures 3.10a and 3.10b. The
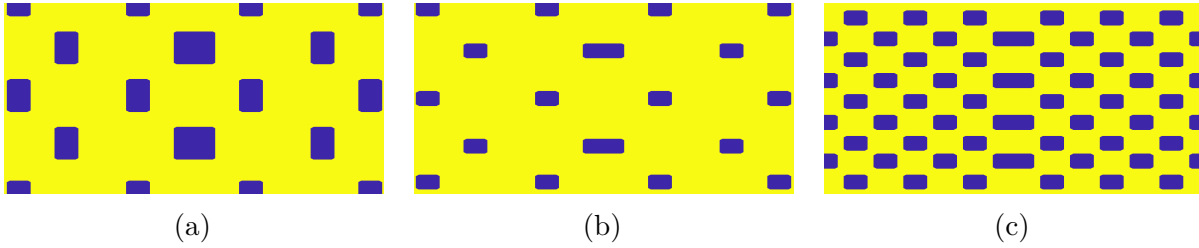
Figure 3.9: Initial designs considered for the compliance minimization problems for the Michell-type structures in case 3 and case 4: (a) case 3a; (b) cases 3b & 4a; (c) case 4b.
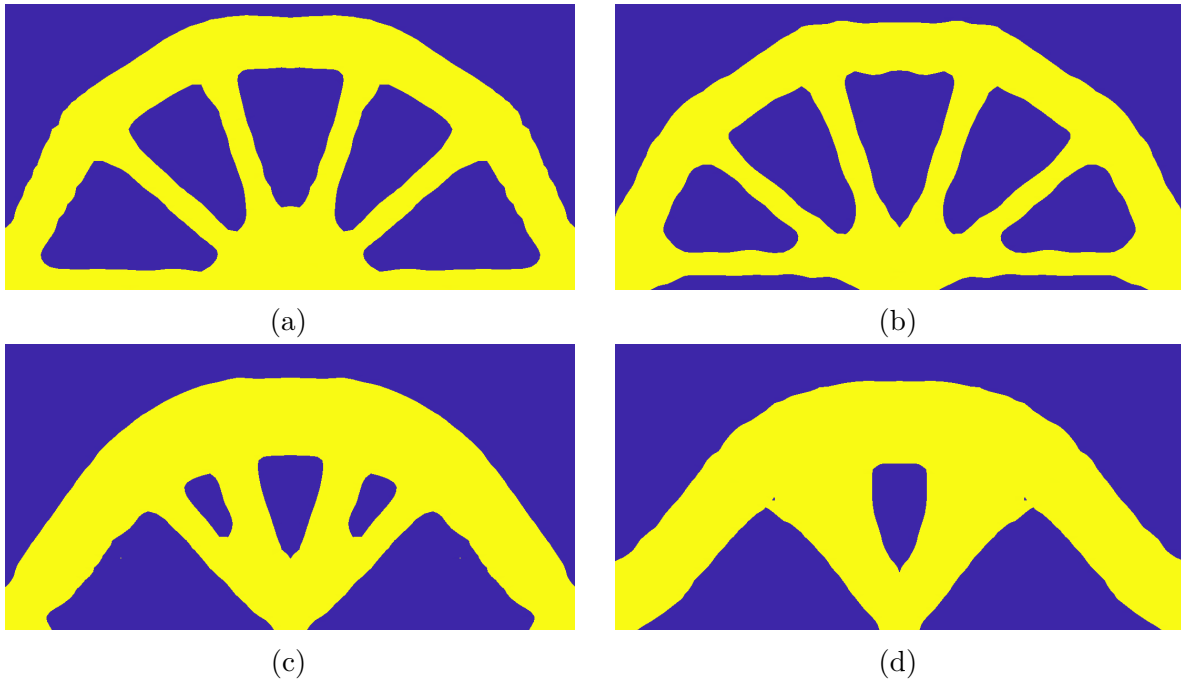
Figure 3.10: Optimal designs obtained from different initial designs for the Michell-type structures in case 3 and case 4: (a) case 3a; (b) case 3b; (c) case 4a; (d) case 4b.

compliance values of the final optimal designs are 0.1448 and 0.1378, respectively. Similar topologies are obtained with other initial designs. For case 4, the optimized designs are as shown in Figures 3.10c and 3.10d. The compliance values of the designs are 0.1006 and 0.1013, respectively. In case 3, additional horizontal members are present in the optimal design, countering deformation in the horizontal direction and subsequently reducing compliance. The number of members linking the bottom center point to the top arch in case 4 exhibits variability based on the chosen initial design. Although not shown here, such variability can
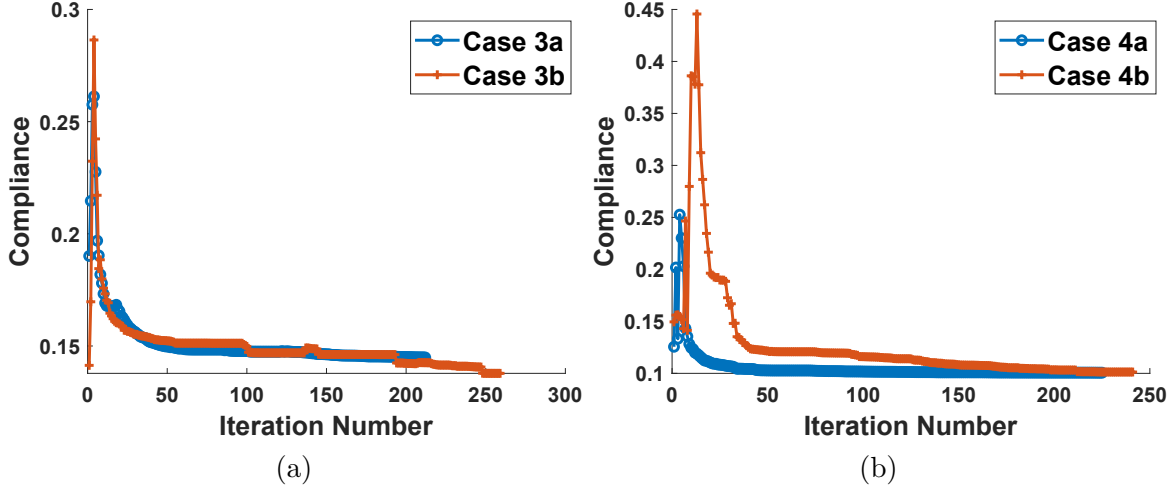
Figure 3.11: Iteration histories of the Michell problem compliance for the different cases considered: (a) case 3; (b) case 4.

also be observed in case 3. The iteration histories of compliance value for case 3 and case 4 are given in Figures 3.11a and 3.11b, respectively. The objective function displays rapid changes during the initial iterations to meet the volume constraint, followed by a stable decrement as the optimization progresses.

3.5 Material design

In this section, several unit cells with extremal or prescribed mechanical properties will be obtained to demonstrate the utility of the proposed method. The main intention of metamaterial design is to obtain the material cell with the desired stiffness or mechanical property, which includes the maximum bulk modulus, maximum shear modulus, prescribed Poisson's ratio, and negative Poisson's ratio.

The general optimization problem for material design can be formulated as follows:

$$\min_{d} \quad f = g(L_{ij}^{\text{eff}}(U(d_k), d_k))$$

$$\text{with} \quad i = 1, 2, 3 \quad \& \quad j = 1, 2, 3$$

$$\text{s.t.} \quad K(d_k)U(d_k) = F$$

$$\frac{A(d_k)}{A_0} = A_f \tag{3.36}$$

$$g_l(U(d_k), d_k) \leq 0 \quad \text{where} \quad l = 1, 2, .., m$$

$$d_k^{lb} \leq d_k \leq d_k^{ub}$$

where $U(d_k)$ contains both displacements and edge nodal forces and is obtained as the solution of the analysis equations $K(d_k)U(d_k) = F$. Here $K(d_k)$ is the augmented matrix that contains coefficients of the constraint equations (Equation 3.23).

The steps involved in the non-conformal Petrov-Galerkin IIFEM (ncPG-IIFEM) with level-set based optimization for material microstructural design can be summarized as follows:

1. Define the boundary value problem.

2. Generate a Cartesian mesh.

3. Consider multiple initial designs. Initialize design variables $d_k = d_{k_0}$.

    (a) Use level-set based design parametrization.

4. Implement ncPG-IIFEM:

    (a) Generate the global augmented stiffness matrix and the global force vector.

    (b) Solve for nodal displacements and edge nodal forces.

5. Compute objective and constraint functions.

(a) Each component of the effective constitutive matrix is calculated as follows: $C^T U$, where C is an appropriate coefficient vector depending on the component required.

(b) The objective or the constraint functions can be a linear or a nonlinear function of the components of the effective constitutive matrix.

6. Compute the sensitivities of the objective and the constraint functions.

   (a) Use the adjoint method to compute gradients.

7. Use an appropriate gradient-based optimization algorithm.

8. Select a stopping criteria based on the optimization algorithm.

9. Obtain the desired unit cell corresponding to the optimized design variable values.

In the upcoming sections, several numerical examples corresponding to specific mechanical properties are provided to demonstrate the effectiveness of the proposed optimization formulation.

3.5.1 Maximising Bulk Modulus without Material Symmetry Constraints

In this section, micro-structured materials with maximum bulk modulus are obtained for various volume fractions. The objective function which is the bulk modulus is given as follows:

$$K = \frac{1}{4} \sum_{i,j=1}^{2} L_{ij}^{\text{eff}} \tag{3.37}$$

where L_{ij}^{eff} represents effective stiffness matrix in Voigt notation. Here, material symmetry constraints are not imposed. However, it is worth noting that many initial designs under

consideration exhibit 2D-square (cubic in 3D) symmetry, leading to optima with the same symmetry. Isotropic and square symmetric cases exhibit uncoupled volumetric and deviatoric responses. In the context of orthotropic or anisotropic material symmetries, it is important to recognize that the bulk modulus measure considered cannot be directly derived from the standard definition of the bulk modulus ($K = \frac{p}{\epsilon_{vol}}$) under general applied strains due to the coupled volumetric and deviatoric responses. Nevertheless, in such scenarios involving general material symmetries, if applied strains of $\epsilon_{11} = \epsilon_{22} = 0.5\epsilon_{vol}$ and $\gamma_{12} = 0$ are considered, where $p = 0.5(\sigma_{11} + \sigma_{22})$ denotes the pressure, the measure in Equation 3.37 can be recovered from the conventional definition of the bulk modulus.

The Young's modulus and Poisson's ratio of the solid material and the void considered for this case are the same as the compliance minimization problems. Thus, the bulk modulus (K_s) and the shear modulus (G_s) of the solid material are 0.7143 and 0.3846, respectively. The design domain which is comprised of a square unit cell is discretized with a 60×60 Cartesian mesh. Plane stress elements are considered. From now on, voids will be represented in black, while the solid material will be depicted in yellow.
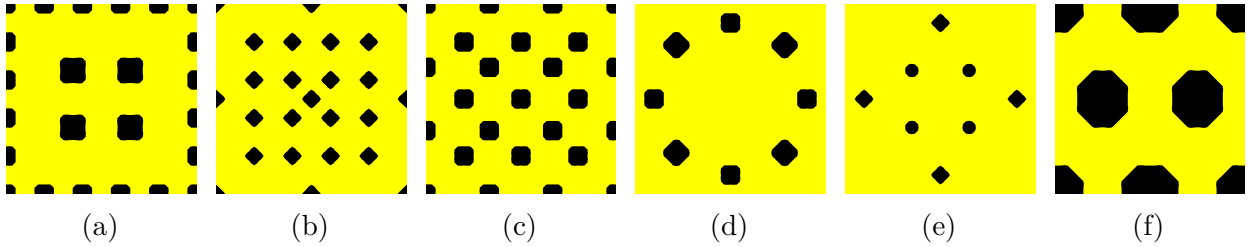
Figure 3.12: Initial designs for maximizing the bulk modulus: (a) case 1; (b) case 2; (c) case 3; (d) case 4; (e) case 5; (f) case 6.

It is well known that there are many local optimums for the problem of design of microstructured materials. Moreover, it is also known that many different topologies of unit cells can correspond to the same mechanical property. In order to study the influence of initial designs of the material cell on the optimized solution and to study the various local optimal

designs, several initial material layouts are considered. Various distributions of voids in the initial designs are tested. For conciseness, only a few initial layouts which result in distinct optimal designs are presented here. Three different solid material volume fractions, mainly 0.3, 0.4, and 0.55 are considered. The knots for the level-set parametrization coincide with a different 30×30 uniform mesh. Thus, the number of design variables is $31 \times 31 = 961$. The support radius is $\frac{7}{3}$ times the side length of an element of the mesh used to generate the knots. The stopping criteria used for SQP is: $\max(g) = 10^{-5}$, KTO $= 10^{-5}$, $\max(S) = 10^{-3}$.

| K=0.0934 | K=0.0933 | K=0.0936 | K=0.0931 | K=0.0933 | K=0.0934 |

| (a) | (b) | (c) | (d) | (e) | (f) |
| (g) | (h) | (i) | (j) | (k) | (l) |
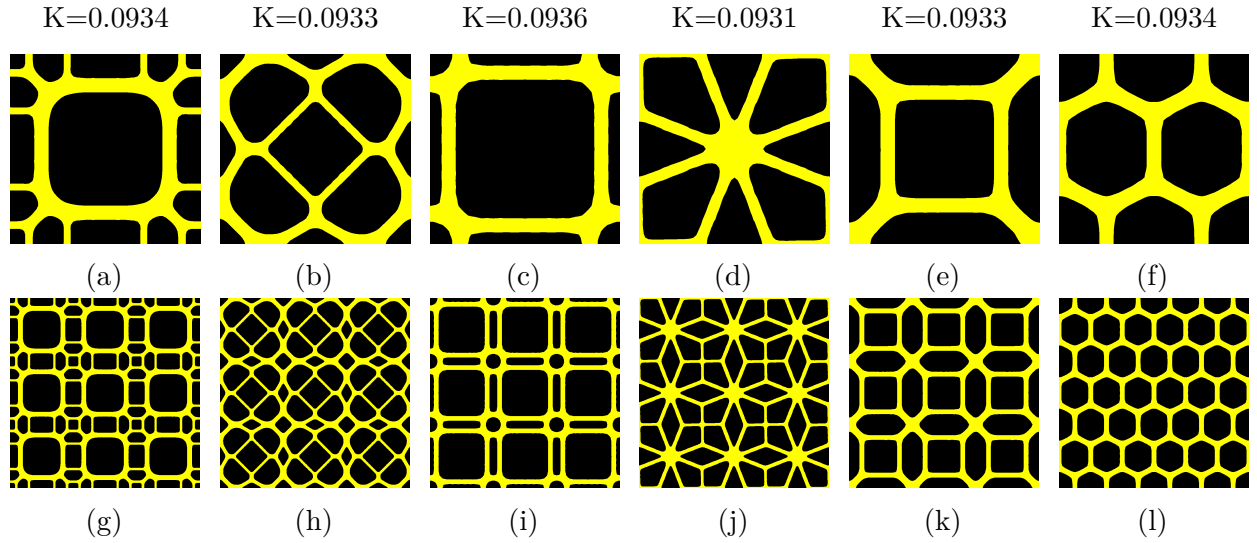
Figure 3.13: Maximal bulk modulus microstructures: (a)-(f) Final optimal material layout for the volume fraction of 0.3 with corresponding bulk modulus values; (g)-(l) 3×3 repetitive material cells corresponding to the optimal designs

The six initial designs considered are shown in Figure 3.12. The initial design in case 1 involves a uniform distribution of four voids within the domain and an additional six voids positioned along each of the outer edges, as illustrated in Figure 3.12(a). Case 4 features a circular distribution of voids. Various configurations in terms of void count, shape, and distribution are observable across the initial design cases 2, 3, 5, and 6. The optimal designs obtained for a volume fraction of 0.3 are given by Figures 3.13(a)-(f). These correspond to initial design cases 1-6 in figure 3.12, respectively. The initial designs are

guided towards neighboring topological configurations by the optimizer, especially if such optimal solutions exist within the proximity of the initial designs. Also, the final designs of material cells feature smooth structural boundaries and distinct material interfaces due to the use of the parametric level set method. A diverse array of member alignments is possible, encompassing not only vertical, horizontal, and diagonal orientations but also various other alignments. Additionally, the optimal designs feature the incorporation of circular members and honeycomb structures. This suggests that while the designs differ significantly in their topologies, they effectively achieve a similar maximal bulk modulus, showcasing the possible varieties in structural arrangements for achieving optimal material behavior. The choice among these multiple optima can be made based on additional manufacturing or stress constraints and restrictions on other moduli. The 3×3 repetitive unit cells for the optimal designs of volume fraction 0.3 are as shown in 3.13(g)-(l). There are other alternate unit cells that generate the same repetitive architecture and thus have the same corresponding bulk modulus. Those unit cells can be obtained by taking a different 1×1 grid snapshot from the 3×3 repetitive unit cells or from other initial designs.

The optimal unit cells for volume fractions 0.4 and 0.55 for the same initial material layouts are as shown in Figures 3.14(a)-(f) and Figures 3.15(a)-(f), respectively. The 3×3 repetitive unit cells for the optimal designs of volume fractions 0.4 and 0.55 are as shown in Figures 3.14(g)-(l) and Figures 3.15(g)-(l), respectively. In many cases, identical topologies are obtained for different volume fractions from the same initial layout. However, it is equally plausible to encounter diverse topologies for different volume fractions originating from the same initial design. At very low volume fractions, if a considerable discrepancy exists between the initial and desired volume fraction, the optimizer rapidly adjusts to meet the prescribed volume constraint. Once this discrepancy is minimized, the optimizer steadily improves the prescribed objective while maintaining the volume fraction nearly constant. This leads to the

K=0.136 K=0.1354 K=0.1357 K=0.1359 K=0.1348 K=0.1354

(a) (b) (c) (d) (e) (f)

(g) (h) (i) (j) (k) (l)
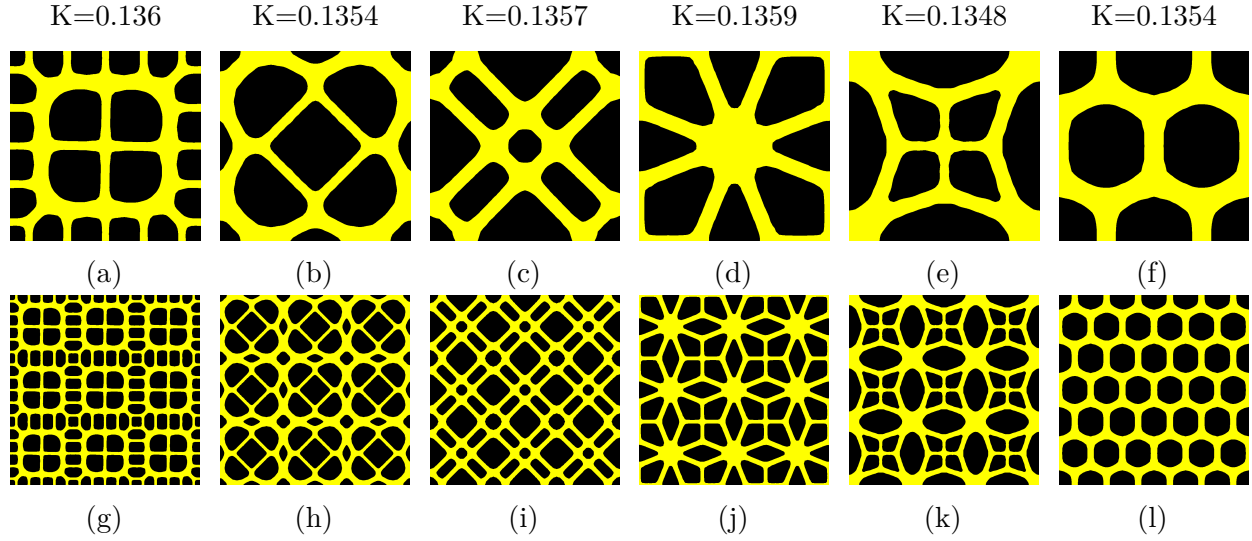
Figure 3.14: Optimal microstructures of cellular materials with extreme bulk modulus: (a)-(f) Optimal layouts with a volume fraction of 0.4 with the respective bulk modulus values for the corresponding six initial material layouts; (g)-(l) the 3×3 repetitive material cells corresponding to the optimal designs.

K=0.2160 K=0.2152 K=0.2146 K=0.2153 K=0.2152 K=0.2148

(a) (b) (c) (d) (e) (f)

(g) (h) (i) (j) (k) (l)
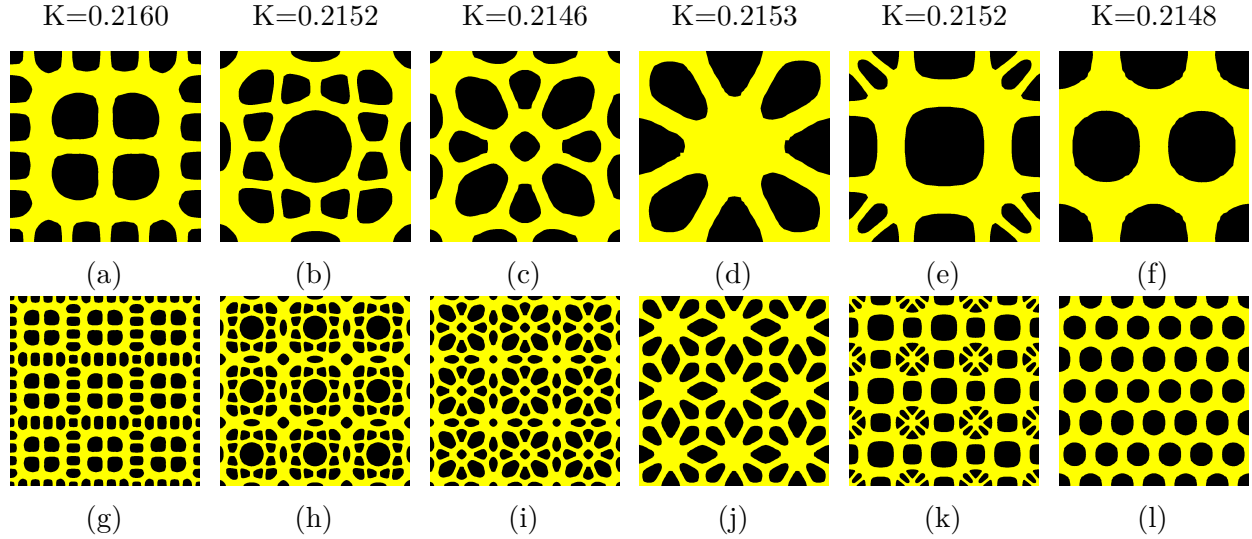
Figure 3.15: Optimal microstructures of cellular materials with extreme bulk modulus: (a)-(f) optimal layouts for a volume fraction of 0.55 with the respective bulk modulus values for the corresponding six initial material layouts; (g)-(l) the 3×3 repetitive material cells corresponding to the optimal designs.

emergence of different structural topologies for different volume fractions even under the same initial layouts. More importantly, as will be illustrated in the upcoming section, an optimal

(a)   (b)   (c)
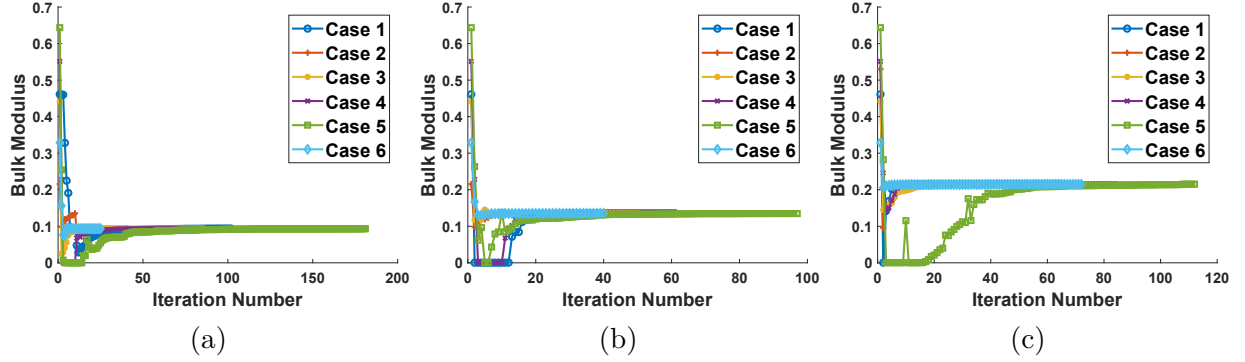
Figure 3.16: Iteration histories for the design of material microstructures with maximal bulk modulus for various volume fractions: (a) 0.3; (b) 0.4; (c) 0.55.

K=0.1356   K=0.1356   K=0.1354   K=0.1350   K=0.1351

(a)   (b)   (c)   (d)   (e)

(f)   (g)   (h)   (i)   (j)
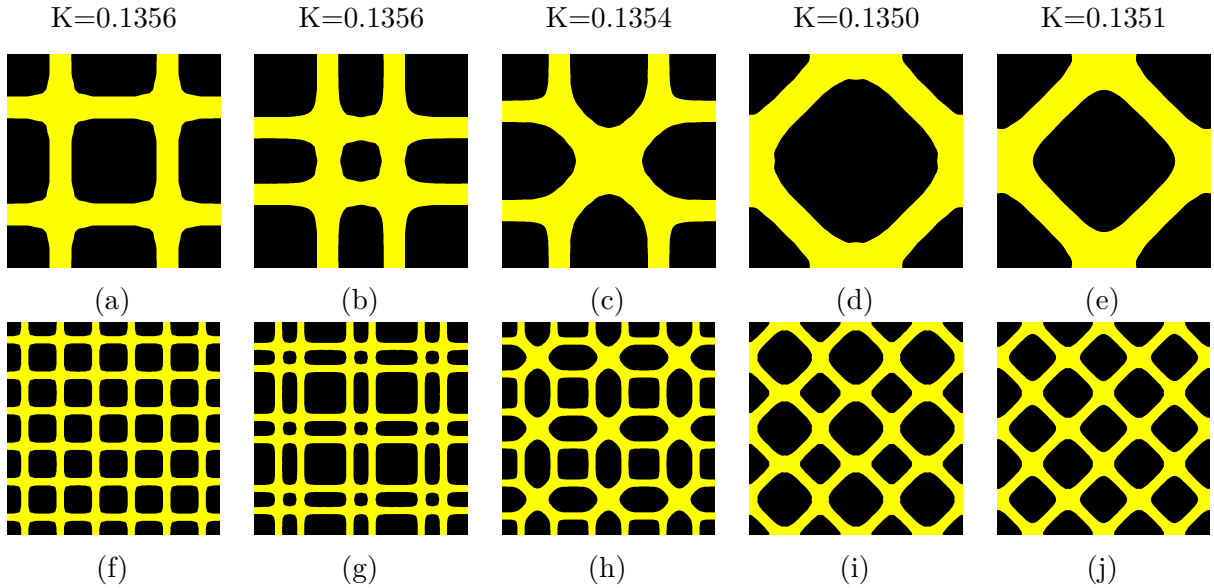
Figure 3.17: Commonly encountered optimal designs for a volume fraction of 0.4 and the corresponding 3×3 repetitive microstructures from various simple initial designs. These designs are frequently encountered in the literature.

structural arrangement may not retain its optimality across all volume fractions. This means that a design that is locally optimal for one volume fraction might be sub-optimal when compared to other locally optimal solutions for that specific volume fraction. This results in the optimizer exploring alternative paths in pursuit of better designs under certain conditions. In a few other cases, certain members within the high volume fraction optimal unit cell are extremely thin, thus achieving an identical topology for corresponding low-volume fractions

becomes unattainable. This discrepancy arises due to the inherent limitations imposed by extremely thin members, rendering the replication of the same topology unfeasible unlike what can occur for lower volume fraction constraints.

Figure 3.16(a)-(c) shows the iteration histories of the bulk modulus under various initial material layouts for 0.3, 0.4, and 0.55 volume fractions, respectively. These plots reveal a consistent pattern: an initial rapid adjustment in the modulus to reach the desired volume fraction, followed by gradual refinements. The majority of the final optimal designs are reached within 50 iterations. Convergence depends on the chosen stopping criteria, and proper scaling of design variables, objectives, and constraint functions. The best local optimal value of bulk modulus for volume fractions 0.3, 0.4, and 0.55 is $0.131K_s$, $0.1904K_s$, and $0.3024K_s$, respectively. As the volume fraction decreases, the decline in bulk modulus is more gradual within the lower volume fraction range. In contrast, in the high-volume fraction regime, this reduction is sharper with decreasing volume fractions.

Several other commonly obtained optimal unit cells for volume fraction 0.4 are displayed in Figures 3.17(a)-(e). These are simpler topologies compared to Figures 3.14(a)-(f). Many simple initial topologies lead to these optimal designs. The 3×3 repetitive unit cells corresponding to the final designs are as shown in Figures 3.17(f)-(j). These designs align with those frequently encountered as optimal solutions for achieving maximum bulk modulus in the existing literature. In general, the members are aligned in both x and y-directions to resist strains in both directions for maximum bulk modulus. However, among these optimal designs, variations are also noticeable. Some configurations exhibit diagonal member alignment, whereas a few have a diverse mix of orientations, featuring combinations of various orientations intermingled with horizontal and vertical members. It is obvious from the obtained optimal unit cells that there are multiple designs of 2D-square symmetry with similar maximal bulk modulus.

3.5.2 Maximising Shear Modulus without Material Symmetry Constraints

In this section, micro-structured materials with maximum shear modulus are obtained for various volume fractions. The shear modulus is given as follows:

$$G = L_{33}^{\text{eff}} \tag{3.38}$$

In the context of general anisotropic material symmetries, this shear modulus measure remains valid only under the application of γ_{12} strain, without the imposition of any other strains ($\epsilon_{11} = \epsilon_{22} = 0$). No such assumptions are required for the isotropic, square symmetric or orthotropic cases to derive the defined measure from the standard definition of shear modulus ($G = \frac{\sigma_{12}}{\gamma_{12}}$).

Multiple local optimal designs exist for the same maximal shear modulus. Thus, the influence of initial material layouts has to be studied. The domain, the material properties, and the mesh size are the same as in the previous example problem. For the level set parametrization, the knots are considered to coincide with a 30×30 mesh, and the support radius is again taken as $\frac{7}{3}$ times the side length of an element of the mesh used to generate the knots. The stopping criteria for the optimization algorithm are the same as the previous example problem.

Five of the initial designs considered are shown in Figure 3.18. The initial material layouts under consideration encompass varying numbers, distributions, and shapes of voids. Similar to the bulk modulus design problem, only a limited number of initial layouts are shown for illustrative purposes. The optimal designs obtained for a volume fraction of 0.3 are given by Figures 3.19(a)-(e). These correspond to initial material layouts in figure 3.18(a)-
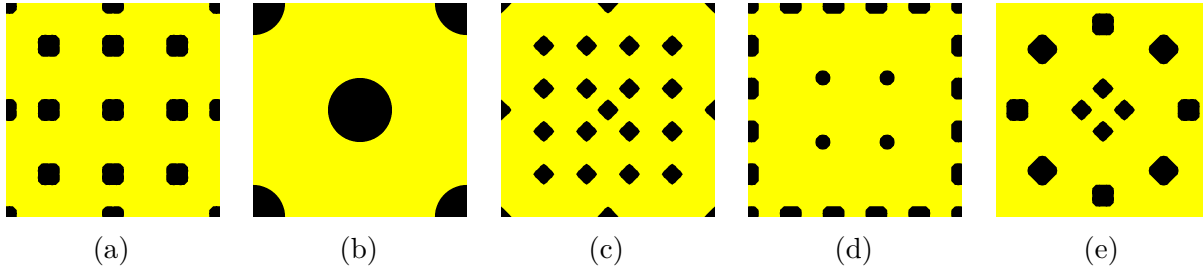
Figure 3.18: Initial designs used for maximizing the shear modulus: (a) case 1; (b) case 2; (c) case 3; (d) case 4; (e) case 5.

(e), respectively. When examining optimal layouts, it becomes apparent that the topological variability in configurations differs between cases involving shear modulus and those involving bulk modulus. In contrast to the considerable variability seen in the alignment and distribution of internal members within a unit cell in cases related to the bulk modulus, the scenario for the shear modulus exhibits lower variability. This distinction is clearly depicted in the 3×3 repetitive unit cells for the optimal designs as given by 3.19(f)-(j). The shear modulus cases demonstrate more uniformity in their configurations, showcasing a more consistent arrangement of structural elements within the unit cells.

The optimal unit cells for volume fractions 0.4 and 0.55 for the same initial material layouts (Figure 3.18) are as shown in Figures 3.20(a)-(e) and Figures 3.21(a)-(e), respectively. Identical topologies are obtained for different volume fractions from the same initial layout. As anticipated, the optimal unit cell showcases a diagonal arrangement of members. However, it is worth noting that how close the shear modulus for a particular locally optimal topology is to the globally optimal value for that volume fraction can change when different volume fractions are considered. This is evident when examining the material layouts corresponding to Figure 3.19(e), Figure 3.20(e), and Figure 3.21(e) against the other locally optimal designs for those volume fractions.

For instance, in the context of a volume fraction of 0.55, the shear modulus for the mentioned
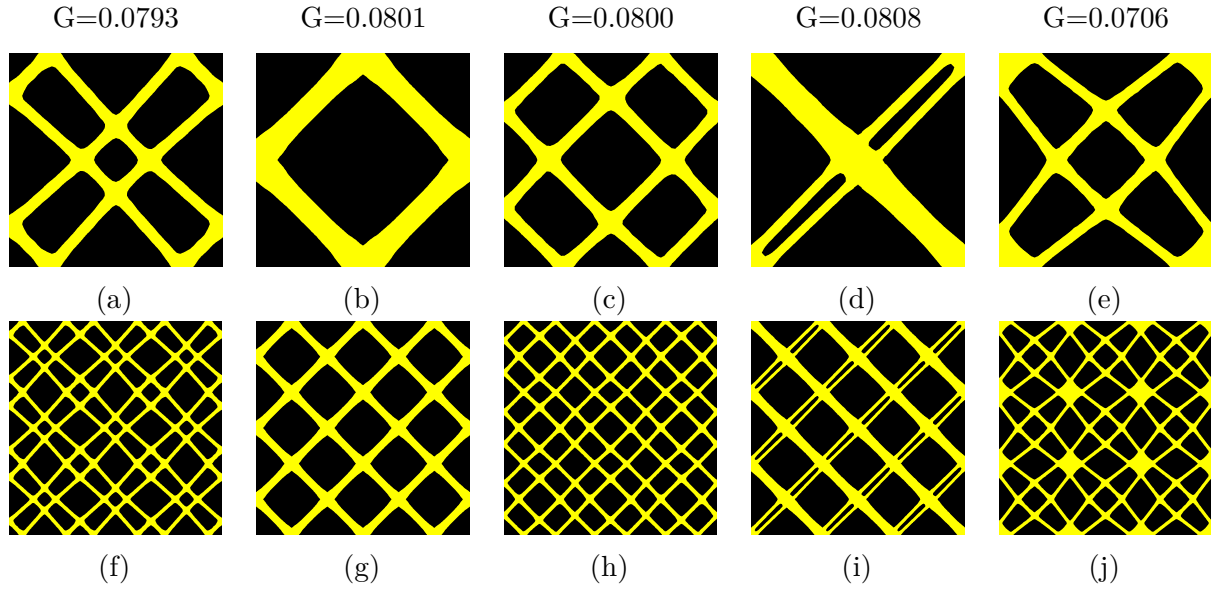
Figure 3.19: Optimal microstructures of cellular materials with extreme shear modulus: (a)-(e) final optimal material layout for the volume fraction of 0.3 with corresponding shear modulus values; (f)-(j) 3×3 repetitive material cells corresponding to the optimal designs.
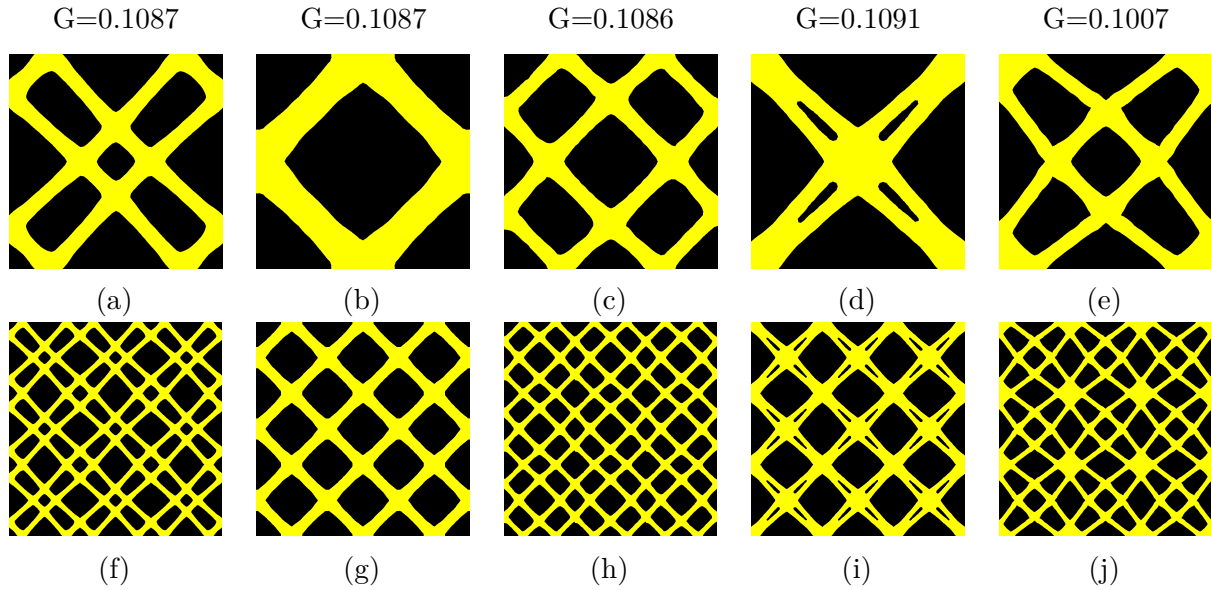
Figure 3.20: Optimal microstructures of cellular materials with extreme shear modulus: (a)-(e) final optimal material layout for the volume fraction of 0.4 with corresponding shear modulus values; (f)-(j) 3×3 repetitive material cells corresponding to the optimal designs.
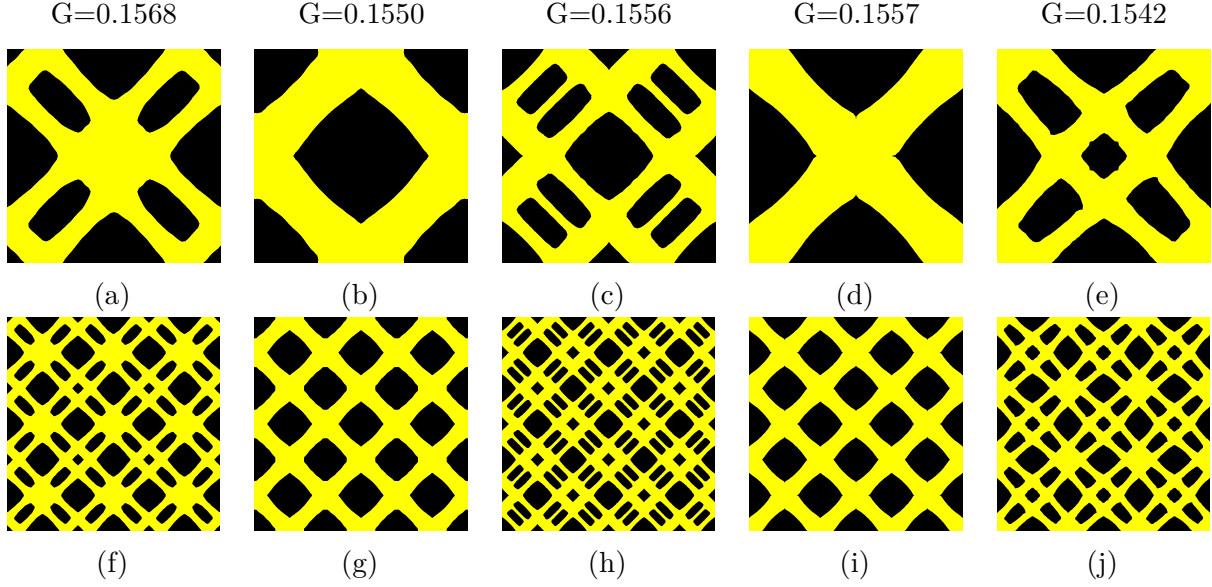
Figure 3.21: Optimal microstructures of cellular materials with extreme shear modulus: (a)-(e) final optimal material layout for a volume fraction of 0.55 with corresponding shear modulus values; (f)-(j) 3×3 repetitive material cells corresponding to the optimal designs.

layout closely aligns with other optimal values. However, as the volume fraction decreases, a noticeable discrepancy emerges between this specific layout and the rest of the optimal layouts. It becomes increasingly apparent that what is optimal for one volume fraction might not sustain its optimality across varying fractions. The lower volume fraction designs also can be attained by initializing with the final design obtained from higher volume fractions. Leveraging this strategy facilitates rapid convergence, streamlining the optimization process.

Figure 3.22(a)-(c) shows the iteration histories of the shear modulus under various initial material layouts for 0.3, 0.4, and 0.55 volume fractions, respectively. Similar to the bulk modulus design problem, an initial rapid adjustment in the modulus to reach the desired volume fraction can be observed, followed by a gradual fine-tuning. Many of the final optimal designs are reached within 100 iterations. There are a few initial material layouts for which the convergence is slower. The best local optimal values of shear modulus for volume fractions 0.3, 0.4, and 0.55 are $0.2101G_s$, $0.2837G_s$, and $0.4077G_s$, respectively. The

comparison depicted in the plots within Figure 3.23 indicates that, in each instance, the ratio between the optimal shear modulus and the solid material shear modulus surpasses the equivalent ratio observed in the bulk modulus optimal designs. In these plots, the scaled modulus is denoted as G/G_s for the shear case and K/K_s for the bulk case. This is contrasted against the scaled modulus values derived from the rule of mixtures, which is equal to A_f for both cases. In the lower volume fraction range, a more gradual decline in the shear modulus is observed, resembling the behavior seen in the bulk modulus design case.
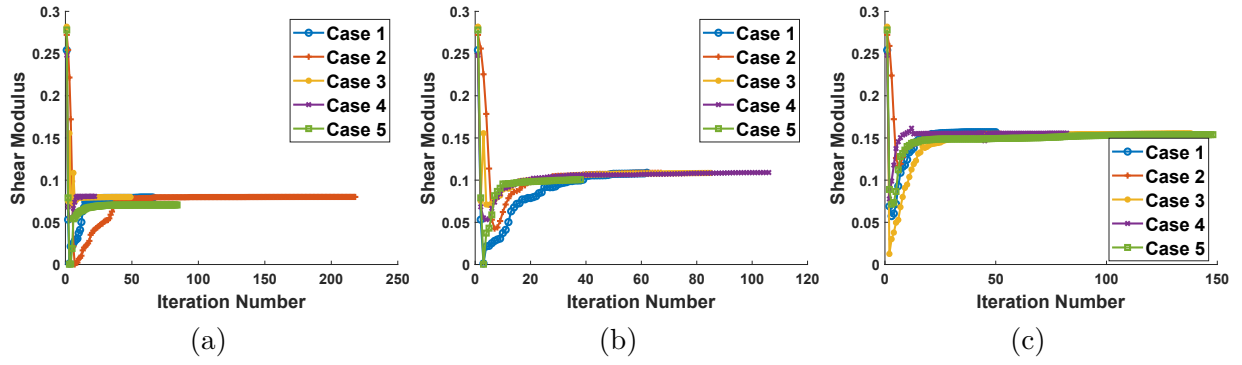
Figure 3.22: Iteration histories for the design of material microstructures with maximal shear modulus for various volume fractions: (a) 0.3; (b) 0.4; (c) 0.55.
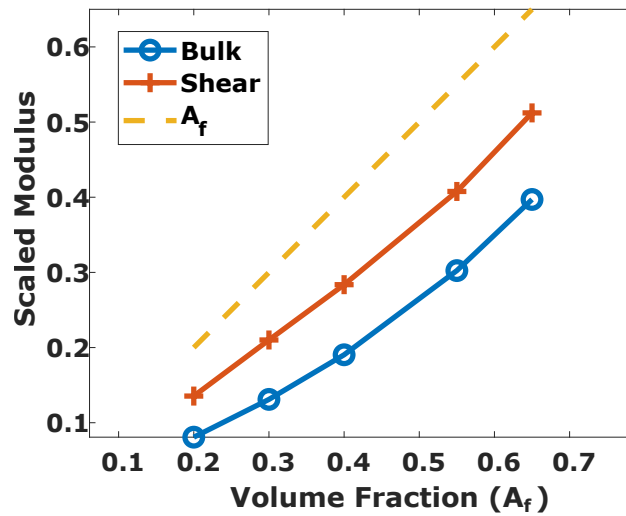
Figure 3.23: Relationship between scaled modulus and volume fraction of bulk and shear modulus optimal designs without material symmetry constraints. These optimal designs inherit the square symmetry of the initial layouts.

Shear strain, represented by the xy component of the strain tensor, for infinitesimal strains, can be visualized as a simultaneous extension at a 45-degree angle and compression at a negative 45-degree angle. For optimal resistance against such deformation, the structural components are ideally oriented along diagonal directions. This is what is observed in the optimal material layouts. However, this assertion might not hold when considering an alternate orientation. Because no restrictions are imposed on material symmetries or the elements of the constitutive matrix, the optimal alignment for resisting shear strains might differ, potentially requiring a different microstructure to achieve maximal resistance against deformation in that specific direction. The subsequent section outlines the conditions required for the shear modulus to exhibit orientation independence.

3.5.3   Conditions for Rotational Invariance

The square symmetric optimal microstructures obtained for the maximum shear modulus design cases have an orientation dependant shear modulus. A 45° rotation of the optimal microstructures can lead to a very different shear modulus. Table 3.1 provides the constitutive matrix of the optimal designs and the resulting constitutive matrix after a 45° rotation for the volume fraction of 0.4. It can be seen that the "optimal" microstructures have a very low shear stiffness (less than 10% of the optimal value) at 45° orientation. To comprehend the influence of microstructure rotation on the components of the constitutive matrix, we begin with a concise overview of the fundamental transformations of the constitutive matrix for no material symmetry. The elasticity matrix of a general anisotropic

material could be expressed as:

$$[L] = \begin{bmatrix} L_{11} & L_{12} & L_{13} \\ L_{21} & L_{22} & L_{23} \\ L_{31} & L_{32} & L_{33} \end{bmatrix} \tag{3.39}$$

To ensure complete generality in the forthcoming expressions, we do not assume the existence of a strain energy function from which the constitutive matrix is derivable, thus including the possibility of the stiffness matrix that is not symmetric (i.e., no major symmetry of the 4th-order tensor while the minor symmetry holds due to the symmetry of the stress and the strain tensor). The rotated constitutive matrix written in Voigt notation in terms of the reference constitutive matrix is as follows:

$$[L^*] = [A][L][R][A]^{-1}[R]^{-1} \tag{3.40}$$

where, $[L]$ denotes the constitutive matrix in the reference system and $[L^*]$ in the rotated system, $[A]$ is the tensor rotation transformation in Voigt notation, and $[R]$ is the tensor strain to engineering strain conversion tensor in Voigt notation.

It can be shown that the bulk modulus measure used is invariant under rotational transformations. Thus, we restrict our attention to shear modulus design cases. The shear modulus after a rotation angle of θ is given as follows:

$$\begin{aligned} L_{33}^* =& \frac{1}{8} \big(L_{11} - L_{12} - L_{21} + L_{22} + 4L_{33} - (L_{11} - L_{12} - L_{21} + L_{22} - 4L_{33}) \cos(4\theta) \\ &+ 2(L_{23} + L_{32} - L_{13} - L_{31}) \sin(4\theta) \big) \end{aligned} \tag{3.41}$$

It can be easily shown that the extremal shear modulus angles, if $L_{13} + L_{31} = L_{23} + L_{32}$, are

$\frac{\pi k}{2}$ and $\frac{1}{4}(\pi + 2\pi k)$, where k can be any integer. The conditions for shear modulus invariance i.e., $L_{33}^* = L_{33}$, is obtained from Equation 3.41 and are given by:

$$L_{13} + L_{31} = L_{23} + L_{32} \tag{3.42}$$

$$L_{33} = \frac{1}{4}(L_{11} - L_{12} - L_{21} + L_{22}) \tag{3.43}$$

The aforementioned conditions do not align with any specific standard material symmetry. Consequently, even an anisotropic material can exhibit shear modulus invariance under arbitrary rotations if it fulfills these criteria. Isotropic material symmetry, as a special case, adheres to these constraints. The necessary and sufficient conditions for a few typical material symmetries can be summarized as follows:

- Orthotropy: Orthotropic materials exhibit distinct elastic properties along two mutually orthogonal axes. The symmetry transformation group includes reflection about the two mutually orthogonal axes. For orthotropic material symmetry to hold, the following equations must be satisfied: $L_{13} = L_{31} = L_{23} = L_{32} = 0$.

- Square symmetry: Square symmetric materials, a subset of orthotropic materials, exhibit identical elastic properties along the orthogonal axes. The symmetry transformation group includes rotations and reflections that map a square back to itself. An orthotropic material exhibits square symmetry if it complies with the following conditions: $L_{11} = L_{22}$ and $L_{21} = L_{12}$.

- Isotropy: Isotropic materials exhibit the same elastic properties in all directions. Symmetry transformations include all orthogonal transformations. A square symmetric material is considered isotropic if it fulfills the following criterion: $L_{33} = \frac{1}{4}(L_{11} - L_{12} - L_{21} + L_{22})$.

Table 3.1: The constitutive matrix of the optimal designs for the shear modulus, along with the matrices of designs subjected to a subsequent 45° rotation, for a volume fraction of 0.4.

Shear Design	Case 1	Case 2	Case 3
Optimal	$\begin{bmatrix} 0.1401 & 0.1248 & 0 \\ 0.1248 & 0.1401 & 0 \\ 0 & 0 & 0.1087 \end{bmatrix}$	$\begin{bmatrix} 0.1441 & 0.1229 & 0 \\ 0.1229 & 0.1441 & 0 \\ 0 & 0 & 0.1087 \end{bmatrix}$	$\begin{bmatrix} 0.1424 & 0.1221 & 0 \\ 0.1221 & 0.1424 & 0 \\ 0 & 0 & 0.1086 \end{bmatrix}$
45° Rotation	$\begin{bmatrix} 0.2412 & 0.0238 & 0 \\ 0.0238 & 0.2412 & 0 \\ 0 & 0 & 0.0077 \end{bmatrix}$	$\begin{bmatrix} 0.2422 & 0.0248 & 0 \\ 0.0248 & 0.2422 & 0 \\ 0 & 0 & 0.0106 \end{bmatrix}$	$\begin{bmatrix} 0.2409 & 0.0237 & 0 \\ 0.0237 & 0.2409 & 0 \\ 0 & 0 & 0.0101 \end{bmatrix}$

	Case 4	Case 5
	$\begin{bmatrix} 0.1404 & 0.1223 & 0 \\ 0.1223 & 0.1404 & 0 \\ 0 & 0 & 0.1091 \end{bmatrix}$	$\begin{bmatrix} 0.1375 & 0.1201 & 0 \\ 0.1201 & 0.1375 & 0 \\ 0 & 0 & 0.1007 \end{bmatrix}$
	$\begin{bmatrix} 0.2404 & 0.0222 & 0 \\ 0.0222 & 0.2404 & 0 \\ 0 & 0 & 0.0090 \end{bmatrix}$	$\begin{bmatrix} 0.2295 & 0.0281 & 0 \\ 0.0281 & 0.2295 & 0 \\ 0 & 0 & 0.0087 \end{bmatrix}$

3.5.4 Degree of Anisotropy

Most of the optimal designs obtained so far showcase a 2D square symmetry because the initial layouts share the same symmetry. Zener [207] introduced an index to quantify the anisotropy of cubic symmetric materials, which is also applicable to 2D square symmetric materials. This widely used index is known as the Zener anisotropy ratio and is frequently employed in the literature [208]. Expressed in terms of the three coefficients of the cubic symmetric material's constitutive matrix, the Zener anisotropy ratio is defined as:

$$Z = \frac{2L_{33}}{L_{11} - L_{12}} \tag{3.44}$$

where, L_{11}, L_{12}, and L_{33} represent the relevant stiffness coefficients of the 2D square symmetric material. Here, L_{33} denotes the material's resistance to shear deformation in the $x - y$ direction and $(L_{11} - L_{12})/2$ denotes the material's resistance to shear deformation along the $x' - y'$ direction which is rotated by 45°. The Zener anisotropy ratio has a value of 1 for isotropic material. A very high or low value compared to 1 indicates higher anisotropy. This ratio provides a simple and effective measure of the degree of anisotropy in square symmetric materials.

Table 3.2: The Zener ratios corresponding to the optimal designs of the shear modulus outlined in Section 3.5.2 for all the volume fractions considered.

	Zener Ratio		
Shear Modulus	$A_f = 0.3$	$A_f = 0.4$	$A_f = 0.55$
Case 1	28.5303	14.2673	6.8633
Case 2	20.7019	10.2257	4.3809
Case 3	22.0343	10.7056	8.9152
Case 4	66.8418	12.0195	4.475
Case 5	21.9317	11.5754	6.204

Table 3.3: The Zener ratios corresponding to the optimal designs of the bulk modulus outlined in Section 3.5.1 for three different volume fractions.

	Zener Ratio		
Bulk Modulus	$A_f = 0.3$	$A_f = 0.4$	$A_f = 0.55$
Case 1	0.1319	0.1685	0.3269
Case 2	2.0641	1.5074	0.5496
Case 3	0.0432	9.4604	0.8891
Case 4	0.2164	0.3623	1.3984
Case 5	0.2025	0.4587	0.4953
Case 6	0.5297	0.4976	0.6765

Tables 3.2 and 3.3 provide Zener ratios for shear modulus and bulk modulus designs obtained in the previous sections for all the volume fractions considered, respectively. It can be

noted that all the shear modulus cases have a higher degree of anisotropy. As evident from the values presented in Table 3.2, in the scenario of the shear modulus at a volume fraction of 0.3, case 4 exhibits a notably higher degree of anisotropy when compared with the remaining designs. Similar comparative analyses can be extended to evaluate distinctions among designs at different volume fractions. Regarding bulk modulus designs, the majority of designs have a Zener ratio close to 1, with only a few exceptions. Through just void shape refinements, there exists the potential to maintain the topology while effectively transitioning many of these bulk modulus designs, especially those with Zener ratios very close to 1, towards exact isotropic behavior. Moreover, as indicated previously, the bulk modulus measure considered is invariant under all rotations for any material symmetry. Given the higher Zener ratio observed in shear modulus cases and for the sake of brevity, our focus will be directed toward maximizing the shear modulus while imposing isotropy constraints.

3.5.5   Optimization with Isotropy Constraints

In the design of materials for specific elastic properties with prescribed material symmetry, such as orthotropy, square symmetry, or isotropy, it is crucial to implement the corresponding symmetry constraints within the optimization problem [209]. This holds particularly true for isotropic symmetry since initialising with an isotropic design poses a considerable challenge. Additionally, designs characterized by other symmetries tend to, more often than not, exhibit higher modulus values. This is due to fewer restrictions imposed on such symmetries. Hence, the incorporation of additional constraints guarantees that the final design not only meets the desired elastic behavior but also the specified material symmetry.

Isotropy, a highly restrictive symmetry, implies that the material's elastic properties are

identical in all directions. Under 2D assumptions, the conditions for isotropy can be expressed as follows:

$$L_{13} = L_{31} = L_{23} = L_{32} = 0 \tag{3.45}$$

$$L_{11} = L_{22}, \quad L_{21} = L_{12} \tag{3.46}$$

$$L_{33} = \frac{1}{4}(L_{11} - L_{12} - L_{21} + L_{22}) \tag{3.47}$$

These conditions ensure that the material exhibits the same stiffness and Poisson's ratio in all directions. Mathematical programming techniques facilitate implementing these symmetry constraints as equality constraints in an optimization problem. Since the shear modulus is sensitive to rotations even for square symmetric designs, only the shear modulus design problem with isotropy will be explicitly illustrated.

The objective and constraint functions for shear modulus maximization with isotropy constraints are as follows:

$$
\begin{aligned}
\min \quad & f = -L_{33}^{\text{eff}} \\
\text{s.t.} \quad & \frac{A(d_k)}{A_0} = A_f \\
& L_{13}^{\text{eff}} = L_{31}^{\text{eff}} = L_{23}^{\text{eff}} = L_{32}^{\text{eff}} = 0 \\
& L_{11}^{\text{eff}} - L_{22}^{\text{eff}} = 0 \quad \text{and} \quad L_{21}^{\text{eff}} - L_{12}^{\text{eff}} = 0 \\
& L_{11}^{\text{eff}} - L_{12}^{\text{eff}} - L_{21}^{\text{eff}} + L_{22}^{\text{eff}} - 4L_{33}^{\text{eff}} = 0
\end{aligned}
\tag{3.48}
$$

The design domain is again comprised of a square unit cell discretized with a 60×60 Cartesian mesh. The knots for the level-set parametrization coincide with a different 45×45 uniform mesh. Thus, the number of design variables is $46 \times 46 = 2116$. A more refined grid for parametrization compared to the previous example problems is considered to account for

| (a) | (b) | (c) | (d) | (e) |
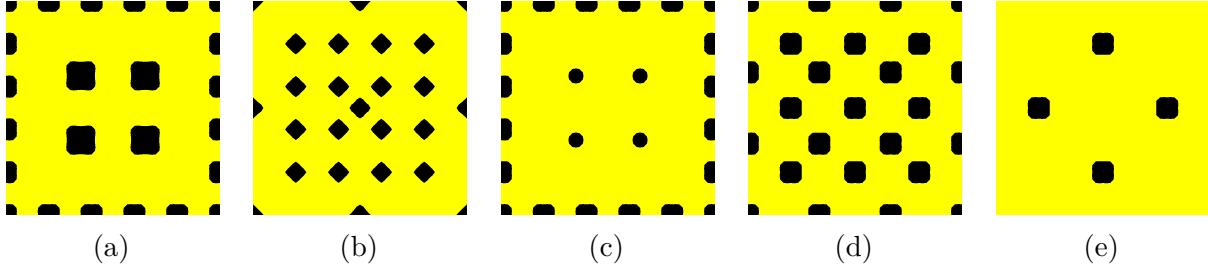
Figure 3.24: Initial designs used for maximizing the shear modulus with isotropy constraint: (a) case 1; (b) case 2; (c) case 3; (d) case 4; (e) case 5.

Table 3.4: Comparison of the scaled shear modulus obtained from IIFE-based material design to that of the HS theoretical upper bound for various volume fractions.

	Scaled Shear Modulus (G/G_s)	
Volume Fraction	Material Design	HS Upper Bound
0.25	0.095	0.0977
0.3	0.1193	0.1223
0.4	0.1732	0.1781
0.55	0.28	0.2843
0.65	0.3739	0.3764

additional topological intricacies resulting from added constraints related to isotropy. The support radius is 3.5 times the side length of an element of the mesh used to generate the knots. The stopping criteria used for SQP is the same as the previous example problems. Five of the initial designs considered are shown in Figure 3.24. The optimal designs obtained for a volume fraction of 0.4 are given by Figures 3.25(a)-(e). The 3×3 repetitive unit cells for the optimal designs as given by 3.25(f)-(j). The arrangement of members along both the coordinate axes and diagonals in the final designs, when compared to designs acquired without material symmetry constraints, results in the cellular materials ability to uniformly withstand shear deformation in all directions.

The obtained results can be compared to established analytical bounds for shear moduli. For well-ordered, quasi-homogeneous, and quasi-isotropic composites, Hashin and Shtrikman

G=0.0666   G=0.0662   G=0.0622   G=0.0664   G=0.0636

(a)   (b)   (c)   (d)   (e)

(f)   (g)   (h)   (i)   (j)
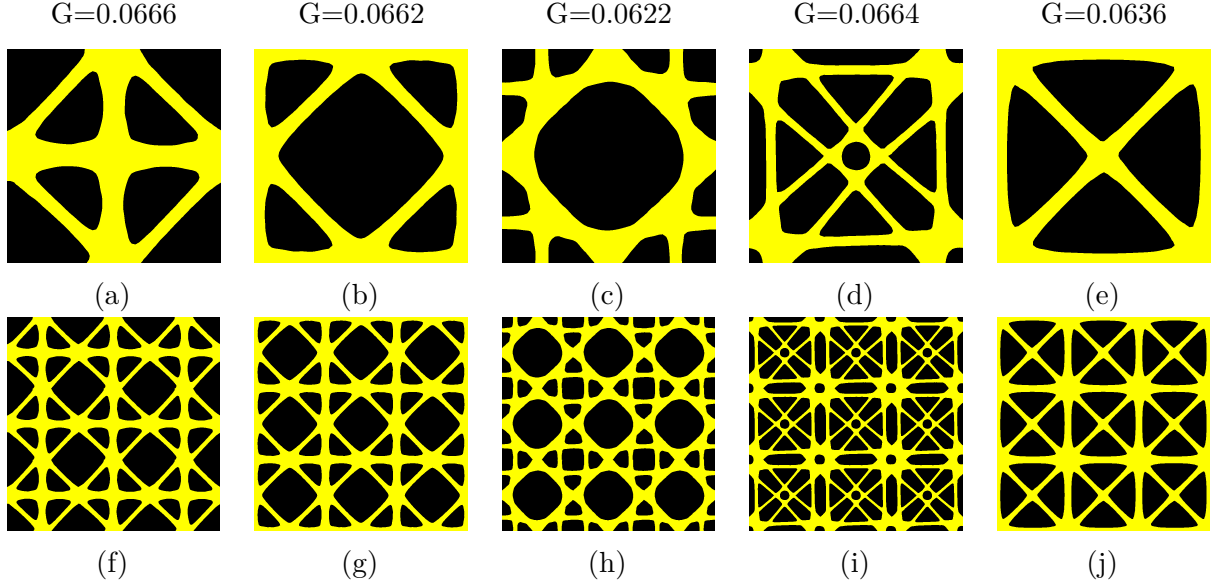
Figure 3.25: Optimal microstructures of cellular materials for extreme shear modulus with isotropy constraints: (a)-(e) final optimal material layout for a volume fraction of 0.4 with corresponding shear modulus values; (f)-(j) 3×3 repetitive material cells corresponding to the optimal designs.

[210] derived the upper and lower bounds for bulk and shear moduli. In the context of metamaterials composed of a void phase and a solid phase with volume fraction A_f, the Hashin-Shtrikman (HS) upper bound for shear modulus in 2D cases are expressed as:

$$G_{\text{HS}}^{\text{up}} = \frac{G_s K_s A_f}{2(G_s + K_s) - A_f(2G_s + K_s)} \tag{3.49}$$

Table 3.4 provides the comparison of scaled shear modulus (G/G_s) obtained from the IIFEM-based material design with that of the HS theoretical upper bounds for volume fractions 0.25, 0.3, 0.4, 0.55, and 0.65. The obtained optima are very close to the theoretical upper bound. Figure 3.26 provides a comparison plot of HS theoretical upper bounds with that of the IIFEM-based computational approach for various volume fractions. Corresponding microstructure layouts obtained for the presented values are also illustrated in the plot.
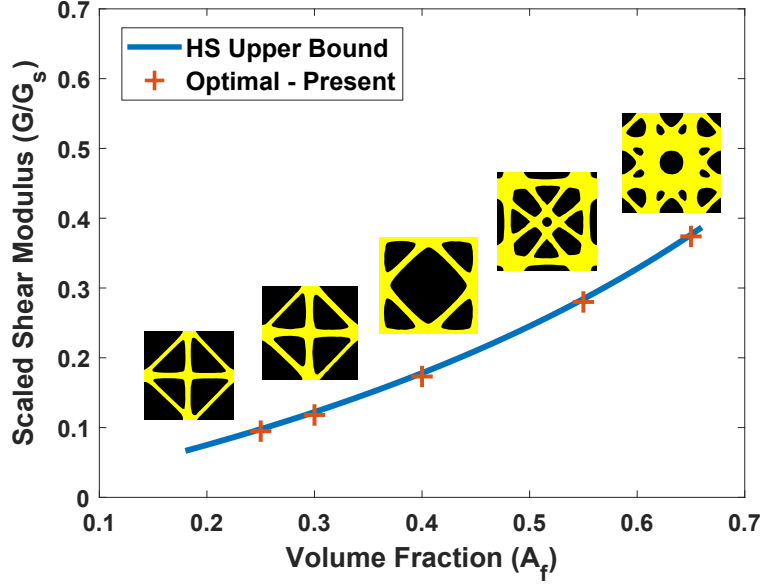
Figure 3.26: Comparison of the HS upper bound with that of the designs obtained from the present approach for the shear modulus case with isotropy constraint for various volume fractions. Corresponding microstructure layouts are also presented.

3.5.6 Programmable Poisson's Ratio

Finally, cases of prescribed Poisson's ratio materials are considered. For a general 2D microstructured materials, the two Poisson's ratios are as follows:

$$\nu_{12} = L_{21}^{\text{eff}}/L_{11}^{\text{eff}}$$
$$\nu_{21} = L_{12}^{\text{eff}}/L_{22}^{\text{eff}}$$

(3.50)

For isotropic materials ν_{12} and ν_{21} are identical. Multiple approaches are available to obtain a design with a specific Poisson's ratio. An elasticity matrix can be prescribed and the least square error of the current value with respect to the prescribed value can be minimized. The objective function is given as follows: $f = \sum_{i,j=1}^{2} c_{ij}(L_{ij}^{\text{eff}} - L_{ij}^{\text{given}})^2$, where c_{ij} are arbitrary weights and L_{ij}^{given} is the prescribed elasticity tensor. In these cases, Poisson's ratio is predetermined from the prescribed elasticity tensor. The disadvantage of this approach is

that an appropriate elasticity tensor has to be prescribed and not all initial conditions can approach the prescribed constitutive tensor effectively.

The other approach frequently encountered to obtain negative Poisson's ratio microstructure is to consider minimization of the following objective function: $f = L_{12}^{\text{eff}} - c(L_{11}^{\text{eff}} + L_{22}^{\text{eff}})$, where c is a prescribed constant. It is obvious that the defined objective function tends to maximize the horizontal and vertical stiffness moduli and minimize L_{12}^{eff} so that the objective is minimized and a negative Poisson's ratio microstructure is obtained. The weight is controlled by the constant c. This constant can be considered to be a function of iteration number. In this approach, there is no control over the exact value of Poisson's ratio obtained. We consider a different approach which includes inequality constraints thus utilizing the potential of mathematical programming methods. The objective and constraint functions are as follows:

$$
\begin{aligned}
\min \quad & f = (L_{21}^{\text{eff}} - \nu_{12}^g L_{11}^{\text{eff}})^2 + (L_{12}^{\text{eff}} - \nu_{21}^g L_{22}^{\text{eff}})^2 \\
\text{s.t.} \quad & \frac{A(d_k)}{A_0} = A_f \\
& L_{11}^{\text{eff}} \geq L_{11}^{\text{given}} \quad \text{and} \quad L_{22}^{\text{eff}} \geq L_{22}^{\text{given}}
\end{aligned}
\tag{3.51}
$$

where ν_{12}^g and ν_{21}^g are the prescribed values of Poisson's ratio. L_{11}^{given} and L_{22}^{given} are prescribed minimum values of the horizontal and vertical stiffness moduli. These values will be chosen based on the initial material layout.

The domain, material properties, mesh size, knot location for the level set parametrization, the support radius, and the stopping criteria for the optimization algorithm are the same as the previous example problems without material symmetry constraints. In order to illustrate the effectiveness of the proposed formulation, consider the designs given by Figures 3.17(a) and 3.17(b) as the initial material layout. For brevity, only two initial design cases are

$\nu = 0$ $\nu = -0.2$ $\nu = -0.4$ $\nu = -0.6$ $\nu = -0.8$

(a)   (b)   (c)   (d)   (e)

(f)   (g)   (h)   (i)   (j)
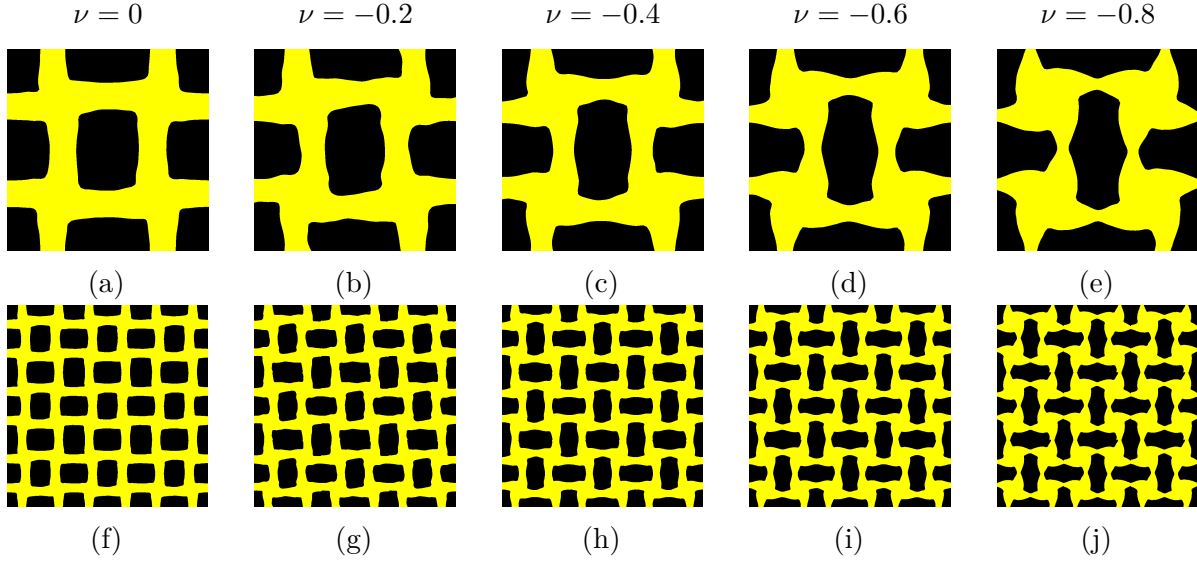
Figure 3.27: Zero and negative Poisson's ratio microstructures related to the initial topology in Figure 3.17a: (a)-(e) material layout obtained for a volume fraction of 0.5 with corresponding Poisson's ratio values; (f)-(j) 3 × 3 repetitive material cells corresponding to the optimal designs.

$\nu = 0$ $\nu = -0.2$ $\nu = -0.4$ $\nu = -0.6$ $\nu = -0.8$

(a)   (b)   (c)   (d)   (e)

(f)   (g)   (h)   (i)   (j)
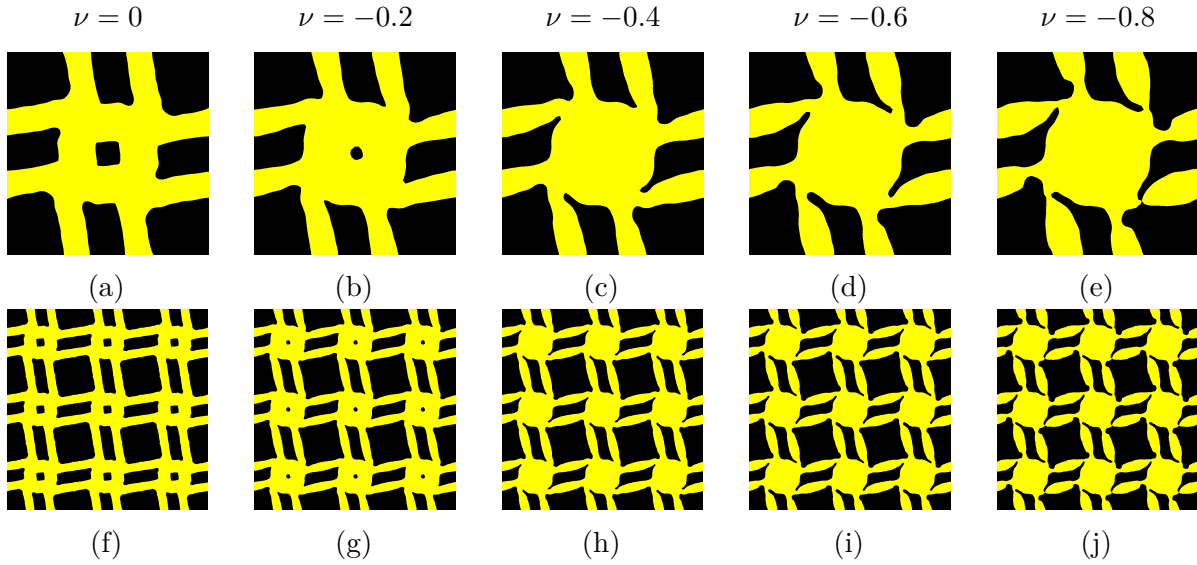
Figure 3.28: Zero and negative Poisson's ratio microstructures related to the initial topology in Figure 3.17b: (a)-(e) material layout obtained for a volume fraction of 0.5 with corresponding Poisson's ratio values; (f)-(j) 3 × 3 repetitive material cells corresponding to the final designs.

presented. The goal is to obtain material layouts that are related to the initial layout but with prescribed Poisson's ratio. The initial designs considered have a positive Poisson ratio. Based on the horizontal and vertical stiffness moduli of the initial layouts, an appropriate minimum value for the moduli values is set. The prescribed Poisson ratio is set to zero. The volume fraction considered for all the cases is 0.5. The final design obtained for the initial material layout in Figure 3.17(a) is as shown in Figure 3.27(a). To accelerate the convergence for the subsequent designs, the zero Poisson's ratio design is considered as the initial design for the -0.2 Poisson's ratio design. Similarly, for the -0.4 design, the layout obtained for Poisson's ratio -0.2 is considered as the initial condition and this pattern is repeated for the subsequent cases. The final designs for the negative Poisson's ratio -0.2, -0.4, -0.6, and -0.8 are as shown in 3.27(b)-(e). The 3×3 repetitive unit cells for the final designs are as shown in 3.27(f)-(j). The same process can also be carried out for cases with positive prescribed Poisson's ratios. For the initial design in Figure 3.17(b), the final material microstructure obtained for the Poisson's ratios 0, -0.2, -0.4, -0.6 and -0.8 are as shown in Figures 3.28(a)-(e). The 3×3 repetitive unit cells for the final designs are as shown in Figures 3.28(f)-(j). For illustration purposes, a few more designs for a specific Poisson's ratio of -0.4 using the same procedure are shown in Figures 3.29(a)-(e). The corresponding 3×3 repetitive unit cells for the final designs are as shown in Figures 3.29(f)-(j). Rotating compliant mechanisms and/or reentrant corners can be observed in these microstructures. Rotating compliant mechanisms which allows for controlled rotations, and reentrant corners, with their inward-pointing angles, contribute to the negative Poisson's ratio of these metamaterials.

The design problems considered thus far show the effectiveness of the proposed approach. Smooth boundaries and material interfaces, accurate finite element analysis, the ease and computational efficiency of sensitivity analysis due to IIFEM, the direct solution-based objective function, and flexibility in handling complex topological changes are important

(a)	(b)	(c)	(d)	(e)

(f)	(g)	(h)	(i)	(j)
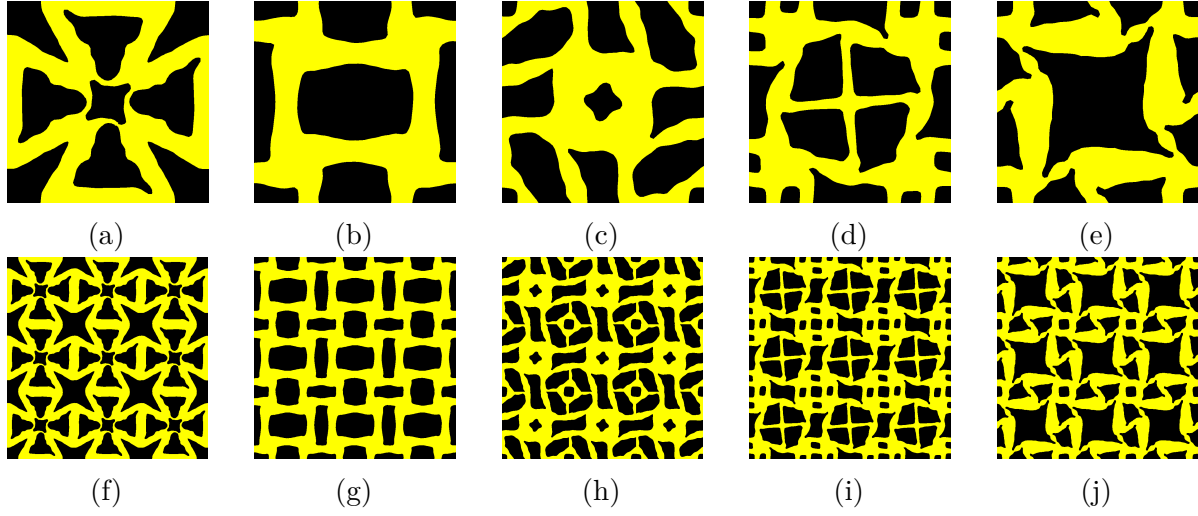
Figure 3.29: Optimal material layouts: (a)-(e) Example material unit cells corresponding to a Poisson's ratio of -0.4; (f)-(j) 3×3 repetitive material layout corresponding to the final designs.

features of this approach. Material islands or other numerical artifacts are also avoided by choosing appropriate parameters for the level set representation. If needed, a regularization scheme for such issues can be incorporated within this framework.

Chapter 4

Material Modeling with Damage for Diver UNDEX Simulations

This chapter focuses on the formulation and implementation of material models for simulating the response of biological tissues to underwater blast events. Hyperelastic and hyperviscoelastic models are explored to capture nonlinear and viscoelastic behavior. The primary challenges in developing these material models revolve around their predictive accuracy and the requisite number of parameters. Some models exhibit accurate predictions in one loading mode, such as uniaxial extension, while performing poorly in other modes. Alternatively, certain models necessitate a large number of parameters, posing difficulties in experimental measurement. The objective is to select a model that, for a given case, accurately reproduces experimental data across various modes like uniaxial tension/compression, biaxial tension/compression, pure shear, and volumetric tension/compression, while also being flexible enough to encompass a subset of other simpler models within them. The chosen model should have a minimal number of parameters, making them easily obtainable through fitting to experimental data. This chapter provides a concise overview of the models designated for UNDEX simulations and outlines their implementation details.

4.1   Hyperelasticty

4.1.1   Overview

Hyperelastic material models, extensively utilized to describe the behavior of elastomers, are total strain models characterized by strain energy potentials. The hyperelastic strain energy density function is a scalar function of the strain tensor that represents the energy stored in the material due to deformation. They are a class of constitutive models that describe the mechanical behavior of materials that exhibit large elastic strains. These models are primarily applied to elastomers, biological tissues, and foam materials. Provisions for introducing damage enable the simulation of partial or complete material failure. Pivotal contributions to the development of hyperelastic models include seminal works by Mooney [211], Rivlin [212], Ogden [213], Treloar [214], and Yeoh [215]. The choice of the hyperelastic model depends on a number of factors, including the type of material being modeled, the loading conditions including modes and expected deformation ranges, as well as desired accuracy and efficiency. For example, the Mooney-Rivlin model is often used for modeling the behavior of elastomers under small and moderate strains. In contrast, the Ogden and Arruda-Boyce models are used for modeling the behavior of elastomers under a wider range of strains. The neo-Hookean model is often used as a starting point for more complex models. The Yeoh and Polynomial models are general-purpose hyperelastic models that can be used for modeling a wide range of materials and loading conditions. The polynomial form can be reduced into a few other cases namely the reduced polynomial form, the neo-Hookean form, the Mooney-Rivlin form, and the Yeoh form [216].

Hyperelastic models can be classified into two broad classes: phenomenological models and mechanistic or micromechanical models. The phenomenological models, as implied by their name, are derived from the observation of rubber-like materials subjected to various

conditions of homogeneous deformation. These models treat the material as a continuum and consider its macroscopic behavior. Subsequently, mathematical equations are fitted to experimental data, leading to polynomial and other formulations. These models can be further subdivided into categories based on the utilization of invariants of the Cauchy-Green deformation tensors, principal stretches, or a combination of both. The choice of the model depends on the material and loading conditions.

In contrast, the micromechanical models employ the tools of statistical mechanics to elucidate the behavior of hyperelastic materials at both the microscopic and macroscopic scales. While phenomenological models constitute a significant portion of hyperelastic models found in the literature, micromechanical-based models are also used extensively due to their capacity to establish connections between material behavior and its underlying physical or chemical structure. In the case of rubber-like materials, their microstructure is characterized by the presence of randomly oriented, elongated polymeric chains interconnected into a complex network structure. Thus, to formulate a micromechanical-based constitutive model, a representative network structure is needed to relate the chain stretch of the individual polymeric chains to the applied deformation. Various micromechanical-inspired hyperelastic models have been developed, each with a corresponding network structure namely the three chain model, the eight chain model (Arruda-Boyce), the tube model, the extended tube model, and the neo-Hookean model. The Gent and van der Waals models are hybrids of phenomenological and mechanistic models.

Within the scope of this study, the third-order polynomial form is employed as the hyperelastic material model of choice. The reason behind this choice lies in the model's inherent generality, as it serves as an umbrella under which various specific models can be accommodated as special cases.

4.1.2   Hyperelasticity Formulation

The constitutive behavior of a hyperelastic material is defined by a relationship between the total stress and the total strain in the material. It is not a rate formulation. Before presenting the specific form of the strain energy density function being used, we will provide some basic definitions and kinematic results [216]. Let the current position of a material point be $\mathbf{x}$ and the reference position or position in the undeformed state of the same point $\mathbf{X}$, then the deformation gradient is

$$\mathbf{F} = \frac{\partial \mathbf{x}}{\partial \mathbf{X}} \tag{4.1}$$

It can be shown that the differential volume element in the deformed configuration (dV) can be related to the differential volume element in the undeformed/reference configuration (dV_0) as follows:

$$dV = J dV_0 \tag{4.2}$$

where $J = \det(\mathbf{F})$ is the determinant of the deformation gradient tensor. For simplicity in the expressions, the deformation is separated into its deviatoric and volumetric components, with the corresponding stress response for isotropic materials depending solely on their respective counterparts. The deformation gradient tensor with the volume change eliminated is given as follows:

$$\bar{\mathbf{F}} = J^{-\frac{1}{3}} \mathbf{F} \tag{4.3}$$

The corresponding left Cauchy-Green deviatoric stretch tensor is

$$\bar{\mathbf{B}} = \bar{\mathbf{F}} \cdot \bar{\mathbf{F}}^T \tag{4.4}$$

The corresponding first and second-strain invariants can be defined as

$$\bar{I}_1 = \text{trace}\left(\bar{\mathbf{B}}\right) = \mathbf{I} : \bar{\mathbf{B}}$$

$$\bar{I}_2 = \frac{1}{2}\left(\bar{I}_1{}^2 - \text{trace}\left(\bar{\mathbf{B}} \cdot \bar{\mathbf{B}}\right)\right) = \frac{1}{2}\left(\bar{I}_1{}^2 - \mathbf{I} : \bar{\mathbf{B}} \cdot \bar{\mathbf{B}}\right) \tag{4.5}$$

The strain energy potential for isotropic, compressible materials will be a function of these invariants and is given as follows

$$U = U\left(\bar{I}_1, \bar{I}_2, J\right) \tag{4.6}$$

Thus,

$$\delta U = \frac{\partial U}{\partial \bar{I}_1}\delta \bar{I}_1 + \frac{\partial U}{\partial \bar{I}_2}\delta \bar{I}_2 + \frac{\partial U}{\partial J}\delta J \tag{4.7}$$

The internal virtual work can be written with respect to integration over the reference volume as follows:

$$\delta W_I = \int_{V_0} J\left(\mathbf{S} : \delta \mathbf{e} + p\delta \epsilon_v\right) dV_0 \tag{4.8}$$

where p is the pressure given by the trace of the Cauchy stress (i.e., $\frac{1}{3}\mathbf{I} : \boldsymbol{\sigma}$), $\mathbf{S}$ is the deviatoric part of the stress given by $\boldsymbol{\sigma} - p\mathbf{I}$, the deviatoric part of rate of deformation tensor ($\delta \mathbf{D}$) is given as $\delta \mathbf{e} = \delta \mathbf{D} - \frac{1}{3}\delta \epsilon_v \mathbf{I}$, and the virtual rate of change of volume per current volume is $\delta \epsilon_v = \mathbf{I} : \delta \mathbf{D}$.

The constitutive equations can be obtained by equating the virtual work of the Cauchy stresses to the variation in the strain energy as follows:

$$\delta W_I = \int_{V_0} J\left(\mathbf{S} : \delta \mathbf{e} + p\delta \epsilon_v\right) dV_0 = \int_{V_0} \delta U dV_0 \tag{4.9}$$

Expanding the variation of the virtual work of the Cauchy stresses by writing the variation of invariants in Equation 4.7 in terms of variations of the rate of deformation tensor, the

constitutive equations can be determined and the resulting deviatoric stress is given by [216]

$$\mathbf{S} = \frac{2}{J}\mathbf{DEV}\left[\left(\frac{\partial U}{\partial \bar{I}_1} + \bar{I}_1\frac{\partial U}{\partial \bar{I}_2}\right)\bar{\mathbf{B}} - \frac{\partial U}{\partial \bar{I}_2}\bar{\mathbf{B}}\cdot\bar{\mathbf{B}}\right] \tag{4.10}$$

and the pressure is given by

$$p = \frac{\partial U}{\partial J} \tag{4.11}$$

Several particular forms of the strain energy potential are available. In this study, the third-order polynomial form is utilized with just one term for compressible behavior. The strain energy potential is given as follows:

$$U = \sum_{i,j=1}^{3} C_{ij}\left(\bar{I}_1 - 3\right)^i \left(\bar{I}_2 - 3\right)^j + \frac{1}{D_1}\left(J - 1\right)^2 \tag{4.12}$$

Several other models as particular cases of the polynomial model can also be obtained by setting specific coefficients to zero such as the neo-Hookean, Mooney-Rivlin, Yeoh, and reduced third-order polynomial models. The small-strain initial shear and bulk modulus for the polynomial form are given by

$$G_0 = 2\left(C_{10} + C_{01}\right) \quad \text{and} \quad K_0 = \frac{2}{D_1} \tag{4.13}$$

The Yeoh form which is an I_1-based model is of special interest in this study and can be viewed as a special case of the polynomial form with

$$U = \sum_{i=1}^{3} C_{i0}\left(\bar{I}_1 - 3\right)^i + \frac{1}{D_1}\left(J - 1\right)^2 \tag{4.14}$$

4.1.3 Abaqus/Explicit VUMAT for Hyperelastic Material Model

This study aims to implement the desired hyperelastic and hyperviscoelastic models with damage as Abaqus/Standard UMAT and Abaqus/Explicit VUMAT user subroutines. Although both Abaqus/Standard and Abaqus/Explicit include continuum damage for a number of a material models, neither includes it for hyperelasticity or hyperviscoelasticity. Hence, the hyperelastic and hyperviscoelastic models have been reimplemented through the SIMULIA/Abaqus user subroutine interfaces such that damage can be added to them.

This work leverages the Abaqus/Standard UMAT for hyperelasticity with damage developed on a previous joint project between M4 Engineering and Virginia Tech[1]. The central difference between Abaqus/Standard UMATs and Abaqus/Explicit VUMATs is that the UMATs process a single integration point at a time, while the VUMATs process a block of integration points at once. Other differences include the UMAT's computation of tangent material moduli for the Newton-Raphson solver in Abaqus/Standard and the ability to use simpler material model time integration in a VUMAT corresponding to the very small time steps typically taken in Abaqus/Explicit. The hyperelastic model with/without damage UMAT is transformed into a proper VUMAT, and a series of numerical tests are conducted to verify that the model was transferred correctly. This hyperelastic model with and without damage VUMAT is then extended to hyperviscoelasticity with and without damage.

For the examples presented in this section, the Yeoh strain energy potential as shown in Equation 4.14 is utilized. The corresponding material parameters are provided in Table 4.1. Only single-element cases for code verification will be shown. The deformation cases

---

[1]The human torso geometry and its simplifications were developed by BMi and M4 Enginnering Inc. The meshing, baseline hyperelastic Abaqus/Standard UMAT, and damage wrapper were handled by M4. Additionally, the diver UNDEX model setup, including the coupled acoustic modeling approach, as well as initial linear elastic results (not displayed), were carried out by M4. The authors' work encompassed the implementation of hyperviscoelastic Abaqus/Standard UMAT, and the realization of hyperelastic and hyperviscoelastic material models with and without damage in Abaqus/Explicit VUMAT. This also included material parameterization and post-processing for damage initiation and final failure parameterization.

Table 4.1: Yeoh hyperelastic model parameters.

C_{10} (kPa)	C_{20} (kPa)	C_{30} (kPa)	D_1 (1/kPa)
3.4	14.4	24	0.018

considered are pure volumetric, simple shear, uniaxial stress, and uniaxial strain as illustrated in Figure 4.1. For all the cases, a single fully-integrated 8-node brick element is used. Displacement control is used for all cases except the uniaxial stress case for which a load control is used to achieve the desired deformation state. Stress versus strain plots obtained from the UMAT subroutine are compared with the results from the intrinsic Abaqus model as shown in Figure 4.2. Here, the presented strains are logarithmic values (i.e., components of the logarithmic left stretch tensor with engineering shear strain components) with volumetric strain corresponding to the trace of logarithmic strain. From stress vs strain plots in Figure 4.2, it is clear that the VUMAT results match those of the intrinsic model.
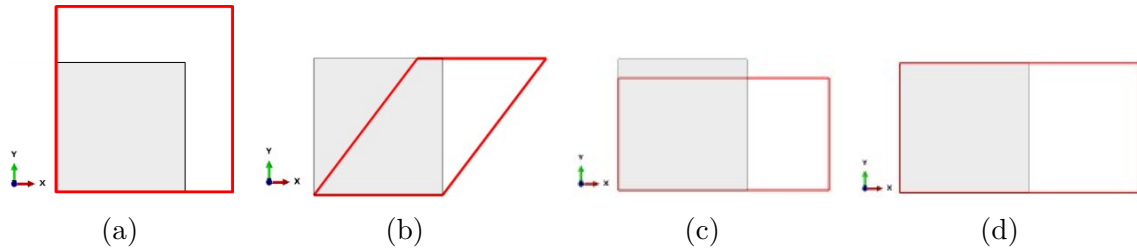
Figure 4.1: Problem definitions: (a) a pure volumetric state; (b) simple shear; (c) uniaxial stress; (d) uniaxial strain.

The critical time step estimate for Abaqus/Explicit is a direct function of the maximum system frequency for a linearized finite element model representation over the current time step. This can be bounded by the minimum time required for a stress wave to cross any element in the mesh. Of course, the stress wave speed is related directly to the ratio of effective material stiffness to mass. Abaqus/Explicit can use a range of time-step estimation techniques. By default, it probes the user material's constitutive response for effective moduli.
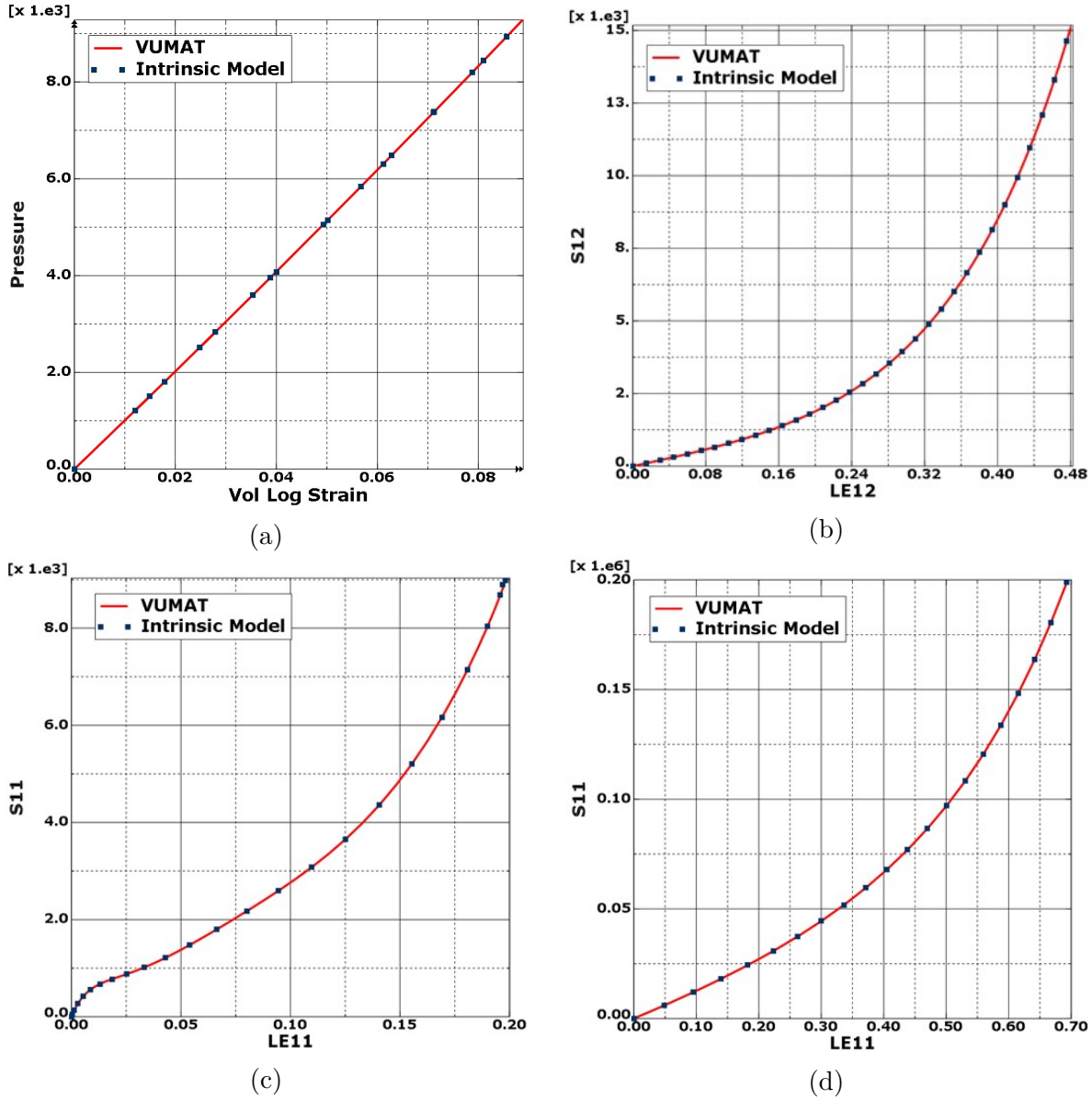
Figure 4.2: Constitutive response comparison between VUMAT and intrinsic model: (a) pressure vs. logarithmic volumetric strain; (b) shear stress vs. logarithmic shear strain; (c) axial stress vs. logarithmic axial strain for uniaxial stress; (d) axial stress vs. logarithmic axial strain for uniaxial strain.

However, such probing could be inaccurate. Hence, in order to get a conservative value of time increment for the cases where the behavior is highly nonlinear, the effective bulk and shear moduli values to be used can be specified directly within the Abaqus/Explicit user

subroutine for material response (i.e., the custom VUMAT subroutine). To compare the critical time steps between the intrinsic model and the VUMAT, a multiple-element example is analyzed using the VUMAT subroutine. Consider a plate with two holes. The VUMAT uses a different rate formulation than the Abaqus/Explicit intrinsic model. Thus, for a general load control for multiple element cases, the VUMAT results do not match exactly with the results from the intrinsic model. The results from the VUMAT for a plate with two holes using half of the domain with an appropriate symmetry boundary condition are given herein. More specifically, a half symmetry plate of dimensions $0.5 \times 1 \times 0.1 \, \text{m}^3$ with hole diameter 0.24 m was considered. Traction in the x-direction was applied on the right edge surface of the plate with a magnitude of 100 N. The load was linearly ramped to the final value in $1\,\text{s}$. The mesh consists of 22,220 fully integrated 8-node linear brick elements. Contours of the von Mises and axial stresses obtained at $1\,\text{s}$ are shown in Figure 4.3. The critical time steps from the VUMAT are close by when compared to those of the intrinsic model.
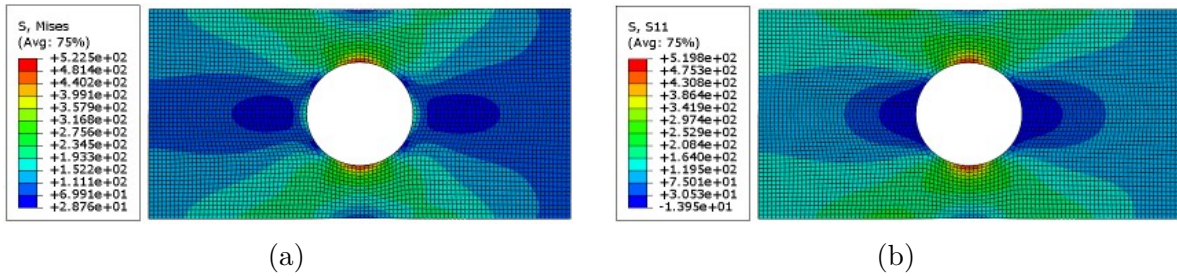
Figure 4.3: Stress response from Abaqus/Explicit VUMAT subroutine at 1 s: (a) von Mises stress (σ_{vm}); (b) axial stress (σ_{11}).

4.2 Hyperviscoelastcity

The hyperviscoelastic or finite strain viscoelastic models in SIMULIA/Abaqus are a time-domain viscoelastic generalization of the hyperelastic models [216, 217]. For such

hyperviscoelastic models, the instantaneous and long-term elastic responses use the same strain energy functional form as the related hyperelastic model, but either with glassy (i.e., instantaneous) or rubbery (i.e., equilibrium) moduli values utilized as appropriate. The time-dependent viscoelastic behavior is achieved by normalizing the underlying hyperelastic model and embedding it inside appropriate hereditary integrals. Such hereditary convolution integrals can be evaluated efficiently by describing the viscoelastic relaxation mechanisms through the Prony series (i.e., a series of decaying exponential terms with characteristic relaxation times spanning multiple decades) and developing appropriate recursion relationships.

4.2.1   Hyperviscoelastcity Formulation

In understanding how the model is constructed, first consider the following small strain viscoelastic model:

$$[S\left(t\right)] = K_0 e^H\left(t\right)[I] + 2G_0\left[e^D\left(t\right)\right] + \int_0^t \dot{K}\left(t'\right)e^H\left(t-t'\right)[I]\,dt' + 2\int_0^t \dot{G}\left(t'\right)\left[e^D\left(t-t'\right)\right]dt'$$

$$(4.15)$$

Here, the "H" and "D" superscripts indicate hydrostatic (volumtric) and deviatoric parts, respectively. Here, $e(t)$ is the small strain measure, and $S(t)$ is the Cauchy stress. K_0 and G_0 are the initial bulk and shear modulus, respectively. For the desired hyperviscoelastic model, the large strain measure will be taken from the scaled hyperelastic stress response. In fact, scaled hyperelastic stress computed using the initial viscoelastic moduli will be used to give the large strain specific to the material being modeled. Here a "0" subscript will denote such initial quantities. That is,

$$e^H\left(t\right) = \frac{1}{K_0}S_0^H(t) \tag{4.16}$$

$$\left[e^D\left(t\right) \right] = \frac{1}{G_0}[S_0^D(t)] \tag{4.17}$$

The left superscript indicates the configuration in which the quantity occurs and the left subscript indicates the configuration with respect to which it is measured [218]. The instantaneous hyperelastic response at any time can be written as a combination of hydrostatic and deviatoric parts. For example, instantaneous Cauchy stress is written as follows:

$$\left[{}_t^t S_0 \right] = \left[{}_t^t S_0^D \right] + \left({}_t^t S_0^H \right) \; [I] \tag{4.18}$$

The distortion part of the deformation gradient tensor is given as follows:

$$\left[{}_0^t \bar{F} \right] = \frac{1}{{}_0^t J^{\frac{1}{3}}} \; \left[{}_0^t F \right] \tag{4.19}$$

where $[{}_0^t F]$ is the deformation gradient tensor and ${}_0^t J$ is the determinant of the deformation gradient tensor. Thus, the hydrostatic and deviatoric parts of hyperviscoelastic formulation can be separated out and are given as follows:

$$\left[{}_t^t S^D \right] = \left[{}_t^t S_0^D \right] + dev \left(\int_0^t \frac{\dot{G}\left(t'\right)}{G_0} \left[{}_t^{t-t'} S_0^D \right] dt' \right) \tag{4.20}$$

$$\left({}_t^t S^H \right) = \left({}_t^t S_0^H \right) + \int_0^t \frac{\dot{K}\left(t'\right)}{K_0} \left({}_t^{t-t'} J \right) \left({}_{t-t'}^{t-t'} S_0^H \right) dt' \tag{4.21}$$

Stress tensors within the hereditary integral must have the same input configuration (here configuration "t" for areas), which is why a different stress measure is used $\left[{}_t^{t-t'} S_0^D \right]$.

$$\left[{}_t^{t-t'} S_0^D \right] \equiv \left({}_t^{t-t'} J \right) \left[{}_t^{t-t'} \bar{F} \right]^{-1} \left[{}_{t-t'}^{t-t'} S_0^D \right] \left[{}_t^{t-t'} \bar{F} \right]^{-T} \tag{4.22}$$

The Prony series for the relaxation modulus is given by:

$$G\left(t\right) = G_{\infty} + \left(G_0 - G_{\infty}\right) \sum_{i=1}^{N} f_{G_i} e^{-\frac{t}{\tau_i}} \tag{4.23}$$

$$K\left(t\right) = K_{\infty} + \left(K_0 - K_{\infty}\right) \sum_{i=1}^{N} f_{K_i} e^{-\frac{t}{\tau_i}} \tag{4.24}$$

This Prony series definition differs from what is used in the viscoelastic models intrinsic to SIMULIA/Abaqus. This form is used to maintain consistency with other implementations. Beyond giving explicit utilization of the initial and equilibrium moduli, it also has Prony coefficients that sum to unity. Hence, $\sum_{i=1}^{N} f_{G_i} = 1$ and $\sum_{i=1}^{N} f_{K_i} = 1$. Nevertheless, this Prony series form can be shown to be equivalent to Abaqus's Prony series form with simple relations available for converting between the two forms. Substituting Equations 4.23 and 4.24 in Equations 4.20 and 4.21, the total stress can be written as follows:

$$\begin{bmatrix} t \\ t \end{bmatrix} S^D \end{bmatrix} = \begin{bmatrix} t \\ t \end{bmatrix} S_0^D \end{bmatrix} - \frac{\left(G_0 - G_{\infty}\right)}{G_0} \sum_{i=1}^{N} f_{G_i} \begin{bmatrix} t \\ t \end{bmatrix} \hat{S}_i^D \end{bmatrix} \tag{4.25}$$

$$\left(\begin{matrix} t \\ t \end{matrix} S^H \right) = \left(\begin{matrix} t \\ t \end{matrix} S_0^H \right) - \frac{\left(K_0 - K_{\infty}\right)}{K_0} \sum_{i=1}^{N} f_{K_i} \left(\begin{matrix} t \\ t \end{matrix} \hat{S}_i^H \right) \tag{4.26}$$

where the state variables $\begin{bmatrix} t \\ t \end{bmatrix} \hat{S}_i^D \end{bmatrix}$ and $\begin{matrix} t \\ t \end{matrix} \hat{S}_i^H$ are as follows:

$$\begin{bmatrix} t \\ t \end{bmatrix} \hat{S}_i^D \end{bmatrix} = \frac{1}{\tau_i} \int_0^t e^{-\frac{t'}{\tau_i}} \begin{bmatrix} t - t' \\ t \end{matrix} \bar{F} \end{bmatrix}^{-1} \begin{bmatrix} t - t' \\ t \end{matrix} S_0^D \end{bmatrix} \begin{bmatrix} t - t' \\ t \end{matrix} \bar{F} \end{bmatrix}^{-T} dt' \tag{4.27}$$

$$\left(\begin{matrix} t \\ t \end{matrix} \hat{S}_i^H \right) = \frac{1}{\tau_i} \int_0^t e^{-\frac{t'}{\tau_i}} \left(\begin{matrix} t - t' \\ t - t' \end{matrix} S_0^H \right) dt' \tag{4.28}$$

Recursion relationships for quickly updating these state variables will be derived by assuming quantities at time t to be known with quantities at time $t + \Delta t$ to be calculated[216]. Change

of variables, integration by parts, and further simplifications are performed to obtain final recursion relations. For compactness, consider the following:

$$\left[{}^{t}_{t+\Delta t} \bar{S}_i^D \right] \equiv \left({}^{t}_{t+\Delta t} J \right) \left[{}^{t+\Delta t}_{t} \bar{F} \right] \left[{}^{t}_{t} \hat{S}_i^D \right] \left[{}^{t+\Delta t}_{t} \bar{F} \right]^T \tag{4.29}$$

$$\left[{}^{t}_{t+\Delta t} \bar{S}_0^D \right] \equiv \left({}^{t}_{t+\Delta t} J \right) \left[{}^{t+\Delta t}_{t} \bar{F} \right] \left[{}^{t}_{t} S_0^D \right] \left[{}^{t+\Delta t}_{t} \bar{F} \right]^T \tag{4.30}$$

The recursion relation for state variables can be written as follows:

$$\left[{}^{t}_{t} \hat{S}_i^D \right] = \alpha_i \left[{}^{t+\Delta t}_{t+\Delta t} S_0^D \right] + \beta_i \left[{}^{t}_{t+\Delta t} \bar{S}_0^D \right] + \gamma_i \left[{}^{t}_{t+\Delta t} \bar{S}_i^D \right] \tag{4.31}$$

$$\left({}^{t}_{t} \hat{S}_i^H \right) = \alpha_i \left({}^{t+\Delta t}_{t+\Delta t} S_0^H \right) + \frac{\beta_i}{\Delta J} \left({}^{t}_{t} S_0^H \right) + \frac{\gamma_i}{\Delta J} \left({}^{t}_{t} S_i^H \right) \tag{4.32}$$

where $\Delta J = \det \left[{}^{t+\Delta t}_{t} F \right]$ and

$$\gamma_i = e^{-\frac{\Delta t}{\tau_i}}, \quad \alpha_i = \left(1 - \frac{\tau_i}{\Delta t} (1 - \gamma_i) \right) \quad \text{and} \quad \beta_i = \left(\frac{\tau_i}{\Delta t} (1 - \gamma_i) - \gamma_i \right) \tag{4.33}$$

These expressions will be substituted back into Equations 4.25 and 4.26 to get the total deviatoric and hydrostatic Cauchy stresses.

4.2.2 Abaqus/Standard UMAT for Hyperviscoelastic Material Model

The hyperviscoelastic model has been implemented as an Abaqus/Standard UMAT that utilizes the hyperelastic UMAT subroutine to compute the instantaneous material response to applied strain increments. As documented previously, that instantaneous response when normalized by the initial moduli forms the effective strain measure used in the hereditary

integrals of the hyperviscoelastic material model. The Abaqus/Standard UMAT subroutine for hyperviscoelasticity has been verified against the intrinsic model already present in Abaqus/Standard. The cases considered are pure volumetric, pure shear stretch, uniaxial stress, and uniaxial strain. The volumetric and pure shear stretch deformations are as illustrated in Figure 4.4. The pure shear stretch deformations are posed carefully such that the volume remains constant even for very large deformations. For all single element cases, a fully integrated 8-node brick element was used. As utilized previously, a Yeoh material model will be considered with the material inputs provided in Table 4.1. Furthermore, a 30-term Prony series is employed. The relaxation times range from 10^{-12} s to 316,000 s with logarithmic spacing of two terms per decade starting from 10^{-6} s. The underlying instantaneous hyperelastic response for volumetric and pure shear behavior is shown in Figure 4.5.

$\qquad$ (a) $\qquad$ (b)
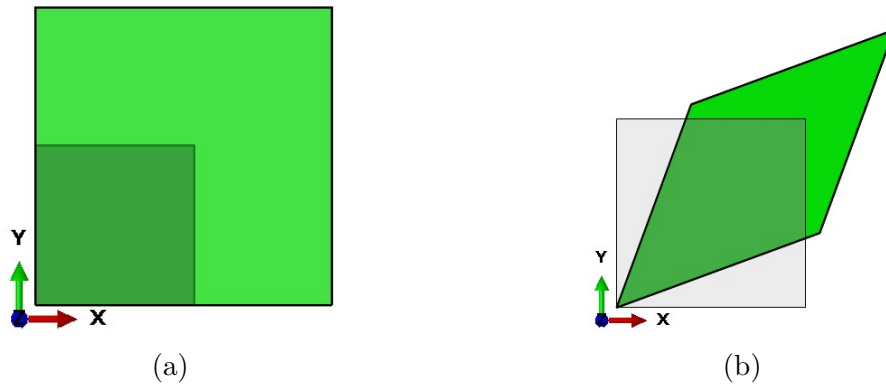
Figure 4.4: Problem definitions for hyperviscoelastic modeling verification: (a) pure volumetric deformations; (b) pure shear stretching.

Consider the pure shear stretching case. Under an appropriate unit step displacement of the diagonal node, the logarithmic shear strain achieved is 1.386. With displacement control, a step displacement corresponds to a step strain. The shear stress behavior under step strain is as shown in Figure 4.6(a). The instantaneous response depends on the strain level and cannot be linearly scaled with the strain magnitude for the underlying nonlinear hyperelastic
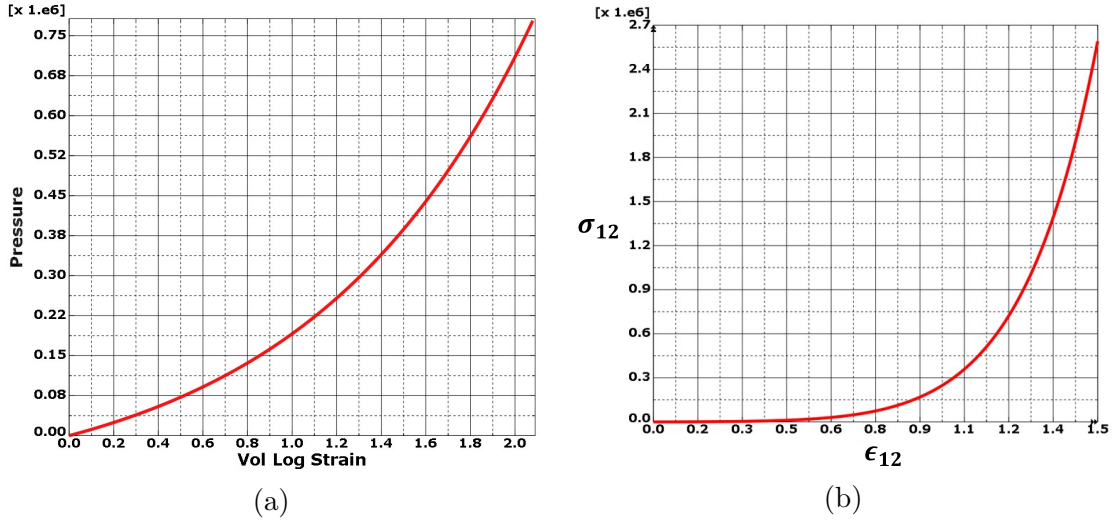
Figure 4.5: Cauchy stress vs logarithmic strain plots for Yeah hyperelastic model: (a) volumetric response; (b) shear response.

response. The relaxing viscoelastic behavior also can be observed where the stress decays for a constant applied strain. With load control, a step shear traction of 500 Pa is applied. The creep strain response is as shown in Figure 4.6(b). A small dip in the stress values can be seen when the strains become large because the stress measure being plotted is the Cauchy stress. With nominal stresses, such a dip will not be present. The creep behavior, where the strains increase for a constant stress can be observed. Excellent agreement between the Abaqus/Standard UMAT and the intrinsic models has been obtained for the resulting relaxation stress and creep strain.

Unit displacements are applied to a unit cube at different ramp rates to demonstrate the viscoelastic dependence on strain rate. More specifically, the diagonal nodes were ramped to the same final displacement in $1\,\mu$s, 10 ms, and 1 s, corresponding to applied strain rates of 1.386×10^{6}/s, 138.6/s, and 1.386/s, respectively, and then held constant. The variation of logarithmic shear strain is given in Figure 4.7(a). The resulting shear stress histories are plotted in Figure 4.7(b) and the different peak stress values reflect a different amount of viscoelastic relaxation occurring during the initial strain ramps with the faster ramps
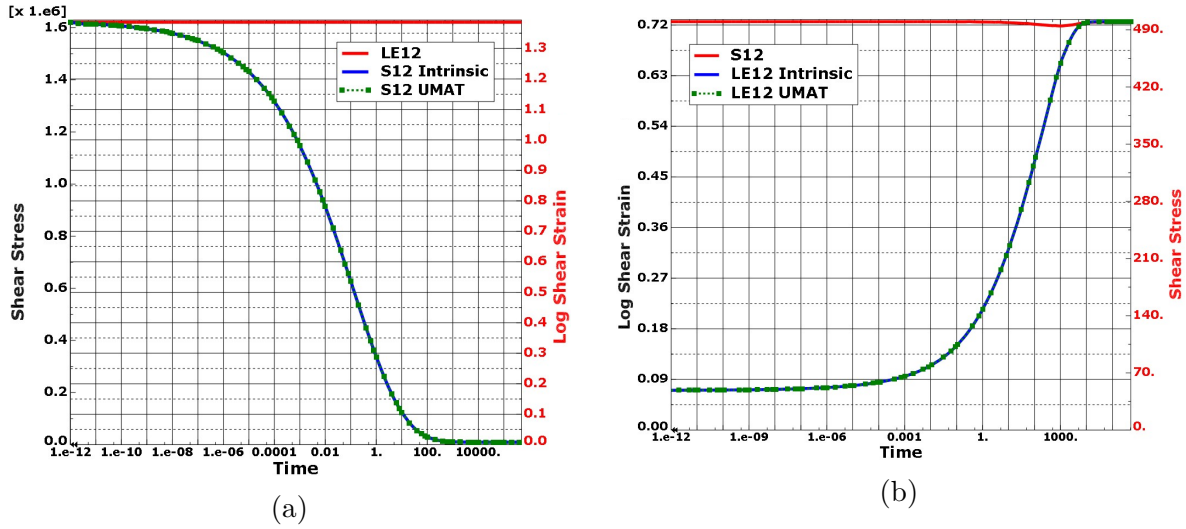
Figure 4.6: Time histories for pure shear stretching: (a) shear stress (S12)/log shear strain (LE12) vs. time for a unit step displacement (relaxation); (b) shear stress (S12)/log shear strain (LE12) vs. time for a unit step load (creep).

incurring less relaxation during the load-up. The net apparent shear stress vs logarithmic shear strain behavior is plotted in Figure 4.7(c) to show this strain rate dependence even more clearly. The Abaqus/Standard UMAT subroutine matches with that of the Abaqus/Standard intrinsic model as can be observed from the plots.

Two staircase step strain loading cases are also considered with the discrete strain increment histories shown in Figure 4.8(a). For consistent stair stepping, care must be taken to make sure the ramp time is the same for all increments to enable a fair comparison of the incremental viscoelastic behaviors. Here, a ramp of 1.386×10^7/s is considered for all the step increases shown in both cases. A comparison between the Abaqus/Standard intrinsic model and UMAT subroutine for cases 1 and 2 is as shown in Figure 4.8(b) and Figure 4.8(c). They match very well as shown in the plots. Also, the stress jumps corresponding to each strain increment increase with increasing base strain level corresponding to the underlying hyperelastic material behavior. The rate of viscoelastic relaxation for the incremental stress corresponding to each incremental strain is the same, even though it can be difficult to

(a)

(b)

(c)
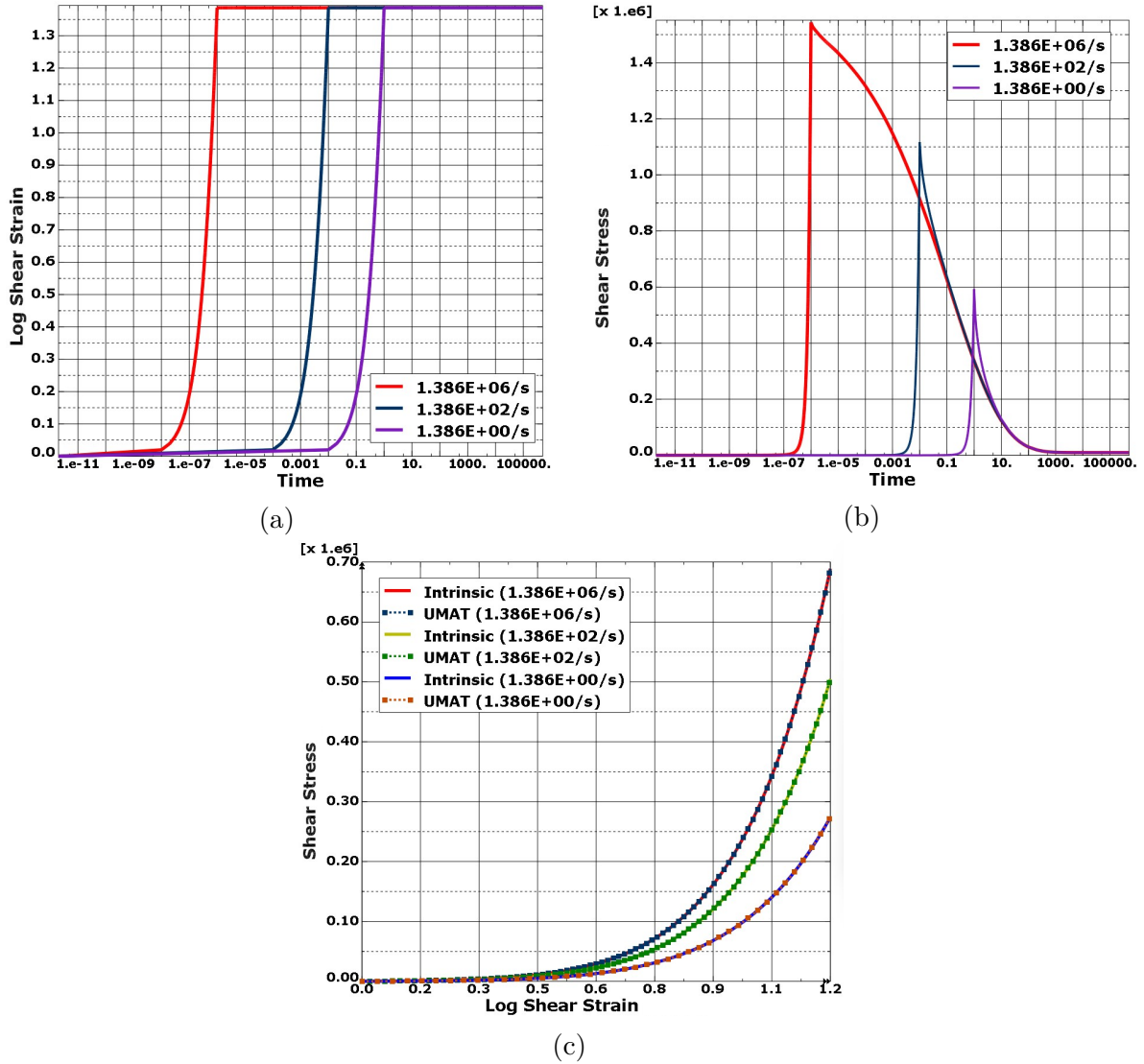
Figure 4.7: Hyperviscoelastic response under several ramp rates: (a) specified shear strain histories; (b) resulting shear stress histories computed using the implemented Abaqus/Standard UMAT; (c) comparison of apparent Cauchy stress vs logarithmic strain between the UMAT and the intrinsic model.

ascertain that on a logarithmic time scale as plotted in Figure 4.8(b) and Figure 4.8(c).

Many multiple-element example problems were also tested including the bending of a plate, twisting of a solid torus, etc. Here, twisting of a torus will be presented. Consider a torus as shown in Figure 4.9(a). The disk that loops around is 2 m in radius and its center is 10

(a)

(b)

(c)
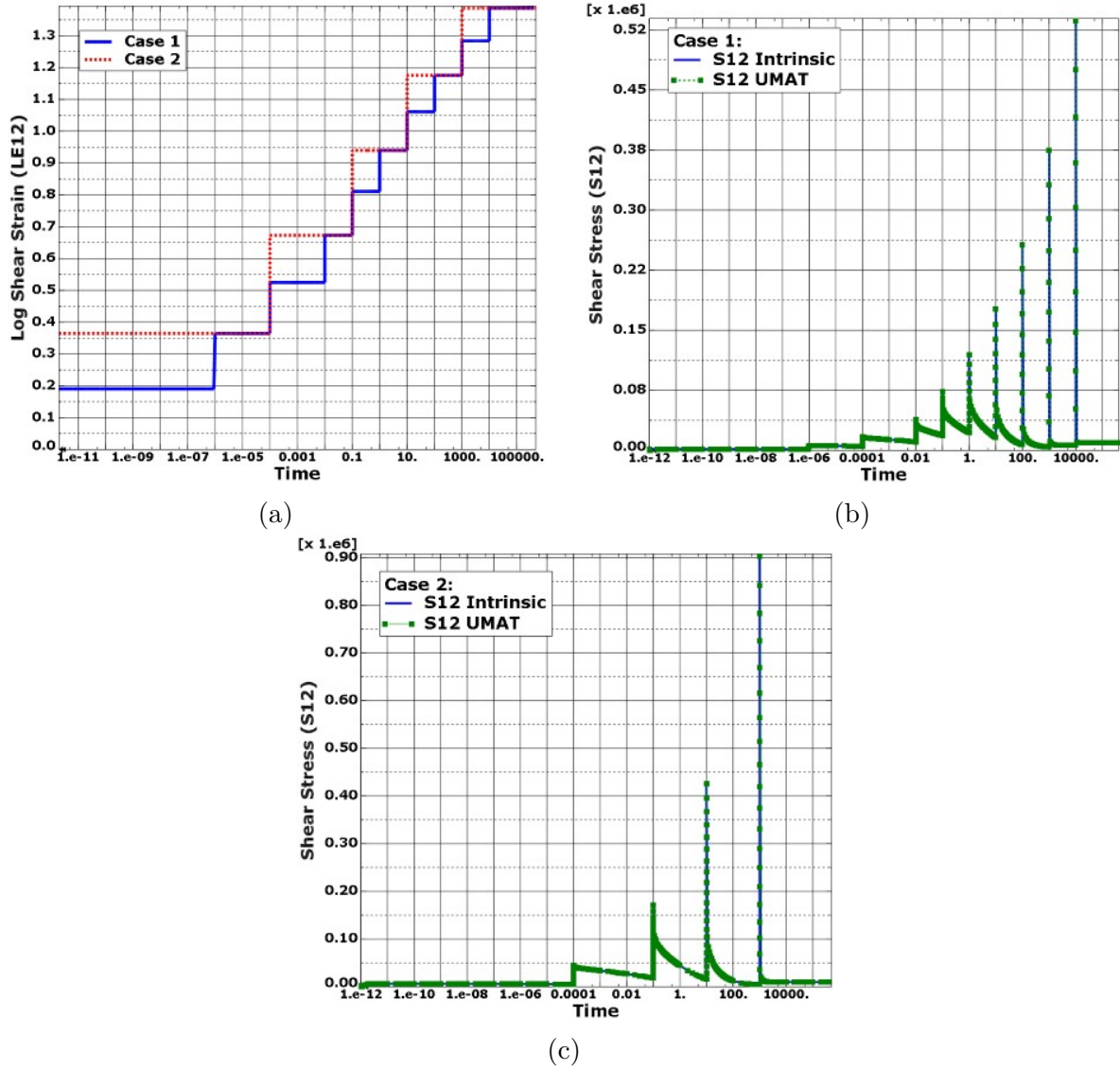
Figure 4.8: Shear case with discrete shear strain incrementation: (a) applied shear strain histories; (b) resulting stress history comparison for case 1; (c) resulting stress history comparison for case 2.

m away from the center of revolution. The left part is fixed and two surface traction loads of magnitude 5000 Pa in the opposite directions are applied as shown in the figure so as to cause a twisting motion. The load is applied as a step amplitude. Brick elements with linear shape functions with reduced integration and hourglass control are utilized. The mesh contains 4900 elements and is as shown in Figure 4.9(b). A comparison of stress contours

between the Abaqus/Standard intrinsic model and Abaqus/Standard UMAT is performed. All results match to high accuracy. The comparison of shear stress S12 between the Abaqus intrinsic model and Abaqus/Standard UMAT is as shown in Figure 4.9(c) and Figure 4.9(d).
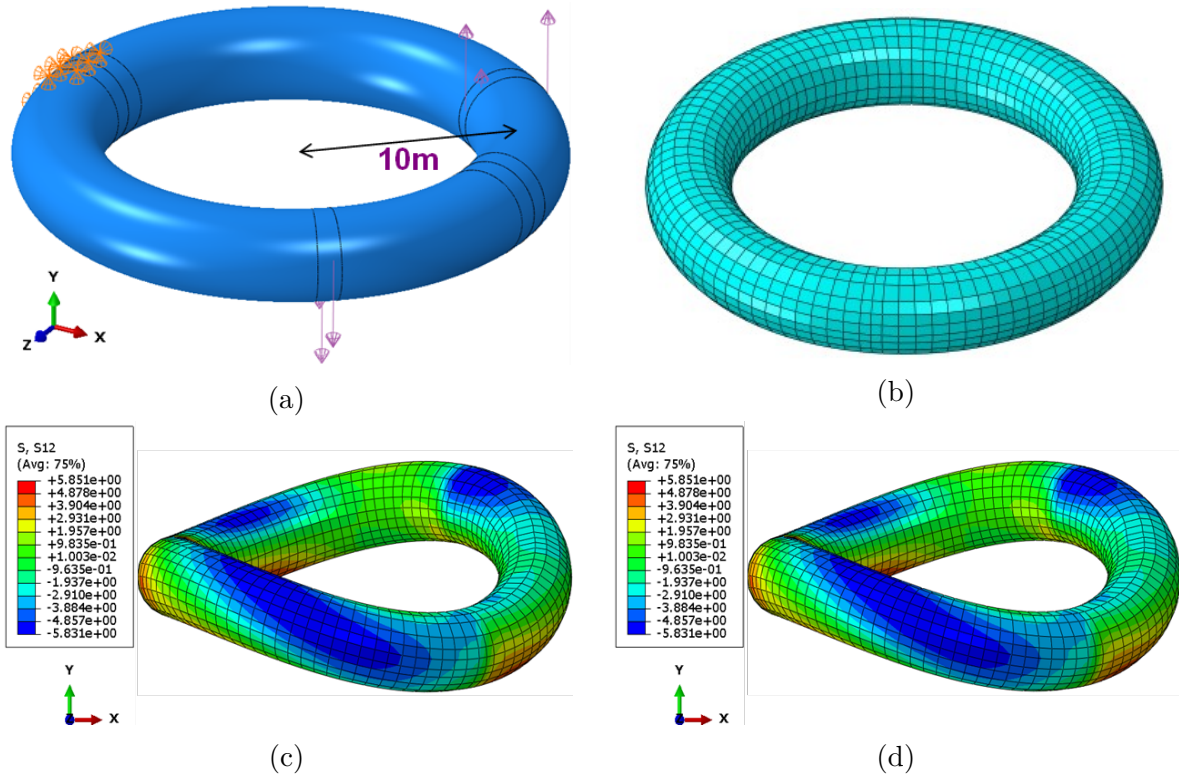
Figure 4.9: Torus under twisting loads: (a) initial geometry with applied loading and boundary conditions; (b) mesh; (c) shear stress contours computed using the intrinsic material model; (d) shear stress contours computed using the implemented Abaqus/Standard UMAT.

4.2.3 Abaqus/Explicit VUMAT for Hyperviscoelastic Material Model

The hyperviscoelastic Abaqus/Standard UMAT is leveraged in creating an equivalent hyperviscoelastic Abaqus/Explicit VUMAT. The Abaqus/Explicit VUMAT subroutine for hyperviscoelasticity has been verified against the intrinsic model already present in

Abaqus/Explicit. The cases presented here are pure volumetric and pure shear stretch. The volumetric and pure shear stretch deformations are as illustrated in Figure 4.4. In the examples provided, we utilize the Yeoh material parameters provided in Table 4.1. As considered previously, a 30-term Prony series is employed. The relaxation times range from 10^{-12} s to 316,000 s with logarithmic spacing of two terms per decade starting from 10^{-6} s. Here, we will focus solely on single-element cases for the purpose of code verification. The VUMAT employs a different rate formulation compared to the Abaqus/Explicit intrinsic model. Consequently, when we extend our analysis to encompass a broader range of scenarios involving multiple elements under general load control, a notable discrepancy emerges between the results at large deformations produced by the Abaqus/Explicit VUMAT subroutine and those generated by the intrinsic model. For all the single element cases, a fully-integrated 8-node brick element is utilized. We apply displacement control for the cases considered. The strains are taken to a final value and held constant as shown in Figure 4.10(a) and Figure 4.10(c). We assess the stress histories obtained from the Abaqus/Explicit VUMAT subroutine and compare them with results generated by the intrinsic model, as illustrated in Figure 4.10(b) and Figure 4.10(d). Results match to high accuracy. The strains presented are logarithmic values, specifically components of the logarithmic left stretch tensor with engineering shear strain components. The volumetric strain corresponds to the trace of the logarithmic strain.

4.3 Damage Modeling

For a diver subjected to blast loading, a spectrum of damage mechanisms are anticipated, encompassing various physiological responses such as contusions, hematoma, perforations, and lacerations, triggered by peak stresses and strains or sustained large-amplitude
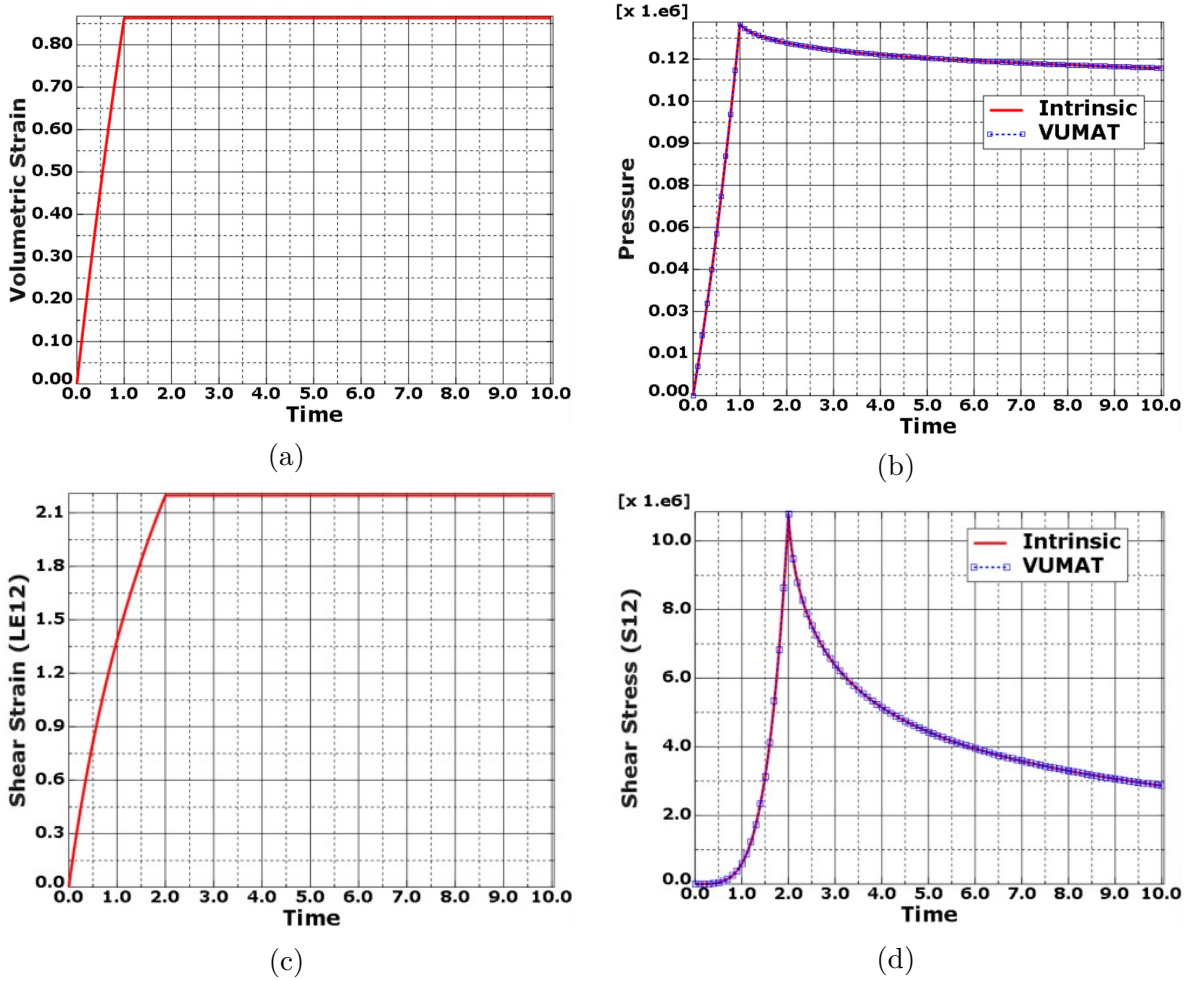
Figure 4.10: Stress history comparison between Abaqus/Explicit VUMAT subroutine and intrinsic model for a given strain amplitude: (a) applied volumetric strain; (b) pressure vs time; (c) applied shear strain; (d) shear stress vs time.

oscillations. Continuum damage modeling and element failure can effectively represent contusions, hematoma, and large-scale tearing, while direct modeling of cuts and lacerations is better suited for techniques such as cohesive zone modeling or the eXtended Finite Element Method (XFEM), both of which could be explored in future studies. In the continuum damage approach, the stress tensor is modified by a factor of $(1 - D)$ where D is the damage parameter which varies from 0 for no damage to 1 for complete damage. Criteria for damage initiation are evaluated to determine when the incurred stress and/or strain

is considered to correspond to the start of significant damage accumulation. Additional equations are given for the damage evolution to describe the damage growth with the evolution of strain and/or relative displacement. Often, the evolution equation parameters are adjusted to give the desired fracture energy following the onset of damage. Of course, the complete set of equations for material response from its initial state through final damage can be parameterized using available experimental data. However, fitting such failure tests typically involves modeling the experiment such that the net load-deflection from the test can be captured sufficiently. Once completely damaged, an element is removed and its mass and velocity are transferred to its component nodes which can be included in subsequent calculations including impact and energy exchange..

The conventional approach to continuum damage typically involves isotropic damage, where a single damage parameter uniformly affects all stress components. However, there is room for more intricate formulations. For materials exhibiting isotropic elasticity, their overall response can be dissected into distinct volumetric and deviatoric components. Volumetric behavior relates to changes in volume, impacting parameters such as pressure and volumetric strain. On the other hand, deviatoric behavior pertains to distortional shape changes, impacting parameters including shear stress, strain, and the non-volumetric aspects of normal stresses and strains, like pure shear. Motivated by this inherent separation of behaviors, we opt for a volumetric/deviatoric damage split. Under this approach, both stress and strain tensors are partitioned into their volumetric and deviatoric constituents. Two damage variables are then introduced: one for volumetric damage and another for deviatoric damage. Volumetric damage influences the material's pressure, while deviatoric damage primarily impacts deviatoric stresses. For the sake of completeness and robustness, coupled (isotropic) volumetric/deviatoric damage is also incorporated into the framework.

A table summarizing the different ways in which the strains (in this case logarithmic strains)

Table 4.2: Damage wrapper strain control.

Type	Evolution	Coupling	Damage Control ϵ_v	ϵ_{vm}	ϵ_I
Coupled Vol/Dev	Linear	Circ/Ellipse	Weighted	Weighted	-
		Line			
	Exponential	Circ/Ellipse	Weighted	Weighted	-
		Line			
	3-Parameter	Circ/Ellipse	Weighted	Weighted	-
		Line			
Uncoupled Vol/Dev	Linear	-	Direct	Direct	-
	Exponential	-			
	3-Parameter	-			
Max Principal	Linear	-	-	-	Direct
	Exponential	-			
	3-Parameter	-			

are to be used to control damage is presented in Table 4.2. There are a total of twelve damage options considered. For the damage type (listed in the first column), either an uncoupled volumetric/deviatoric strain split, a coupled volumetric/deviatoric strain, or a max principal strain-based approach can be utilized. In the coupled case, there is a single damage parameter that is applied to all stress components. That coupled damage parameter is computed using a single scalar effective or scaled strain corresponding to combining together the volumetric (ϵ_v) and von Mises strains (ϵ_{vm}) scaled relative to their independent failure values. In the uncoupled case, there are two independent damage parameters, one for the volumetric behavior and another for the deviatoric behavior. In the max principal case, a single damage parameter is applied to all stress components, just like in the coupled volumetric/deviatoric damage model. The damage parameter is computed using the max principal strain (ϵ_I).

For the coupled case, the exact way in which the scaled volumetric and von Mises strains are combined together can be accomplished in several ways as listed in the third column in Table 4.2. In the designated "circ/ellipse" approach, the scaled strains are squared and added together and compared to one. In the "line" approach the scaled strains are just added together. For the strain or damage control, either volumetric and deviatoric strains, or max principal strains can be utilized. Here, the deviatoric strain tensor is condensed into a von Mises type of scalar with its definition written so that the resulting "von Mises strain" is work conjugate with the von Mises stress to capture the total deviatoric work. Linear, exponential, or three-parameter damage models can be employed for the damage evolution, as indicated in the second column of Table 4.2.

4.3.1 Damage Formulations

The damage wrapper utilizes true logarithmic strain i.e., the natural logarithm of the left stretch tensor which can be calculated easily using the eigenvalues and eigenvectors of the left Cauchy Green tensor computed using the deformation gradient tensor. The expression for the logarithmic strain measure employed for damage initiation/evolution is as follows:

$$\boldsymbol{\epsilon} = \ln\mathbf{V} \tag{4.34}$$

where $\boldsymbol{\epsilon}$ is the logarithmic strain and $\mathbf{V}$ is the left stretch tensor.

For volumetric/deviatoric damage split, a stress and strain decomposition into volumetric and deviatoric parts are required. The tensorial logarithmic strain decomposition is defined using the volumetric strain ϵ_v and the deviatoric strain tensor $\boldsymbol{\epsilon}'$ as follows:

$$\boldsymbol{\epsilon} = \frac{1}{3}\epsilon_v\mathbf{I} + \boldsymbol{\epsilon}' \tag{4.35}$$

where

$$\epsilon_v = \text{Tr}(\boldsymbol{\epsilon}) = \mathbf{I} : \boldsymbol{\epsilon} = \epsilon_{kk} \tag{4.36}$$

Similarly, the stress tensor $\boldsymbol{\sigma}$ can also be decomposed into a pressure p and a deviatoric stress tensor $\mathbf{S}$

$$\boldsymbol{\sigma} = p\mathbf{I} + \mathbf{S} \tag{4.37}$$

where

$$p = \frac{1}{3}\text{Tr}(\boldsymbol{\sigma}) = \frac{1}{3}\mathbf{I} : \boldsymbol{\sigma} = \frac{1}{3}\sigma_{kk} \tag{4.38}$$

For the deviatoric damage, a scalar representative is required for damage control/evolution. The convenient von Mises strain will be utilized and is given as follows:

$$\epsilon_{vm} = \sqrt{\frac{2}{3}\boldsymbol{\epsilon}' : \boldsymbol{\epsilon}'} = \sqrt{\frac{2}{3}\epsilon'_{ij}\epsilon'_{ij}} \tag{4.39}$$

The von Mises stress is defined as follows:

$$\sigma_{vm} = \sqrt{\frac{3}{2}\mathbf{S} : \mathbf{S}} = \sqrt{\frac{3}{2}S_{ij}S_{ij}} \tag{4.40}$$

Uncoupled Volumetric/Deviatoric Damage:

Two damage variables, the volumetric damage D_v and the deviatoric damage D_{vm}, are introduced in the uncoupled volumetric/deviatoric damage approach. The volumetric and deviatoric damage is computed as follows

$$D_v = f(\hat{\epsilon}_v^{max})$$
$$D_{vm} = f(\hat{\epsilon}_{vm}^{max}) \tag{4.41}$$

where the effective/scaled volumetric strain $\hat{\epsilon}_v$ and the effective/scaled von Mises strain $\hat{\epsilon}_{vm}$ is computed using the volumetric strain ϵ_v, the von Mises strain ϵ_{vm}, the volumetric failure strain ϵ_v^f and the deviatoric failure strain ϵ_{vm}^f as follows

$$\hat{\epsilon}_v = \frac{\langle \epsilon_v \rangle}{\epsilon_v^f} \quad \text{and} \quad \hat{\epsilon}_{vm} = \frac{\epsilon_{vm}}{\epsilon_{vm}^f} \tag{4.42}$$

The max superscript represents the following:

$$\hat{\epsilon}^{max} = \max\{\hat{\epsilon}(t')\} \quad \text{for} \quad t' < t \tag{4.43}$$

The symbol $\langle \cdot \rangle$ denotes the Macaulay bracket given by

$$\langle \epsilon_v \rangle = \begin{cases} \epsilon_v & \epsilon_v \geq 0 \\ 0 & \epsilon_v < 0 \end{cases} \tag{4.44}$$

This operation is used to preserve only positive values of the volumetric strain and avoid compressive volumetric strain leading to damage. Once the volumetric and deviatoric damage is computed, the pressure and the deviatoric stress are updated as follows:

$$p_D = (1 - D_v)\, p$$
$$\mathbf{S_D} = (1 - D_{vm})\, \mathbf{S} \tag{4.45}$$

Coupled Volumetric/Deviatoric Damage:

In the coupled damage case, both volumetric and deviatoric damage values D_v and D_{vm} are combined into a single damage parameter D_m that is computed using an effective coupled

strain as shown below.

$$D_m = f(\hat{\epsilon}_m^{max}) \tag{4.46}$$

where $\hat{\epsilon}_m$, the effective/scaled coupling strain is computed using the coupled strain ϵ_m and a single failure strain ϵ^f as follows

$$\hat{\epsilon}_m = \frac{\epsilon_m}{\epsilon_m^f} \tag{4.47}$$

Here, the coupling strain ϵ_m can be a linear coupling strain or a circular/elliptical coupling strain. The scaled linear coupling strain measure is given as follows:

$$\hat{\epsilon}_m = \frac{\langle \epsilon_v \rangle}{\epsilon_v^f} + \frac{\epsilon_{vm}}{\epsilon_{vm}^f} \tag{4.48}$$

The scaled circular/elliptical coupling strain measure is given as follows:

$$\hat{\epsilon}_m = \sqrt{\left(\frac{\langle \epsilon_v \rangle}{\epsilon_v^f}\right)^2 + \left(\frac{\epsilon_{vm}}{\epsilon_{vm}^f}\right)^2} \tag{4.49}$$

Subsequently, the updated pressure and deviatoric stress tensor are computed using D_m as follows:

$$\begin{aligned} p_D &= (1 - D_m)\, p \\ \mathbf{S_D} &= (1 - D_m)\, \mathbf{S} \end{aligned} \tag{4.50}$$

These two equations can be combined together to obtain the equation for the entire stress tensor given by

$$\boldsymbol{\sigma} = (1 - D_m)\, \boldsymbol{\sigma} \tag{4.51}$$

Max Principal Damage:

In the max principal damage case, a single damage parameter D_I is computed using a scaled max principal strain as shown below:

$$D_I = f(\hat{\epsilon}_I^{max}) \tag{4.52}$$

where $\hat{\epsilon}_I$, the scaled max principal strain is computed using the max principal strain ϵ_I and a single failure strain ϵ_I^f as follows:

$$\hat{\epsilon}_I = \frac{\langle \epsilon_I \rangle}{\epsilon_I^f} \tag{4.53}$$

The updated pressure and deviatoric stress tensor are expressed using D_I as follows:

$$p_D = (1 - D_I)\,p$$
$$\mathbf{S_D} = (1 - D_I)\,\mathbf{S} \tag{4.54}$$

The equation for the updated stress tensor is given by

$$\boldsymbol{\sigma} = (1 - D_I)\,\boldsymbol{\sigma} \tag{4.55}$$

Damage Initiation and Evolution:

For coupled volumetric/deviatoric strain measures, scaled failure initiation and completion are defined as follows:

$$0 \le \hat{\epsilon}_m^i \le 1 \qquad \hat{\epsilon}_m^f = 1 \tag{4.56}$$

where $\hat{\epsilon}_m^i$ is the coupled scaled strain value for damage initiation. Care needs to be taken to make sure the coupled scaled initiation strains are below 1. Figures representing the initiation and failure boundaries in the scaled volumetric/von Mises strain space using linear and circular/elliptical coupling strains are provided in Figure 4.11(a) and Figure 4.11(b), respectively. The arcs at the strain points shown in Figure 4.11(a)-(c) encompass the local directions in the strain space around those points that correspond to damage accumulation. For instance, for the circular coupled volumetric/deviatoric damage case illustrated in Figure 4.11(b), any path proceeding outward within $-90°$ to $+90°$ from a radial line at the indicated point would result in additional damage accumulation, while the maximum damage accumulation at that point would be in the gradient direction which is along the radial line itself.

For uncoupled volumetric/deviatoric strain measures, failure initiation and completion are defined as follows:

$$
\begin{aligned}
0 \le \hat{\epsilon}_v^i \le 1 \qquad \hat{\epsilon}_v^f = 1 \\
0 \le \hat{\epsilon}_{vm}^i \le 1 \qquad \hat{\epsilon}_{vm}^f = 1
\end{aligned}
\tag{4.57}
$$

where $\hat{\epsilon}_v^i$ and $\hat{\epsilon}_{vm}^i$ are the corresponding scaled volumetric and von Mises strain values for damage initiation. The graph illustrating the initiation and failure boundary for the uncoupled volumetric/deviatoric damage case in the scaled volumetric/von Mises strain space is given in Figure 4.11(c). There are three different regions that have different damage accumulation directions at a given strain state as shown in Figure 4.11(c).

Three types of damage evolution are taken into account: linear, exponential, and 3-parameter damage evolution. The linear damage evolution is computed using the following function:

$$
D_{lin}(\hat{\epsilon}_{max}) = \frac{1}{\hat{\epsilon}_{max}} \left(\frac{\hat{\epsilon}_{max} - \hat{\epsilon}^i}{1 - \hat{\epsilon}^i} \right)
\tag{4.58}
$$
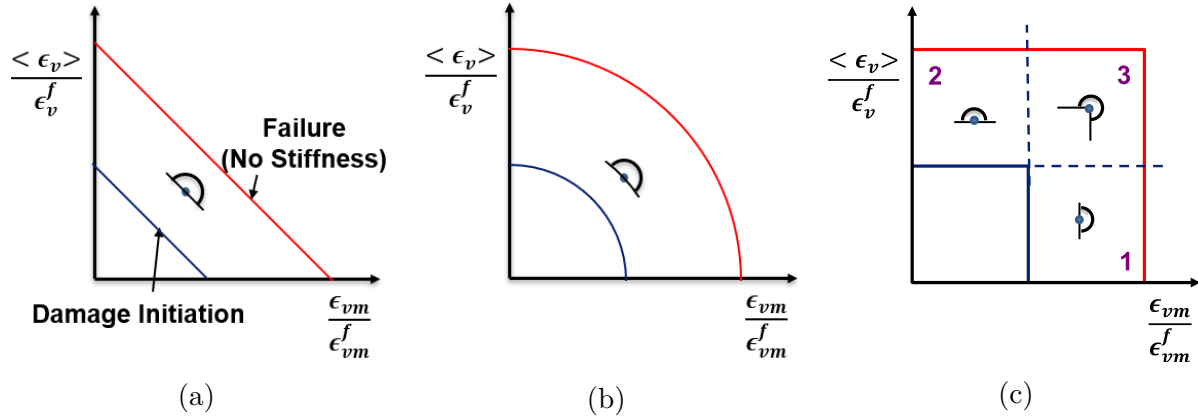
Figure 4.11: Damage initiation and failure boundary in terms of scaled strain for (a) linearly coupled volumetric/deviatoric damage; (b) circular/elliptical coupled volumetric/deviatoric damage; (c) uncoupled volumetric/deviatoric damage.

where $\hat{\epsilon}^i$ denotes the effective damage initiation strain and $\hat{\epsilon}_{max}$ is the maximum strain reached. The use of $\hat{\epsilon}_{max}$ ensures that the damage never decreases.

$$\hat{\epsilon}_{max} = \max\{\hat{\epsilon}(t')\} \quad \text{for} \quad t' < t \tag{4.59}$$

$$D(\hat{\epsilon}_{max}) = \begin{cases} 0 & \hat{\epsilon}_{max} < \hat{\epsilon}^i \\ 0 < D < 1 & \hat{\epsilon}^i < \hat{\epsilon}_{max} < \hat{\epsilon}^f \\ 1 & \hat{\epsilon}^f \leq \hat{\epsilon}_{max} \end{cases} \tag{4.60}$$

The exponential damage evolution is computed as follows:

$$D_{exp}(\hat{\epsilon}_{max}) = 1 - \frac{\hat{\epsilon}^i}{\hat{\epsilon}_{max}} \left(1 - \frac{1 - \exp\left(-\alpha \left(\frac{\hat{\epsilon}_{max} - \hat{\epsilon}^i}{1 - \hat{\epsilon}^i}\right)\right)}{1 - \exp\left(-\alpha\right)} \right) \tag{4.61}$$

where α is a damage parameter that can take any value greater than zero. For $\alpha = 0$, it reduces to linear evolution.

The variable rate three-parameter damage model employs the following function to define

nonzero damage rates:

$$\dot{D}_{3p}(\hat{\epsilon}, D) = a(1 - D)^b (\hat{\epsilon})^c \tag{4.62}$$

where a, b, and c are the three damage parameters. Here, damage increase is taken to only occur for positive strain rates with positive overall strains as described below:

$$\dot{D}_{3p}(\hat{\epsilon}, D) = \begin{cases} \dot{D} & \dot{\hat{\epsilon}} > 0, \ \ \hat{\epsilon} > 0, \ \ \text{and} \ \ D < 1 \\ \\ 0 & \dot{\hat{\epsilon}} \le 0, \ \ \text{or} \ \ \hat{\epsilon} \le 0, \ \ \text{or} \ \ D = 1 \end{cases} \tag{4.63}$$

The damage value at the time increment $i = n + 1$ is computed as follows:

$$D_{n+1} = D_n + \dot{D}_n \Delta t_{n+1} \tag{4.64}$$

where $\Delta t_{n+1} = t_{n+1} - t_n$ is the time increment.

4.3.2 Abaqus/Explicit VUMAT for Hyperelastic Material Model with Damage

As indicated previously, an Abaqus/Standard UMAT for hyperelasticity with damage developed on a previous project is leveraged for conversions to Abaqus/Explicit VUMAT subroutine. The Abaqus/Standard UMAT damage wrapper was extended to interface with the viscoelastic and hyperviscoelastic UMAT material models. The existing Abaqus/Standard UMAT for hyperelasticity with damage follows a compartmentalized approach, where damage-related calculations and stress tensor modifications are computed separately from the underlying undamaged material response. This modular coding style allows for the application of the same damage framework across various material models seamlessly. Specifically in this study, it means that a single damage wrapper can serve both

the hyperelastic and hyperviscoelastic material models as shown in the flowchart in Figure 4.12. This UMAT's damage implementation includes criteria for damage initiation and evolution equations governing damage accumulation. Moreover, users have the flexibility to choose between coupled, max principal damage, which uniformly degrades all stress components, and split volumetric/deviatoric damage, which affects the pressure (volumetric damage) and the deviatoric stresses (deviatoric damage) in a different manner.

(a)
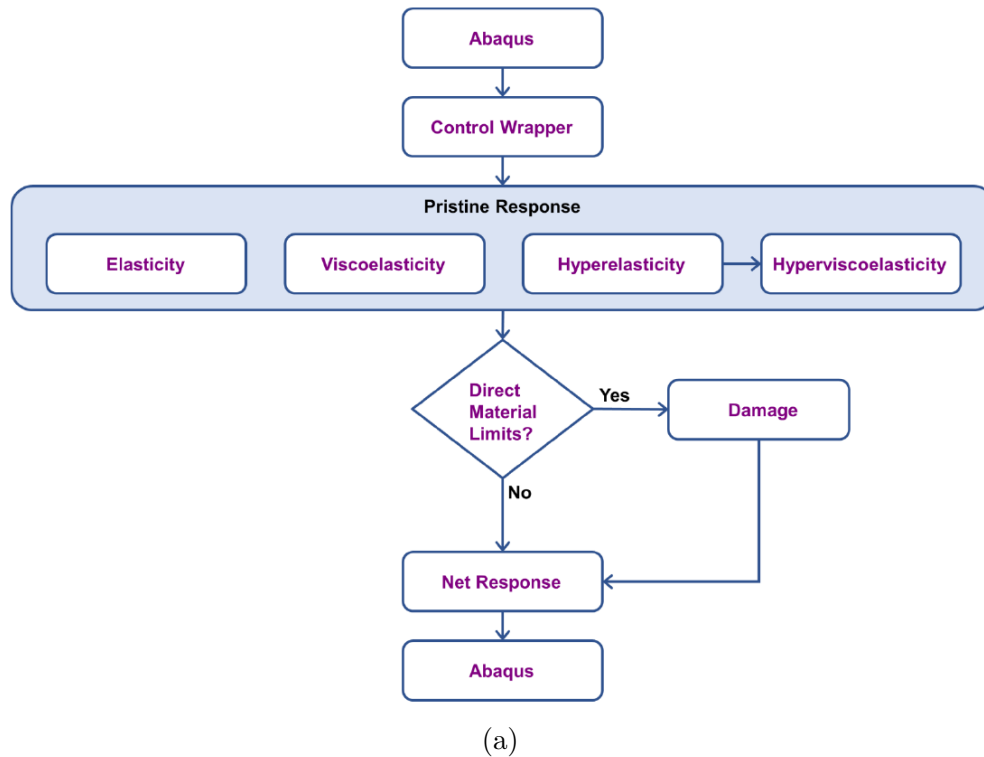
Figure 4.12: Code structure for damage modeling in Abaqus/Standard UMAT and Abaqus/Explicit VUMAT subroutines.

Leveraging the previously coded Abaqus/Standard UMAT damage wrapper, the equivalent Abaqus/Explicit VUMAT damage wrapper coding is completed and the coded hyperelastic VUMAT is incorporated into this VUMAT damage wrapper. A series of regression tests using a single element were run to verify partially the damage calculations for all twelve damage modeling options. These include cases with uncoupled volumetric and deviatoric

strains, strain loops with coupled shear/axial behavior, and strain cycles to increasing strain levels. These verification tests correspond to comparing damaged stress results from the combined VUMAT codes against results from the Abaqus/Explicit intrinsic material model with damage added during post-processing via a separately coded Python script. Such verification is not sufficient for full conclusions about whether the implemented code utilizes the posed equations correctly, as it involves another code created by the same developers, albeit in another software language. However, further confidence in the developed code is accomplished by careful review of all results against expectations.

Table 4.3: Third-order polynomial hyperelastic model parameters.

C_{10} (Pa)	C_{01} (Pa)	C_{20} (Pa)	C_{11} (Pa)	C_{02} (Pa)	C_{30} (Pa)	C_{21} (Pa)	C_{12} (Pa)	C_{03} (Pa)	D_1 (1/Pa)
8.35	16.85	4	2.4	7.32	2.7	3.6	2	3	0.03

(a)

(b)
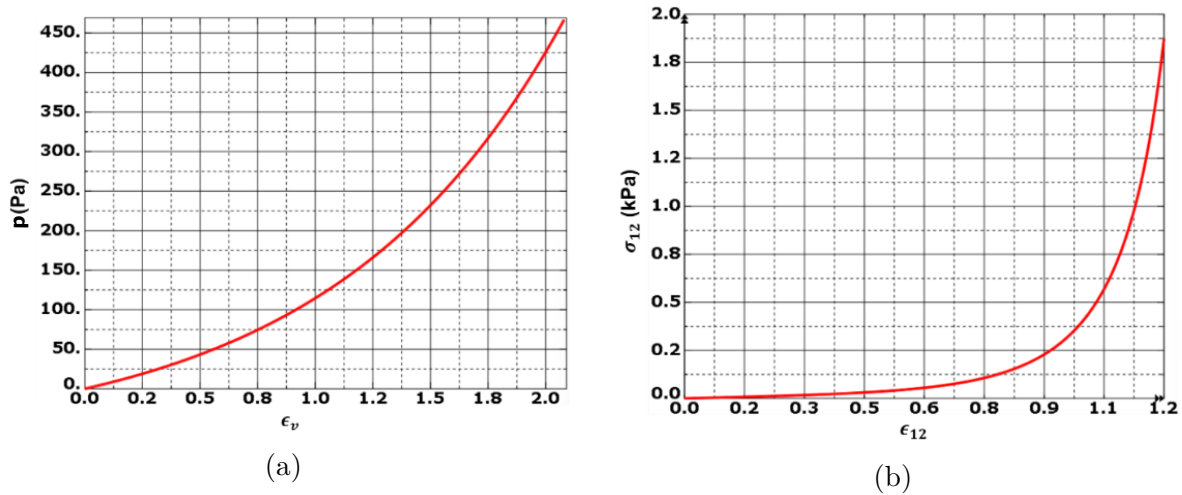
Figure 4.13: Undamaged hyperelastic constitutive behavior: (a) volumetric response; (b) deviatoric response.

For brevity, only sample results for uncoupled volumetric/deviatoric damage with linear damage evolution will be presented in this section. A fully integrated 8-node brick element was employed to avoid spurious effects from hourglass forces which are necessary for

numerical stability when a reduced integration element is used. A third-order polynomial model for the hyperelastic behavior was used with the material parameters provided in Table 4.3. This selection of parameters results in their individual stress contributions having similar sizes to allow for easier debugging. The density is taken as 1140 kg/m³. Sample undamaged hyperelastic responses for pressure and shear behaviors are shown in Figure 4.13.

(a)   (b)   (c)   (d)   (e)
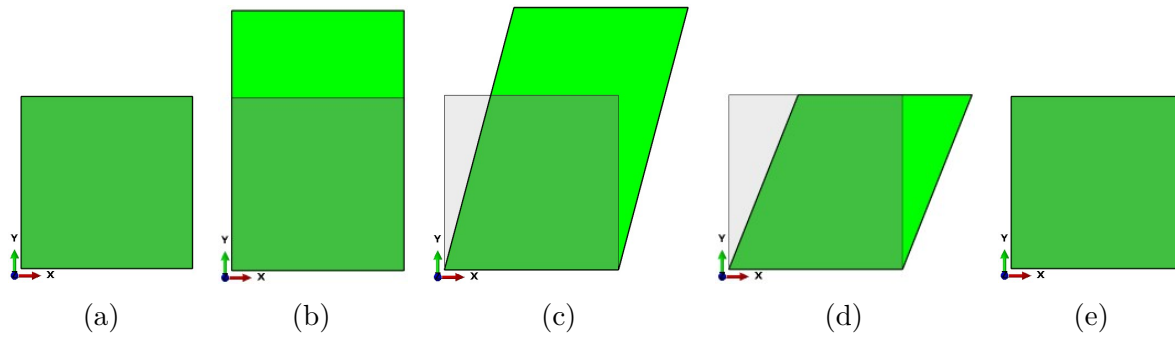
Figure 4.14: Closed strain loop: (a) undeformed unit block; (b) uniaxial stretch; (c) shear; (d) unstretch; (e) unshear.

The example with damage involves a closed strain loop where an extensional displacement in the 2-direction is applied, followed by simple shear in the 1-2 plane, a removal of extension in the 2-direction, and finally, removal of the 1-2 shear, as shown in Figure 4.14. The history of the strain components is shown in Figure 4.15. The volumetric and deviatoric (von Mises) damage initiation are plotted in Figure 4.16(a) and Figure 4.16(b) where $\hat{\epsilon}_v$ and $\hat{\epsilon}_{vm}$ represent volumetric and von Mises strains scaled by their respective failure values, $\hat{\epsilon}_v^i$ and $\hat{\epsilon}_{vm}^i$ are the corresponding scaled values for damage initiation, respectively. The accumulated damage is shown in Figure 4.16(c) and Figure 4.16(d) where D_v and D_{vm} are the volumetric and deviatoric (von Mises) damage variables, respectively. For the current parameter values, both of the volumetric and von Mises damage initiation conditions are met, but the damage does not proceed to completion for either response. The damage and undamaged stress response plots are shown in Figure 4.17. Additional results are generated using the intrinsic Abaqus/Explicit material model with damage assessed using the
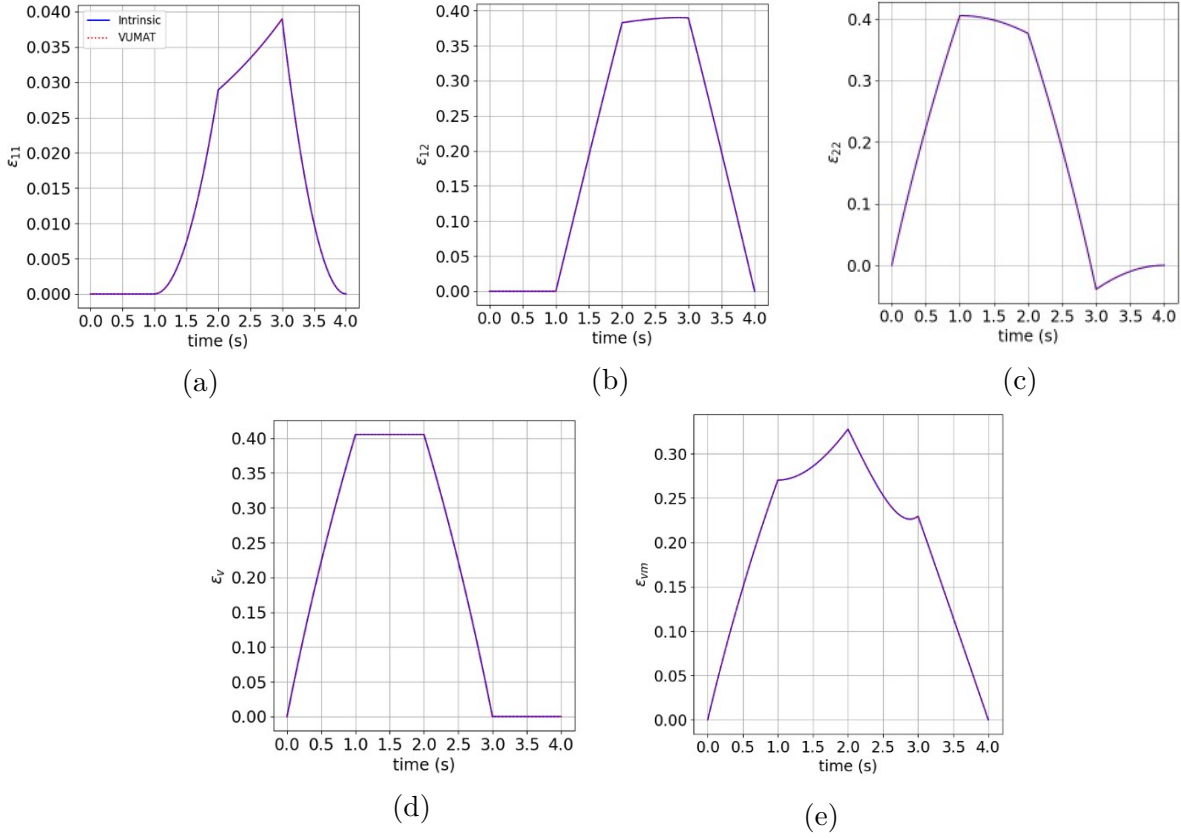
Figure 4.15: Applied logarithmic strain components: (a) 1-normal; (b) 12-shear; (c) 2-normal; (d) volumetric; (e) von Mises.

enforced strains and then applied to the intrinsic undamaged stress results via a Python post-processing script. Excellent agreement between the VUMAT subroutine and the modified intrinsic model results has been obtained.

Although not shown here, similar results and agreement have been obtained in partially verifying the other damage options. For the 3-parameter damage case, there is a need for tolerancing the positive strain rate for additional damage accumulation. That is, it is desirable to not let damage increase for small positive strain rates corresponding to numerical noise.
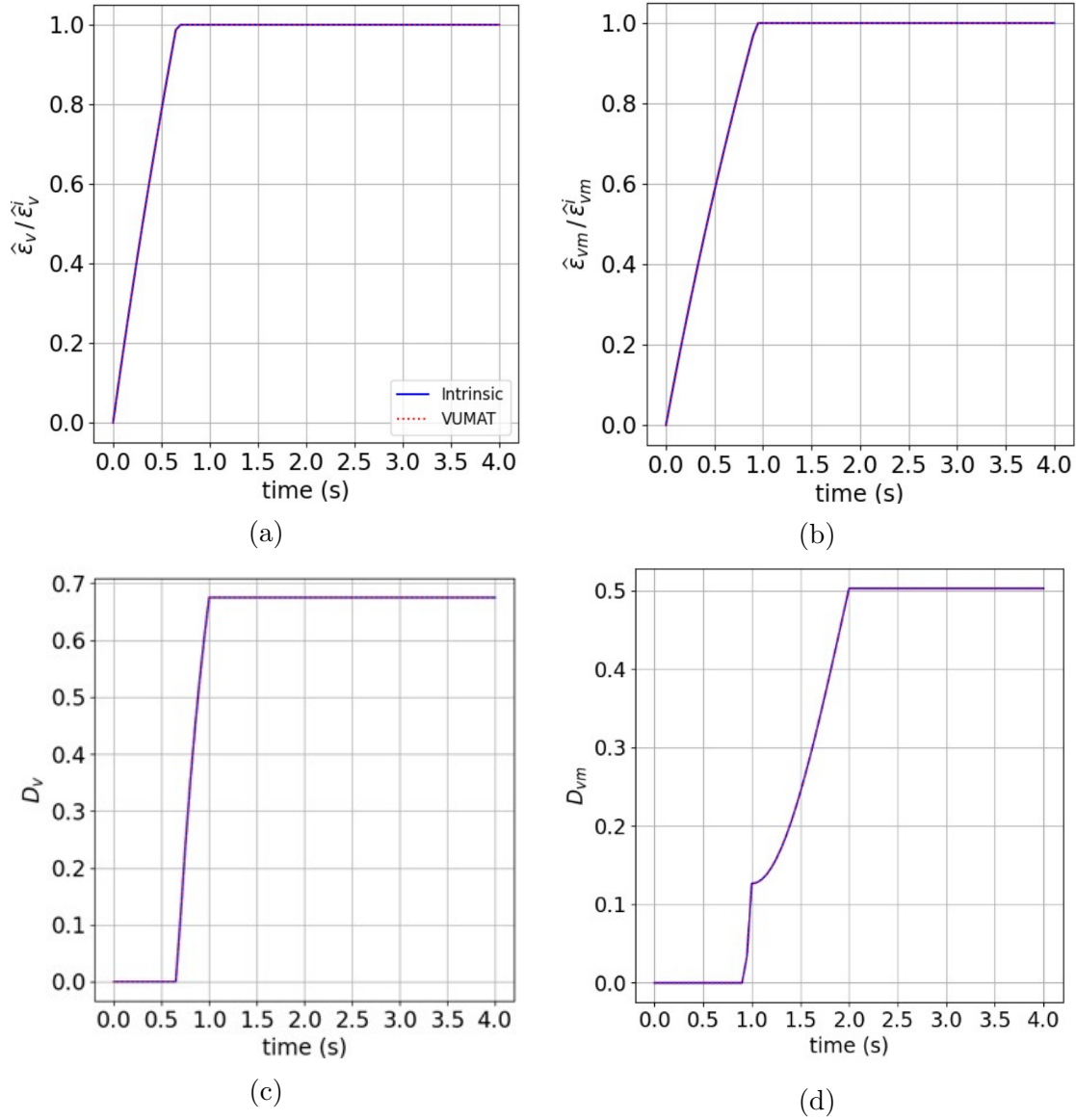
Figure 4.16: Damage initiation criteria: (a) volumetric; (b) deviatoric (von Mises) and continuum damage parameter: (c) volumetric; (d) deviatoric (von Mises).

4.3.3 Abaqus/Explicit VUMAT for Hyperviscoelastic Material Model with Damage

The coded hyperviscoelastic Abaqus/Explicit VUMAT subroutine is incorporated into the VUMAT damage wrapper. A series of regression tests using a single element is run to
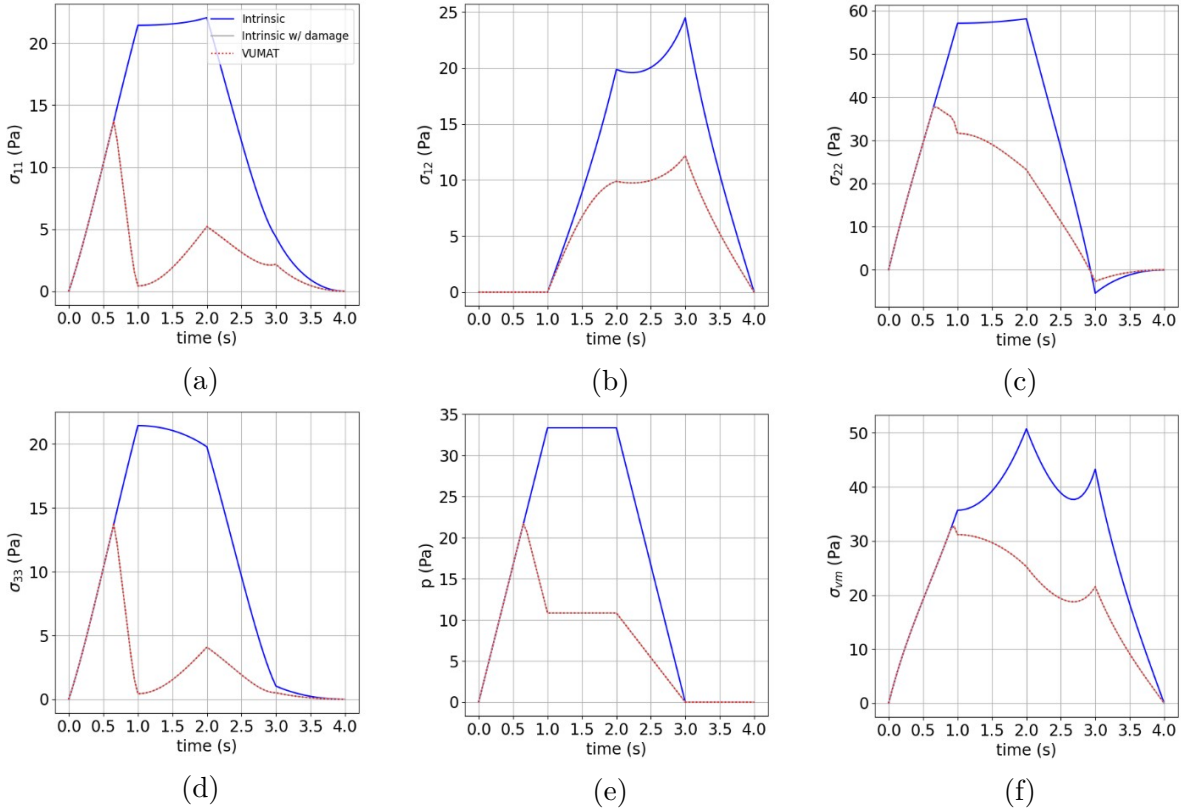
Figure 4.17: Undamaged and damaged Cauchy stress: (a) 1-normal; (b) 12-shear; (c) 2-normal; (d) 3-normal; (e) volumetric; (f) von Mises.

verify partially the damage calculations corresponding to all of the damage modeling options. These verification tests correspond to comparing damaged stress results from the combined VUMAT against results from the Abaqus/Explicit intrinsic material model with damage added during postprocessing via a separately coded Python script.

Only sample results for coupled volumetric/deviatoric damage with exponential damage evolution will be presented in this section. A fully integrated 8-node brick element has been employed. As utilized previously, a Yeoh material model has been used. The material parameters are provided in Table 4.1. For viscoelastic behavior, a 30-term Prony series with Prony coefficient and relaxation times for bulk and shear behavior as in the previous example runs have been utilized. The relaxation times range from 10^{-12} to 316,000 s with logarithmic

spacing of two terms per decade starting from 10^{-6} s. Finally, the density has been specified as $1140 \, \text{kg/m}^3$. For reference, the underlying instantaneous hyperelastic response for pressure and shear is as shown in Figure 4.5.
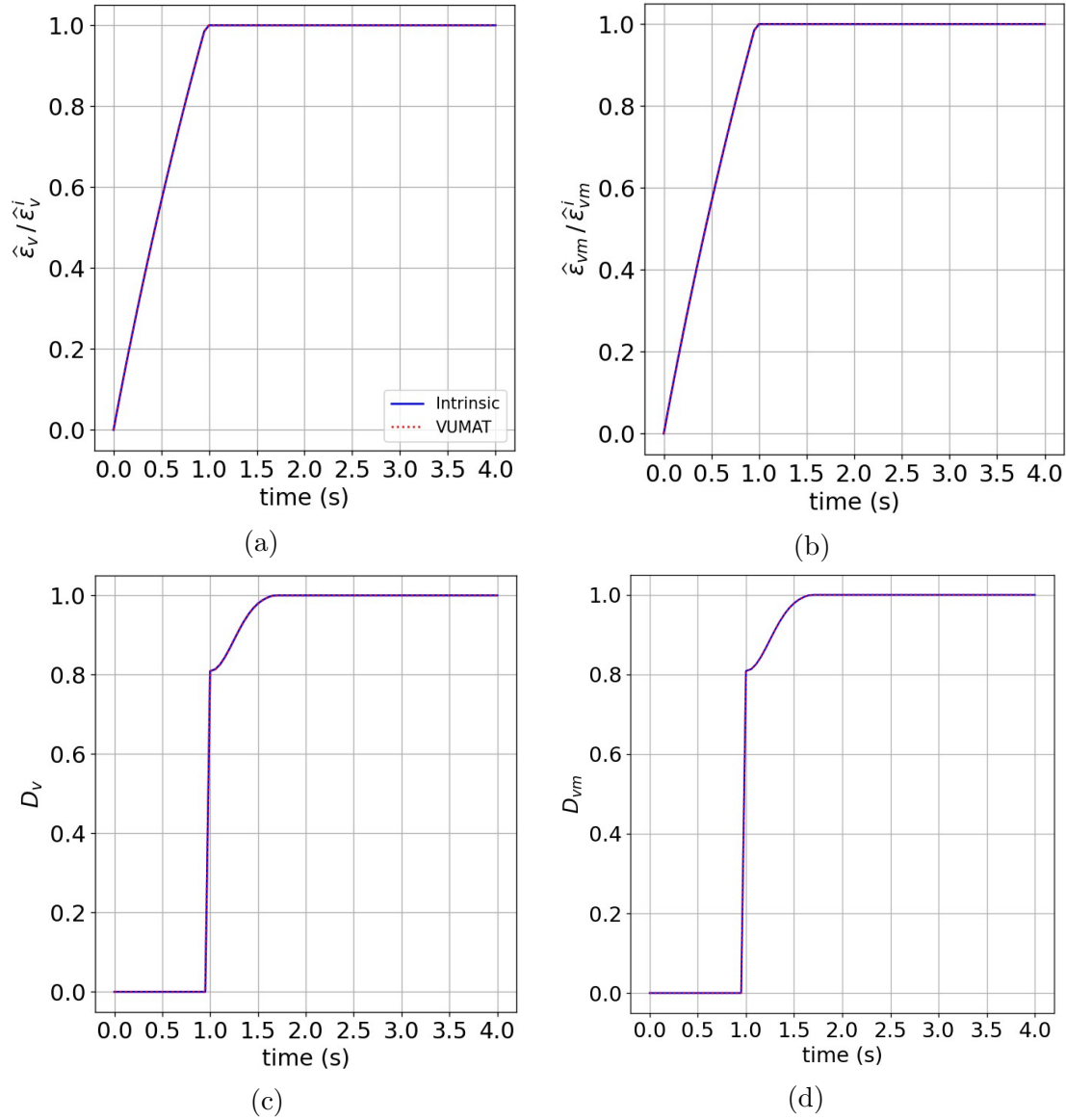
Figure 4.18: Volumetric and von Mises damage: (a) volumetric damage initiation criterion; (b) von Mises damage initiation criterion; (c) volumetric damage; (d) von Mises damage.

The damage example involves a closed strain loop of stretching, shearing, unstretching, and unshearing as given by the strain histories shown in Figure 4.15. The volumetric and
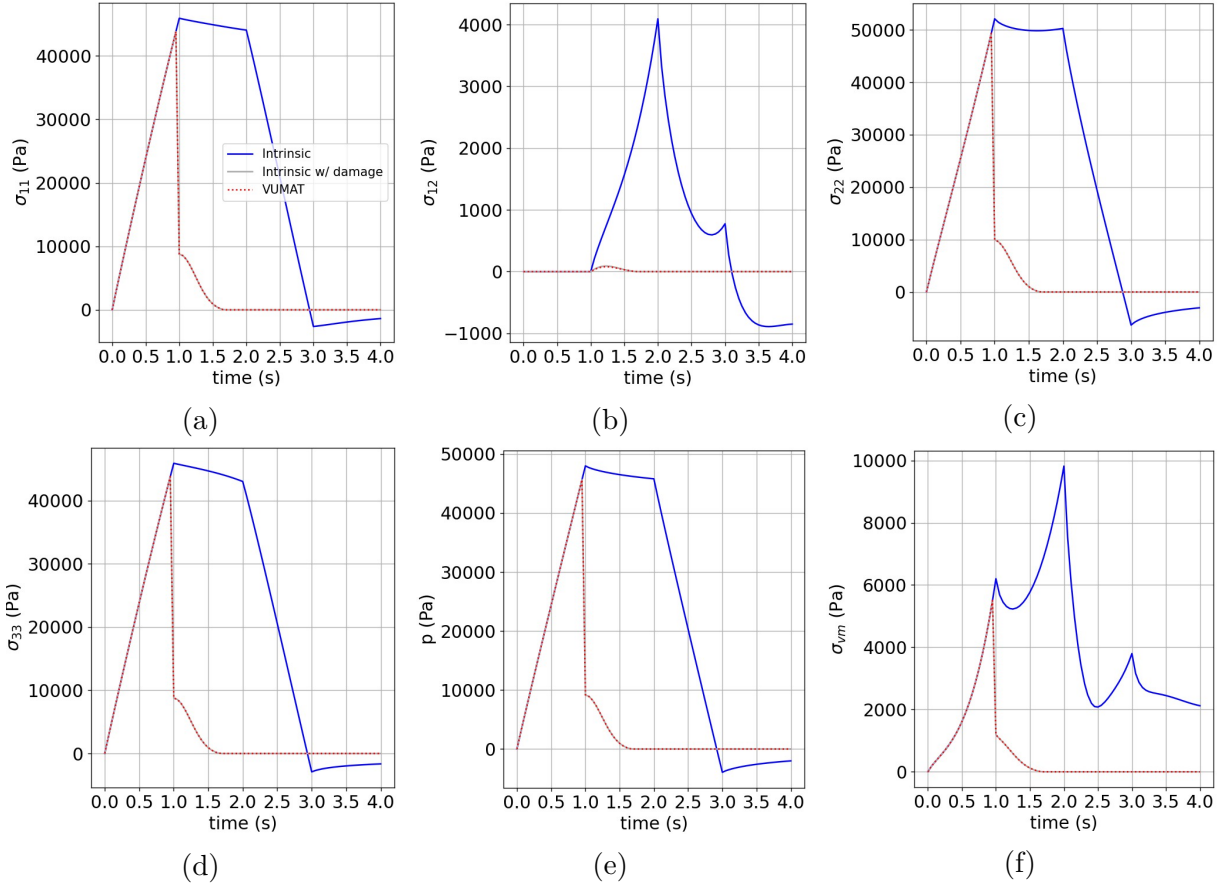
Figure 4.19: Undamaged and damaged Cauchy stress: (a) 1-normal; (b) 12-shear; (c) 2-normal; (d) 3-normal; (e) volumetric; (f) von Mises.

deviatoric damage initiation and damage evolution parameters are plotted in Figure 4.18 where $\hat{\varepsilon}_v$ and $\hat{\varepsilon}_{vm}$ represent volumetric and von Mises strains scaled by their respective failure values, $\hat{\epsilon}^i_v$ and $\hat{\epsilon}^i_{vm}$ are the corresponding scaled values for damage initiation, and D_v and D_{vm} are the volumetric and deviatoric damage variables, respectively. The damage initiation conditions are met and the damage proceeds to completion for both responses. Because the volumetric and deviatoric damage are coupled in this example, the damage parameters evolve identically. The pristine and damaged stress histories are shown in Figure 4.19. Excellent agreement between the VUMAT subroutine and the modified intrinsic model results has been obtained. Although not shown here, similar results and agreement have been

obtained in partially verifying the other damage options. Some discrepancies can be found in some cases where significant simple shear deformations occur. This is due to different stress rate formulations between Abaqus/Explicit VUMAT and intrinsic model formulations.

Chapter 5

Biological Material Response Parametrization

Characterizing material properties often involves just employing uniaxial tests, primarily due to their simplicity and ease of execution. While uniaxial tests offer a reasonable approximation, they may not precisely replicate the material's behavior under other deformation modes. Reducing the number of experiments can compromise the accuracy of material parameters within the strain energy potential when hyperelastic and hyperviscoelastic models are used. This highlights the necessity for comprehensive understanding and careful consideration of the implications of the chosen characterization techniques within the broader context of material modeling.

In this study, experimental tests on biological materials will not be directly conducted. Representative material properties are acquired through alternative methods. Literature sources have been systematically collected and organized, including those that offer empirically derived data concerning the responses of lung and other biological tissues, as well as others providing practical values suitable for meaningful simulations. In addition to direct extraction from these sources, refitting of any contained experimental data will also be carried out. A series of focused small-scale trade studies are also performed, designed to simulate diver response for likely injury levels under various conditions, generating stress-strain responses. These responses can then be analyzed against engineering judgment to

ensure their accuracy and usefulness.

5.1 Undamaged Tissue Material Parameterization

5.1.1 Comaprison between Hyperelastic Model Fitting in Abaqus/CAE and SIMULIA/Isight

To highlight distinctions between hyperelastic model fits derived directly from Abaqus/CAE and those from SIMULIA/Isight, fitting procedures were executed using experimental data in Gaur *et al.* [219] for human diaphragms. The Yeoh hyperelastic model is considered for all the fits presented in this section. Table 5.1 gives the values of material parameters obtained from Abaqus/CAE fits with incompressibility assumed in the deviatoric behavior fit. Figure 5.1 shows the comparison of the uniaxial response from the Yeoh model fits against the source experimental data with the numerical results computed using a hybrid element to handle the incompressibility condition directly. Cases HD5-03, HD1-01, and HD1-04 correspond to the sample IDs of the quasi-static uniaxial tension tests with the listed order based on fitting error. That is, case HD5-03 corresponds to the lowest fitting error value, whereas HD1-04 corresponds to the highest fitting error.

Table 5.1: Yeoh hyperelastic model fits for quasi-static cases of the human diaphragm test samples in order of fitting error.

Yeoh	C_{10} (kPa)	C_{20} (MPa)	C_{30} (MPa)
HD5-03	271.97	-6.71	136.47
HD1-01	68.75	1.77	41.31
HD1-04	19.96	-0.39	24.11

For hyperelastic model parameterization, by default Abaqus/CAE uses incompressibility
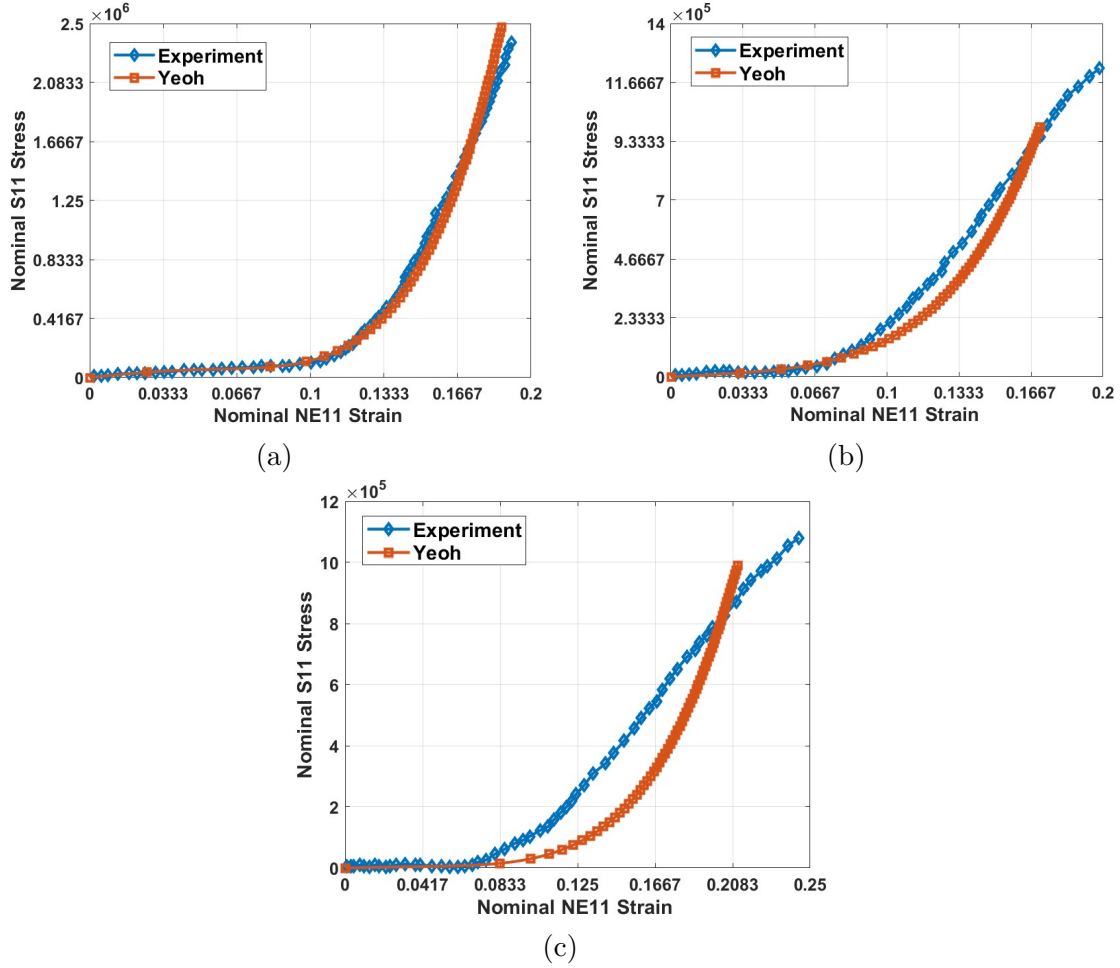
Figure 5.1: Comparison between the experimental data and hyperelastic simulations for several diaphragm test samples: (a) HD5-03; (b) HD1-01; (c) HD1-04.

when it fits the deviatoric material parameters governing distortional behavior. The D_i's corresponding to the volumetric behavior are calculated based upon the resulting initial shear modulus and the specified Poisson's ratio if a Poisson's ratio is given. If compressibility data is not specified, Abaqus/Explicit assumes compressible behavior with Poisson's ratio of 0.475 to calculate a constant bulk modulus based on the initial shear modulus. Abaqus/Explicit does not have hybrid elements and must use material models with finite compressibility. For high enough specified Poisson's ratios, this inconsistency has a relatively small effect and typically only at higher strain levels. The model choice also influences the fitting

error. Polynomial models would provide a better fit as the Yeoh model is a subset of the polynomial model, but I_2-based models are not recommended if complete experimental data is not available. Such models lead to stability issues and inconsistencies for other modes of deformation. In order to assess the importance of such inconsistencies, optimization using SIMULIA/Isight was also utilized to determine consistent volumetric and deviatoric material parameters that can be used in Abaqus/Explicit without any special techniques (e.g., hybrid elements for incompressible behavior).

The optimization problem in SIMULIA/Isight is formulated to minimize the square of the difference in nominal engineering stress obtained from the experiment to that of the simulation. The objective function to minimize is defined as follows:

$$f = \sum_{i=1}^{N} \left(1 - \frac{\sigma_i^{th}}{\sigma_i^{exp}} \right)^2 \tag{5.1}$$

where N represents the number of sample points from the experiment, σ_i^{exp} and σ_i^{th} are the nominal stress from the experiment and the simulation for the ith strain value, respectively. The design variables are the Yeoh material parameters with only one parameter used to define volumetric behavior. Proper scaling must be employed during optimization, as the resulting material parameters can be different orders of magnitude in size. The initial Poisson's ratio is constrained to be between 0.4 and 0.475. Sequential Quadratic Programming (SQP) is used as the optimization algorithm. The experimental data is limited to uniaxial loading conditions, and, therefore, only this specific loading case is taken into consideration. A single hybrid element with reduced integration was employed for the Abaqus/Standard simulations with Poisson's ratio of 0.5. A single fully integrated element in Abaqus/Standard is employed for other cases. Experimental data from Case HD5-03 corresponding to one of the quasi-static uniaxial tension tests in [219] is utilized for the representative material behavior.

Table 5.2 provides the material parameter values obtained from Abaqus/CAE and Isight. As listed in Table 5.2, the deviatoric parameters obtained using Abaqus/CAE do not depend on the initial Poisson's ratio employed. Using Isight, the deviatoric parameters for Poisson's ratio of 0.475 differs significantly from those fit using Abaqus/CAE under the incompressibility assumptions. In order to test the dependence on initial design during the Isight optimization process, a few more initial parameter values were considered as delineated in Table 5.3. The final optimized material parameters obtained are provided in Table 5.4. Similar values with close-by fitting errors are obtained in all of the Isight cases. Because an inequality constraint was used for the Poisson's ratio, different initial Poisson's ratio values are attainable. Figure 5.2 shows the comparison between Abaqus/CAE, SIMULIA/Isight fits, and the experimental data. It is obvious from the plots that the Isight fits are better for the compressible cases at larger strains.

Table 5.2: Yeoh hyperelastic model fits for a quasi-static case of the human diaphragm test sample HD5-03.

Fit	C_{10} (MPa)	C_{20} (MPa)	C_{30} (MPa)	K (MPa)	ν_{init}
Abaqus/CAE	0.272	-6.711	136.468	-	0.5
Abaqus/CAE	0.272	-6.711	136.468	10.697	0.475
Initial-2 (Isight)	0.323	-10.928	217.023	12.739	0.5

Table 5.3: Initial material model parameters used for optimization.

Fit	C_{10} (MPa)	C_{20} (MPa)	C_{30} (MPa)	K (MPa)	ν_{init}	Fit Error
Initial-1	0.3919	-6.71	136.5	8.89	0.457	12.2
Initial-2	0.2719	-6.71	136.5	8.89	0.470	5.6
Initial-3	0.3000	-1.00	100.0	10.00	0.4706	21.3

Table 5.4: Final material model parameters obtained from optimization.

Fit	C_{10} (MPa)	C_{20} (MPa)	C_{30} (MPa)	K (MPa)	ν_{init}	Fit Error
Final-1	0.317	-10.98	221	9.90	0.470	3.31
Final-2	0.323	-10.93	217	12.70	0.475	3.22
Final-3	0.317	-10.03	202	12.48	0.475	3.26
Abaqu/CAE	0.272	-6.71	136	10.70	0.475	
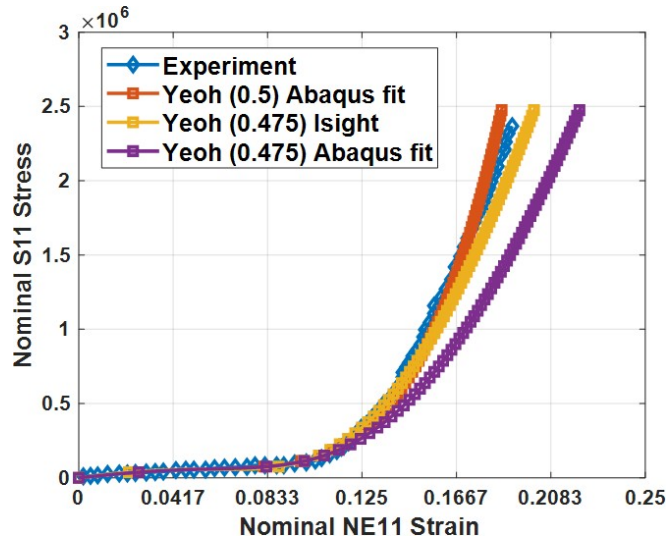
Figure 5.2: Comparison of Abaqus/CAE and SIMULIA/Isight fits against experimental data of the human diaphragm test sample HD5-03.

5.1.2 Lung Material Parameters

Various hyperelastic models and parameters are available in the literature for lung and other biological tissues. The variability of test-based lung tissue parameters across the literature can be attributed to many factors including the tissue source type (e.g., rat, pig, human, etc), the age and health of the source, the extraction location, the specimen size, the transpulmonary pressure, the type of material testing, etc. Material parameters and data obtained from the literature are compiled to guide modeling studies. Many of the values available in the literature for the lung's linear elastic modulus lie between 1-5 kPa.

Table 5.5: Yeoh model parameters obtained from SIMULIA/Isight and Abaqus/CAE optimization for the lungs.

Fit	C_{10} (Pa)	C_{20} (Pa)	C_{30} (Pa)	K (kPa)	ν_{init}	Fit Error
SIMULIA/Isight	557.85	-181.999	111.433	55.413	0.490	1.432
Abaqus/CAE	550.58	-165.900	98.500	91.396	0.494	1.478

Abaqus/CAE and SIMULIA/Isight have been utilized to calibrate hyperelastic material constants using lung data exhibiting closer alignment with established averages in the literature references. For the parameters chosen, experimental data available from Birzle *et al.* [220] was used. The optimization problem formulation for parameterization using SIMULIA/Isight is the same as in the previous section. The initial Poisson's ratio was constrained to be between 0.49 and 0.494. The experimental data is limited to uniaxial loading conditions. The fitting error from SIMULIA/Isight in this case is close but slightly better than the Abaqus/CAE fit which fits the deviatoric behavior assuming incompressibility. Figure 5.3 shows the comparison of the uniaxial response from the Abaqus/CAE and SIMULIA/Isight material model fits against the source experimental data. The values obtained from SIMULIA/Isight, as presented in Table 5.5, will be employed for the UNDEX simulations. The density of lungs is taken to be 100 kg/m^3.

5.1.3   Diaphragm and Torso Material Parameters

The diaphragm which is a skeletal soft tissue has a toe region in its tensile stress-strain curve which is characterized by low stiffness. This toe region is followed by a transition to much higher stiffness [219]. Physically, the elastin fibers initially stretch in a linear fashion and as the load increases, the collagen fibers reorient to carry a greater proportion of load. Thus, as the load increases, there is a stiffening effect. For the initial studies, both the diaphragm and
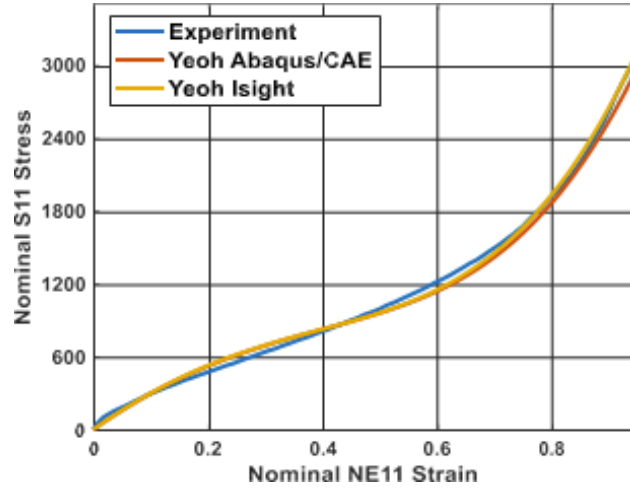
Figure 5.3: Comparison of Abaqus/CAE and SIMULIA/Isight material parameter fits against experimental data.

torso are modeled as linear elastic, and the properties are provided in Table 5.6 [221, 222].

Table 5.6: Material properties for human diaphragm and torso.

Tissue	ρ (kg/m³)	E (MPa)	ν
Diaphragm	1000	480	0.450
Torso	1000	0.53	0.494

5.2 Damage Parametrization using UNDEX Simulations

5.2.1 Acoustic Domain

Acoustic simulations for underwater explosion (UNDEX) scenarios will be employed to parameterize lung tissue damage. In this regard, this section will provide a concise overview of key implementation details and elucidate the rationale behind the acoustic setup.

Table 5.7: Recommendations for minimum acoustic medium stand-off as a function of frequency for a wave speed of 1462.87 m/s corresponding to nominal water.

	Min Standoff Radius r_1 (m)	
fmin (Hz)	mmin=1/3	mmin=1/2
22	22.164	33.247
100	4.876	7.314
243.5	2.003	3.004
500	0.975	1.463
1000	0.488	0.731
20,000	0.024	0.037

Currently, Coupled Eulerian-Lagrange (CEL) approaches such as combined CFD and FEM can achieve relatively high accuracy, but can be very expensive, requiring hundreds of cores operating over days of wall clock time [223]. Moreover, such UNDEX modeling may require a subject matter expert (SME) running a highly specialized, limited availability simulation code such as DYSMAS. The accuracy achieved may be exceptional, but not necessary when the complete range of blast scenario uncertainties is considered, especially for potential accidents. Hence, it can be prudent to use a lower fidelity modeling approach that has the following features: (1) is available commercially to a broad audience; (2) is able to be run on practical computing resources (e.g., a desktop workstation); (3) has a quick turn-around time; and (4) is easy-to-use for both SME and non-SME personnel. Achieving such modeling goals would allow a large number of scenarios and scenario variations to be analyzed to aid planning and decision-making. Moreover, the limited loss in accuracy which may result would not be problematic, as factors of safety would be used in any reasonable UNDEX planning. Essentially, the goal is to get medium-fidelity models and their quickly generated results into the hands of engineers and program managers for informed and timely decision-making. Finally, if higher accuracy is needed, the worst-case scenarios needing such additional resource dedication could be identified using the medium fidelity approach.

Table 5.8: Recommendations for characteristic acoustic element dimension for a wave speed of 1462.87 m/s corresponding to nominal water.

	Max Internodal Interval L_{max} (mm)	
fmax (Hz)	nmin=8	nmin=12
22	8311.78	5541.19
100	1828.59	1219.06
180	1015.88	677.26
500	365.72	243.81
1000	182.86	121.91
12000	15.24	10.16
20000	9.14	6.10

SIMULIA/Abaqus's acoustic shock modeling has been demonstrated to work well for traditional engineering structures where the structures are significantly more rigid than the surrounding acoustic medium [216] (e.g., water or air). Of particular importance is the interaction between the shock wave and the diver. Those interactions arising from the impedance mismatch and diver accelerations has been shown to alter the shock pressures realized on the diver to a significant extent. Also important for shock wave reflection and scattering determination has been the shape of the modeled diver/diver parts. In this study, SIMULIA/Abaqus including Abaqus/Explicit is used for sophisticated diver UNDEX modeling.

The Abaqus documentation [216] provides guidelines on the acoustic medium domain size necessary to capture the relevant frequency response where the recommended stand-off distance (i.e., acoustic medium domain size) is inversely proportional to the minimum frequency to be captured. Additionally, recommendations for acoustic element size are given where the maximum characteristic element dimension is inversely proportional to the maximum frequency to be captured. Applying the provided equation-based recommendations, sample results for a water wave speed of 1462.87 m/s are given in Table

5.7 and Table 5.8. Thus far, it has been found that the downsized domain for continued diver response need not be as large as recommended in Table 5.7 when a proper non-reflecting boundary condition is utilized on the acoustic domain. One key part of the response is ensuring that the water domain boundary does not act to reflect the incident shock wave. Associated with this is ensuring that the water domain is large enough to facilitate proper modeling of desired response frequencies. Modal analysis of an approximate spherical lung by itself indicated frequencies starting at around 22 Hz. Presumably, the surrounding water and contained air will increase these vibrational frequencies. Nevertheless, such low frequencies indicate the need for a stand-off distance of 22.2 m, as given in Table 5.7. Modeling such a large domain with sufficiently small acoustic element size for high frequency response would lead to significant solution times which may not be required during initial studies. As such, a stand-off distance of 10 m was used to define the water domain, while the blast source was still taken to be 20m from the center of the diver. This water domain size allows the key response to be captured, before any residual reflections arrive back at the diver.

Choosing a spherical acoustic domain centered around the diver results in improper radiation of the blast shock wave from the back side of the spherical domain. This has been concluded to be a pathological numerical wave reflection issue particular to this case where there are naturally two spheres of radiation that are tangent at a point. One is larger and is centered around the blast source, while the other corresponds to the practical acoustic domain centered about the diver, as given respectively by the red and blue domain boundaries shown in Figure 5.4(a). Zooming into the region near the diver has suggested a bullet-shaped modeling domain as shown. This model considers a blast scenario where a blast is located outside the modeled acoustic domain as shown in Figure 5.4. As illustrated in this figure, the Outer Mold Line (OML) of the acoustic domain resembles a bullet, while it is composed of three distinct domains consisting of an ellipsoid surrounding the diver which is then
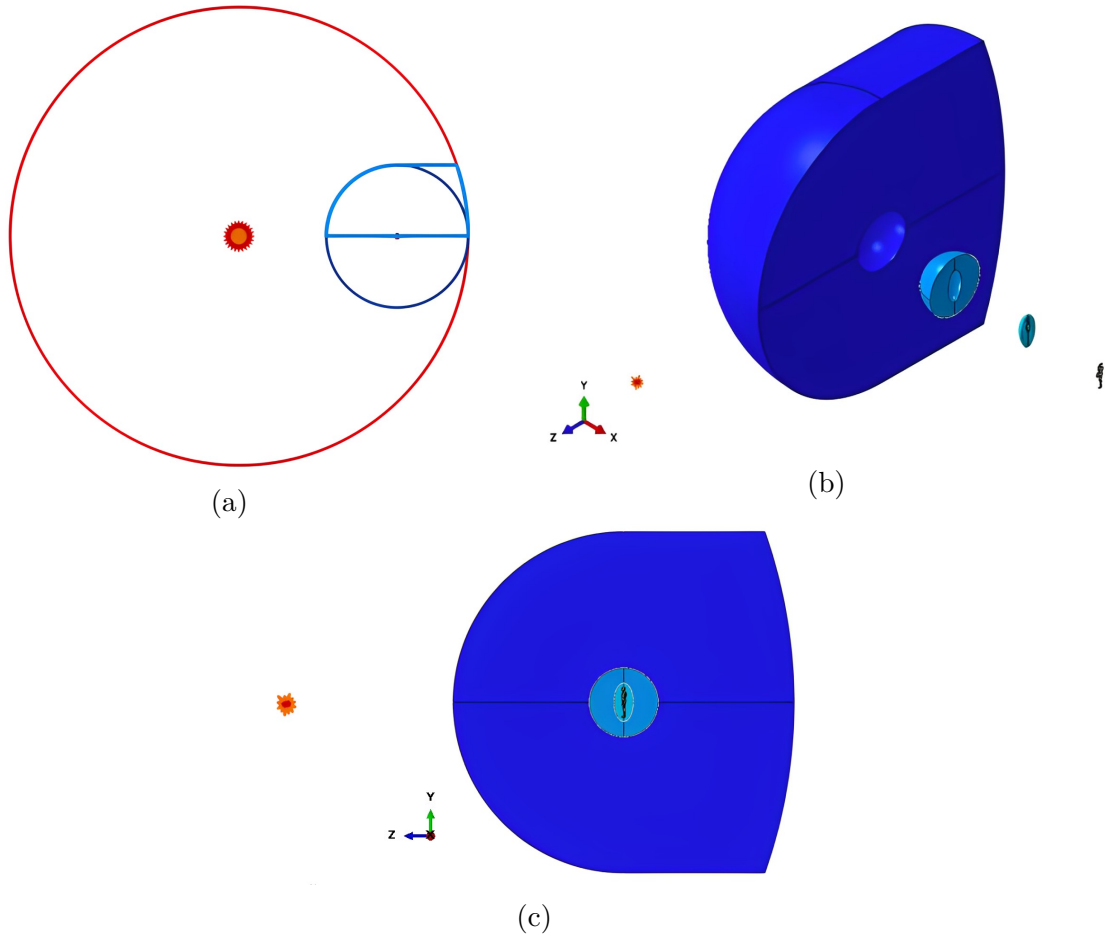
Figure 5.4: Sample UNDEX modeling paradigm illustrated using cut-aways with approximate blast location indicated: (a) Acoustic "bullet" modeling domains naturally defined from a sphere of radius 10m centered at a point on the diver with blast wave offset at 20m; (b) isometric expanded view; and (c) side view.

embedded in a sphere that is finally enclosed in the surrounding outer bullet. Such an approach for acoustic domain subdivisioning will aid the development of an acoustic mesh with variable element sizes for efficiency. Furthermore, it enables easy setup of models with different diver orientations by simply rotating the diver, ellipsoid, and inner sphere, while holding the outer bullet domain fixed. Finally, it will be possible to replace the inner ellipsoid and the modeled diver with various diver submodels (e.g., only the lungs) which then would be encapsulated in an ellipsoid of the same OML as the original ellipsoid. In such approaches,

it would not be necessary to redevelop or even remesh the largest part of the acoustic domain shown in dark blue in Figure 5.4.

5.2.2   Baseline Diver Geometry and Meshing

Initial anatomically correct geometry for a 50th percentile male was obtained from BioMedical Modeling Inc. (BMi). The review of all geometry and initial scoping on creating a baseline and improved mesh has been conducted by M4 Engineering Inc.

While all geometry has been able to be meshed individually, significant challenges had to be overcome to produce a viable mesh without poorly formed elements. Furthermore, the mesh needed to have a critical time step which was practical for explicit dynamic time simulations, as well as mesh-based defeaturing that was consistent at mating interfaces such that no significant gaps or overlaps occurred that could not be handled as part of the initial contact adjustments. As such for the initial study, only a subset of the respiratory system geometry has been used in producing the initial mesh. The modeled diver geometry includes the lungs, diaphragm, and surrounding torso, as well as a sequence of water domains. Modeling the diaphragm with solid elements requires a very small element size which ultimately results in a very large mesh size and associated computational cost. Therefore, the diaphragm is switched in this effort into a shell representation to save in mesh size while accurately capturing its bending/stretching behavior.

The current diaphragm surface (supremum) is tied to the torso mesh through shared nodes (i.e., the diaphragm is fully attached to the torso on both sides). The diver model parts are shown in Figure 5.5. In order to create an imprint of the diaphragm surface on the torso, the surrounding had to be partitioned as shown in Figure 5.6.

In order to successfully mesh the diver geometry, the virtual topology features of
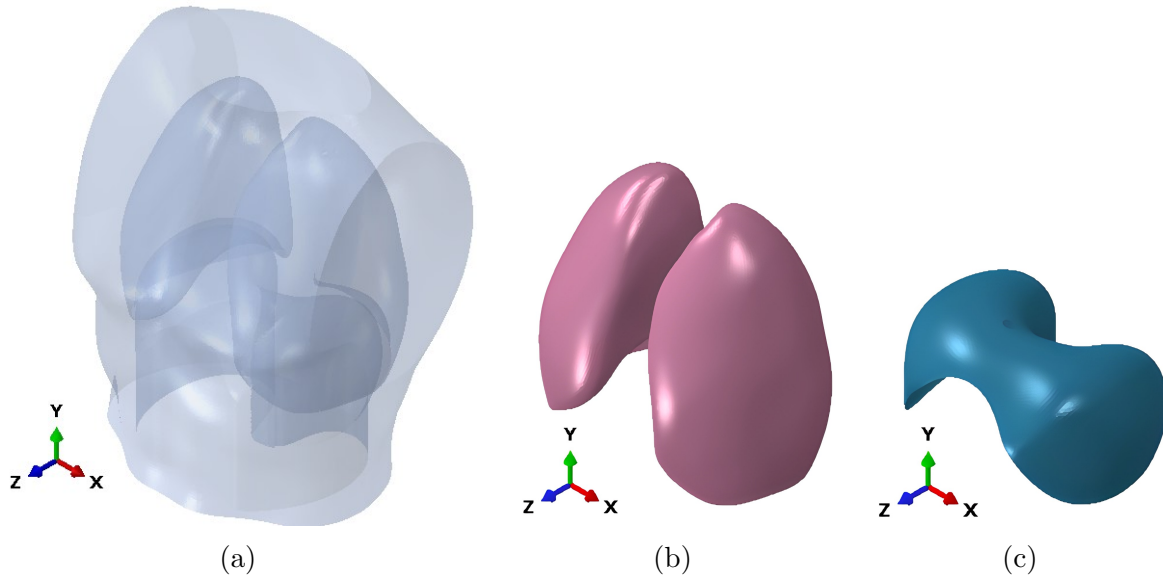
Figure 5.5: Diver model geometry: (a) torso; (b) lungs; (c) diaphragm surface.
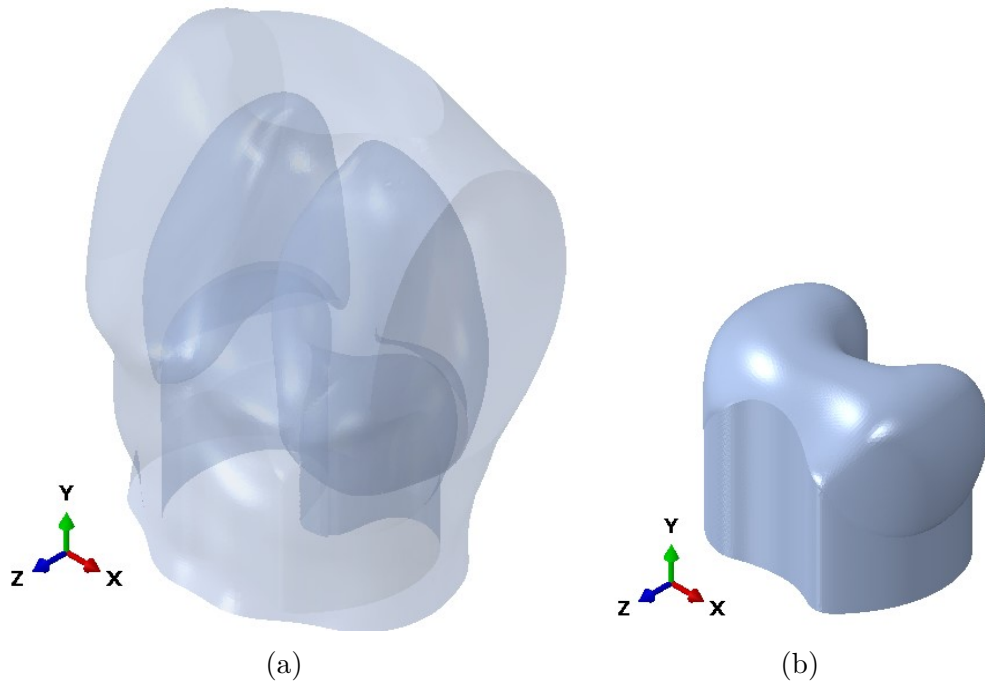
Figure 5.6: Torso partitioning: (a) torso minus abdominal cavity; (b) abdominal cavity.

Abaqus/CAE are leveraged through combining faces and subsequently releasing the unnecessary constraints associated with respecting internal edges on the meshing algorithm,
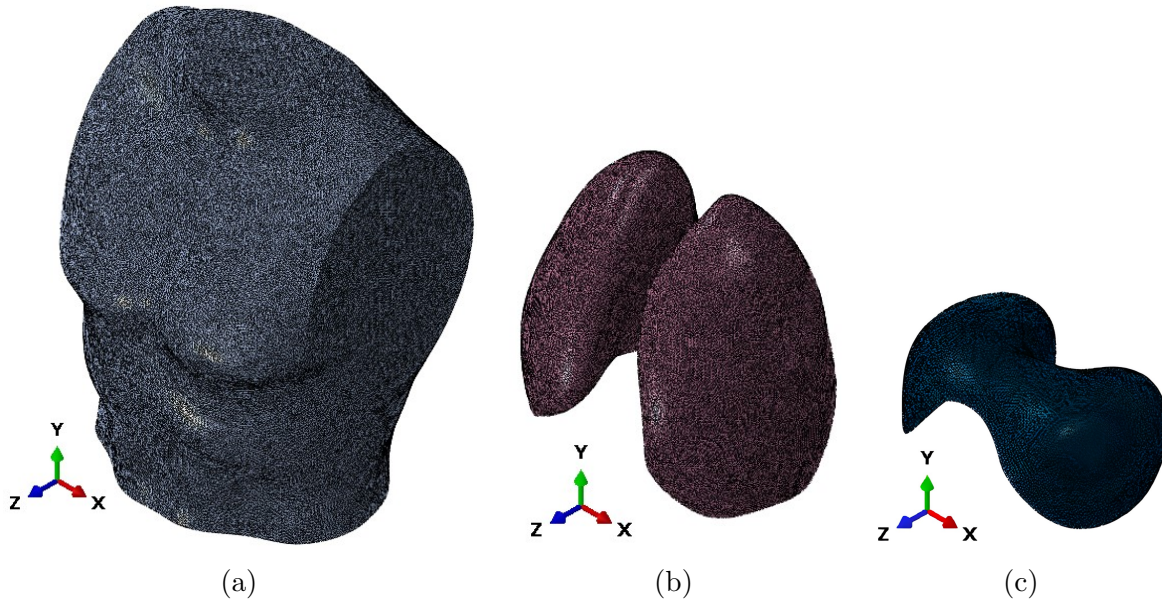
Figure 5.7: Meshed geometry: (a) torso; (b) lungs; (c) diaphragm.

while still respecting the underlying "combined" geometry. Moreover, the virtual topology operation increases the meshing options and enables improved automatic algorithmic identification. Following this meshing strategy, the obtained mesh solid and shell elements are shown in Figure 5.7, while the full mesh stats are presented in Table 5.9.

Table 5.9: Diver model (with rib cage) mesh.

Instance	Element Type	Elements	Nodes
Water	AC3D4 AC3D8R	12,650,079	10,749,929
Lungs	C3D4	689,403	134,739
Torso	C3D4	2,441,469	453,852
Diaphragm	S3R	21,161	
	Total	16,135,392	11,424,611

5.2.3 Hyperelastic Damage Parametrization and Injury Evaluation

The VUMAT damage wrapper for Abaqus/Explicit was adapted to passively monitor relevant strain measures for damage initiation and evolution, allowing post-simulation identification of critical strain values. This facilitates injury prediction in lungs under blast loading by tracking damage-relevant strains without actual damage application. The maximum value of the strain measures, up to the current time, is used to pinpoint critical regions exceeding initiation and final strain thresholds.

A diver mesh with lungs, diaphragm, and torso has been utilized for the preliminary calculation of damage initiation and final failure values for a blast scenario in which the diver and charge are horizontally separated by a distance of 20 meters at a depth of 50 meters. The water domain as depicted in Figure 5.4 is structured like a bullet to enable the application of non-reflecting/perfectly matched layer boundary conditions for the shock wave. The blast wave pressure history near the diver is taken from the digitization of the data in Fetherston *et al.* [224] for a 1 kg pentolite charge. Additional studies have been conducted by scaling this pressure history to correspond to pentolite charges of 1, 1.5, 2, 3, 4, 6, 8, 10, and 12 kg mass, all at a depth of 50 m and a stand-off of 20 m. In order to capture the hyperelastic behavior of lungs, a Yeoh model was used with the chosen material parameters obtained from SIMULIA/Isight fit given in Table 5.5.

Figure 5.8 depicts the placement of multiple chest wall nodal sensors utilized to capture the acoustic pressure impacting a diver and of the subsequent chest wall movement in response. The resulting chest wall velocities, pressures, and impulses integrated over the first half pressure-wave for 1.5 kg charge mass are given in Figure 5.9. Analysis corresponding to 1, 1.5, 2, 3, 4, 6, 8, 10, and 12 kg charge masses were conducted. Simulations considered 50 ms

of physical time for all cases. The peak pressures, maximum and average impulses applied to the chest wall, along with the resulting maximum outward chest wall velocities are given in Table 5.10. The peak pressure and impulse determined from the chest wall sensors exhibit a nearly linear relationship with the applied pentolite charge mass, as anticipated. Additionally, the maximum outward velocities of the chest wall, resulting from these conditions, also demonstrate a nearly linear relation with the charge mass.
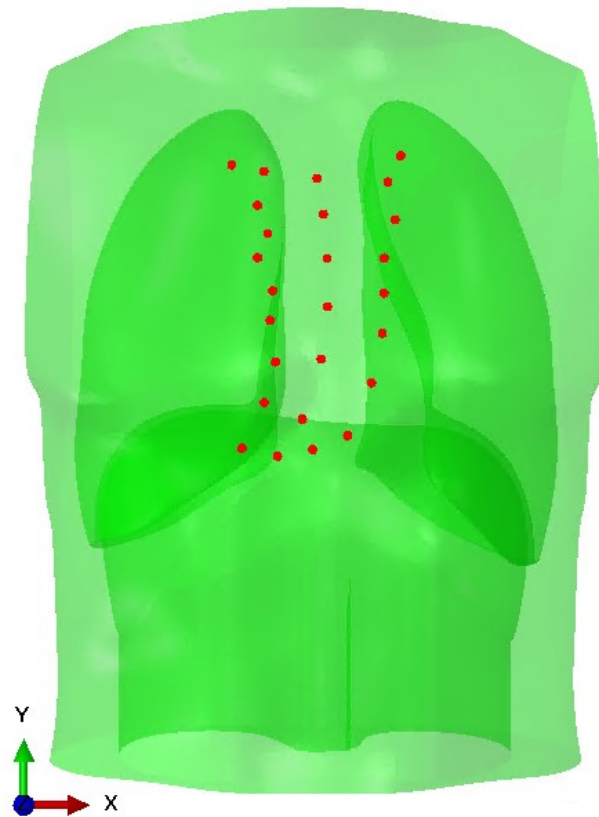
Figure 5.8: Outer chest wall nodal sensors for chest wall velocity, peak pressure, and impulse extraction.

Injury Evaluation Criteria

Assessing the potential severity of injuries sustained by divers during underwater explosions can be achieved through various established criteria. These criteria employ measures of

(a)

(b)

(c)
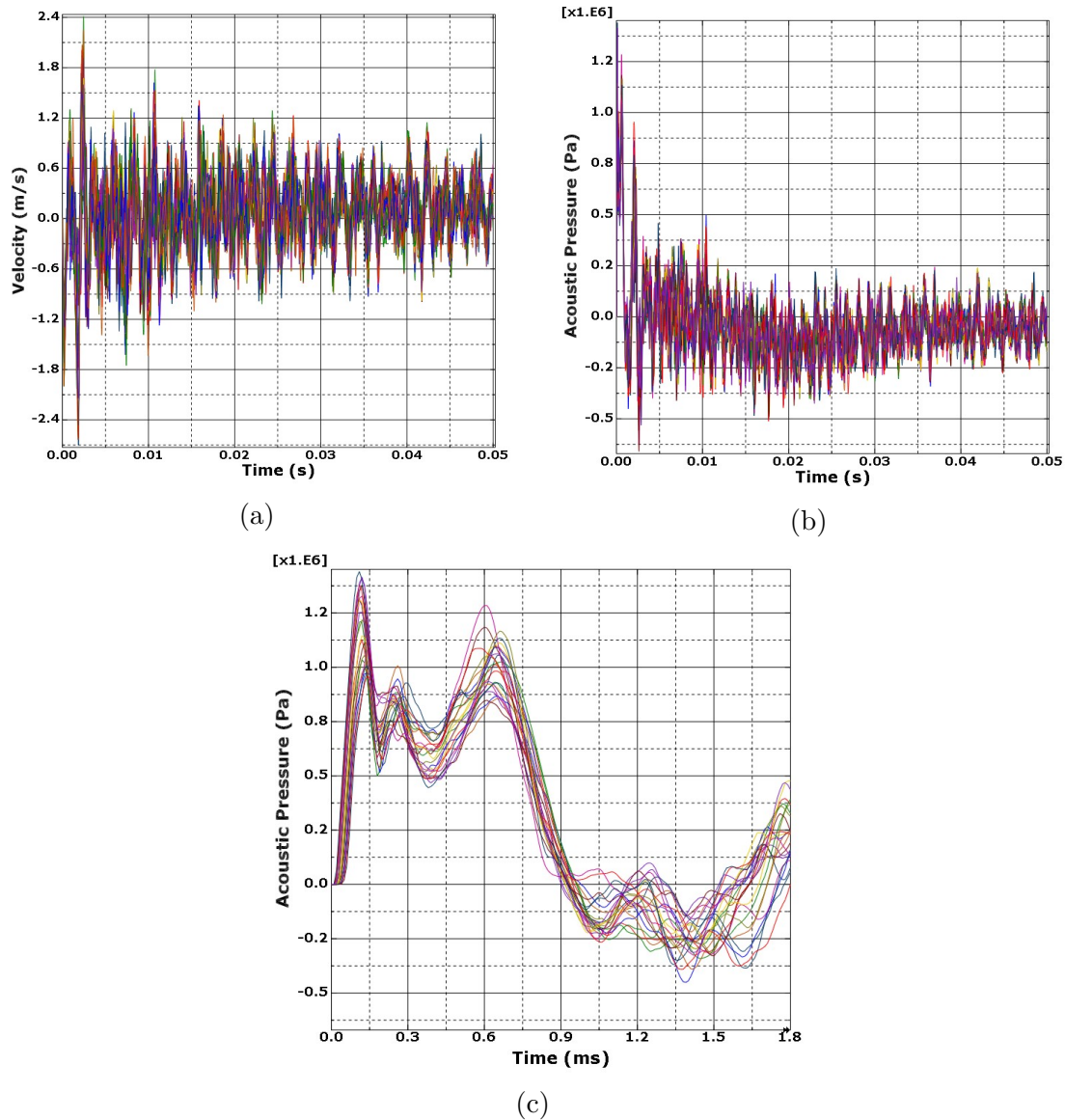
Figure 5.9: Diver outer mold line (OML) response at outer chest wall sensors for 1.5kg charge mass: (a) chest wall velocity (negative values are diver chest wall compression); (b) pressure; (c) initial pressure for impulse calculations.

both the physical forces exerted on the diver (applied loading) and the diver's physiological response to those forces. One measure used is the resultant velocity of the diver's chest wall. Table 5.11 ([225]) provides expected injury levels based on this velocity. For example, a velocity exceeding 7.5 m/s might correspond to a high risk of serious internal injuries.

Table 5.10: Imparted loading on diver as measured using chest wall nodal sensors.

Pentolite Charge Mass (kg)	Chest Wall Nodal Sensors				
	Max Outward Velocity (m/s)	Peak Pressure (psi)	Peak Pressure (kPa)	Max Impulse (Pa · s)	Avg Impulse (Pa · s)
1	1.80	139.33	960.6	438.04	416.44
1.5	2.70	208.98	1440.8	656.62	624.20
2	3.60	278.63	1921.1	874.88	831.64
3	5.39	417.95	2881.7	1310.35	1245.45
4	7.14	557.31	3842.5	1744.31	1657.72
6	10.58	835.98	5763.9	2607.59	2477.20
8	14.15	1114.79	7686.2	3462.43	3289.67
10	17.71	1393.66	9608.9	4308.61	4093.05
12	21.93	1672.55	11531.8	5145.06	4887.34

Another approach focuses on the peak overpressure experienced by the diver. The U.S. Navy Diving Manual ([226]) offers a set of criteria for underwater TNT explosions, with expected outcomes outlined in Table 5.12. For instance, a peak pressure exceeding 345 kPa suggests a possibility of lung damage. Additional criteria delve deeper into the specific details of the diver's response, considering factors beyond just peak pressure. Table 5.13 ([227]) provides an example for 5-lb TNT explosions at 100 ft depth, detailing expected effects at various distances from the blast. This table indicates, for example, temporary disorientation at a certain distance while suggesting paralysis and substantial pain closer to the explosion.

Gauging the potential severity of injuries sustained by divers exposed to underwater blasts can also be achieved by estimating the impulse i.e., force imparted to the chest over a certain time frame. Injury assessment via impulse imparted to the diver chest that accounts for both the intensity of the blast and the diver's physical characteristics can be evaluated

Table 5.11: Expected injury level based upon chest wall velocity.

Injury Level	Chest Wall Velocity (m/s)
No injury	0.0 − 3.6
Trace to slight	3.6 − 7.5
Slight to moderate	4.3 − 9.8
Moderate to extensive	7.5 − 16.9
> 50% mortality	>12.8

Table 5.12: Expected injury based upon peak pressure.

Injury Level	Peak Pressure	
	(psi)	(kPa)
Unlikely to cause injury	< 50	< 345
Likely to cause injury	50 − 500	345 − 3450
Likely to cause death or severe injury	500 − 2000	3450 − 13,800
Death certain	> 2000	> 13,800

by comparing against values computed using the following expression [228]:

$$I_{injury} = CM^{\frac{1}{3}} \left(1 + \frac{D}{10.1} \right)^{\frac{1}{6}} \tag{5.2}$$

where I_{injury} is the injury level impulse in Pa · s, C is a parameter giving the injury level, M is the diver mass in kg, and D is the depth in m. The injury level parameter reflects the expected severity of harm. Higher values correspond to more serious injuries. The diver's weight plays a role in determining the injury level they experience for a given blast. Also, lung resonance frequency increases with increasing depth, affecting the force transmitted to the diver. Based on this formula and typical diver characteristics, Table 5.14 categorizes anticipated injury levels according to the calculated impulse. For instance, an impulse exceeding 282 Pa · s indicates the onset of injuries. It is worth noting that alternative

Table 5.13: Diver response to 5-lb TNT at various ranges.

Range		Sensations	Estimated Peak Pressure		Estimated Impulse	
(ft)	(m)	**Subjective Comment**	(psi)	(MPa)	(psi · ms)	(Pa · s)
110	33.5	Sound of intense bang	160	1.1	75	516
100	30.5	Intense bang. Mild blow on chest.	175	1.2	85	585
90	27.4	Severe blow on chest.	195	1.3	95	654
80	24.4	Blow on head and torso. Body shaken. Brief paralysis of arms and legs.	220	1.5	105	720
75	22.9	Violent blow. Brief paralysis of limbs. Substantial pain for ½ to 1 hour.	240	1.65	110	760
70	21.3	Violent blow. Temporary paralysis of limbs. Substantial pain lasting several hours. Aural damage. Tongue lacerated. Mask blown off. Mild concussion.	260	1.8	115	790

impulse criteria exist. Table 5.13, for example, presents impulses expected from 5-lb TNT explosions at 100 ft depth and various distances from the blast. Thus, Table 5.14 offers additional data for understanding the potential injury risk for divers in various underwater blast scenarios.

The anticipated injury levels were assessed using the aforementioned criteria, and the outcomes are presented in Table 5.15. It is crucial to highlight that only the highest injury level from each criterion is shown, and assessments for results surpassing these top levels have been left blank. Notably, the analysis indicates that a 1 kg pentolite charge at a range of 20 meters is not anticipated to result in significant injury. In contrast, the 10 or 12 kg charge

Table 5.14: Expected injury levels from imparted impulse for a typical diver of 85.9 kg mass at a depth of 50 m.

Condition	C	Injury (Pa · s)
Onset slight lung injury	47.5	282.1
50% slight lung injury	65.8	390.8
Onset mortality	103	611.8
50% mortality	144	855.3

at the same range either meets or exceeds the highest injury level on each scale employed.

Upon careful examination of the results in Table 5.15 alongside the actual criteria detailed in Table 5.11 through Table 5.14, it becomes apparent that the expected injury scales exhibit some variation among themselves. For instance, a 2 kg charge mass is anticipated to cause only a trace to slight injury based on chest wall velocity (Table 5.11). However, when considering chest wall impulse (Table 5.14), this same charge mass poses a risk of over 50% mortality. This highlights the potential for conflicting predictions depending on the criteria used. Thus, it underscores the importance of considering multiple evaluation methods when assessing diver injury risk. Relying solely on one scale might underestimate or overestimate the damage parameters and thus the injury evaluation. These correlations will be improved by including other organs like skin, bones, etc., in the diver model. It can also be improved by considering more sophisticated material models for representing the diver's bones, skin, and tissues.

Table 5.15 offers valuable insights into potential lung damage caused by underwater blast exposure, categorized by various levels of injury severity. These levels of expected injury were correlated to incurred damage and failure for chosen thresholds and representative contour plots are shown herein. In addition to plotting the lung surface results, cut sections for internal views are given with the cuts as shown in Figure 5.10. For brevity, only the figures

Table 5.15: Expected injury levels for the diver as a function of pentolite charge mass.

Pentolite Charge Mass (kg)	Chest Wall Velocity	Chest Wall Peak Pressure		Chest Wall Impulse	
	Table 5.11	Table 5.12	Table 5.13	Table 5.13	Table 5.14
1	No injury	Injury	Intense bang	Intense bang	50% Slight lung injury
1.5	No injury	Injury	Blow, brief paralysis	Severe blow on chest	Onset mortality
2	Trace/slight injury	Injury	Violent blow, aural damage, temp limb paralysis, mild concussion	Violent blow, aural damage, temp limb paralysis, mild concussion	50% Mortality
3	Trace/slight injury	Injury			
4	Trace/slight injury	Severe injury or death			
6	Moderate/ extensive injury	Severe injury or death			
8	Moderate/ extensive injury	Severe injury or death			
10	>50% Mortality	Severe injury or death			
12	>50% Mortality	Severe injury or death			

corresponding to damage initiation and final failure from von Mises strain distribution are presented. Similar distribution characteristics apply for assessing damage through volumetric
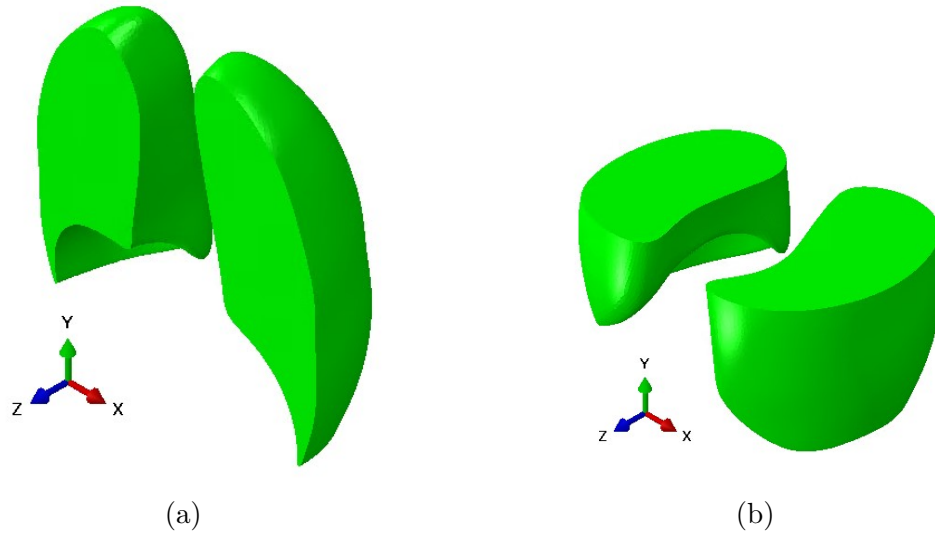
Figure 5.10: Cut view of lungs presented in (c) and (f) of Figure 5.11, Figure 5.12, and Figure 5.13: (a) z-plane cut; (b) y-plane cut.

and max principal strains.

In order to delve deeper and understand the underlying extent of lung tissue affected at each level, and to calculate damage initiation and failure strain values the following interpretation is applied:

1. **No Injury:** This corresponds to the explosion from lower charge masses. In the absence of predicted injury, it is assumed that blast forces have not initiated any damage within the lung tissue. No regions, whether on the surface or deeper inside, have experienced edema or stiffness reduction.

2. **Trace or Slight Injury:** At this injury level, initial damage within the lung's surface layers will be assumed. Edema is present on the outer portions, but the majority of the inner lung tissue will be assumed to remain largely intact and functional. This aligns with the trace to slight descriptor, suggesting minimal and localized harm. The upper limit of what is considered as slight injury is provided in Figure 5.11. The figure 5.11 also provides a color scale for damage visualization.
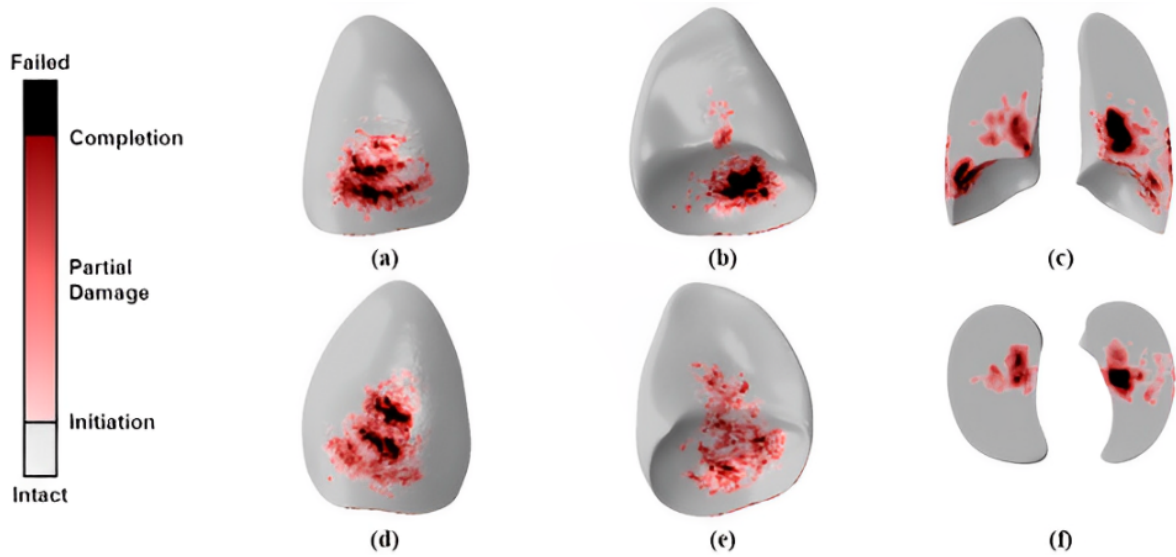
Figure 5.11: Strain-based damage color coding for sample upper bound for slight lung injury: (a) right lung (lateral); (b) right lung (medial); (c) front view cut; (d) left lung (lateral); (e) left lung (medial); (f) top view cut.
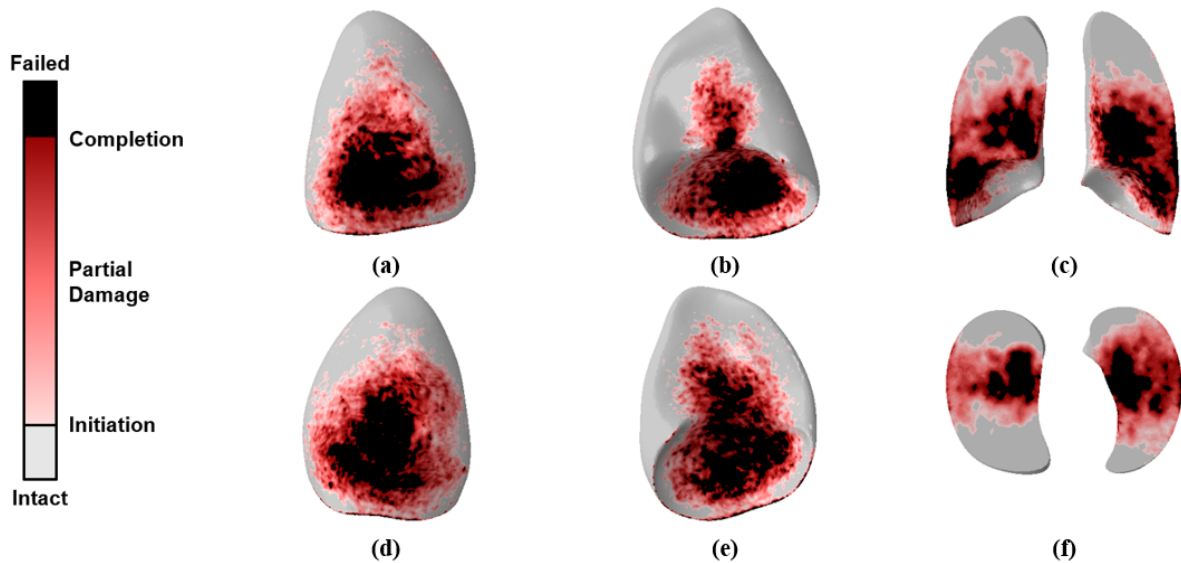
Figure 5.12: Strain-based damage color coding for sample upper bound for extensive lung injury: (a) right lung (lateral); (b) right lung (medial); (c) front view cut; (d) left lung (lateral); (e) left lung (medial); (f) top view cut.
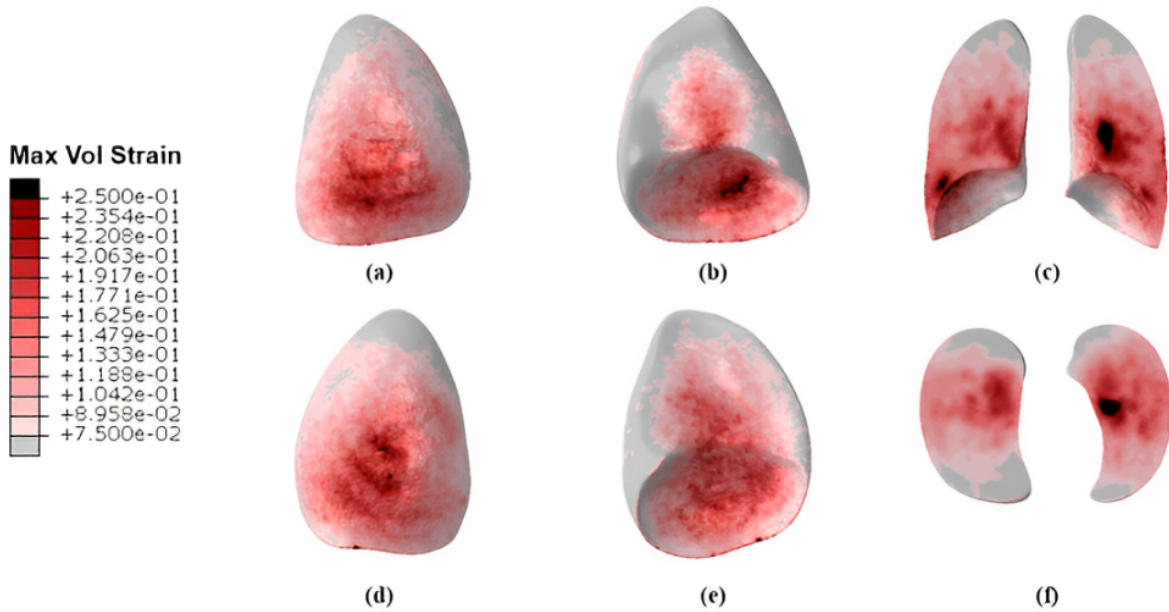
Figure 5.13: Volumetric strain-based damage for diver exposed to 2 kg pentolite charge at 20 m stand-off and 50 m depth: (a) right lung (lateral); (b) right lung (medial); (c) front view cut; (d) left lung (lateral); (e) left lung (medial); (f) top view cut.

3. **Extensive Injury:** Significant damage encompassing both the outer and inner layers of the lung is assumed for this case. The blast forces are strong enough to cause widespread tearing of membranes and vessel walls, contusions, and hemorrhaging throughout the tissue, impacting a substantial portion of the lung's structure and function. A serious threat to vital lung function is assumed at this level. The upper limit of what is considered as extensive injury is shown in Figure 5.12.

4. **50% Mortality or Death:** This represents the most severe category, suggesting a high risk of potentially fatal consequences. In this scenario, nearly all parts of the lung have reached at least the initial damage strain value, with a significant portion experiencing complete structural failure. This extensive and severe damage significantly compromises the lung's ability to function, leading to a high likelihood of respiratory failure and potentially death.

Based on the following assumptions, Table 5.16 presents the obtained damage parameters for volumetric, deviatoric, and max principal strain. Application of the damage color scale for a diver exposed to a 2 kg Pentolite charge at 20 m stand-off with the diver and charge both at 50 m depth is shown in Figure 5.13 for a volumetric strain-based damage approach. Discrepancies in injury evaluation across different criteria result in variations in the reported values for damage initiation and failure. While Table 5.12 provides a broader picture of blast wave pressures and potential lung damage across a wider range (345 kPa to 13800 kPa), its injury descriptions are categorized into four general levels. Due to the lack of detailed description, analysis from 3 kg and 4 kg charge mass, where the transition from injury to severe injury happens, were utilized to deduce the damage parameters while maintaining the precision of vague injury indicators across the other charge masses. In contrast, Table 5.13 focuses on a specific pressure range (1100 kPa to 1800 kPa) and offers a more detailed injury description, enabling a more precise evaluation of lung damage within this narrower range. Damage parameters derived from both impulse and peak pressure criteria in Table 5.13 exhibit negligible difference, as evidenced by Table 5.16. This is expected as both impulse and peak pressure have a linear variation with charge mass, and the injury table has a similar rise in these values for the corresponding progression of injury levels. The relatively wider impulse range covered in Table 5.14 compared to Table 5.13, and variations in the predicted onset of injury between them contribute to the discrepancies in values derived using the chest wall impulse criteria.

It is important to note that the above interpretation and the visualization-based approach provide a simplified framework for understanding the damage parameters and calculating them. Inherent approximations and the potential for error exist within this approach, therefore a transition to a more robust numerical methodology is indicated for future work. This shift will enable the calculation of damage parameters with greater accuracy.

Table 5.16: Damage strain initiation and final failure values utilizing available injury assessment tables.

Damage Strain Measure		Chest Wall Velocity	Chest Wall Peak Pressure		Chest Wall Impulse	
		Table 5.11	Table 5.12	Table 5.13	Table 5.13	Table 5.14
Volumetric Only	Initiation	0.3	0.16	0.125	0.115	0.075
	Final	0.5	0.4	0.3	0.3	0.25
Deviatoric Only	Initiation	2	0.45	0.3	0.265	0.175
	Final	3.5	1.75	0.8	0.8	0.45
Max Principal	Initiation	0.6	0.35	0.28	0.25	0.125
	Final	0.75	0.65	0.45	0.45	0.35

The primary driver for quantifying damage parameters will be the assumed quantitative relationship between different injury levels and the corresponding percentage of lung tissue affected, as outlined in Table 5.17. Additionally, visualization-based checks will still be employed to understand the spatial distribution achieved and provide valuable insights. Several crucial considerations must be taken into account, as outlined below.

1. Determining the correlation between specific injury descriptions and the extent or percentage of lung tissue damage is a complex challenge without a straightforward solution, thus necessitating careful assumptions.

2. Even in the case of severe injuries, damage can manifest as either widespread, diffuse harm affecting a significant portion of the lung's volume or result from highly localized, severe damage in a smaller region, yet crucially impacting vital areas such as major blood vessels.

3. Different types of injuries, such as alveolar air sac destruction, interstitial fibrosis, or

Table 5.17: Correlation between injury level descriptions and percentage of lung tissue damage.

Injury Descriptor	% Region Above Damage Initiation Strain	% Region Above Final Failure Strain
No Injury. Unlikely to cause injury. Sound of intense bang.	< 1	< 0.1
Trace to slight. Intense bang. Mild blow on chest. Onset slight lung injury	3-10	1-3
Slight to moderate. Likely to cause injury. Severe blow on chest. 50% slight lung injury	7.5-20	3-5
Moderate to extensive, Blow on head and torso. Body shaken. Brief paralysis of arms and legs. Onset mortality	15-40	5-10
Violent blow. Brief paralysis of limbs. Substantial pain for ½ to 1 hour.	25-50	7.5-15
50% mortality. Likely to cause death or severe injury. Violent blow. Temporary paralysis of limbs. Substantial pain lasting several hours. Aural damage. Tongue lacerated. Mask blown off. Mild concussion.	40-70	15-25
>50% mortality. Death certain	>65	>25

vascular damage, can have varying impacts on lung function and survival.

4. Underlying health conditions and pre-existing lung capacity can significantly influence the impact of damage.

In conclusion, any injury descriptor cannot be directly translated to a specific percentage of lung tissue damage. The actual nature and extent of lung damage caused by underwater blasts can be complex and vary depending on the specific circumstances of the exposure. Other factors beyond peak overpressure, chest wall velocity, and impulse, such as the diver's individual characteristics and pre-existing medical conditions, can also influence the severity

of lung injuries. At present, the interpretation outlined in Table 5.17 serves as a tool for further analysis and discussion, not a definitive diagnosis or prediction of individual outcomes. Nevertheless, the chosen modeling approach will still provide meaningful data for blast event planning and post-accident forensics.

In sponsored future work outside of the scope of this dissertation, the analysis will be expanded to encompass additional anatomical structures, including ribs, costal cartilages, trachea, partial bronchial tubes, and a simplified spine. Enhanced material models for organs and bones will be used, including hyperviscoelasticity for the lungs. Moreover, we will adapt our assessment of different injury outcomes to account for variations in diver orientation, thereby basing it on damage in each lung (right and left) separately. By broadening our scope and refining our criteria, the aim is to enhance the accuracy and applicability of our modeling approach, ultimately contributing to a more comprehensive understanding of the effects of underwater blasts on lung physiology and aiding in the development of effective injury mitigation strategies.

Chapter 6

Summary and Outlook

The thesis aimed at developing a four-noded rectangular immersed-interface element circumventing the need for interface-fitted mesh for finite element analysis, and mesh morphing or re-meshing for shape optimization. Additional applications involved evolving the boundaries within the unit cell to generate effective materials consisting of optimal periodic microstructure. Finally, the desired hyperelastic and hyperviscoelastic models with damage were implemented as Abaqus/Explicit VUMAT user subroutines for diver UNDEX simulations. The hyperelastic model was parametrized with the associated damage initiation and final failure.

6.1 Shape Optimization Using IIFEM

This study introduced a gradient-based shape optimization formulation based on the Immersed Interface Finite Element Method (IIFEM), offering significant advantages in the context of structural shape optimization. The IIFEM brings forth two major benefits. Firstly, it effectively captures weak discontinuities along an interface within an element, eliminating the need for an interface-fitted mesh in finite element analysis. Secondly, it permits the utilization of a simple structured mesh during the optimization process, reducing computational complexity and costs associated with mesh movement or remeshing. Additionally, it eliminates mesh distortion issues encountered in traditional Lagrangian

approaches for shape optimization.

The study employs a four-noded rectangular immersed-interface element, utilizing a fixed structured grid where the interface can reside within an element. The analysis problem is solved using a non-conformal, Petrov-Galerkin (ncPG) formulation. The validation of the ncPG-IIFEM is demonstrated through a bi-material patch test. Subsequent analysis of a bi-material problem with a uniform Cartesian mesh reveals convergence and error analysis results, demonstrating comparable or slightly improved convergence rates compared to interface-fitted Finite Element Methods (FEM). The notable reduction in displacement and stress errors is attributed to the uniformity of the mesh, enhancing the accuracy of solutions. The improved condition number of the global stiffness matrix further attests to the efficiency of ncPG-IIFEM, which reduces meshing costs without compromising solution accuracy. Analytical design sensitivities are utilized to compute structural responses to changes in shape design variables, crucial for performing gradient-based shape optimization. Fourier-like representations parametrize the design space, with recommendations for enrichments in specific cases. The method's effectiveness is verified through benchmark problems, and three case studies showcase its capabilities in structural shape optimization without the need for mesh movement or remeshing.

6.2 Material Design Using IIFEM

Continuing the application of the ncPG-IIFEM, this study introduces a level-set-based topological shape optimization methodology for the design of metamaterials. The implementation incorporates compactly supported Wendland functions for level set representation, effectively minimizing the computational costs associated with gradient calculations. This choice ensures smooth boundaries and clear material interfaces.

Demonstrative examples, including compliance minimization of a cantilever beam and a Michell structure, highlight the method's potential. In the context of metamaterial design, the effectiveness of the proposed method is demonstrated through numerical examples featuring maximization of bulk and shear moduli for prescribed volumetric and shear deformations, respectively with and without material symmetry constraints, and microstructures with prescribed Poisson's ratios, including negative values. A range of new and intriguing microstructured materials exhibiting specific mechanical properties are achieved. The application of periodic boundary conditions for homogenization, facilitated by the uniform Cartesian mesh in IIFEM, ensures accurate prediction of effective elastic properties, even with a high volume fraction of voids. Calculation of the effective stiffness tensor through edge nodal forces simplifies sensitivity analysis for material interface evolution. The proposed approach ensures smooth material interfaces, accurate FEM which maintains fidelity even with a large number of voids or inclusions, and circumvents material islands and numerical artifacts by employing appropriate level set function parameter choices. Thus, in terms of numerical implementations and the resulting optimized designs, several advantageous aspects of the proposed design formulation for analysis and optimization suggest that it can be considered an effective method suited for the topological shape design of cellular metamaterials.

6.3 Material Modeling and Parametrization for UNDEX Simulations

The exploration of hyperelastic and hyperviscoelastic models for simulating the response of biological tissues to underwater blast events reveals the challenges associated with achieving predictive accuracy and managing the requisite number of parameters. In this study, a

material model was chosen such that it not only accurately reproduces experimental data across various loading modes, but it is also flexible enough to encompass simpler models within it, with a minimized number of parameters for practical implementation.

The study adopts alternative methods for parametrization, bypassing direct experimental tests on biological materials. Representative material properties are sourced from systematically collected literature, incorporating both empirically derived data and practical values suitable for simulations. The quantification of damage parameters relies on assumed quantitative relationships between injury levels and the percentage of lung tissue affected. Correlating specific injury descriptions with the extent of damage is complex and requires careful assumptions. The diverse manifestations of severe injuries, varying impacts of different injury types on lung function, and the influence of underlying health conditions further underscore the complexity of the modeling process. A visualization-based approach, while providing a simplified framework for understanding damage parameters is user-specific and error-prone, and thus a shift to a more robust numerical methodology for greater accuracy in calculating damage parameters will be made in future studies.

Overall, this study highlights the challenges and complexities involved in simulating the response of biological tissues to underwater blast events. With various material models and damage quantification methods being explored, the groundwork for developing more accurate and personalized simulations in the future has been laid. The current interpretation provided for damage parametrization serves as a valuable tool for analysis and discussion, despite its limitations as a definitive diagnostic or predictive tool for individual outcomes. Although challenges remain, this study lays the foundation for future studies in blast injury modeling. Future directions involve a transition to a more accurate numerical methodology, addressing complexities in injury correlation, and refining the modeling approach for enhanced predictive capabilities in understanding and mitigating the impact of underwater

blast events.

6.4 Future Directions in IIFEM and Its Applications

Future studies can leverage the IIFEM expanding its applicability, robustness, and practical relevance in the design and optimization of structures and materials. The following avenues can be explored:

- **Extension to Three-Dimensional (3D) Geometries**: Investigate the applicability and efficiency of the developed ncPG-IIFEM in handling three-dimensional geometries. Expanding the methodology to 3D will address the challenges associated with more complex structures and enhance its versatility for real-world engineering applications.

- **Incorporate Advanced Material Models**: Develop immersed formulations that handle complex material properties like nonlinear elasticity, or viscoelasticity for broader design applications.

- **Multi-Physics Integration**: Extend the ncPG-IIFEM to accommodate multi-physics problems, integrating capabilities for analyzing coupled phenomena such as fluid-structure interactions, acoustics, heat transfer, or electromagnetics. This expansion would enhance the methodology's utility across a broader spectrum of applications. It would also facilitate the design of metamaterials with tailored functionalities across diverse disciplines.

- **Advanced Optimization Objectives**: Explore more diverse optimization objectives within the framework of IIFEM, such as energy absorption, frequency tuning, or dynamic response control. This could lead to the creation of structures or materials optimized for specific engineering applications.

- **Manufacturing Constraints**: Incorporate manufacturing constraints within the IIFEM framework, considering factors like additive manufacturing limitations, cost constraints, stress constraints, and ease of fabrication. This would enhance the practical applicability of the methodology within real-world manufacturing scenarios.

- **Uncertainty Quantification**: Investigate the impact of uncertainties, both in material properties and geometry, on the optimized designs within the IIFEM framework. Implement uncertainty quantification techniques in IIFEM to assess the robustness of designs under variations.

6.5 Future Directions on Material Modeling and Parametrization for Diver UNDEX Simulations

1. **Material Modeling**:

   (a) **Enhanced material models**: Hyperviscoelasticity, poroelasticity or equation of state models can be used to capture the complex behavior of lung tissues under various loading conditions.

   (b) **Incorporate microstructural information**: Integrate microstructural features of biological tissues (e.g., cell structure, fiber network) into the material models for improved accuracy.

   (c) **Multiscale modeling**: Employ multiscale modeling techniques that bridge the gap between micro/meso models with alveoli sacs and lung continuum response for a deeper understanding of blast-induced damage mechanisms.

2. **Damage Quantification**:

(a) **Image-based damage assessment**: Utilize medical imaging techniques (e.g., CT scans, MRIs) to validate and refine the visualization-based damage quantification approach.

(b) **Functional impact modeling**: Link the predicted damage to functional impairments on lung mechanics and gas exchange for a more comprehensive understanding of injury severity.

3. **Simulation Enhancements**:

(a) **Multi-organ simulations**: Include other organs potentially affected by blast waves (e.g., brain, ears) for a holistic assessment of injury risk.

4. **Validation and Application**:

(a) **Experimental validation with surrogates**: Utilize tissue-mimicking materials or animal models to experimentally validate the material models and damage quantification methods.

(b) **Personalized simulations**: Integrate individual diver characteristics into the simulations for personalized injury risk assessment and mitigation strategies.

(c) **Develop design optimization tools**: Use the simulation framework to optimize diving equipment and procedures to minimize blast wave impact and injury risk.

With these advancements, improved underwater blast safety is aimed for, and personalized risk assessment and mitigation strategies for divers may potentially be provided.

List of Publications

Srivatsa Bhat Kaudur and Mayuresh J. Patil, "Material Design using Topology Optimization with Immersed Interface Finite Element Method." International Journal of Mechanical Sciences, 2024. (Under Review)

Srivatsa Bhat Kaudur and Mayuresh J. Patil, "Shape Optimization using Immersed Interface Finite Element Method." in International Journal of Numerical Methods in Engineering, 123, 5907–5936, 2022.

Srivatsa Bhat Kaudur and Mayuresh J. Patil, "Shape Optimization using Immersed Interface Finite Element Method" in U.S. National Congress on Computational Mechanics, July 2021.

Daniel C. Hammerand, **Srivatsa Bhat Kaudur**, Timothy Cuatt, Brendan Arnold, Rakesh K. Kapania, Pamela VandeVord, "Coupled Acoustic Shock Modeling of Diver Lung UNDEX Response" in Military Health System Research Symposium, Aug 2023.

Bibliography

[1] Ted Belytschko, Wing Kam Liu, Brian Moran, and Khalil Elkhodary. *Nonlinear finite elements for continua and structures*. John wiley & sons, 2013.

[2] Olgierd Cecil Zienkiewicz and Robert Leroy Taylor. *The finite element method: solid mechanics*, volume 2. Butterworth-heinemann, 2000.

[3] Ted Belytschko, Yury Krongauz, Daniel Organ, Mark Fleming, and Petr Krysl. Meshless methods: an overview and recent developments. *Computer methods in applied mechanics and engineering*, 139(1):3–47, 1996.

[4] Thomas-Peter Fries, Hermann G Matthies, et al. Classification and overview of meshfree methods. *Department of Mathematics and Computer Science, Technical University of Braunschweig*, 2003.

[5] Thomas-Peter Fries and Ted Belytschko. The intrinsic xfem: a method for arbitrary discontinuities without additional unknowns. *International journal for numerical methods in engineering*, 68(13):1358–1385, 2006.

[6] Ivo Babuška and Jens M Melenk. The partition of unity method. *International journal for numerical methods in engineering*, 40(4):727–758, 1997.

[7] Ivo Babuška, Uday Banerjee, and John E Osborn. Survey of meshless and generalized finite element methods: a unified approach. *Acta Numerica*, 12:1–125, 2003.

[8] Jens M Melenk and Ivo Babuška. The partition of unity finite element method: basic theory and applications. *Research Report/Seminar für Angewandte Mathematik*, 1996.

[9] Theofanis Strouboulis, Ivo Babuška, and Kevin Copps. The design and analysis of the generalized finite element method. *Computer methods in applied mechanics and engineering*, 181(1-3):43–69, 2000.

[10] Theofanis Strouboulis, Kevin Copps, and Ivo Babuška. The generalized finite element method. *Computer methods in applied mechanics and engineering*, 190(32-33):4081–4193, 2001.

[11] Ted Belytschko, Nicolas Moës, Shuji Usui, and Chandu Parimi. Arbitrary discontinuities in finite elements. *International Journal for Numerical Methods in Engineering*, 50(4):993–1013, 2001.

[12] Nicolas Moës, John Dolbow, and Ted Belytschko. A finite element method for crack growth without remeshing. *International journal for numerical methods in engineering*, 46(1):131–150, 1999.

[13] Charles S Peskin. Numerical analysis of blood flow in the heart. *Journal of computational physics*, 25(3):220–252, 1977.

[14] Randall J LeVeque and Zhilin Li. The immersed interface method for elliptic equations with discontinuous coefficients and singular sources. *SIAM Journal on Numerical Analysis*, 31(4):1019–1044, 1994.

[15] Sining Yu, Yongcheng Zhou, and Guo-Wei Wei. Matched interface and boundary (mib) method for elliptic problems with sharp-edged interfaces. *Journal of Computational Physics*, 224(2):729–756, 2007.

[16] David M Ingram, Derek M Causon, and Clive G Mingham. Developments in cartesian cut cell methods. *Mathematics and Computers in Simulation*, 61(3-6):561–572, 2003.

[17] Marsha Berger and Michael Aftosmis. Aspects (and aspect ratios) of cartesian mesh methods. In *Sixteenth International Conference on Numerical Methods in Fluid Dynamics*, pages 1–12. Springer, 1998.

[18] Holavanahalli S Udaykumar, Wei Shyy, and Madhukar M Rao. Elafint: a mixed eulerian–lagrangian method for fluid flows with complex and moving boundaries. *International journal for numerical methods in fluids*, 22(8):691–712, 1996.

[19] Rajat Mittal and Gianluca Iaccarino. Immersed boundary methods. *Annu. Rev. Fluid Mech.*, 37:239–261, 2005.

[20] Ivo Babuška. The finite element method for elliptic equations with discontinuous coefficients. *Computing*, 5(3):207–213, 1970.

[21] Thomas-Peter Fries and Ted Belytschko. The extended/generalized finite element method: an overview of the method and its applications. *International journal for numerical methods in engineering*, 84(3):253–304, 2010.

[22] Ivo Babuška and Uday Banerjee. Stable generalized finite element method (sgfem). *Computer methods in applied mechanics and engineering*, 201:91–111, 2012.

[23] Soheil Soghrati, Alejandro M Aragón, C Armando Duarte, and Philippe H Geubelle. An interface-enriched generalized fem for problems with discontinuous gradient fields. *International Journal for Numerical Methods in Engineering*, 89(8):991–1008, 2012.

[24] Soheil Soghrati. Hierarchical interface-enriched finite element method: an automated technique for mesh-independent simulations. *Journal of Computational Physics*, 275: 41–52, 2014.

[25] Erik Burman, Susanne Claus, Peter Hansbo, Mats G Larson, and André Massing.

Cutfem: discretizing geometry and partial differential equations. *International Journal for Numerical Methods in Engineering*, 104(7):472–501, 2015.

[26] Zhilin Li. A note on immersed interface method for three-dimensional elliptic equations. *Computers & Mathematics with Applications*, 31(3):9–17, 1996.

[27] Zhilin Li. The immersed interface method using a finite element formulation. *Applied Numerical Mathematics*, 27(3):253–267, 1998.

[28] Zhilin Li, Tao Lin, and Xiaohui Wu. New cartesian grid methods for interface problems using the finite element formulation. *Numerische Mathematik*, 96(1):61–98, 2003.

[29] Slimane Adjerid and Tao Lin. A p-th degree immersed finite element for boundary value problems with discontinuous coefficients. *Applied Numerical Mathematics*, 59(6): 1303–1321, 2009.

[30] Zhilin Li and Xingzhou Yang. An immersed finite element method for elasticity equations with interfaces. *Contemporary Mathematics*, 383:285–298, 2005.

[31] Tao Lin, Dongwoo Sheen, and Xu Zhang. A locking-free immersed finite element method for planar elasticity interface problems. *Journal of Computational Physics*, 247:228–247, 2013.

[32] Yan Gong and Zhilin Li. Immersed interface finite element methods for elasticity interface problems with non-homogeneous jump conditions. *Numer. Math. Theory Methods Appl*, 3(1):23–39, 2010.

[33] Tao Lin and Xu Zhang. Linear and bilinear immersed finite elements for planar elasticity interface problems. *Journal of Computational and Applied Mathematics*, 236(18):4681–4699, 2012.

[34] Tao Lin, Yanping Lin, Robert Rogers, and M Lynne Ryan. A rectangular immersed finite element space for interface problems. *Scientific computing and applications (Kananaskis, AB, 2000)*, 7:107–114, 2000.

[35] Xiaoming He, Tao Lin, and Yanping Lin. Approximation capability of a bilinear immersed finite element space. *Numerical Methods for Partial Differential Equations: An International Journal*, 24(5):1265–1300, 2008.

[36] Xiaoming He, Tao Lin, Yanping Lin, and Xu Zhang. Immersed finite element methods for parabolic equations with moving interface. *Numerical Methods for Partial Differential Equations*, 29(2):619–646, 2013.

[37] Tao Lin, Yanping Lin, and Xu Zhang. A method of lines based on immersed finite elements for parabolic moving interface problems. *Advances in Applied Mathematics and Mechanics*, 5(4):548–568, 2013.

[38] Tao Lin, Yanping Lin, and Xu Zhang. Partially penalized immersed finite element methods for elliptic interface problems. *SIAM Journal on Numerical Analysis*, 53(2): 1121–1144, 2015.

[39] Peiqi Huang and Zhilin Li. Partially penalized ife methods and convergence analysis for elasticity interface problems. *Journal of Computational and Applied Mathematics*, 382:113059, 2021.

[40] Ruchi Guo, Tao Lin, and Yanping Lin. Approximation capabilities of immersed finite element spaces for elasticity interface problems. *Numerical Methods for Partial Differential Equations*, 35(3):1243–1268, 2019.

[41] Liqun Wang, Songming Hou, Liwei Shi, and James Solow. A numerical method for

solving elasticity equations with interface involving multi-domains and triple junction points. *Applied Mathematics and Computation*, 251:615–625, 2015.

[42] Yuan Chen, Songming Hou, and Xu Zhang. A bilinear partially penalized immersed finite element method for elliptic interface problems with multi-domain and triple-junction points. *Results in Applied Mathematics*, 8:100100, 2020.

[43] Tao Lin, Dongwoo Sheen, and Xu Zhang. A nonconforming immersed finite element method for elliptic interface problems. *Journal of Scientific Computing*, 79(1):442–463, 2019.

[44] Zhangxin Chen and Peter Oswald. Multigrid and multilevel methods for nonconforming q_1 elements. *Mathematics of computation*, 67(222):667–693, 1998.

[45] Peter Bastian and Christian Engwer. An unfitted finite element method using discontinuous galerkin. *International journal for numerical methods in engineering*, 79(12):1557–1576, 2009.

[46] Xu-Dong Liu, Ronald P Fedkiw, and Myungjoo Kang. A boundary condition capturing method for poisson's equation on irregular domains. *Journal of computational Physics*, 160(1):151–178, 2000.

[47] Songming Hou and Xu-Dong Liu. A numerical method for solving variable coefficient elliptic equation with interfaces. *Journal of Computational Physics*, 202(2):411–445, 2005.

[48] Songming Hou, Peng Song, Liqun Wang, and Hongkai Zhao. A weak formulation for solving elliptic interface problems without body fitted grid. *Journal of Computational Physics*, 249:80–95, 2013.

[49] Songming Hou, Zhilin Li, Liqun Wang, and Wei Wang. A numerical method for solving elasticity equations with interfaces. *Communications in computational physics*, 12(2): 595, 2012.

[50] Mayuresh J Patil. Immersed-interface finite element method based on a nonconformal petrov–galerkin formulation. *International Journal for Numerical Methods in Engineering*, 2021.

[51] Bruce M Irons and Abdur Razzaque. Experience with the patch test for convergence of finite elements. In *The mathematical foundations of the finite element method with applications to partial differential equations*, pages 557–587. Elsevier, 1972.

[52] OC Zienkiewicz and Richard Lawrence Taylor. The finite element patch test revisited a computer test for convergence, validation and error estimates. *Computer methods in applied mechanics and engineering*, 149(1-4):223–254, 1997.

[53] Ming Wang. On the necessity and sufficiency of the patch test for convergence of nonconforming finite elements. *SIAM journal on numerical analysis*, 39(2):363–384, 2001.

[54] Do Y Kwak, Sangwon Jin, and Daehyeon Kyeong. A stabilized p1-nonconforming immersed finite element method for the interface elasticity problems. *ESAIM: Mathematical Modelling and Numerical Analysis*, 51(1):187–207, 2017.

[55] Wolfgang A Wall, Moritz A Frenzel, and Christian Cyron. Isogeometric structural shape optimization. *Computer methods in applied mechanics and engineering*, 197 (33-40):2976–2988, 2008.

[56] Attila P Nagy, Mostafa M Abdalla, and Zafer Gürdal. Isogeometric sizing and

shape optimisation of beam structures. *Computer Methods in Applied Mechanics and Engineering*, 199(17-20):1216–1230, 2010.

[57] JJ Ródenas, FJ Fuenmayor, and JE Tarancón. A numerical methodology to assess the quality of the design velocity field computation methods in shape sensitivity analysis. *International Journal for Numerical Methods in Engineering*, 59(13):1725–1747, 2004.

[58] Raphael T Haftka and Ramana V Grandhi. Structural shape optimization—a survey. *Computer methods in applied mechanics and engineering*, 57(1):91–106, 1986.

[59] Yunliang Ding. Shape optimization of structures: a literature survey. *Computers & Structures*, 24(6):985–1004, 1986.

[60] SS Bhavikatti and CV Ramakrishnan. Optimum shape design of rotating disks. *Computers & Structures*, 11(5):397–401, 1980.

[61] M Hasan Imam. Three-dimensional shape optimization. *International Journal for Numerical Methods in Engineering*, 18(5):661–673, 1982.

[62] JA Bennett and ME Botkin. Structural shape optimization with geometric description and adaptive mesh refinement. *AIAA journal*, 23(3):458–464, 1985.

[63] Daniel N Wilke, Schalk Kok, and Albert A Groenwold. A quadratically convergent unstructured remeshing strategy for shape optimization. *International journal for numerical methods in engineering*, 65(1):1–17, 2006.

[64] AD Belegundu and SD Rajan. A shape optimization approach based on natural design variables and shape functions. *Computer Methods in Applied Mechanics and Engineering*, 66(1):87–106, 1988.

[65] Chau Le, Tyler Bruns, and Daniel Tortorelli. A gradient-based, parameter-free approach to shape optimization. *Computer Methods in Applied Mechanics and Engineering*, 200(9-12):985–996, 2011.

[66] R Meske, J Sauter, and E Schnack. Nonparametric gradient-less shape optimization for real-world applications. *Structural and Multidisciplinary Optimization*, 30(3):201–218, 2005.

[67] F Daoud, M Firl, and KU Bletzinger. Filter techniques in shape optimization with cad-free parametrization. In *Proceedings of 6th World Congress of Structural and Multidisciplinary Optimization*. Citeseer, 2005.

[68] V Mallardo and C Alessandri. Inverse problems in the presence of inclusions and unilateral constraints: a boundary element approach. *Computational mechanics*, 26 (6):571–581, 2000.

[69] Deyong Sun and Chunying Dong. Shape optimization of heterogeneous materials based on isogeometric boundary element method. *Computer Methods in Applied Mechanics and Engineering*, 370:113279, 2020.

[70] Thomas JR Hughes, John A Cottrell, and Yuri Bazilevs. Isogeometric analysis: Cad, finite elements, nurbs, exact geometry and mesh refinement. *Computer methods in applied mechanics and engineering*, 194(39-41):4135–4195, 2005.

[71] Charbel Farhat, Christoph Degand, Bruno Koobus, and Michel Lesoinne. Torsional springs for two-dimensional dynamic unstructured fluid meshes. *Computer methods in applied mechanics and engineering*, 163(1-4):231–245, 1998.

[72] Patrick Knupp. Introducing the target-matrix paradigm for mesh optimization via node-movement. *Engineering with Computers*, 28(4):419–429, 2012.

[73] Jeroen Witteveen. Explicit and robust inverse distance weighting mesh deformation for cfd. In *48th AIAA Aerospace Sciences Meeting Including the New Horizons Forum and Aerospace Exposition*, page 165, 2010.

[74] Xueqiang Liu, Ning Qin, and Hao Xia. Fast dynamic grid deformation based on delaunay graph mapping. *Journal of Computational Physics*, 211(2):405–423, 2006.

[75] A De Boer, MS Van der Schoot, and Hester Bijl. Mesh deformation based on radial basis function interpolation. *Computers & structures*, 85(11-14):784–795, 2007.

[76] Hong Fang, He Zhang, Fanli Shan, Ming Tie, Xing Zhang, and Jinghua Sun. Efficient mesh deformation using radial basis functions with a grouping-circular-based greedy algorithm. *Journal of Computational Physics*, 433:110200, 2021.

[77] Jibum Kim, Brian J Miller, and Suzanne M Shontz. A hybrid mesh deformation algorithm using anisotropic pdes and multiobjective mesh optimization. *Computers & Mathematics with Applications*, 70(8):1830–1851, 2015.

[78] Brian T Helenbrook. Mesh deformation using the biharmonic operator. *International journal for numerical methods in engineering*, 56(7):1007–1021, 2003.

[79] Phillip A Sackinger, Peter Randall Schunk, and Rekha R Rao. A newton–raphson pseudo-solid domain mapping technique for free and moving boundary problems: a finite element implementation. *Journal of Computational Physics*, 125(1):83–103, 1996.

[80] Ezequiel J López, Norberto M Nigro, Mario A Storti, and Jorge A Toth. A minimal element distortion strategy for computational mesh dynamics. *International Journal for Numerical Methods in Engineering*, 69(9):1898–1929, 2007.

[81] Alfred Edward Jules Bogaers, Schalk Kok, and AG Malan. Highly efficient optimization

mesh movement method based on proper orthogonal decomposition. *International Journal for Numerical Methods in Engineering*, 86(8):935–952, 2011.

[82] Josh Danczyk and Krishnan Suresh. Finite element analysis over tangled meshes. In *International Design Engineering Technical Conferences and Computers and Information in Engineering Conference*, volume 45011, pages 89–95. Citeseer, 2012.

[83] Keith Stein, Tayfun E Tezduyar, and Richard Benney. Automatic mesh update with the solid-extension mesh moving technique. *Computer Methods in Applied Mechanics and Engineering*, 193(21-22):2019–2032, 2004.

[84] Shankar P Sastry, Suzanne M Shontz, and Stephen A Vavasis. A log-barrier method for mesh quality improvement and untangling. *Engineering with Computers*, 30(3): 315–329, 2014.

[85] Pierre Duysinx, Laurent Van Miegroet, Thibault Jacobs, and Claude Fleury. Generalized shape optimization using x-fem and level set methods. In *IUTAM Symposium on Topological Design Optimization of Structures, Machines and Materials*, pages 23–32. Springer, 2006.

[86] Erik Burman, Daniel Elfverson, Peter Hansbo, Mats G Larson, and Karl Larsson. Shape optimization using the cut finite element method. *Computer Methods in Applied Mechanics and Engineering*, 328:242–261, 2018.

[87] Jaroslav Haslinger, Jean-Francois Maitre, and Laurent Tomas. Fictitious domains methods with distributed lagrange multipliers part ii: application to the solution of shape optimization problems. *Mathematical Models and Methods in Applied Sciences*, 11(03):549–563, 2001.

[88] Nam H Kim and Youngmin Chang. Eulerian shape design sensitivity analysis

and optimization with a fixed grid. *Computer methods in applied mechanics and engineering*, 194(30-33):3291–3314, 2005.

[89] Florin Bobaru and Srinivas Rachakonda. Boundary layer in shape optimization of convective fins using a meshfree approach. *International journal for numerical methods in engineering*, 60(7):1215–1236, 2004.

[90] Martin P Bendsøe. Optimal shape design as a material distribution problem. *Structural optimization*, 1(4):193–202, 1989.

[91] Yi M Xie and Grant P Steven. A simple evolutionary procedure for structural optimization. *Computers & structures*, 49(5):885–896, 1993.

[92] Dan Wang and Weihong Zhang. A general material perturbation method using fixed mesh for stress sensitivity analysis and structural shape optimization. *Computers & Structures*, 129:40–53, 2013.

[93] Yu-Deok Seo, Hyun-Jung Kim, and Sung-Kie Youn. Isogeometric topology optimization using trimmed spline surfaces. *Computer Methods in Applied Mechanics and Engineering*, 199(49-52):3270–3296, 2010.

[94] Yu-Deok Seo, Hyun-Jung Kim, and Sung-Kie Youn. Shape optimization and its extension to topological design based on isogeometric analysis. *International Journal of Solids and Structures*, 47(11-12):1618–1640, 2010.

[95] Zhen Luo, Michael Yu Wang, Shengyin Wang, and Peng Wei. A level set-based parameterization method for structural shape and topology optimization. *International Journal for Numerical Methods in Engineering*, 76(1):1–26, 2008.

[96] Laurent Van Miegroet, Nicolas Moës, Claude Fleury, and Pierre Duysinx. Generalized

shape optimization based on the level set method. In *Proceedings of the 6th World Congress of Structural and Multidisciplinary Optimization (WCSMO6)*, 2005.

[97] Ahmad R Najafi, Masoud Safdari, Daniel A Tortorelli, and Philippe H Geubelle. A gradient-based shape optimization scheme using an interface-enriched generalized fem. *Computer Methods in Applied Mechanics and Engineering*, 296:1–17, 2015.

[98] Ahmad R Najafi, Masoud Safdari, Daniel A Tortorelli, and Philippe H Geubelle. Shape optimization using a nurbs-based interface-enriched generalized fem. *International Journal for Numerical Methods in Engineering*, 111(10):927–954, 2017.

[99] Ruchi Guo, Tao Lin, and Yanping Lin. Recovering elastic inclusions by shape optimization methods with immersed finite elements. *Journal of Computational Physics*, 404:109123, 2020.

[100] Jun Wu, Ole Sigmund, and Jeroen P Groen. Topology optimization of multi-scale structures: a review. *Structural and Multidisciplinary Optimization*, 63:1455–1480, 2021.

[101] Martin Philip Bendsoe and Ole Sigmund. *Topology optimization: theory, methods, and applications.* Springer Science & Business Media, 2003.

[102] Ji-Hong Zhu, Wei-Hong Zhang, and Liang Xia. Topology optimization in aircraft and aerospace structures design. *Archives of computational methods in engineering*, 23: 595–622, 2016.

[103] RJ Yang and AI Chahande. Automotive applications of topology optimization. *Structural optimization*, 9:245–249, 1995.

[104] Lauren L Beghini, Alessandro Beghini, Neil Katz, William F Baker, and Glaucio H

Paulino. Connecting architecture and engineering through structural topology optimization. *Engineering Structures*, 59:716–726, 2014.

[105] Xiaojian Wang, Shanqing Xu, Shiwei Zhou, Wei Xu, Martin Leary, Peter Choong, Ma Qian, Milan Brandt, and Yi Min Xie. Topological design and additive manufacturing of porous metals for bone scaffolds and orthopaedic implants: A review. *Biomaterials*, 83:127–141, 2016.

[106] Martin Philip Bendsøe and Noboru Kikuchi. Generating optimal topologies in structural design using a homogenization method. *Computer methods in applied mechanics and engineering*, 71(2):197–224, 1988.

[107] Katsuyuki Suzuki and Noboru Kikuchi. A homogenization method for shape and topology optimization. *Computer methods in applied mechanics and engineering*, 93 (3):291–318, 1991.

[108] Grégoire Allaire, Eric Bonnetier, Gilles Francfort, and François Jouve. Shape optimization by the homogenization method. *Numerische Mathematik*, 76:27–68, 1997.

[109] Behrooz Hassani and Ernest Hinton. A review of homogenization and topology optimization i—homogenization theory for media with periodic structure. *Computers & Structures*, 69(6):707–717, 1998.

[110] Ming Zhou and George IN Rozvany. The coc algorithm, part ii: Topological, geometrical and generalized shape optimization. *Computer methods in applied mechanics and engineering*, 89(1-3):309–336, 1991.

[111] Ole Sigmund and Joakim Petersson. Numerical instabilities in topology optimization: a survey on procedures dealing with checkerboards, mesh-dependencies and local minima. *Structural optimization*, 16:68–75, 1998.

[112] Hans A Eschenauer and Niels Olhoff. Topology optimization of continuum structures: a review. *Appl. Mech. Rev.*, 54(4):331–390, 2001.

[113] JA Sethian. Advancing interfaces: level set and fast marching methods. In *Proceedings of the international conference on industrial and applied mathematics: plenary lectures*, 1999.

[114] James A Sethian. Evolution, implementation, and application of level set and fast marching methods for advancing fronts. *Journal of computational physics*, 169(2): 503–555, 2001.

[115] Stanley Osher and Ronald P Fedkiw. Level set methods: an overview and some recent results. *Journal of Computational physics*, 169(2):463–502, 2001.

[116] Stanley Osher and Ronald P Fedkiw. *Level set methods and dynamic implicit surfaces*, volume 1. Springer New York, 2005.

[117] Michael Yu Wang, Xiaoming Wang, and Dongming Guo. A level set method for structural topology optimization. *Computer methods in applied mechanics and engineering*, 192(1-2):227–246, 2003.

[118] Grégoire Allaire, François Jouve, and Anca-Maria Toader. Structural optimization using sensitivity analysis and a level-set method. *Journal of computational physics*, 194(1):363–393, 2004.

[119] Grégoire Allaire, F de Gournay, François Jouve, and A-M Toader. Structural optimization using topological and shape sensitivity via a level set method. *Control and cybernetics*, 34(1):59–80, 2005.

[120] Mei Yulin and Wang Xiaoming. A level set method for structural topology optimization and its applications. *Advances in Engineering software*, 35(7):415–441, 2004.

[121] Jan Sokolowski and Antoni Zochowski. On the topological derivative in shape optimization. *SIAM journal on control and optimization*, 37(4):1251–1272, 1999.

[122] Blaise Bourdin and Antonin Chambolle. Design-dependent loads in topology optimization. *ESAIM: Control, Optimisation and Calculus of Variations*, 9:19–48, 2003.

[123] Y Mike Xie, Grant P Steven, YM Xie, and GP Steven. *Basic evolutionary structural optimization.* Springer, 1997.

[124] Ole Sigmund and Kurt Maute. Topology optimization approaches: A comparative review. *Structural and multidisciplinary optimization*, 48(6):1031–1055, 2013.

[125] Nico P Van Dijk, Kurt Maute, Matthijs Langelaar, and Fred Van Keulen. Level-set methods for structural topology optimization: a review. *Structural and Multidisciplinary Optimization*, 48:437–472, 2013.

[126] NP Van Dijk, M Langelaar, and F Van Keulen. Explicit level-set-based topology optimization using an exact heaviside function and consistent sensitivity analysis. *International Journal for Numerical Methods in Engineering*, 91(1):67–97, 2012.

[127] Zhenyu Liu, Jan G Korvink, and Ruoyu Huang. Structure topology optimization: fully coupled level set method via femlab. *Structural and Multidisciplinary Optimization*, 29:407–417, 2005.

[128] Xianghua Xing, Peng Wei, and Michael Yu Wang. A finite element-based level set method for structural optimization. *International journal for numerical methods in engineering*, 82(7):805–842, 2010.

[129] MJ De Ruiter and F Van Keulen. Topology optimization using a topology description function. *Structural and Multidisciplinary Optimization*, 26(6):406–416, 2004.

[130] Zhen Luo, Liyong Tong, Michael Yu Wang, and Shengyin Wang. Shape and topology optimization of compliant mechanisms using a parameterization level set method. *Journal of Computational Physics*, 227(1):680–705, 2007.

[131] Alexandra A Gomes and Afzal Suleman. Application of spectral level set methodology in topology optimization. *Structural and Multidisciplinary Optimization*, 31:430–443, 2006.

[132] Martin Burger and Stanley J Osher. A survey on level set methods for inverse problems and optimal design. *European journal of applied mathematics*, 16(2):263–301, 2005.

[133] Vivien J Challis and James K Guest. Level set topology optimization of fluids in stokes flow. *International journal for numerical methods in engineering*, 79(10):1284–1308, 2009.

[134] Eldad Haber. A multilevel, level-set method for optimizing eigenvalues in shape design problems. *Journal of Computational Physics*, 198(2):518–534, 2004.

[135] Laurent Van Miegroet and Pierre Duysinx. Stress concentration minimization of 2d filets using x-fem and level set description. *Structural and Multidisciplinary Optimization*, 33(4):425–438, 2007.

[136] J Norato, R Haber, D Tortorelli, and Martin P Bendsøe. A geometry projection method for shape optimization. *International Journal for Numerical Methods in Engineering*, 60(14):2289–2312, 2004.

[137] Junzhao Luo, Zhen Luo, Shikui Chen, Liyong Tong, and Michael Yu Wang. A new level set method for systematic design of hinge-free compliant mechanisms. *Computer Methods in Applied Mechanics and Engineering*, 198(2):318–331, 2008.

[138] T Belytschko, SP Xiao, and C Parimi. Topology optimization with implicit functions and regularization. *International Journal for Numerical Methods in Engineering*, 57 (8):1177–1196, 2003.

[139] Ole Sigmund. Materials with prescribed constitutive parameters: an inverse homogenization problem. *International Journal of Solids and Structures*, 31(17):2313–2329, 1994.

[140] Katia Bertoldi, Pedro M Reis, Stephen Willshaw, and Tom Mullin. Negative poisson's ratio behavior induced by an elastic instability. *Advanced materials*, 22(3):361–366, 2010.

[141] Roderic Lakes. Foam structures with a negative poisson's ratio. *Science*, 235(4792): 1038–1040, 1987.

[142] Erik Andreassen, Boyan S Lazarov, and Ole Sigmund. Design of manufacturable 3d extremal elastic microstructure. *Mechanics of Materials*, 69(1):1–10, 2014.

[143] Anders Clausen, Fengwen Wang, Jakob S Jensen, Ole Sigmund, and Jennifer A Lewis. Topology optimized architectures with programmable poisson's ratio over large deformations. *Adv. Mater*, 27(37):5523–5527, 2015.

[144] Mengli Ye, Liang Gao, and Hao Li. A design framework for gradually stiffer mechanical metamaterial induced by negative poisson's ratio property. *Materials & Design*, 192: 108751, 2020.

[145] Tiemo Bückmann, Michael Thiel, Muamer Kadic, Robert Schittny, and Martin Wegener. An elasto-mechanical unfeelability cloak made of pentamode metamaterials. *Nature communications*, 5(1):4130, 2014.

[146] Muamer Kadic, Tiemo Bückmann, Nicolas Stenger, Michael Thiel, and Martin Wegener. On the practicability of pentamode mechanical metamaterials. *Applied Physics Letters*, 100(19), 2012.

[147] Johan Christensen, Muamer Kadic, Oliver Kraft, and Martin Wegener. Vibrant times for mechanical metamaterials. *Mrs Communications*, 5(3):453–462, 2015.

[148] Roderic S Lakes, T Lee, A Bersie, and Yun-Che Wang. Extreme damping in composite materials with negative-stiffness inclusions. *Nature*, 410(6828):565–567, 2001.

[149] Zachary G Nicolaou and Adilson E Motter. Mechanical metamaterials with negative compressibility transitions. *Nature materials*, 11(7):608–613, 2012.

[150] Bryan Gin-ge Chen, Nitin Upadhyaya, and Vincenzo Vitelli. Nonlinear conduction via solitons in a topological mechanical insulator. *Proceedings of the National Academy of Sciences*, 111(36):13004–13009, 2014.

[151] Jayson Paulose, Bryan Gin-ge Chen, and Vincenzo Vitelli. Topological modes bound to dislocations in mechanical metamaterials. *Nature Physics*, 11(2):153–156, 2015.

[152] Lisa M Nash, Dustin Kleckner, Alismari Read, Vincenzo Vitelli, Ari M Turner, and William TM Irvine. Topological mechanics of gyroscopic metamaterials. *Proceedings of the National Academy of Sciences*, 112(47):14495–14500, 2015.

[153] Ole Sigmund. A new class of extremal composites. *Journal of the Mechanics and Physics of Solids*, 48(2):397–428, 2000.

[154] Xiaodong Huang, Arash Radman, and Yi Min Xie. Topological design of microstructures of cellular materials for maximum bulk or shear modulus. *Computational Materials Science*, 50(6):1861–1870, 2011.

[155] Christian Rye Thomsen, Fengwen Wang, and Ole Sigmund. Buckling strength topology optimization of 2d periodic materials based on linearized bifurcation analysis. *Computer Methods in Applied Mechanics and Engineering*, 339:115–136, 2018.

[156] Fengwen Wang and Ole Sigmund. Numerical investigation of stiffness and buckling response of simple and optimized infill structures. *Structural and Multidisciplinary Optimization*, 61(6):2629–2639, 2020.

[157] Yan Zhang, Mi Xiao, Hao Li, and Liang Gao. Topology optimization of material microstructures using energy-based homogenization method under specified initial material layout. *Journal of Mechanical Science and Technology*, 33:677–693, 2019.

[158] Jinhu Cai, Chunjie Wang, and Zhifang Fu. Robust concurrent topology optimization of multiscale structure under single or multiple uncertain load cases. *International Journal for Numerical Methods in Engineering*, 121(7):1456–1483, 2020.

[159] Vivien J Challis, James K Guest, Joseph F Grotowski, and Anthony P Roberts. Computationally generated cross-property bounds for stiffness and fluid permeability using topology optimization. *International Journal of Solids and Structures*, 49(23-24): 3397–3408, 2012.

[160] Ole Sigmund and Salvatore Torquato. Composites with extremal thermal expansion coefficients. *Applied Physics Letters*, 69(21):3203–3205, 1996.

[161] S Torquato, S Hyun, and Aleksandar Donev. Multifunctional composites: optimizing microstructures for simultaneous transport of heat and electricity. *Physical review letters*, 89(26):266601, 2002.

[162] Jakob Søndergaard Jensen and Ole Sigmund. Topology optimization for nano-photonics. *Laser & Photonics Reviews*, 5(2):308–321, 2011.

[163] Ole Sigmund and Jakob Søndergaard Jensen. Systematic design of phononic band–gap materials and structures by topology optimization. *Philosophical Transactions of the Royal Society of London. Series A: Mathematical, Physical and Engineering Sciences*, 361(1806):1001–1019, 2003.

[164] Zhen Luo, Liyong Tong, and Zhan Kang. A level set method for structural shape and topology optimization using radial basis functions. *Computers & Structures*, 87(7-8): 425–434, 2009.

[165] Jie Gao, Hao Li, Zhen Luo, Liang Gao, and Peigen Li. Topology optimization of micro-structured materials featured with the specific mechanical properties. *International Journal of Computational Methods*, 17(03):1850144, 2020.

[166] Yiqiang Wang, Zhen Luo, Nong Zhang, and Zhan Kang. Topological shape optimization of microstructural metamaterials using a level set method. *Computational Materials Science*, 87:178–186, 2014.

[167] Jie Gao, Zhen Luo, Hao Li, and Liang Gao. Topology optimization for multiscale design of porous composites with multi-domain microstructures. *Computer Methods in Applied Mechanics and Engineering*, 344:451–476, 2019.

[168] Hao Li, Zhen Luo, Liang Gao, and Paul Walker. Topology optimization for functionally graded cellular composites with metamaterials by level sets. *Computer Methods in Applied Mechanics and Engineering*, 328:340–364, 2018.

[169] Yiqiang Wang, Zhen Luo, Zhan Kang, and Nong Zhang. A multi-material level set-based topology and shape optimization method. *Computer Methods in Applied Mechanics and Engineering*, 283:1570–1586, 2015.

[170] Sattar Mohammadi Esfarjani, Ali Dadashi, and Mohammad Azadi. Topology

optimization of additive-manufactured metamaterial structures: A review focused on multi-material types. *Forces in Mechanics*, 7:100100, 2022.

[171] Jinglai Wu, Zhen Luo, Hao Li, and Nong Zhang. Level-set topology optimization for mechanical metamaterials under hybrid uncertainties. *Computer Methods in Applied Mechanics and Engineering*, 319:414–441, 2017.

[172] Srivatsa Bhat Kaudur and Mayuresh J Patil. Shape optimization with immersed interface finite element method. *International Journal for Numerical Methods in Engineering*, 123(23):5907–5936, 2022.

[173] Boris Lande and Wayne Mitzner. Analysis of lung parenchyma as a parametric porous medium. *Journal of applied physiology*, 101(3):926–933, 2006.

[174] Ruben G Carbonell and Stephen Whitaker. Heat and mass transfer in porous media. In *Fundamentals of transport phenomena in porous media*, pages 121–198. Springer, 1984.

[175] Matthias Ochs, Jens R Nyengaard, Anja Jung, Lars Knudsen, Marion Voigt, Thorsten Wahlers, Joachim Richter, and Hans Jørgen G Gundersen. The number of alveoli in the human lung. *American journal of respiratory and critical care medicine*, 169(1): 120–124, 2004.

[176] Benoit B Mandelbrot and Benoit B Mandelbrot. *The fractal geometry of nature*, volume 1. WH freeman New York, 1982.

[177] Y Lanir. Constitutive equations for the lung tissue. *Journal of biomechanical engineering*, 105(4):374–380, 1983.

[178] B Budiansky and E Kimmel. Elastic moduli of lungs. *Journal of applied mechanics*, 54(2):351–358, 1987.

[179] Felipe Concha, Mauricio Sarabia-Vallejos, and Daniel E Hurtado. Micromechanical model of lung parenchyma hyperelasticity. *Journal of the Mechanics and Physics of Solids*, 112:126–144, 2018.

[180] Béla Suki and Jason HT Bates. Lung tissue mechanics as an emergent phenomenon. *Journal of applied physiology*, 110(4):1111–1118, 2011.

[181] Jason HT Bates, Charles G Irvin, Ramon Farré, and Zoltán Hantos. Oscillation mechanics of the respiratory system. *Comprehensive Physiology*, 1(3):1233–1272, 2011.

[182] P John Dale, Frank L Matthews, and Robert C Schroter. Finite element analysis of lung alveolus. *Journal of Biomechanics*, 13(10):865–873, 1980.

[183] B Suki, AL Barabási, and KR Lutchen. Lung tissue viscoelasticity: a mathematical framework and its molecular basis. *Journal of applied physiology (Bethesda, Md.: 1985)*, 76(6):2749–2759, 1994.

[184] Jason HT Bates. A micromechanical model of lung tissue rheology. *Annals of biomedical engineering*, 26:679–687, 1998.

[185] D Stamenović, KR Lutchen, and GM Barnas. Alternative model of respiratory tissue viscoplasticity. *Journal of Applied Physiology (Bethesda, Md.: 1985)*, 75(3):1062–1069, 1993.

[186] B Suki and JH Bates. A nonlinear viscoelastic model of lung tissue mechanics. *Journal of Applied Physiology*, 71(3):826–833, 1991.

[187] SM Mijailovich, D Stamenović, and JJ Fredberg. Toward a kinetic theory of connective tissue micromechanics. *Journal of Applied Physiology (Bethesda, Md.: 1985)*, 74(2): 665–681, 1993.

[188] Y Lanir. On the structural origin of the quasilinear viscoelastic behavior of tissues. In *Frontiers in Biomechanics*, pages 130–136. Springer, 1986.

[189] J Hildebrandt. Comparison of mathematical models for cat lung and viscoelastic balloon derived by laplace transform methods from pressurevolume data. *The Bulletin of mathematical biophysics*, 31:651–667, 1969.

[190] Mark A Lewis and Markus R Owen. The mechanics of lung tissue under high-frequency ventilation. *SIAM Journal on Applied Mathematics*, 61(5):1731–1761, 2001.

[191] Natarajan Sukumar, David L Chopp, Nicolas Moës, and Ted Belytschko. Modeling holes and inclusions by level sets in the extended finite-element method. *Computer methods in applied mechanics and engineering*, 190(46-47):6183–6200, 2001.

[192] V Kobelev. "bubble-and-grain" method and criteria for optimal positioning inhomogeneities in topological optimization. *Structural and Multidisciplinary Optimization*, 40(1):117–135, 2010.

[193] AV Cherkaev, Yu Grabovsky, AB Movchan, and SK Serkov. The cavity of the optimal shape under the shear stresses. *International Journal of Solids and structures*, 35(33): 4391–4410, 1998.

[194] Robert A Canfield. Quadratic multipoint exponential approximation: Surrogate model for large-scale optimization. In *World Congress of Structural and Multidisciplinary Optimisation*, pages 648–661. Springer, 2017.

[195] Klaus Schittkowski. Nlpql: A fortran subroutine solving constrained nonlinear programming problems. *Annals of operations research*, 5(2):485–500, 1986.

[196] Ahmad Najafi, Masoud Safdari, and Philippe H Geubelle. Material design using

a nurbs-based shape optimization. In *57th AIAA/ASCE/AHS/ASC Structures, Structural Dynamics, and Materials Conference*, page 1170, 2016.

[197] Jianmin Qu and Mohammed Cherkaoui. *Fundamentals of micromechanics of solids*, volume 735. Wiley Online Library, 2006.

[198] Gary Don Seidel. Micromechanics modeling of the multifunctional nature of carbon nanotube-polymer nanocomposites. *Ph. D. Thesis*, 2007.

[199] Stefan Jansson. Homogenized nonlinear constitutive properties and local stress concentrations for composites with periodic internal structure. *International Journal of Solids and Structures*, 29(17):2181–2200, 1992.

[200] Toufik Kanit, Samuel Forest, Isabelle Galliet, Valérie Mounoury, and Dominique Jeulin. Determination of the size of the representative volume element for random composites: statistical and numerical approach. *International Journal of solids and structures*, 40 (13-14):3647–3679, 2003.

[201] Zihui Xia, Yunfa Zhang, and Fernand Ellyin. A unified periodical boundary conditions for representative volume elements of composites and applications. *International journal of solids and structures*, 40(8):1907–1921, 2003.

[202] A Amine Benzerga. On the structure of poroplastic constitutive relations. *Journal of the Mechanics and Physics of Solids*, 178:105344, 2023.

[203] Martin D Buhmann. *Radial basis functions: theory and implementations*, volume 12. Cambridge university press, 2003.

[204] Holger Wendland. Piecewise polynomial, positive definite and compactly supported radial functions of minimal degree. *Advances in computational Mathematics*, 4(1): 389–396, 1995.

[205] Holger Wendland. Sobolev-type error estimates for interpolation by radial basis functions. *Surface fitting and multiresolution methods*, pages 337–344, 1997.

[206] Holger Wendland. Error estimates for interpolation by compactly supported radial basis functions of minimal degree. *Journal of approximation theory*, 93(2):258–272, 1998.

[207] Clarence Zener. *Elasticity and anelasticity of metals.* University of Chicago Press, 1965.

[208] Hassel Ledbetter and Albert Migliori. A general elastic-anisotropy measure. *Journal of applied physics*, 100(6), 2006.

[209] Arash Radman, Xiaodong Huang, and YM Xie. Topological optimization for the design of microstructures of isotropic cellular materials. *Engineering optimization*, 45 (11):1331–1348, 2013.

[210] Zvi Hashin and Shmuel Shtrikman. A variational approach to the theory of the elastic behaviour of multiphase materials. *Journal of the Mechanics and Physics of Solids*, 11 (2):127–140, 1963.

[211] Melvin Mooney. A theory of large elastic deformation. *Journal of applied physics*, 11 (9):582–592, 1940.

[212] RSl Rivlin. Large elastic deformations of isotropic materials. i. fundamental concepts. *Philosophical Transactions of the Royal Society of London. Series A, Mathematical and Physical Sciences*, 240(822):459–490, 1948.

[213] Raymond William Ogden. Large deformation isotropic elasticity–on the correlation of theory and experiment for incompressible rubberlike solids. *Proceedings of the Royal Society of London. A. Mathematical and Physical Sciences*, 326(1567):565–584, 1972.

[214] LRG Treloar. The elasticity and related properties of rubbers. *Reports on progress in physics*, 36(7):755, 1973.

[215] Oon H Yeoh. Characterization of elastic properties of carbon-black-filled rubber vulcanizates. *Rubber chemistry and technology*, 63(5):792–805, 1990.

[216] Abaqus Inc. *SIMULIA—Abaqus theory guide*. Abaqus, Inc. Palo Alto, CA, 2016.

[217] Juan Carlos Simo. On a fully three-dimensional finite-strain viscoelastic damage model: formulation and computational aspects. *Computer methods in applied mechanics and engineering*, 60(2):153–173, 1987.

[218] Klaus-Jürgen Bathe. *Finite element procedures*. Klaus-Jurgen Bathe, 2006.

[219] Piyush Gaur, Anoop Chawla, Khyati Verma, Sudipto Mukherjee, Sanjeev Lalvani, Rajesh Malhotra, and Christian Mayer. Characterisation of human diaphragm at high strain rate loading. *Journal of the mechanical behavior of biomedical materials*, 60: 603–616, 2016.

[220] Anna M Birzle, Sophie MK Hobrack, Christian Martin, Stefan Uhlig, and Wolfgang A Wall. Constituent-specific material behavior of soft biological tissue: experimental quantification and numerical identification for lung parenchyma. *Biomechanics and Modeling in Mechanobiology*, 18:1383–1400, 2019.

[221] Piyush Gaur, Khyati Verma, Anoop Chawla, Sudipto Mukherjee, Mohit Jain, Christian Mayer, Ravi Kiran Chitteti, Pronoy Ghosh, Rajesh Malhotra, and Sanjeev Lalvani. A bilinear structural constitutive model for strain rate-dependent behaviour of human diaphragm tissue. *International journal of crashworthiness*, 2019.

[222] Clayton T McKee, Julie A Last, Paul Russell, and Christopher J Murphy. Indentation

versus tensile measurements of young's modulus for soft biological tissues. *Tissue Engineering Part B: Reviews*, 17(3):155–164, 2011.

[223] Emily L Guzas, Stephen E Turner, Matthew Babina, Brandon Casper, Thomas N Fetherston, and Joseph M Ambrico. Validation of a surrogate model for marine mammal lung dynamics under underwater explosive impulse. In *Verification and Validation*, volume 41174, page V001T08A001. American Society of Mechanical Engineers, 2019.

[224] Thomas Fetherston, Stephen Turner, Glenn Mitchell, and Emily Guzas. Marine mammal lung dynamics when exposed to underwater explosion impulse. *The Anatomical Record*, 302(5):718–734, 2019.

[225] Hakan Axelsson and John T Yelverton. Chest wall velocity as a predictor of nonauditory blast injury in a complex wave environment. *Journal of Trauma and Acute Care Surgery*, 40(3S):31S–37S, 1996.

[226] U.S. Navy. U.s. navy diving manual. 1970.

[227] H Wright, W Davidson, and H Silvester. The effects of underwater explosions on shallow water divers submerged in 100 ft of water. *Royal Navy Physiological Report*, 50:639, 1950.

[228] JJ Finneran and AK Jenkins. Criteria and thresholds for us navy acoustic and explosive effects analysis. *SPAWAR Marine Mammal Program, San Diego, California*, 2012.

Appendices

Appendix A

Immersed Elements

A.1 The Method of Mesh-Movement vs ncPG-IIFEM

To demonstrate the contrast between the method of mesh movement and the application of shape optimization using ncPG-IIFEM, a case of double inclusion will be considered. The optimization problem is formulated as follows: Optimize the shape of double elliptical inclusion whose x-coordinates are fixed at $x_{c1} = 0.25$ and $x_{c2} = 0.75$ embedded in a matrix to minimize the compliance. To minimize the mesh distortion, only circles or ellipses are allowed in the mesh movement case. A plane strain formulation is considered, and a total inclusion area constraint and two area inequality constraints are also specified. The domain is a square of unit length. A shear load of 0.5 is applied on the top edge, with a pinned support on the bottom edge. The matrix is stiffer than the inclusion with material property ratios as follows: $E_1/E_2 = 10$ and $\nu_1 = \nu_2 = 0.3$. The total area of the inclusions is 0.04π and the minimum area for each inclusion is 0.01π. For the method of mesh movement, the design variables are the radius of the ellipse in the x-direction and y-direction and the y-coordinates of the center of the two ellipses. Let d_1 and d_2 be the radius in the x-direction and y-direction of the ellipse located at $(0.25, d_5)$, d_3 and d_4 be the radius in the x-direction and y-direction of the ellipse located at $(0.25, d_6)$. The lower and upper bounds on the design variables are $0.05 \leq d_1, d_2, d_3, d_4 \leq 0.2$ and $0.35 \leq d_5, d_6 \leq 0.65$.

The alignment of the mesh with the moving ellipse is required for the finite element analysis

during each iteration. Pseudo-solid mesh movement is employed for generating a new mesh for each iteration. A different elasticity problem is solved in which the nodal displacement of the initial mesh nodes of the ellipse is specified, determining the movement of the other nodes. In essence, all the edges are immobilized, and the movement of the ellipse is predefined. The below system of equations is solved:

$$
\begin{bmatrix} K_{uu} & K_{uk} \\ K_{uk} & K_{kk} \end{bmatrix} \begin{Bmatrix} u_{uu} \\ u_{kk} \end{Bmatrix} = \begin{Bmatrix} 0 \\ f \end{Bmatrix}
\tag{A.1}
$$

where, u_{uu} are the unknown displacements and u_{kk} are the known nodal displacements, f is the unknown reaction forces. The K matrix is partitioned as shown and the first set of equations are solved. Thus, the unknown displacements are as follows:

$$
u_{uu} = -K_{uu}^{-1} \, K_{uk} \, u_{kk}
\tag{A.2}
$$

To prescribe the displacement of the ellipse, the following parametric representation is used

$$
x_{old} = x_0 + a_{old} \cos \theta
$$
$$
y_{old} = y_0 + b_{old} \sin \theta
\tag{A.3}
$$

x_{old} and y_{old} are the coordinates of the nodes on the ellipse in the initial mesh. The $\cos \theta$ and $\sin \theta$ calculated from Equation A.3 is used and substituted into the following equation

$$
x_{new} = x_{0_{new}} + a_{new} \cos \theta
$$
$$
y_{new} = y_{0_{new}} + b_{new} \sin \theta
\tag{A.4}
$$

Then, the prescribed displacements are as follows:

$$u = x_{new} - x_{old}$$
$$v = y_{new} - y_{old}$$

(A.5)

Depending on the parametrization, there are other ways mesh movement can be achieved. Consider the initial ellipse as shown in the left of Figure A.1(a). If an ellipse with its x-axis and y-axis lengths flipped is desired, this can be achieved in two ways from the initial configuration. The ellipse can either be rotated without altering the lengths of the axes, or the axes lengths can be switched. However, it is recommended to avoid rotation as it leads to mesh distortions and overlaps. Examples of the mesh movement for single ellipse and double ellipses are provided below (Figure A.1(a) and A.1(b)). Moving the mesh through large distances can generate a bad mesh with elements of high taper ratio and skew angles (Figure A.2(b)). Rotations cause problems like overlaps as shown in Figure A.2(a). Thus, the two important problems that arise during mesh movement are the overlapping of elements and bad aspect ratio elements. As previously discussed, there exist several approaches to address these challenges, but they come with a high computational cost. These issues are circumvented by avoiding rotations and excessive movements of the center of the inclusion. Additionally, multiple starting meshes can be selected based on the inclusion's center location.

A comparison of the obtained optimums from mesh movement with that of ncPG-IIFEM is made. In order to ensure a fair comparison, shape optimization is performed using the ncPG-IIFEM approach with the inclusion center bounds identical to those employed in the mesh movement method. To guarantee that the inclusion remains within the plate, the radius inequality constraint is enforced. Figure A.3(a) shows the optimums obtained for a few initial configurations using the method of mesh movement. Figure A.3(b) shows the
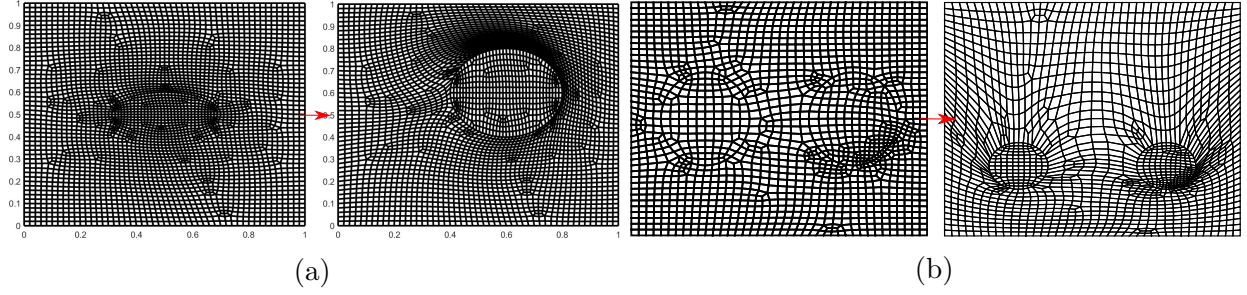
Figure A.1: Transformation of initial mesh through mesh movement: (a) a single ellipse; (b) a double elliptical inclusion.
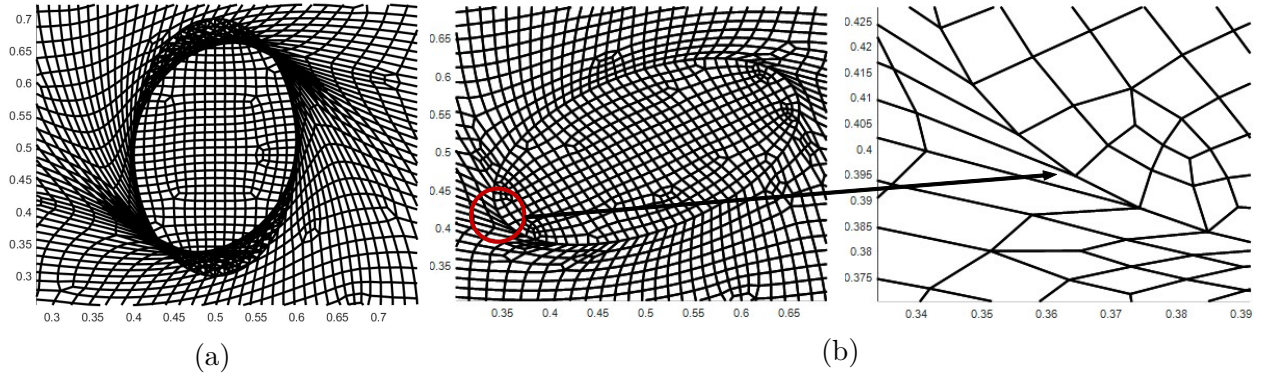

Figure A.2: Rotation of inclusions causing (a) overlapping of elements and (b) bad aspect ratio elements.

optimums obtained for the same initial configurations using the ncPG-IIFEM based shape optimization. Because of the expanded design space in the case of ncPG-IIFEM based shape optimization better optimums are obtained. Rotated shapes are expected in this case. Allowing rotations causes major problems in the case of elasticity-based method of mesh movement. Computationally expensive methods are required to improve the quality of the mesh. This is unnecessary with a fixed mesh shape optimization. For comparison, the best optimum obtained from the method of mesh movement and ncPG-IIFEM based shape optimization is 0.1974 and 0.1864, respectively (values are calculated in post-processing considering the same mesh for comparison). Figure A.4 provides the objective vs iteration history for both the methods. It is evident that complicated shapes can be obtained from the ncPG-IIFEM without the problems associated with mesh movement or remeshing.
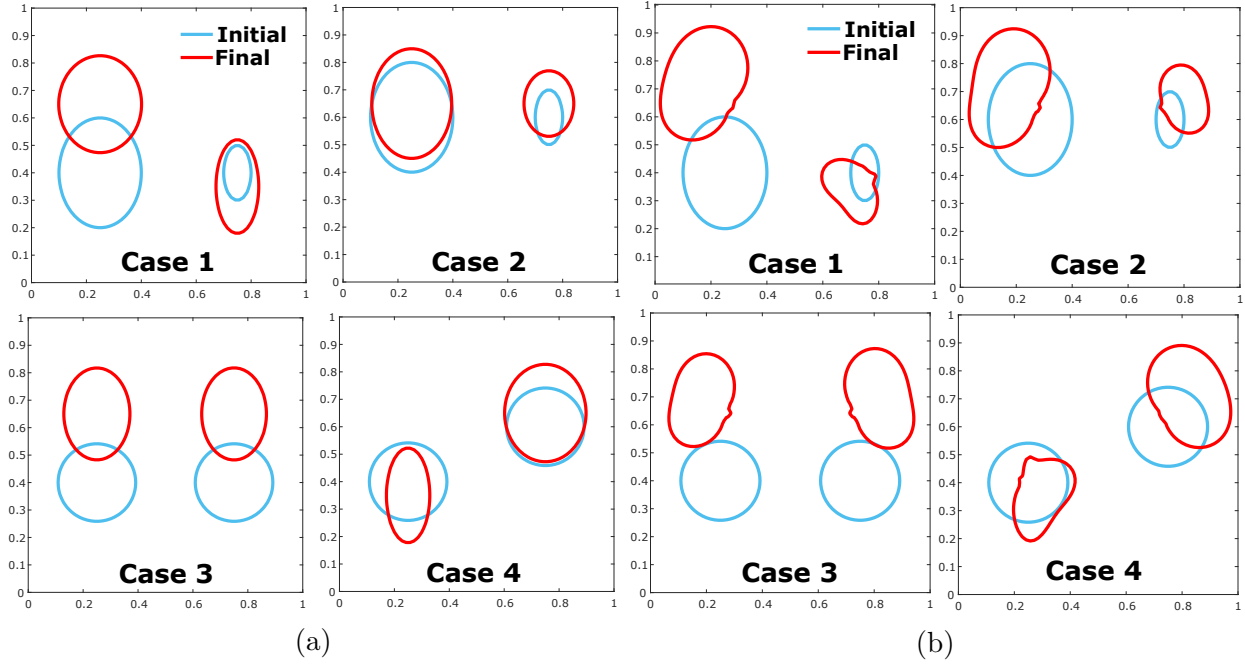
Figure A.3: Optimum inclusions obtained from four different initial designs for a square plate with double inclusions under shear loading: (a) the method of mesh movement; (b) the ncPG-IIFEM shape optimization.
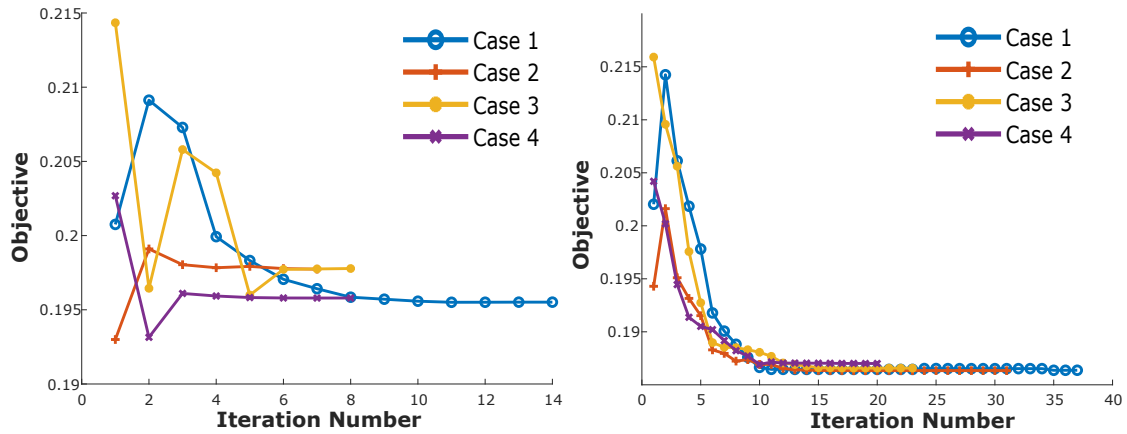

Figure A.4: Iteration histories of the plate compliance: (a) the method of mesh movement; (b) the ncPG-IIFEM shape optimization.

A.2 Representation of Voids and Unisolvance of Trial Functions

Voids can be modeled as an ersatz material [118] with modulus less than or equal to 10^{-3} times the solid material and the Poisson's ratio the same as that of the solid material that surrounds it. Trial functions of an immersed element for a high material property ratio with some interface configurations cannot be generated as the coefficient matrix used during its calculation becomes singular. We show the existence of such singular configurations for various modulus ratios and for some set of Poisson's ratio. Consider an immersed element as shown in Figure 3.1. Let $E^- = 10^{-4}$, $E^+ = 1$, $\nu^- = \nu^+ = 0.3$. In this section, we fix E^+ to be equal to 1 and change all other properties when necessary. Let the four corners in the immersed element in Figure 3.1 correspond to the locations $(0,0), (1,0), (1,1)$ and $(0,1)$, respectively. Let one of the the intersection points which is node 5 in Figure 3.1 be at $(1,1)$ and the other intersection point be $(0, y_6)$. The material distribution is such that the region above the interface is the blue region (softer material) and below is the yellow region (stiff material). The goal is to find values of y_6 that make the coefficient matrix [172] during the trial function calculation singular, thus resulting in the non-uniqueness of trial functions for such configurations.

There are two physically admissible values of y_6 which make the coefficient matrix singular (i.e., determinant zero). The values to 6 significant digits are 0.971138 and 0.997739. All reflections about the horizontal and vertical midline of the square element and successive 90 degree rotations of the singular configurations are also singular. There are other singular configurations. For the intersection points $(1, 0.98)$ and $(0, 0.9997626)$ with same material distribution (top is soft and bottom is stiff), we have a singularity. Here, just the existence of such singular configurations is shown. An exhaustive list of all such configurations is

not provided. For modulus $E^- = 10^{-2}$ and Poisson's ratio $\nu^- = \nu^+ = 0.3$, no singular configurations were found. Here, we do not provide a theoretical proof that such singular configurations doesn't exist for modulus 10^{-2} with all admissible Poisson's ratio values. Lin and Zhang [33] provide possible ranges that guarantee the unisolvent property of bilinear IFE nodal basis functions. They provide general conditions for which the IFE functions are guaranteed to exist.

Table A.1: Singular locations with fixed modulus for different Poisson's ratio of the stiff and softer material.

Location of singularity (y_6) for $E^- = 10^{-4}$			
Poisson's ratio		Two possibilities	
ν^+	ν^-		
0.3	0.3	0.971138	0.997739
0.28	0.25	0.985344	0.995494
0.28	0.28	0.985324	0.995516
0.3	0.25	0.971148	0.997726
0.33	0.3	0.953385	0.998615
0.33	0.33	0.953385	0.998616
0.33	0.28	0.953387	0.998612
0.33	0.25	0.953392	0.998606
0.4	0.4	0.917526	0.999238
0.4	0.3	0.917521	0.999238
0.25	0.25	No singularity	

Table A.2: Singular locations for varying modulus.

Location of singularity (y_6)			
E^-	$\nu^- = \nu^+$	Two possibilities	
10^{-3}	0.4	0.925426	0.991568
2.5×10^{-3}	0.4	0.947118	0.970261
10^{-3}	0.375	0.939462	0.989521
10^{-4}	0.3	0.971138	0.997739
10^{-5}	0.3	0.969066	0.999789
10^{-6}	0.3	0.968874	0.999979
10^{-7}	0.3	0.968855	0.999998
10^{-8}	0.3	0.968853	1
10^{-9}	0.3	0.968853	1

The singular configurations change when the Poisson's ratio and the modulus is changed. The y_6 values that correspond to singular configurations for a fixed modulus of the softer and stiff material with varying Poisson's ratio are given in Table A.1. As the Poisson's ratio of the stiff material is increased, there is one singular configuration for which the interface node moves away from the element node, and one more that moves towards it. The singular configurations for different modulus and Poisson's ratio is as shown in Table A.2. When the modulus of the soft material decreases, the same behavior of the interface node movement for singular configurations can be observed.

The interface traction magnitudes are high for singular configurations. The traction discontinuity becomes very large for all the configurations very close to singularity. This is the result of traction continuity being not exactly satisfied for bilinear rectangular elements. A small vertical displacement at the node $(0, 1)$ can result in a very large displacement at the interface point which passes through $x = 1$ line. Remedies to overcome such issues for extreme moduli ratios and Poisson's ratio values is an ongoing research.